

**HZDR-041**

# **DEVELOPMENT AND VALIDATION OF MODELS FOR BUBBLE COALESCENCE AND BREAKUP**

Yixiang Liao

Wissenschaftlich-Technische Berichte  
HZDR-041 · ISSN 2191-8708

**WISSENSCHAFTLICH-  
TECHNISCHE BERICHTE**

**hZDR**




HELMHOLTZ  
ZENTRUM DRESDEN  
ROSSENDORF

Wissenschaftlich-Technische Berichte  
**HZDR-041**

Yixiang Liao

**DEVELOPMENT AND VALIDATION OF MODELS FOR  
BUBBLE COALESCENCE AND BREAKUP**

**HZDR**

 **HELMHOLTZ**  
ZENTRUM DRESDEN  
ROSSENDORF

Druckausgabe: ISSN 2191-8708

Elektronische Ausgabe: ISSN 2191-8716

Die elektronische Ausgabe erscheint unter Creative Commons License (CC BY-NC-ND):

Qucosa: <http://fzd.qucosa.de/startseite/>

Die vorliegende Arbeit wurde sowohl als Dissertation an der Fakultät Maschinenwesen der Technischen Universität Dresden sowie als Wissenschaftlich-Technischer Bericht des Helmholtz-Zentrum Dresden – Rossendorf mit der Berichtsnummer **HZDR-041** veröffentlicht.

2013

Herausgegeben vom

Helmholtz-Zentrum Dresden - Rossendorf

Bautzner Landstr. 400

01328 Dresden

Germany

# **Development and Validation of Models for Bubble Coalescence and Breakup**

by

M. Sc. Yixiang Liao

born on 9th September 1974 in Hunan China

from Dresden

## **Ph.D. Thesis**

approved by the

Faculty of Mechanical Engineering

of

Dresden University of Technology

to receive the academic degree of

Doctor of Engineering (Dr.-Eng.)

Date of submission: January 4<sup>th</sup>, 2013

Date of defense: October 8<sup>th</sup>, 2013

Referees:

Prof. Dr.-Ing. habil. Uwe Hampel

Prof. Dr.-Ing. habil. Jochen Fröhlich

Chairman of the doctoral committee:

Prof. Dr.-Ing. Michael Beckmann

Supervisor:

Prof. Dr.-Ing. habil. Uwe Hampel

Dr. Dirk Lucas

Doctoral Committee:

Prof. Dr.-Ing. Michael Beckmann

Prof. Dr.-Ing. habil. Uwe Hampel

Prof. Dr.-Ing. habil. Jochen Fröhlich

Prof. Dr.-Ing. habil. Antonio Hurtado

PD Dr.-Ing. habil. Jörg Stiller

# **Entwicklung und Validierung von Modellen für Blasenkoaleszenz und -zerfall**

von der  
Fakultät Maschinenwesen  
der  
Technischen Universität Dresden  
zur  
Erlangung des akademischen Grades  
Doktoringenieur (Dr.-Ing.)  
angenommene

## **Dissertation**

von  
M. Sc. Yixiang Liao  
geboren am 09. September 1974 in Hunan China  
aus Dresden

Tag der Einreichung: 04. Januar 2013

Tag der Verteidigung: 08. Oktober 2013

Gutachter: Prof. Dr.-Ing. habil. Jochen Fröhlich

Prof. Dr.-Ing. habil. Uwe Hampel

Vorsitzender der Promotionskommission: Prof. Dr.-Ing. Michael Beckmann

Betreuer:

Prof. Dr.-Ing. habil. Uwe Hampel

Dr. Dirk Lucas

Promotionskommission:

Prof. Dr.-Ing. Michael Beckmann

Prof. Dr.-Ing. habil. Uwe Hampel

Prof. Dr.-Ing. habil. Jochen Fröhlich

Prof. Dr.-Ing. habil. Antonio Hurtado

PD Dr.-Ing. habil. Jörg Stiller

## Abstract

A generalized model for bubble coalescence and breakup has been developed, which is based on a comprehensive survey of existing theories and models. One important feature of the model is that all important mechanisms leading to bubble coalescence and breakup in a turbulent gas-liquid flow are considered. The new model is tested extensively in a 1D Test Solver and a 3D CFD code ANSYS CFX for the case of vertical gas-liquid pipe flow under adiabatic conditions, respectively. Two kinds of extensions of the standard multi-fluid model, i.e. the discrete population model and the inhomogeneous MUSIG (multiple-size group) model, are available in the two solvers, respectively. These extensions with suitable closure models such as those for coalescence and breakup are able to predict the evolution of bubble size distribution in dispersed flows and to overcome the mono-dispersed flow limitation of the standard multi-fluid model.

For the validation of the model the high quality database of the TOPFLOW L12 experiments for air-water flow in a vertical pipe was employed. A wide range of test points, which cover the bubbly flow, turbulent-churn flow as well as the transition regime, is involved in the simulations. The comparison between the simulated results such as bubble size distribution, gas velocity and volume fraction and the measured ones indicates a generally good agreement for all selected test points. As the superficial gas velocity increases, bubble size distribution evolves via coalescence dominant regimes first, then breakup-dominant regimes and finally turns into a bimodal distribution. The tendency of the evolution is well reproduced by the model. However, the tendency is almost always overestimated, i.e. too much coalescence in the coalescence dominant case while too much breakup in breakup dominant ones. The reason of this problem is discussed by studying the contribution of each coalescence and breakup mechanism at different test points. The redistribution of the gaseous phase from the injection position at the pipe wall to the whole cross section is overpredicted by the Test Solver especially for the test points with high superficial gas velocity. Besides the models for bubble forces, the simplification of the Test Solver to a 1D model has an influence on the redistribution process. Simulations performed using CFX show that a considerable improvement is achieved with comparison to the results delivered by the standard closure models. For the breakup-dominant cases, the breakup rate is again overestimated and the contribution of wake entrainment of large bubbles is underestimated. Furthermore, inlet conditions for the liquid phase, bubble forces as well as turbulence modeling are shown to have a noticeable influence, especially on the redistribution of the gaseous phase.



## Kurzfassung

Es wurde ein verallgemeinertes Modell für Blasenkoaleszenz und -zerfall entwickelt, das auf einer umfangreichen Recherche bestehender Theorien und Modellen basiert. Ein wichtiges Merkmal des Modells ist, dass alle wichtigen Mechanismen, die in einer turbulenten Blasenströmung zu Koaleszenz und Zerfall führen können, berücksichtigt werden. Das neue Modell wurde ausführlich jeweils in einem 1D Testsolver und dem 3D-CFD-Code ANSYS CFX für den Fall einer vertikalen Luft-Wasser-Rohrströmung unter adiabatischen Bedingungen getestet. Zwei Varianten für Erweiterungen des Standard-Multi-Fluid-Modells, das diskrete Populationsmodell und inhomogene MUSIG (MULTiple-Size-Gruppe) Modell, stehen in den Solvern zur Verfügung. Mit geeigneten Schließungsmodellen für Blasenkoaleszenz und -zerfall, sind sie grundsätzlich in der Lage die Entwicklung der Blasengrößenverteilung in dispersen Strömungen vorherzusagen und die Beschränkung des Standard-Multi-Fluid-Modells auf mono-disperse Strömungen zu überwinden.

Für die Validierung des Modells wurde die hochwertige Datenbasis der TOPFLOW-L12-Experimente für Luft-Wasser-Strömungen in einem vertikalen Rohr genutzt. Eine große Auswahl von Messpunkten, die die Blasenströmung, die turbulente-aufgewühlte Strömung sowie den Übergangsbereich abdecken, wurde in den Simulationen einbezogen. Der Vergleich zwischen den Simulationsergebnissen für Blasengrößenverteilungen, Gasgeschwindigkeiten und dem Gasvolumenanteil sowie den experimentellen Daten zeigt eine allgemein gute Übereinstimmung für alle ausgewählten Messpunkte. Mit zunehmender Gas-Leerrohrgeschwindigkeit ist die Entwicklung der Blasengrößenverteilung zuerst von Koaleszenz dominiert, dann von Zerfall und führt schließlich zu bi-modalen Verteilungen. Die jeweilige Tendenz wird in den Simulationen richtig wiedergegeben, allerdings fast immer überschätzt, d.h. in dem von Koaleszenz dominierten Fall wird die Koaleszenzrate überschätzt, in dem von Zerfall dominierten Fall ist die Zerfallsrate zu groß. Die Ursachen werden durch die Untersuchung des Beitrags der einzelnen Koaleszenz- und Zerfallsmechanismen für verschiedene Messpunkte diskutiert. Die Umverteilung der Gasphase von der Einspeisung an der Wand über den gesamten Rohrquerschnitt wird im Testsolver insbesondere für große Gasleerrohrgeschwindigkeiten überschätzt. Neben den Modellen für die Blasenkräfte hat die Vereinfachung des Testsolvers auf ein 1D-Modell einen Einfluss auf die Umverteilung. Die mit CFX durchgeführten Simulationen zeigen, dass eine erhebliche Verbesserung der Ergebnisse im Vergleich zu den Standardschließungsmodellen für Blasenkoaleszenz und -zerfall erzielt wird. Für die durch Zerfall dominierten Fälle wird die Zerfallsrate wiederum überschätzt und der Beitrag des Blaseneinfangs in die Nachlaufströmung einer großen Blase zur Koaleszenz wird unterschätzt. Darüber hinaus haben die Eintrittsbedingungen der flüssigen Phase, Blasenkräfte sowie Turbulenzmodellierung einen spürbaren Einfluss auf die Ergebnisse, vor allem auf die Umverteilung der Gasphase.

## Acknowledgements

This work has been carried out at the Institute of Safety Research, Helmholtz-Zentrum Dresden-Rossendorf, Germany within the framework of a project funded by the German Federal Ministry of Economics and Technology, project number 150 1348. Many people have contributed to the success of this project by their constant support and inspiration. I would like to take this opportunity to express my sincere gratitude to all of them for their constant support, discussion and valuable suggestion.

First of all I would like to thank my supervisor Professor Uwe Hampel for accepting to be my “Doktorvator”. Furthermore, many thanks go to Professor Frank-Peter Weiß for giving me the possibility to carry out this work. He always supported my work and guaranteed excellent working conditions as director of the Institute of Safety research.

I am deeply indebted to my internal advisor Dr. Dirk Lucas of Helmholtz-Zentrum Dresden-Rossendorf, Germany, whose patience, encouragement and constant guidance helped me during my research work and helped me to finish my work in time. For me, he has always been a constant source of inspiration and motivation. I have learned many things from him and I hope this work partially satisfy his expectation.

I am proudly thankful to all the scientist of the Department of Accident Analysis, especially Heads of the Department, Dr. Ulrich Rohde and subsequently Dr. Sören Kliem, for supporting me in all the administrative issues, as e.g. the part-time work at home after the birth of my son and the prolongation of my contract.

I would like to acknowledge my colleagues of the CFD group especially Dr. Eckhard Krepper and Pavel Apanasevich for their valuable suggestions and discussions, Swapna Singha Rabha and Dr. Gregory Cartland-Glover for checking and improving the English language of my thesis. I am also grateful for my colleagues of the TOPFLOW experiment group for providing the experimental data and supporting me in using the data for my work.

Besides, I would like to extend my gratitude to all support staff at the Institute of Safety Research for their assistance, especially the secretaries, Claudia Losinski, Petra Vetter, Annett Richter and special thanks to the computer administrator Torsten Berger.

I am most thankful to the German Federal Ministry of Economics and Technology for funding my research work through the program of competence maintenance in nuclear technology.

Finally, a great thanks to my husband Wenxing, for his love and continuous support, and my children Ye and Lei.

Yixiang Liao



## Contents

1	Introduction.....	1
1.1	Background and motivation for the thesis.....	1
1.2	Aim and tasks of this thesis.....	3
1.3	Outline of the thesis.....	4
2	State of the art.....	6
2.1	Standard Eulerian multi-fluid model.....	6
2.2	Modern extensions of the multi-fluid model.....	6
2.2.1	Four-field multi-fluid model.....	7
2.2.2	Population balance equation model.....	7
2.2.3	Transport equation for interfacial area density.....	7
2.2.4	Method of moments.....	8
2.2.5	The inhomogeneous MUSIG model.....	8
2.3	Coalescence models.....	10
2.3.1	Mechanisms leading to bubble coalescence.....	10
2.3.2	Collision frequency.....	11
2.3.3	Coalescence efficiency.....	19
2.4	Breakup models.....	28
2.4.1	Mechanisms leading to bubble breakup.....	28
2.4.2	Breakup frequency.....	30
2.4.3	Daughter bubble size distribution.....	45
2.5	Conclusions and discussions.....	53
2.5.1	Mechanisms and models for bubble coalescence.....	53
2.5.2	Mechanisms and models for bubble breakup.....	55
3	A generalized model for coalescence and breakup.....	56
3.1	Coalescence frequency.....	56
3.1.1	Collision frequency.....	56
3.1.2	Coalescence efficiency.....	60
3.1.3	Final expression for the coalescence frequency.....	62
3.2	Breakup frequency.....	64
3.2.1	Extensions.....	65
3.2.2	Final expression for the breakup frequency.....	68
3.3	Characteristics of the new model.....	68
3.3.1	Collision frequency.....	69
3.3.2	Coalescence efficiency.....	73
3.3.3	Total coalescence frequency.....	76
3.3.4	Breakup frequency.....	79
3.3.5	Daughter size distribution.....	80
3.4	Summary.....	83
4	Strategy for model test and validation.....	84
4.1	Interfacial force models.....	85

---

4.2	Two-phase turbulence modeling.....	89
4.2.1	General approach .....	89
4.2.2	BIT source term models.....	90
4.3	Solver .....	93
4.3.1	The Multi Bubble Size Class Test Solver .....	93
4.3.2	ANSYS 12.1 CFX-Solver .....	96
4.4	Experimental database.....	97
4.4.1	Requirements .....	98
4.4.2	TOPFLOW air-water experiment in a vertical pipe .....	99
5	Validation of the new model in frame of Test Solver.....	104
5.1	Extensions of the Test Solver.....	104
5.1.1	Turbulence modeling .....	104
5.1.2	Cross-sectional averaged gas void fraction.....	107
5.1.3	Cross-sectional averaged gas velocity .....	109
5.2	Parameter study by using CFD results.....	111
5.2.1	Single-phase flow.....	111
5.2.2	Two-phase flow .....	114
5.3	Implementation and test of available models .....	117
5.3.1	Test cases .....	117
5.3.2	Results.....	118
5.4	Implementation and test of the new model .....	126
5.4.1	Cross-sectional averaged bubble size distribution at Level R .....	126
5.4.2	Evolution of bubble size distribution along the pipe .....	127
5.4.3	Evolution of average bubble size along the pipe .....	129
5.4.4	Radial gas volume fraction profile at Level R.....	132
5.4.5	Evolution of radial gas volume fraction profiles along the pipe.....	133
5.4.6	Radial gas velocity profile .....	135
5.4.7	Influence of turbulent dispersion force.....	136
5.4.8	Influence of lift force .....	137
5.4.9	Influence of wall lubrication force.....	138
5.4.10	Contribution of each coalescence and breakup mechanism .....	139
5.4.11	Contribution of the mechanism of wake-entrainment .....	140
5.4.12	Influence of two-phase turbulence modeling.....	141
5.5	Discussions .....	155
6	Validation of the new model in ANSYS 12.1 CFX-Solver.....	157
6.1	Setups .....	157
6.1.1	Mesh details .....	157
6.1.2	Boundary conditions .....	159
6.1.3	Initial conditions .....	160
6.1.4	Convergence criteria .....	160
6.1.5	Discretization of bubble size.....	160
6.2	Results .....	161
6.2.1	Evolution of bubble size distribution along the pipe .....	161
6.2.2	Evolution of radial gas volume fraction profile along the pipe .....	167
6.2.3	Evolution of radial gas velocity profiles along the pipe .....	169

---

## Contents

---

6.2.4	Influence of liquid inlet conditions .....	170
6.2.5	Influence of wall lubrication force.....	172
6.3	Influence of two-phase turbulence modeling .....	174
6.4	Comparison with the predictions by standard closure models.....	180
6.5	Comparison with the results of Test Solver .....	183
6.6	Influence of interphase drag force .....	185
6.7	Discussion .....	185
7	Conclusion .....	187
8	Nomenclature.....	191
9	Reference .....	195
10	List of Publications .....	204

---



# 1 Introduction

Two-phase flow refers to any fluid flow consisting of two phases or a liquid immiscibility. One can classify them according to the state of the two phases or components, e.g. gas-liquid, gas-solid, liquid-liquid and liquid-solid. Of the four types of two-phase flows, it is gas-liquid flows, which will be discussed in this work. These flows are the most complex since they combine the characteristics of a deformable interface and the compressibility of the gaseous phase [1].

## 1.1 Background and motivation for the thesis

The range of gas-liquid flow applications in today's technology is immense. Examples can be found in nuclear reactors, chemical reactors, food production, gas and oil pipelines and automotive industry. In the design and optimization of light water-cooled nuclear reactors, e.g. BWR (Boiling Water Reactor) and PWR (Pressurized Water Reactor), basic understanding of gas-liquid flow is of special importance to guarantee the safety of the system. For example, under normal operation conditions of BWR plants, saturated steam is produced in the reactor core and directly used to drive a turbine. On the other hand, modern PWR benefits from the effective heat transfer coefficient achieved by nucleate boiling in the reactor core although steam driving the turbine is produced in a steam generator outside the core. Furthermore, knowledge of gas-liquid flow is indispensable when considering postulated accidents in the nuclear system. For example, one of the most severe accidents in a PWR plant is the loss of coolant (LOCA), where the re-circulating coolant may flash into steam. The involved processes are extremely complex and have been one of the main focus areas for the research in gas-liquid flows for many decades [1].

Since nuclear experimentation at full scale or with entire systems is only possible in a limited number of cases, numerical simulations play an important role in the research of complex gas-liquid flow situations that arise in a normal or accident situation. The traditional system codes, which have been successfully used for this purpose for many years are based on empirical correlations that are specific for certain two-phase flow regimes. These regime-dependent empirical correlations are implemented into 1D system codes where the boundaries between regimes are specified through static regime transition criteria. Such an approach, however, does not represent the flow dynamics since the static flow regimes are neither able to predict the change of flow regime along the flow path in the case of stationary flows nor the time and space dependent flow structure in the case of transient flows [2]. As it is known in gas-liquid flow, the distribution of interfacial structure can take any possible flow regime. Taking vertical pipe flow as an example possible regimes are bubbly flow, slug flow, churn-turbulent flow, wispy annular flow and annular flow. The particular flow regime that is observed to occur is dependent on the properties and flow parameters of the phases, pipe size and orientation, configuration of the inlet and so on. Moreover, the flow regimes continuously evolve along the flow path via various bubble dynamic mechanisms such as bubble coalescence and breakup. Sommerfeld [3] pointed out that in gas-liquid flow, if the volume fraction of gas exceeds c.a. 3% collision and coalescence between bubbles becomes important. As a result, the flow regime changes from homogenous mono-dispersed bubbly flow to heterogeneous poly-dispersed flow. On the other hand, bubbles are subject to



destroying stresses from the surrounding continuous liquid phase. When the destroying force is larger than the restoring force such as surface stress, the bubble will deform and break up into small bubbles. In conclusion, in order to obtain accurate predictions for the transient evolution of flow regime, it is necessary to develop more sophisticated numerical methods than system codes.

The considerable increase in the available computational power and tools allows the use of CFD (Computational Fluid Dynamics) codes to approach local phenomena in much greater detail. In the CFD simulations of gas-liquid flows there are three basic numerical methods discussed in the literature, that is, Direct Numerical Simulation (DNS), Euler-Lagrange (E-L) and Euler-Euler (E-E) methods. The three methods differ in the scale range that is explicitly solved. The DNS or interface resolving method is at the lowest level of time and length scale. It aims to resolve all interactions between two phases and needs no turbulence and interfacial exchange models. The main difficulty of the DNS method is the highest computational load, and as a result numerical methods of this type have been applied mostly to flows around a single bubble or to systems involving only a relatively small number of bubbles or particles. Another difficulty is the moving phase-interface whose shape is a part of the solution. To keep the interface numerically sharp, i.e. to avoid any artificial smearing of the interface during the computation, special numerical algorithms have to be developed. Nowadays mainly three types of methods are used, the volume-of-fluid method (VOF), the level-set method (LS) and the front-tracking (FT) method [4].

For systems at intermediate scale, the E-L or discrete bubble approach can be used where the liquid phase is solved by phase-averaged equations while bubbles are modelled by point force distributions at the discrete location of bubbles and the equation of motion is solved by Newton's second law. This method is particularly suited to study the effect of bubble-bubble and/or bubble-wall interactions and it provides for closure for bubble-bubble interactions since the scale of distances between bubbles is explicitly solved. However, contrary to the DNS approach, the flow field at the scale of an individual bubble is not resolved, and therefore closure laws for bubble-liquid interaction, e.g. bubble forces, have to be provided [5]. The major disadvantage of the Euler-Lagrange approach is the complexity of the interfacial coupling, since the coupling between two different solvers, i.e. the Eulerian and Lagrangian solver, is difficult. Therefore, numerical simulations of this type are often done by one-way coupling where the effects that the presence of bubbles may have on the liquid phase are neglected. As a result, the Eulerian velocity field of liquid can be computed independently of trajectories of bubbles. Furthermore, such a method is still limited to dilute gas-liquid flows otherwise a statistical approach is used as an approximation where a computation parcel contains thousands of real bubbles.

Finally, the E-E or continuum approach is at the largest time and length scales where both the gas and liquid phase are solved by phase-averaged equations and the macroscopic effect of interactions between phases is modelled by constitutive equations. Since it is the most computationally efficient this numerical method is particularly suited to model gas-liquid flows in industrial scale equipments. Another advantage of the Euler-Euler model is that instead of limiting to dilute bubbly flow it can be used to compute any flow regime provided that adequate closure relations

about bubble-bubble and bubble-liquid interactions are known. Nevertheless, the reliance on closure models is exactly a weak link in this approach. To date, more effort is still required to develop phenomenological closure models for bubble forces, turbulence generated by the bubble and bubble dynamics such as bubble coalescence and breakup.

### **1.2 Aim and tasks of this thesis**

This work is aimed at developing a generally applicable closure model for bubble coalescence and breakup in the framework of the E-E approach. The goal of the new model is to take into account all important mechanisms that lead to bubble coalescence and breakup in turbulent gas-liquid flow.

In the last half century, numerous achievements have been made in the theoretical analysis and modeling of bubble coalescence and breakup processes. Correspondingly, a number of theories and models were proposed. Nevertheless, they are found to be the weakest point in the modeling of poly-dispersed flows [6] [7]. There are still some obstacles to be overcome such as the superposition of different mechanisms, determination of critical conditions, and insufficient knowledge about two-phase turbulence modeling. As it is known, bubble coalescence and breakup rates depend on turbulence parameters since turbulence is one important promoting reason for it. Up to now no mature turbulence modeling approaches for two-phase flows exist, i.e. when bubble coalescence and breakup models are used in CFD codes, their input parameters are often not well defined. Many CFD codes consider the bubble induced turbulence by modifying the turbulent viscosity, e.g. using the model of Sato et al. [8]. This method might result in a satisfactory simulation of velocity fields, but it hardly reflects the influence of bubbles on the turbulent kinetic energy and dissipation rate.

Due to all the difficulties, the models at hand for bubble coalescence and breakup are only validated for certain cases. No model is available which is applicable for a wide range of flow situations.

In general, all of the models available in literature have one or more following shortcomings:

- Only turbulence is considered while other mechanisms are neglected without further validation
- Bubble-eddy collision are assumed and detailed information about the size, shape as well as energy of eddies is required
- Turbulence parameters are not correctly calculated, e.g. simple empirical correlations are used and the influence of bubble-induced turbulence is not considered
- Integrals over the size or/and energy of turbulent eddies are included, which restricts the computation speed dramatically and make the model more difficult to implement into CFD codes
- Most breakup models need to assume a separate daughter size distribution function (e.g. Beta function, Normal function), which usually has no physical meaning

In a word, further effort is required to develop and validate suitable closure models for bubble coalescence and breakup.

Accordingly, the main tasks of this work are:

- (1) Extensive literature research on available theories and models for bubble coalescence and breakup
- (2) Implementation and testing of some typical models taken from literature in the Multi Bubble Size Class Test Solver [2] with help of TOPFLOW experimental data [9]
- (3) Theoretical development of a new model framework for bubble coalescence and breakup which are aimed to overcome the limitations in the existing models
- (4) Implement and test of the new model framework in the Multi Bubble Size Class Test Solver [2]. The calculated results of bubble size distribution, mean bubble size as well as gas volume fraction and velocity were compared with the TOPFLOW experimental data [9]
- (5) Implement and test the new model framework in CFX. The predicted bubble size distributions were compared with those delivered by the standard closure models in CFX and by the Test Solver
- (6) Study via the Test Solver and CFX, the influence of two-phase turbulence modeling on the results of turbulence parameters as well as bubble size distribution, gas volume fraction as and velocity fields

### 1.3 Outline of the thesis

The remainder of this thesis consists of six chapters. Brief overview of these chapters follows:

Chapter 2: In this chapter state of the art of basic theory regarding simulation of poly-dispersed gas-liquid flows is reviewed. The information is confined to Eulerian multi-fluid model and those subjects that are relevant for the prediction of local bubble size distribution. Information is presented about the following items: (a) the limitation of the standard Eulerian multi-fluid model, (b) the extended Eulerian multi-fluid model for taking into account the evolution of local bubble size or interfacial area density distribution, (c) status of closure models for bubble coalescence and breakup, (d) discussion about limitations and possible improvements of existing models.

Chapter 3: A new generalized closure model is proposed for bubble coalescence and breakup. The underlying theory and the advantage of the extended model are introduced. The characteristics of the collision frequency, coalescence efficiency, breakup frequency and daughter bubble size distribution predicted by the new model are analyzed

Chapter 4: The strategy for the test and validation of the new model is discussed. The presented information includes (a) the reason for the choice of a vertical upward flow configuration, (b) closure models for interfacial forces and bubble-induced turbulence, (c) the requirement for experimental data and the review on available databases, (d) advantages and examples of TOPFLOW experimental data [9], (e)

solvers, i.e. Test Solver and ANSYS 12.1 CFX-Solver, used for the validation calculations

Chapter 5: Models for bubble coalescence and breakup are tested in the Test Solver by using TOPFLOW experimental data [9]. Firstly, the original Test Solver is extended and validated with the results obtained by the CFX solver for some crucial parameters such as turbulence parameters. Then, some typical models for bubble coalescence and breakup taken from the literature are tested by the prediction on the bubble size distribution and mean bubble diameter. The new model is extensively tested by predicting the evolution of (a) bubble size distribution, (b) radial gas volume fraction profile, (c) radial gas velocity profile, and the influence of (d) the non-drag forces, i.e. the turbulent dispersion force, the lift force and the wall lubrication force, (e) the two-phase turbulence modeling approaches.

Chapter 6: The new model is implemented and validated in the commercial ANSYS 12.1 CFX-Solver. The mesh information, boundary condition and convergence criteria are introduced. The predicted results are compared with the TOPFLOW experimental data [9], the results predicted by the standard models used by the CFX Solver for bubble coalescence and breakup as well as the results obtained by the Test Solver. The influence of the liquid inlet conditions, interphase drag force, wall lubrication force as well as the two-phase turbulence modeling methods is reviewed.

Chapter 7: Conclusions and the recommendations for the future research are given in this chapter.

## 2 State of the art

In this chapter, the state of the art of Eulerian multi-fluid model and the corresponding constitutive models for the modelling of poly-dispersed bubbly flows are discussed.

### 2.1 Standard Eulerian multi-fluid model

A general form of the Eulerian multi-fluid fundamental equations for bubbly flows at adiabatic conditions is [10]:

Mass conservation:

$$\frac{\partial}{\partial t}(\alpha_\alpha \rho_\alpha) + \nabla \cdot (\alpha_\alpha \rho_\alpha \vec{u}_\alpha) = S_\alpha \quad \text{Eq. 2-1}$$

Momentum conservation:

$$\begin{aligned} \frac{\partial}{\partial t}(\alpha_\alpha \rho_\alpha \vec{u}_\alpha) + \nabla \cdot [\alpha_\alpha \rho_\alpha (\vec{u}_\alpha \otimes \vec{u}_\alpha)] \\ = \nabla \cdot [\alpha_\alpha \mu_\alpha (\nabla \vec{u}_\alpha + (\nabla \vec{u}_\alpha)^T)] - \alpha_\alpha \nabla p_\alpha + \alpha_\alpha \rho_\alpha \vec{g} + \vec{M}_\alpha \end{aligned} \quad \text{Eq. 2-2}$$

where  $\alpha_\alpha$ ,  $\rho_\alpha$ ,  $\mu_\alpha$ ,  $u_\alpha$ ,  $p_\alpha$  represent void fraction, density, viscosity, velocity and pressure of the phase  $\alpha$ , respectively, and  $g$  is the gravitational acceleration.

Source terms  $S_\alpha$  represent the mass transfer between gaseous phases due to bubble breakup and coalescence processes and the momentum transfer caused by bubble breakup and coalescence is neglected.  $M_\alpha$  is the interfacial momentum transfer per unit time (interfacial force) between gaseous and liquid phases, which is taken into account by drag and non-drag forces. That means that the sum of interfacial forces for phase  $\alpha$  is given by:

$$\vec{M}_\alpha = \vec{F}_{\alpha,D} + \vec{F}_{\alpha,TD} + \vec{F}_{\alpha,L} + \vec{F}_{\alpha,W} \quad \text{Eq. 2-3}$$

At the right hand side of the Eq. 2-3 are drag force, turbulent dispersion force, lift force and wall lubrication force, respectively. Since bubble forces depend not only on the velocity field but also on bubble size and turbulence, further constitutive models or extensions are needed to capture local bubble size evolution and turbulence parameters.

### 2.2 Modern extensions of the multi-fluid model

With the standard multi-fluid model presented above in a strict sense only mono-dispersed flows with single-value bubble size can be simulated. In a real dispersed flow, often a spectrum of bubble sizes is present (poly-dispersed flow). Moreover, the bubble size is not spatially and temporarily constant if bubble coalescence and breakup occurs. To overcome this restriction, the standard multi-fluid model is often

extended in the modern simulation of poly-dispersed flow. In general, there are five different extension approaches under development.

### 2.2.1 Four-field multi-fluid model

The first approach is the four-field multi-fluid model, which was firstly proposed by Lahey and Drew [11]. The main difference between the extended and standard multi-fluid model is that in the extended model each of the two fluids maybe either continuous or dispersed in different regions of space. The four fields are therefore given by continuous liquid, continuous gas, dispersed liquid and dispersed gas. Mass and momentum conservative equations are solved for each of the four fields. This model seems to be very promising for slug flow or annular flow regimes especially with phase transfer. However, it is not ideal for the modelling of bubble-bubble interactions in a poly-dispersed flow, since the dispersed gas is still treated in a mono-dispersed way.

### 2.2.2 Population balance equation model

Another promising concept to overcome the mono-dispersed flow limitation of the standard multi-fluid model is the Population Balance Equation Model (PBEM), which is based on the introduction of population classes. In the PBEM, an additional transport equation analogous to Boltzmann's transport equation is introduced to trace the evolution of local bubble number density. By considering source or sink terms caused by bubbles entering and leaving a control volume through different mechanisms, the number density transport equation can be written as [12] ~ [14]

$$\frac{\partial n(V, \vec{r}, t)}{\partial t} + \nabla_x \cdot [u(V, \vec{r}, t) \cdot n(V, \vec{r}, t)] = S \quad \text{Eq. 2-4}$$

where  $n$ ,  $u$ ,  $V$ ,  $\vec{r}$ ,  $t$ , are bubble number density, convective velocity, bubble volume, spatial and temporal coordinate, respectively. On the right hand side of the equation are source or sink terms caused by different mechanisms.

The equation can be solved by dividing the internal coordinate (here is the volume of bubbles,  $V$ ) into  $N$  classes. This discretization method called method of classes or spectral method. Each of these classes is treated as a dispersed phase with single size and separate velocity field. A mass and momentum conservative equation is respectively solved for each class leading to  $2(N+1)$  equations in adiabatic condition. If discretization is fine enough, the size-dependent source term processes can be well modelled by this approach, however, it can consume extensive computer resources. In order to capture the effect of the transient change of bubble size at low computational costs, a variety of approximate methods have been proposed such as interfacial area transport equation (IATE), method of moments (MOM), and multiple-size group model (MUSIG).

### 2.2.3 Transport equation for interfacial area density

The method of interfacial area transport equation (IATE) was first proposed by Ishii and his co-workers [15] [16]. It is based on the intuition that in a two-phase flow the interfacial area density is of importance, since it determines directly the interfacial transfer processes. Therefore, similarly to the PBEM method, a transport equation is introduced to trace the evolution of interfacial area density. Instead of a globally

---

mono-dispersed flow in the standard multi-fluid model a local equivalent bubble size can be obtained from the interfacial area density if the shape of the bubble is specified. The equivalent bubble size is adopted for the calculation of interfacial transfer terms in the extended multi-fluid model. On the other hand, the velocity of the dispersed phase in the multi-fluid model is used as the convective velocity of interfacial area density in the transport equation. In contrast to the PBEM model, this method is much more efficient since no additional mass and momentum conservative equations are introduced. However, it can only model a change of bubble size but not a change of bubble shape since the shape of bubble has to be specified for the calculation of equivalent bubble size. Recently, the concept of two-group IATE has been proposed by Ishii and his co-workers [17] ~ [19] as a more general model. In this approach bubbles are divided into two groups, i.e. the spherical/distorted bubble group and the cap/slug bubble group. For each group a separate transport equation is solved for interfacial area density. In addition a mass equation and a momentum conservative equation are needed to be solved for each group.

In a way similar to the PBEM method, different phenomena create or absorb interfacial area, such as bubble coalescence and breakup. They are taken into account through source terms on the right hand side of the transport equation. Nevertheless, these size-dependent source terms can hardly be predicted correctly by an assumption of one or two size groups.

#### **2.2.4 Method of moments**

The method of moments (MOM) solves the evolution of the bubble size distribution by tracking the time dependence of bulk properties, i.e., moments of the distribution function. Transport equations are solved for some lower-order moments and the corresponding bubble size distribution is approximately reconstructed from the prognostic moments. One of the main limitations in the MOM is the closure problem. In the traditional MOM the evolution of lower-order moments usually cannot be expressed by the moments themselves due to size-dependent source terms. As an alternative, McGraw [20] developed the so-called quadrature method of moments (QMOM), which is based on the approximation of the unclosed terms by means of n-points Gaussian quadrature. The main limitation of QMOM is the assumption of spatial homogeneity. In other word, the convective term is neglected in the transport equation of moments. Recently, the QMOM is extended to handle inhomogeneous cases where each prognostic moment is transported by its own velocity, the so-called DQMOM method [21]. In DQMOM, the transport equations are solved directly for the abscissas and weights of the quadrature approximation instead of moments. Another difficulty of the moment model is the reconstruction procedure. The chosen prognostic moments must fulfil certain conditions in order to ensure the existence of a function for the corresponding bubble size distribution [22].

#### **2.2.5 The inhomogeneous MUSIG model**

The last method discussed here is the multiple-size group model (MUSIG), which is similar to the PBEM. The MUSIG model was firstly proposed by Lo [23], in which a mass conservative equation is solved for each bubble size group while a common velocity field is assumed for all size groups. With this simplification, up to 60 classes can be taken into account. However, the performance of this so-called homogeneous

MUSIG model is limited to convection dominated bubbly flows or bubbles with small inertia, since it is based on the assumption of a homogeneous velocity field applied to all bubble size classes. Alternatively, an inhomogeneous MUSIG model is presented by Krepper for poly-dispersed flow [7]. As shown in Figure 2.1, in the new MUSIG model, the gaseous phase is divided firstly into  $N$  phases/velocity groups, where each group is characterized by its own velocity field. Furthermore, each velocity group  $j$  is divided into a number of sub-size groups  $M_j$ ,  $j=1, 2, \dots, N$ . The PBEM considering coalescence and breakup is applied to the sub-size groups,  $k=1, 2, \dots, \Sigma M_j$ . Therefore, the inhomogeneous MUSIG model is able to take into account the heterogeneous velocity fields of bubbles with different size and at the same time it allows sufficient size groups to model the process of coalescence and breakup accurately with acceptable computation cost.

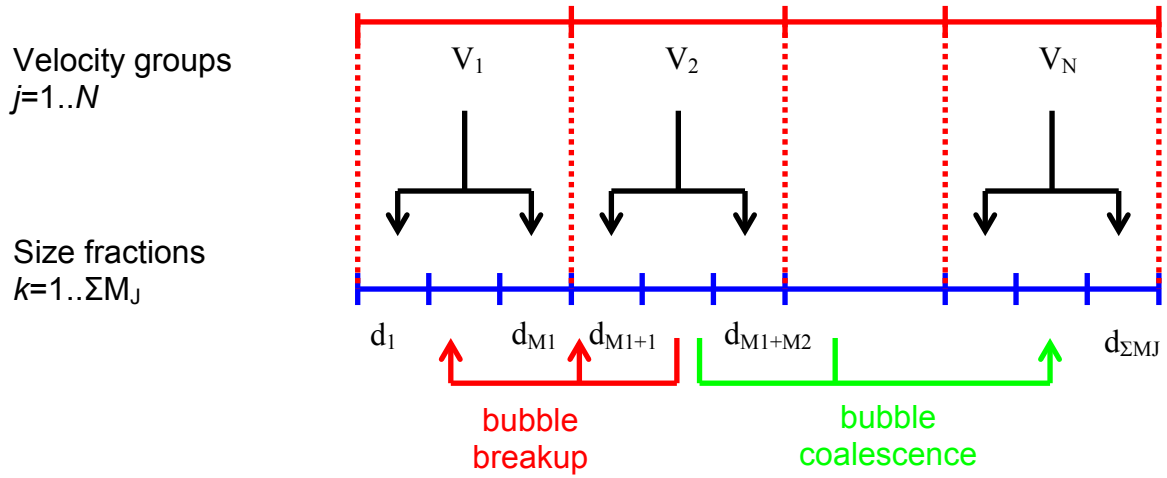


Figure 2.1 Schematic view of the inhomogeneous MUSIG model [24]

Defining  $f_k$  as the size fraction of the sub-size group  $k$ , we have

$$f_k \alpha_j = \alpha_k; \quad \sum_{k=1}^{M_j} f_k = 1; \quad \sum_{j=1}^N \alpha_j = \alpha_g \quad \text{Eq. 2-5}$$

where  $j$  is the velocity group that the sub-size group  $k$  belongs to (see Figure 2.1) and  $\alpha_g$  is the volume fraction of the whole gaseous phase.

The inhomogeneous MUSIG model solves the transport equations for all size fractions  $f_k$ :

$$\frac{\partial}{\partial t} (\rho_j \alpha_j f_k) + \nabla \cdot (\rho_j \alpha_j f_k \vec{u}_j) = S_k \quad \text{Eq. 2-6}$$

In adiabatic situation, the source term  $S_k$  accounts for: (i) the birth of bubbles of size  $k$  due to breakup of bubbles of larger size and coalescence of bubbles of smaller size,  $B_{bk}, B_{ck}$ ; and (ii) the death of bubbles of size  $k$  due to both break up and coalescence encountered in this size group,  $D_{bk}, D_{ck}$ .

$$S_k = B_{bk} - D_{bk} + B_{ck} - D_{ck} \quad \text{Eq. 2-7}$$



These rate terms may further be expressed as

$$B_{bk} = \rho_j \alpha_j \sum_{i>k} \Omega(d_i, d_k) f_k \quad \text{Eq. 2-8}$$

$$D_{bk} = \rho_j \alpha_j \sum_{i<k} \Omega(d_k, d_i) f_k \quad \text{Eq. 2-9}$$

$$B_{ck} = (\rho_j \alpha_j)^2 \frac{1}{2} \sum_{l<k} \sum_{i<k} \Gamma(d_l, d_i) X_{ilk} f_i f_l \frac{d_l^3 + d_i^3}{d_l^3 d_i^3} \quad \text{Eq. 2-10}$$

$$D_{ck} = (\rho_j \alpha_j)^2 \sum_i \Gamma(d_k, d_i) \frac{1}{d_i^3} f_i f_k \quad \text{Eq. 2-11}$$

where  $\Omega$  and  $\Gamma$  are breakup and coalescence kernel functions, respectively.

From the above it can be seen that in order to trace the spatial and temporary evolution of bubble size by using the different extended methods of the multi-fluid model, kernel functions for bubble coalescence and breakup must be known. Bubble coalescence and breakup has been a subject of many theoretical and experimental investigations over the past years. A variety of theories and models were proposed in the literature for the calculation of bubble coalescence and breakup rate in gas-liquid flow. Since detailed information about the difference between bubble-bubble coalescence and drop-drop coalescence is still missing, mechanisms and models for these two cases are usually assumed to be transferable from one to another.

## 2.3 Coalescence models

Compared to breakup processes, bubble coalescence is considered more complex [25], since it involves not only interactions of bubbles with the surrounding liquid, but also those between bubbles themselves once they are brought together by the external flow.

### 2.3.1 Mechanisms leading to bubble coalescence

It is obvious that the collision of bubbles is the premise of coalescence between them. The collision between bubbles is caused by relative motion, which may be caused by a variety of mechanisms, i.e. the flow conditions in the external flow. At least five sources of velocity difference between bubbles can be distinguished in a turbulent gas-liquid flow:

- i) turbulent fluctuations in the surrounding liquid
- ii) velocity gradients in the bulk flow
- iii) shear rate inside eddies
- iv) size-dependent rise velocities
- v) wake interactions

After colliding, bubbles can either coalesce or separate without coalescing. For the calculation of the probability of coalescence during a collision event, there are in general three kinds of theories discussed in the literature, i.e. film drainage model, energy model and critical approach velocity model. The first is the most popular one. Shinnar and Church [26] stated that after colliding two bubbles may cohere together and they be prevented from coalescing by a thin film of liquid trapped between them.

Attractive forces between the interfaces drive the film to drain out until it collapses, and coalescence follows. According to the film drainage model, coalescence will occur only if the interaction time exceeds the time needed for the intervening film to drain out down to the critical rupture thickness. However, in reality the duration of collisions is limited due to the relative motion between two colliding bubbles.

In contrast, Howarth [27] believed that the attraction force between two colliding interfaces is usually of molecular nature and it is too weak in comparison with the turbulent dynamic force to control the coalescence probability. Howarth [27] argued that whether coalescence will occur or not, it depends on the impact of collisions. During “energetic collisions”, when the approach velocity of the two colliding bubbles exceeds a critical value, immediate coalescence without liquid film capturing and thinning will be the dominant mechanism.

However, the experimental findings of Doubiez [28] and Duineveld [29] showed that small approach velocities lead to high coalescence efficiency. According to these results, in the recent work of Lehr et al. [30] [31], a so-called critical approach velocity model was introduced. If the approach velocity is smaller than a critical value, the coalescence efficiency is set as 1.0 otherwise the efficiency is equal to the ratio of the critical velocity to the approach velocity.

In summary, the coalescence process consists of two subprocesses, i.e. collision and coalescence. For the calculation of coalescence frequency or specific coalescence rate, a general physical model is obtained by multiplying the collision frequency  $h(d_i, d_j)$  with a coalescence efficiency  $\lambda(d_i, d_j)$ :

$$\Gamma(d_i, d_j) = h(d_i, d_j) \lambda(d_i, d_j) \quad \text{Eq. 2-12}$$

The collision frequency is determined by bubble size and the mechanism causing relative motion between bubbles. On the other hand, the coalescence efficiency depends on the feature of the colliding interface, flow conditions in the liquid film as well as the theory telling whether coalescence occurs. There are a large number of models available in the literature for the calculation of collision frequency and coalescence efficiency, respectively. Some representable theories and models are illustrated in Figure 2.2 on the next page.

### 2.3.2 Collision frequency

As mentioned already there are a variety of mechanisms that promote collisions among bubbles. For the calculation of the collision frequency caused by different mechanisms, different models should be employed.

#### **Turbulent random motion-induced collisions**

The random motion of bubbles caused by turbulent fluctuation is usually assumed to be similar to the case of gas molecules' movement. Following the classical kinetic gas theory, the frequency of turbulence-induced collisions can be interpreted as the effective volume swept by the two approaching bubbles per unit time [55], i.e.

$$h(d_i, d_j) = S_{ij} u_{rel} \quad \text{Eq. 2-13}$$

where  $S_{ij}$  is the cross-sectional area of the two colliding bubbles and calculated as:

$$S_{ij} = \frac{\pi}{4} (d_i + d_j)^2 \quad \text{Eq. 2-14}$$

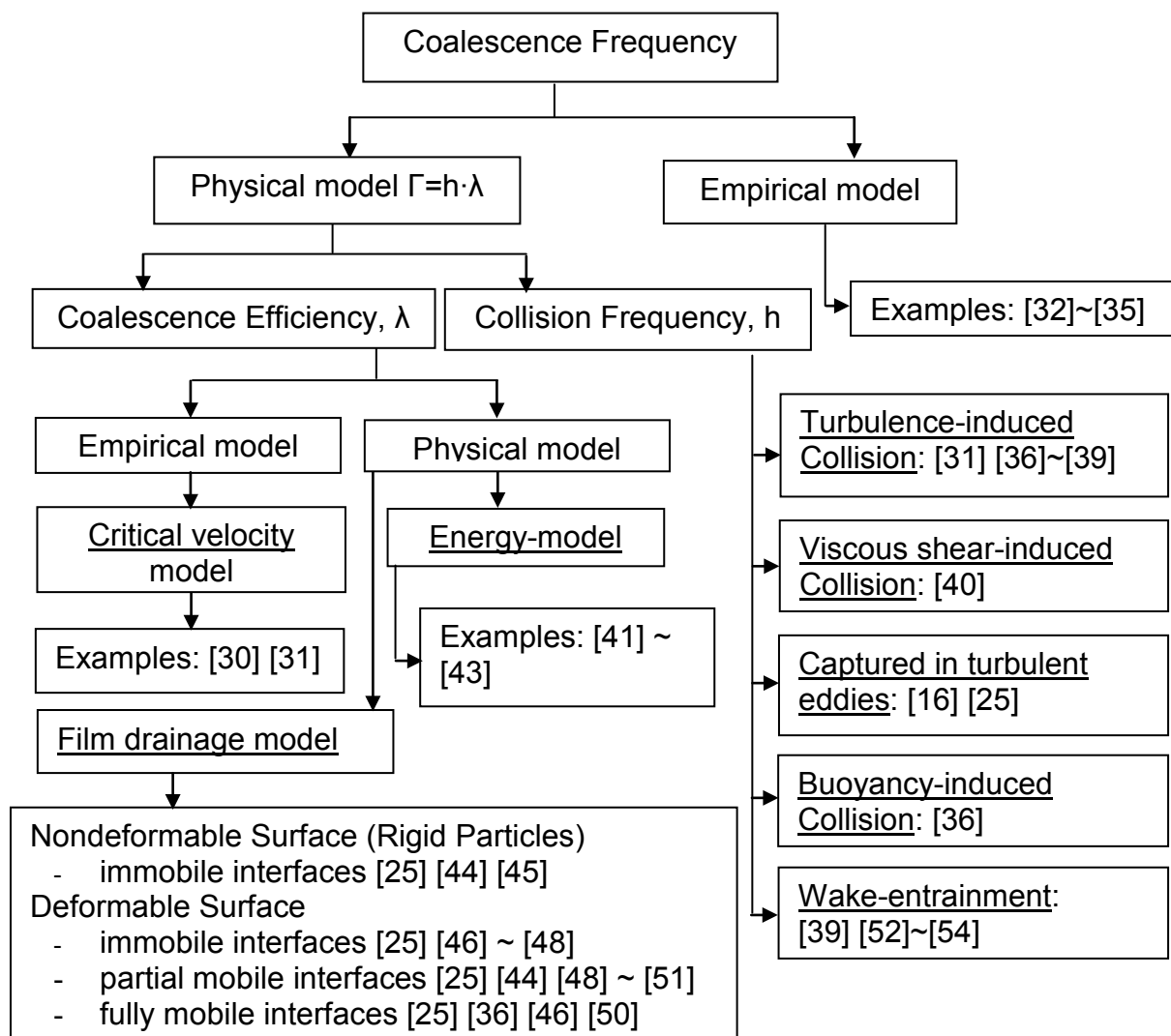


Figure 2.2 Classification of theories and models for coalescence frequency

In order to determine the approach velocity  $u_{rel}$  in Eq. 2-13 it is assumed that bubbles always take the velocity of an eddy of equal size [56] ~ [59]. As a result, the turbulence-induced relative velocity between two bubbles with size  $d_i$  and  $d_j$  is approximated by the mean-square root of two equivalent eddy-velocities:

$$u_{rel} = (u_{ti}^2 + u_{tj}^2)^{1/2} \quad \text{Eq. 2-15}$$

where  $u_{ti}$  is the velocity of eddy with size  $d_i$ .

For the determination of eddy velocity  $u_t$ , the inertial subrange of isotropic turbulence is frequently assumed. Thus, by applying classical turbulence theories one can get:

$$u_t^2 = C_1 (\varepsilon d)^{2/3} \quad \text{Eq. 2-16}$$

where  $C_1$  is an empirical constant and often assumed to have a value of about 2.0 except that 8.2 used by Martínez-Bazán et al. [59].

Finally, the collision frequency can be expressed as [57] [58]:

$$h(d_i, d_j) = C_2 \frac{\pi}{4} (d_i + d_j)^2 (d_i^{2/3} + d_j^{2/3})^{1/2} \varepsilon^{1/3} \quad \text{Eq. 2-17}$$

Although Eq. 2-17 is widely used, some modifications were proposed in most recent work. Firstly, the effect of size ratio between bubbles and eddies is considered, while in the original model bubbles are always assumed to be in the inertial turbulence subrange and have the same velocities as equal-sized eddies. According to Colin et al. [60], eddies are not efficient to move the bubbles if a bubble is larger than the integral length scale of the turbulence  $l_e$ . As a result, turbulence-induced collisions may occur only in the following two cases

$$\text{Case 1: } (d_i < l_e; d_j < l_e), u_{rel} = \frac{C_t}{\sqrt{1.61}} \left( \varepsilon \frac{d_i + d_j}{2} \right)^{1/3} \quad \text{Eq. 2-18}$$

$$\text{Case 2: } (d_i < l_e; d_j > l_e), u_{rel} = \frac{C_t}{\sqrt{1.61}} (\varepsilon d_i)^{1/3} \quad \text{Eq. 2-19}$$

where the coefficient,  $C_t$ , takes into account the velocity difference between bubbles and eddies, while the factor  $1/\sqrt{1.61}$  considers the deceleration during the approach process due to an increase in the virtual mass of bubbles.

The second modification is to consider the existence of bubbles reducing the free space for bubble movement, which can cause an increase in collision frequency. The effect can be described by multiplying the collision frequency in Eq. 2-17 with a factor  $\gamma$ . Different expressions used for the factor  $\gamma$  in the literature are summarized in Table 2.1 and its dependence on gas volume fraction  $\alpha_g$  is shown in Figure 2.3.

Table 2.1 Different expressions used for the factor  $\gamma$

References	Factor $\gamma$	$\alpha_{\max}^*$
Wu et al. [39]	$\frac{1}{\alpha_{\max}^{1/3} (\alpha_{\max}^{1/3} - \alpha_g^{1/3})}$	0.8
Hibiki and Ishii [61] [62]	$\frac{1}{(\alpha_{\max} - \alpha_g)}$	0.520 [61] 0.741 [62]
Wang et al. [37] [38]	$\frac{\alpha_{\max}}{\alpha_{\max} - \alpha_g}$	0.8

\* maximum possible gas holdup

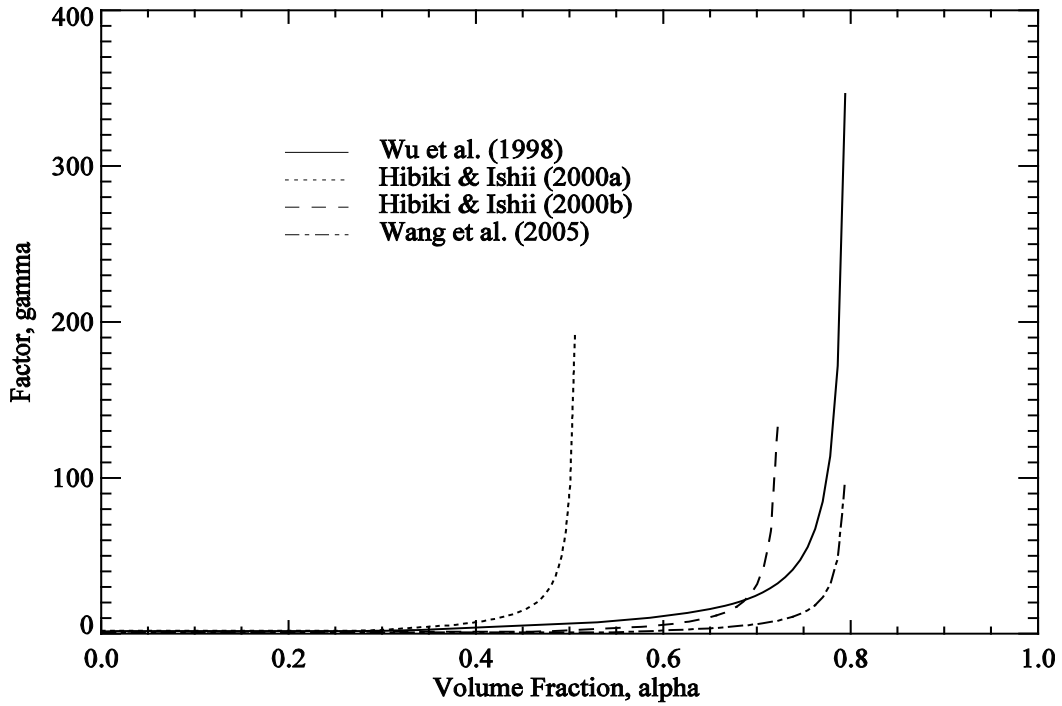


Figure 2.3 Dependence of factor  $\gamma$  on gas volume fraction  $\alpha_g$

From Table 2.1 and Figure 2.3, one can see that all the expressions have a similar form, which give a small value for dilute flow and approach infinity when the packing of bubbles arrives at the maximum value.

The last modification one can find in the literature is the decreasing factor  $\Pi$  which is introduced to reflect the limited range of turbulent fluctuations affecting the motion of the bubbles. Wu et al. [39] and Wang et al. [37] suggested that when the mean distance between bubbles is larger than the average turbulent path length, no collision should be counted.

Wu et al. [39] proposed the following expression for the factor  $\Pi$ :

$$\Pi = \left[ 1 - \exp\left(-C_3 \frac{h_t}{h_{b,ij}}\right) \right] \quad \text{Eq. 2-20}$$

where  $h_t$  is the average size of eddies that drive bubbles together, and  $h_{b,ij}$  is the mean distance between bubbles.

By assuming the average size of eddies to be of the same order as the bubble size, the final form for the factor  $\Pi$  derived by Wu et al. [39] for one-group case is:

$$\Pi = \left[ 1 - \exp\left(-C_4 \frac{\alpha_{\max}^{1/3} \alpha_g^{1/3}}{\alpha_{\max}^{1/3} - \alpha_g^{1/3}}\right) \right] \quad \text{Eq. 2-21}$$

where  $C_4$  is an adjustable parameter that depends on the properties of the fluid. Wu et al. [39] used a value of 3 for the air-water system. Furthermore,  $\alpha_{\max}$  is defined as the maximum packing density of the bubbles and a value of 0.8 was applied.

Recently, Wang et al. [37] [38] employed a different correlation by considering that  $\Pi$  should approach unity when the ratio  $h_{b,ij}/h_{t,ij}$  is small and approach zero at large ratios:

$$\Pi = \exp \left[ - \left( \frac{h_{b,ij}}{h_{t,ij}} \right)^6 \right] \quad \text{Eq. 2-22}$$

where the mean relative turbulent path length scale of bubbles  $h_{t,ij}$  and the mean distance between bubbles  $h_{b,ij}$  is calculated by,

$$h_{bt,ij} = 0.89 (d_i^2 + d_j^2)^{1/2}, \quad h_{b,ij} = k (n_i + n_j)^{-1/3}$$

respectively.

On the other hand, Lehr et al. [31] assume that the effective range of turbulent fluctuation obeys a normal distribution with  $\lambda=d$  as the mean value. The factor  $\Pi$  has the following expression:

$$\Pi = \exp \left[ - \left( \frac{\alpha_{\max}^{1/3} - \alpha_g^{1/3}}{\alpha_g^{1/3}} \right)^2 \right] \quad \text{with } \alpha_{\max} = 0.6 \quad \text{Eq. 2-23}$$

Finally, the modified form for collision frequency can be rewritten as:

$$h(d_i, d_j) = C_5 \cdot \gamma \cdot \Pi \cdot (d_i + d_j)^2 (d_i^{2/3} + d_j^{2/3})^{1/2} \varepsilon^{1/3} \quad \text{Eq. 2-24}$$

The turbulence-induced collision frequency of two equal-sized bubbles calculated from various models is illustrated in Figure 2.4. It shows that the collision frequency always increases with an increasing bubble size. This is because both the cross-sectional area and the relative velocity increase with the bubble size. The main difference lies in the calculation of the relative velocity  $u_{\text{rel}}$  and the modification factors,  $\gamma$ ,  $\Pi$ . The model of Prince and Blanch [36] predicts a smaller collision frequency, which might be caused by not considering the cross-sectional area of the moving bubble. Chesters [25] calculates the relative velocity as  $u_{\text{rel}} \propto (d_1 + d_2)^{1/3}$  (see Eq. 2-18 and Eq. 2-19), while others use the common expression in Eq. 2-17, i.e.  $u_{\text{rel}} \propto (d_1^{2/3} + d_2^{2/3})^{1/2}$ . On the other hand, the model of Wang et al. [37] [38] considers the modification factors,  $\gamma$ ,  $\Pi$ , and gives a small collision frequency for small bubbles, since the mean distance between small bubbles is larger than between bigger bubbles if the bubble number density is the same. If the mean distance between two bubbles is larger than their average relative turbulent path, the collision frequency decreases exponentially. Other discrepancies result from the coefficient  $C_1$  in the calculation of eddy velocity see Eq. 2-16.

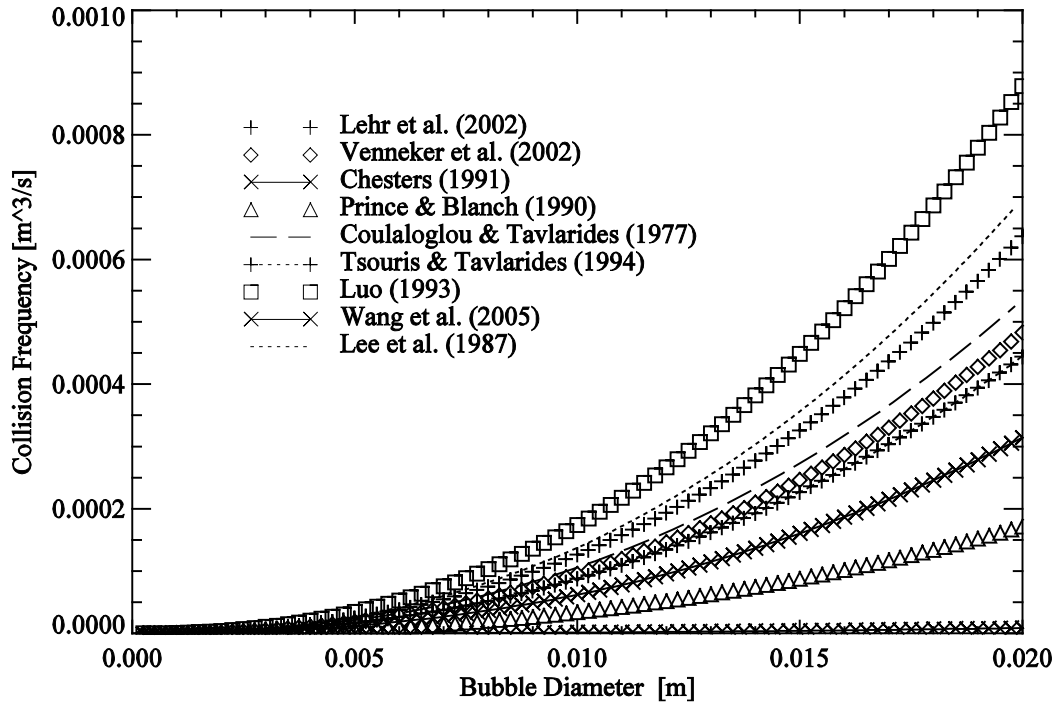


Figure 2.4 Dependence of turbulent collision frequency on bubble size  
 $\rho_l=1000 \text{ kg}\cdot\text{m}^{-3}$ ,  $\rho_g=1 \text{ kg}\cdot\text{m}^{-3}$ ,  $\varepsilon=1 \text{ m}^2\cdot\text{s}^{-3}$ ,  $\mu_l=0.001 \text{ Pa}\cdot\text{s}$ ,  $\mu_g=1.8\times 10^{-5} \text{ Pa}\cdot\text{s}$ ,  $\alpha_g=0.3$

### Velocity gradient-induced collisions

In contrast to the mechanism of turbulent-fluctuation, velocity-gradient, eddy-capture, buoyancy as well as wake effects are normally neglected in the existing models.

As pointed out by Friedlander [40], bubbles in a uniform, laminar shear flow may collide with each other because of velocity gradients, which also prevail in the bulk of a turbulent flow. By assuming that the streamlines are straight and the bubble motion rectilinear, an expression was proposed for the frequency of shear-induced collisions in a uniform laminar flow,

$$h(d_i, d_j) = \frac{4}{3} \left( \frac{d_i}{2} + \frac{d_j}{2} \right)^3 \dot{\gamma} \quad \text{Eq. 2-25}$$

where  $\dot{\gamma}$  is the shear rate in the bulk flow. Theoretically, the Eq. 2-25 can be applied to any collision case resulting from a velocity gradient. For example, Prince and Blanch [36] used it to describe the gross liquid circulation induced by high gas rates in an air-sparged bubble column. For a turbulent flow, collisions induced by the velocity gradient in the bulk flow can also be described by Eq. 2-25.

### Eddy shear rate-induced collisions

According to Chesters [25], when the bubble size is much smaller than the size of the energy-dissipating eddies that are found in a turbulent flow, the force governing the collision will be predominantly viscous. In other words, the bubble velocity will be very close to the velocity of the continuous phase flow field. It is the same case when the density difference is negligible [16]. Under this condition, the collision frequency

will be determined mainly by the local shear of the flow inside turbulent eddies, which can be described in a similar way as a uniform laminar shear flow, see Eq. 2-25.

$$h(d_i, d_j) = 0.618 \left( \frac{d_i}{2} + \frac{d_j}{2} \right)^3 \sqrt{\varepsilon / \nu} \quad \text{Eq. 2-26}$$

In analogy to  $\dot{\gamma}$  the term  $\sqrt{\varepsilon / \nu}$  is the characteristic shear strain-rate in the smallest eddy [63]. In contrast to laminar shear,  $\sqrt{\varepsilon / \nu}$  is often referred as turbulent shear rate, and we call this collision mechanism here as eddy-capture.

### **Buoyancy-induced collision**

According to Prince and Blanch [36], bubble-bubble collision may result from the difference in rise velocities of the bubbles having different sizes. The calculation of buoyant collision frequency is consistent in the literature. A typical model is given by Friedlander [40] as:

$$h(d_i, d_j) = S_{ij} |u_{ri} - u_{rj}| \quad \text{Eq. 2-27}$$

which has the same form as turbulent collisions in Eq. 2-13. The term  $S_{ij}$  is also the same as Eq. 2-14. The unique difference is that the relative velocity in this case is calculated from the terminal rise velocities. For the calculation of  $u_r$ , Prince and Blanch [36] used the expression of Clift et al. [64], while the Fan-Tsuchiya equation [65] used in [37], [38].

### **Wake-entrainment**

During the free-rise of gas bubbles through the liquid an amount of liquid is inevitably carried up and accelerated behind the bubbles, which is known as wake effect. In the last few decades, it has been realized that the wake plays a significant role in the interaction between bubbles [66]. When bubbles enter the wake region, they will be accelerated and collide with the preceding one [67], who generates the wake. In the experimental investigation of Stewart [68], the wake was found to be the sole driving force and mechanism for bubble interaction. Wake-induced collisions result in coalescence primarily between pairs of large cap bubbles in fluids sufficiently viscous to keep their wakes laminar.

Unlike the previous mechanisms, the description of the wake interaction does not yet have a consistent method and each model is quite different from one another. For the transition from bubbly to slug flow regimes, Kalkach et al. [54] used a linear instability analysis of the extended multi-fluid model including the population balance equation. The coalescence rate caused by wake entrainment was calculated based on the work of Bilicki and Kestin [67].

According to Kalkach et al. [54], the collision frequency between a trailing bubble in the wake and its leading bubble can be defined as the volume it has to occupy at time  $t+dt$  to group with the leading bubble at time  $t$ , per unit time. By using the correlation of Schlichting [69] for the velocity distribution in the wake, they derived the collision frequency as:



$$h(d_i, d_j) = C_6 (d_i^3 + d_j^3) (d_i + d_j)^2 \quad \text{Eq. 2-28}$$

where  $C_6$  has a unit of rate per unit area and contains a number of unknowns.

By taking into account the wake interaction, swarm effect and bubble shape, Colella et al. [52] developed a novel model especially tailored for the bubble-bubble interactions in bubble columns:

$$h(d_i, d_j) = u_{rel} \frac{V_i^{BOX}}{h_{b,ij}} \quad \text{Eq. 2-29}$$

where  $u_{rel}$  is the relative velocity between the two colliding bubbles.  $V_i^{BOX}$  is the volume influenced by the wake of a bubble with size  $d_i$ , which is assumed to have a conical shape according to Nevers and Wu [70]. The base of the cone is the cross-sectional area of the leading bubble, while the height was assumed to be 5 times of the base diameter on the basis of experimental results.  $h_{b,12}$  is the mean distance between bubbles in the considered system. In addition, the swarm effect was considered with the equation of Richardson and Zaki [71].

Wu et al. [39] proposed the basic modeling concept of bubble coalescence due to wake entrainment in a vertical pipe by assuming a homogeneous flow. Hibiki and Ishii [61] modified the model for a two-group model to formulate the bubble coalescence between spherical and cap bubbles due to wake entrainment, which was recently extended by Wang et al. [37] [38] to the multi-group case:

$$h(d_i, d_j) = C_7 d_i^2 u_{ri} \quad \text{Eq. 2-30}$$

where the constant  $C_7$  depends on the geometry and size of the wake region. A value of 15.4 was used by Wang and his coworkers.

Since the relative velocity between the leading and following bubbles in the wake depends not only on the relative velocity between the leading bubble and the continuous phase  $u_{rel}$ , the wake geometry, but also the drag coefficient  $C_D$ , Hibiki et al. [72] further refined their model by including the term of  $C_D^{1/3}$ , but only for one-group case:

$$h(d, d) = C_8 C_D^{1/3} d^2 u_r \quad \text{Eq. 2-31}$$

Since the wake length and geometry is further dependent on flow conditions and fluid properties, the determination of the constant  $C_7$  and  $C_8$  is a tough problem. For the case of homogenous air-water upward flow in a small pipe (DN9), Hibiki et al. [72] used a value of about 0.984 for  $C_8$ . For a medium pipe,  $C_7$  was adjusted to 0.23 in [62] for the case of a spherical bubble entrained by a cap bubble, while for the entrainment between two cap bubbles the value has to be reduced to one thousandth. That means that the coalescence rate of a small bubble entrained by a large cap bubble is higher than the coalescence between two cap bubbles. However,

the work of Stewart [67] shows that coalescence due to wake-entrainment requires bubbles of approximately similar size. Recently, Wang et al. [37] extended the model of Hibiki [62] to a multi-group model. They applied the extended model to bubble columns and adopted a quite large value for  $C_7$ .

In conclusion, bubble collision in a turbulent flow can be promoted by a variety of mechanisms. Note that no existing model takes all of the mechanisms into account. At the same time, it is difficult to decide which mechanism plays the most important role in a certain case. Generally speaking, if the size of the bubble is inside the inertial subrange of turbulence, it will be exposed to eddies' stresses from all directions and the random motion will be the most important. If the bubbles are smaller than the Kolmogorov dissipation scale, the slip velocity is negligible and the relative velocity will be determined mainly by local turbulent characteristics, e.g. turbulent shear, while the laminar shear, i.e. the mean velocity gradient, affects the relative motion of bubbles with all sizes. Furthermore, the buoyancy mechanism becomes more significant with increasing density differences. The mechanism of wake entrainment is the most ambiguous one. It is the dominant interaction mechanism of cap bubbles and accounts for the transition from bubbly to slug flow. As for the modification factors,  $\gamma$ ,  $\Pi$ , in Eq. 2-24 and  $C_t$  in the model of Colin et al. [60], further investigations are indispensable.

### 2.3.3 Coalescence efficiency

As discussed in §2.3.1, there are at least three kinds of theories or models proposed for the calculation of coalescence efficiency or probability. They are the energy model, the critical approach velocity model and the film drainage model, see Figure 2.2.

#### 1. Energy model

The energy model was originally proposed by Howarth [27] [40]. It was confirmed by the optical records of coalescence in liquid-liquid dispersions [73] [74], which found that significant fraction of collisions result in immediate coalescence and the probability increases with increasing energy of collision, which was called "energetic collisions". On the basis of the pioneering work, Sovová [43] developed a model by relating the kinetic collision energy  $E_{kin}$  to the interfacial energy  $E_\sigma$  of the drop:

$$\lambda(d_i, d_j) = \exp\left(-C_9 \frac{E_\sigma}{E_{kin}}\right) \quad \text{Eq. 2-32}$$

The interfacial energy of drops is proportional to the surface tension and drop surface area,

$$E_\sigma = \sigma(V_i^{2/3} + V_j^{2/3}) \quad \text{Eq. 2-33}$$

while the kinetic collision energy  $E_{kin}$  is assumed to be correlated with the average volume and the relative velocity of the two interacting drops:

$$E_{kin} = \frac{1}{2} \rho_g \bar{V} \cdot u_{rel}^2, \quad \bar{V} = V_i V_j / (V_i + V_j) \quad \text{Eq. 2-34}$$

where the turbulent relative velocity  $u_{rel}$  is calculated according to Eq. 2-15 and Eq. 2-16.

Finally, the expression for coalescence efficiency ends up with:

$$\lambda(d_i, d_j) = \exp \left[ -C_{10} \frac{\sigma(d_i^2 + d_j^2)(d_i^3 + d_j^3)}{\rho_g \varepsilon^{2/3} d_i^3 d_j^3 (d_i^{2/3} + d_j^{2/3})} \right] \quad \text{Eq. 2-35}$$

A similar model was derived recently by Simon [42] but he calculated the kinetic energy from the momentum balance during the collision,

$$E_{kin} \propto \rho_g \varepsilon^{2/3} \cdot (V_i^{11/9} + V_j^{11/9}) \quad \text{Eq. 2-36}$$

He concluded the coalescence efficiency as:

$$\lambda(d_i, d_j) = \exp \left[ -C_{11} \frac{\sigma(d_i^2 + d_j^2)}{\rho_g \varepsilon^{2/3} (d_i^{11/3} + d_j^{11/3})} \right] \quad \text{Eq. 2-37}$$

In the work of Sovová [43] the overall coalescence efficiency was further calculated by combining the energy model in Eq. 2-35 with the film drainage model, which was adopted afterwards by a few scientists [74] [75]:

$$\lambda(d_i, d_j) = \lambda_1(d_i, d_j) + \lambda_2(d_i, d_j) - \lambda_1(d_i, d_j)\lambda_2(d_i, d_j) \quad \text{Eq. 2-38}$$

where  $\lambda_1$  and  $\lambda_2$  is calculated by the energy and the film drainage model, respectively.

## 2. Critical approach velocity model

According to the energy model, coalescence will occur immediately when the approach velocity exceeds a critical value at the instant of collision. However, the experimental investigation of Doublez [28] and Duineveld [29] gives a contradictory conclusion that coalescence behavior favors gentle collisions. A simple expression was used by Lehr et al. [30] [31] for the observed relationship between coalescence efficiency and approach velocity:

$$\lambda(d_i, d_j) = \min \left( \frac{u_{crit}}{u_{rel}}, 1 \right) \quad \text{Eq. 2-39}$$

where the critical velocity  $u_{crit}$  is determined experimentally for a given system.

## 3. Film drainage model

According to the film drainage model, the coalescence efficiency of a collision depends on two timescales, i.e. the contact time  $t_{contact}$  and film drainage time  $t_{drainage}$ . The starting point of the theory is the work of Ross [76]. By assuming that the

drainage and contact time are random variables, Ross applied the probability density function of a normal distribution for the computation of coalescence efficiency:

$$\lambda(d_i, d_j) = \frac{1}{2} \exp\left(-\frac{t_{drainage}}{t_{contact}}\right) \exp\left(\frac{1}{2} \frac{c_{t_{drainage}}^2}{t_{contact}^2}\right) \operatorname{erfc}\left(\frac{\sqrt{2} c_{t_{drainage}}^2 - t_{drainage} t_{contact}}{2 t_{contact} c_{t_{drainage}}}\right) \quad \text{Eq. 2-40}$$

Later on Eq. 2-40 was simplified by Coulaloglou [77] to the following form by assuming that the film drainage time is not distributed while the contact time remains a random variable, i.e.  $c_{drainage} = 0$ :

$$\lambda(d_i, d_j) = \exp\left(-\frac{t_{drainage}}{t_{contact}}\right) \quad \text{Eq. 2-41}$$

Although a few criticisms appear in the literature on the validity of the two timescales, e.g. the assumption of random variables as well as a normal distribution [78], the film drainage model is still the most popular approach. It has become the starting point of almost all subsequent models. The main difference amongst the different models lies in the expressions for the two timescales.

### **Film drainage time**

According to Lee and Hodgson [79], various regimes of the film drainage process may be distinguished according to the rigidity of particle surfaces (deformable, non-deformable, see Figure 2.5) and the mobility of the contact interfaces (immobile, partially mobile, fully mobile, see Figure 2.6). A great deal of analysis of these regimes is to be found in the literature. Most of them use the lubrication theory, which starts with the Navier Stokes Equation and the continuity equation, and ends with a film-thinning equation. For simple boundary conditions such as constant interaction force or approach velocity, the drainage time can be obtained by integrating the thinning equation. For further details about the derivation and solution of the film-thinning equation, the reader is referred to the dissertation of Hagesaether [80].

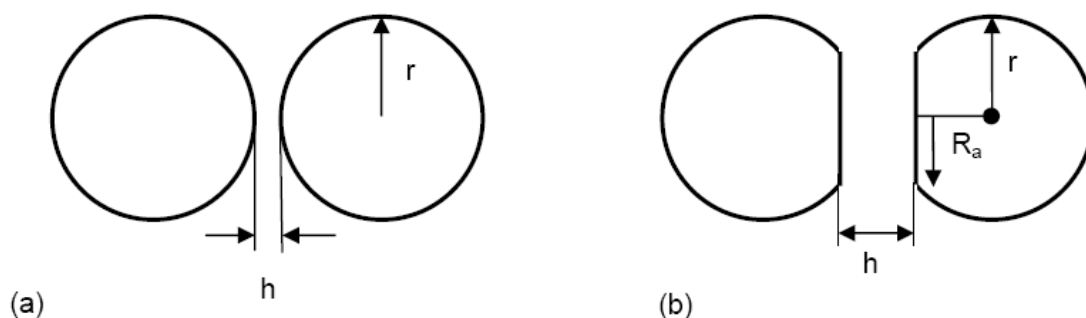


Figure 2.5 Influence of particle surface rigidity on liquid film drainage flow [42]  
 (a) Nondeformable surfaces (b) Deformable surfaces

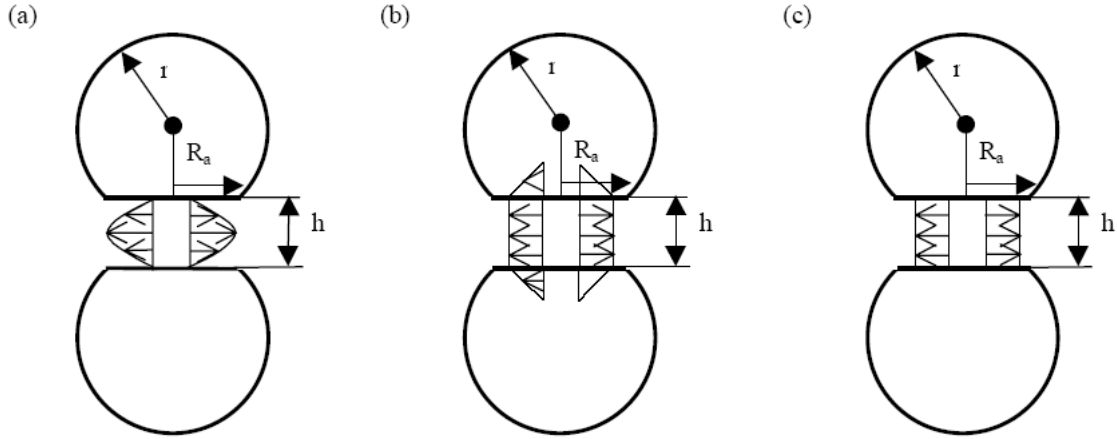


Figure 2.6 Influence of particle surface mobility on drainage process [42]  
 (a) Immobile interfaces (b) Partially mobile interfaces (c) Fully mobile interfaces

When bubbles are highly viscous compared to the continuous phase or have very small sizes ( $d < 1$  mm), at large distance their interfaces are slightly deformed and behave nearly as rigid spherical particles. For two non-deformable spheres with equal sizes, the drainage time can be derived by using the Poiseuille relation according to Chesters [25]:

$$t_{drainage} = \frac{3\pi\mu_l}{2F} r^2 \ln\left(\frac{h_0}{h_{crit}}\right) \quad \text{Eq. 2-42}$$

If replacing the bubble radius  $r$  with an equivalent one  $r_{eq}$

$$r_{eq} = \frac{2r_i r_j}{r_i + r_j} \quad \text{Eq. 2-43}$$

The Eq. 2-42 can be extended to describe the case of unequal bubble sizes. Then it becomes identical to the drainage time given by Davis et al. [44] and Jeffreys and Davies [45] with the form:

$$t_{drainage} = \frac{6\pi\mu_l}{F} \left(\frac{r_i r_j}{r_i + r_j}\right)^2 \ln\left(\frac{h_0}{h_{crit}}\right) \quad \text{Eq. 2-44}$$

However, in most practical applications where large bubbles exist, the deformation of the bubble surface during the collision must be considered [42]. The simplest model for the film drainage between deformable interfaces is a so-called parallel model, which assumes that the surfaces of the coalescing bubbles deform into two parallel discs with radius  $R_a$ , see Figure 2.5(b). However, during the experimental investigation Derjaguin and Kussakov [81] found a dimple in the film, which implies that there is a pressure gradient on the deformable interfaces. That means that it is impossible to have a parallel plane film, since a flat film cannot support a gradient in the pressure. In order to maintain this pressure gradient the film needs change to a curved shape. A dimple can be defined as a reverse curvature so that a central lens

of liquid is entrapped by a thin barrier ring. The dimple phenomenon was first modeled by Frankel and Mysels [82]. However, although the dimple theory was proposed and shown to be more close to the physical reality, the parallel model is still the basis of most drainage models. It is acceptable with the consideration that the film thickness is much smaller than its radius.

The classification of drainage regimes in the case of deformable particles depends on the mobility. For immobile interfaces, film drainage is controlled by a viscous thinning. The liquid is expelled from between these rigid surfaces by a laminar flow. The velocity profile in the film is parabolic with no slip at the surface. The interaction between the film drainage and the circulation inside particles is not coupled; see Figure 2.6(a). Based on the preceding work of MacKay and Mason [47], Chesters [25] derived the drainage time as Eq. 2-45 by assuming constant forces,

$$t_{drainage} = \frac{3\mu_l F}{16\pi\sigma^2} r^2 \left( \frac{1}{h_{crit}^2} - \frac{1}{h_0^2} \right) \quad \text{Eq. 2-45}$$

which has the same form as the model of Chappellear [83], if the bubble radius  $r$  is replaced by the equivalent radius  $r_{eq}$  (see Eq. 2-43).

$$t_{drainage} = \frac{3\mu_l F}{16\pi\sigma^2} \left( \frac{d_i d_j}{d_i + d_j} \right)^2 \left( \frac{1}{h_{crit}^2} - \frac{1}{h_0^2} \right) \quad \text{Eq. 2-46}$$

Based on Eq. 2-46 Coualoglou and Tavlarides [56] developed a coalescence model by assuming a constant initial and critical film thickness  $h_0$  and  $h_{crit}$ . It is one of the most famous models for liquid-liquid dispersions.

The approximation of immobility of the film surface is applicable only to systems with extremely high dispersed-phase viscosity or with a certain concentration of soluble surfactant. In many liquid-liquid systems where the drainage process is predominantly controlled by the motion of film surface, the contribution of the additional flow within the film due to the prevailing pressure gradient is much smaller. By assuming a quasi-steady creeping flow, Chesters [25] calculated the drainage time for partially mobile interfaces using the following expression:

$$t_{drainage} = \frac{\pi\mu_g F^{1/2}}{2(2\pi\sigma / r)^{3/2}} \left( \frac{1}{h_{crit}} - \frac{1}{h_0} \right) \quad \text{Eq. 2-47}$$

Lee et al. [57] used the model of Sagert and Quinn [50] for the partially mobile case:

$$t_{drainage} = -3M\mu_l R_a^2 \int_{h_0}^{h_{crit}} \frac{1}{8h^3 [2\sigma / r + A_n / (6\pi h^3)]} dh \quad \text{Eq. 2-48}$$

By investigating the resisting hydrodynamic force during the film drainage process, Davis et al. [44] concluded the relationship between the force  $F$  and the drainage velocity  $dh/dt$  as:

---

$$-F = \frac{6\pi\mu_l}{h} \left( \frac{r_i r_j}{r_i + r_j} \right)^2 \frac{dh}{dt} \frac{1 + 0.38M}{1 + 1.69M + 0.43M^2} \quad \text{Eq. 2-49}$$

where M characterizes the interfacial mobility. Based on Eq. 2-49, Tsouris and Tavarides [51] proposed a new coalescence model for drops in turbulent dispersions.

The drainage regime with fully mobile interfaces, e.g. bubbles in pure systems, is the most complicated closure model. In this case, the drainage process is controlled by both inertia and viscous forces. Using the parallel-film model, Chesters [84] proposed the following drainage equation:

$$\frac{dH}{dt} = \left( \frac{\sigma}{3\mu_l r} \cdot \frac{dH}{dt} \right) \cdot \exp\left( -\frac{12\mu_l t}{\rho_l R_a^2} \right) - \frac{\sigma}{3\mu_l r}, \quad \text{with } H = \frac{1}{2} \ln h \quad \text{Eq. 2-50}$$

Since there is no analytical solution for the general expression in Eq. 2-50, two limits are usually considered in the literature. For highly viscous liquids, the film is thinning viscously and the drainage velocity is independent of the film size, and hence the force. At this limit, the film drainage time is calculated by

$$t_{\text{drainage}} = \frac{3\mu_l r}{2\sigma} \ln \frac{h_0}{h_{\text{crit}}} \quad \text{Eq. 2-51}$$

In the inertia-controlled limit, which is the case of gas bubbles in turbulent flow, Eq. 2-50 is shown to reduce to:

$$t_{\text{drainage}} = \frac{\rho_l u_{\text{rel}} r^2}{8\sigma} \ln \frac{h_0}{h_{\text{crit}}} \quad \text{Eq. 2-52}$$

In the numerical study of Chesters and Hofman [63], they found that in the inviscid case Eq. 2-52 can be approximated as

$$t_{\text{drainage}} = 0.5 \frac{\rho_l u_{\text{rel}} r^2}{\sigma} \quad \text{Eq. 2-53}$$

which was extended further by Luo [58] to unequal bubbles with sizes  $d_i, d_j$ :

$$t_{\text{drainage}} = 0.5 \frac{u_{\text{rel}} \rho_l d_i^2}{(1 + d_i / d_j)^2 \sigma} \quad \text{Eq. 2-54}$$

From Eq. 2-53 and Eq. 2-54 one can see that the drainage time for the inertia thinning is proportional to the approach velocity. That means that the drainage time is small or the coalescence efficiency is high when the approach velocity is low, which is consistent with the idea of the critical velocity model.

Lee et al. [57] applied a different model, which is proposed originally by Sagert and Quinn [50]:

$$t_{drainage} = \frac{R_a}{4} \left( \frac{\rho_l d}{2\sigma} \right)^{1/2} \ln \left( \frac{h_0}{h_{crit}} \right) \quad \text{Eq. 2-55}$$

Prince and Blanch [36] simplified the model of Oolman and Blanch [85] by neglecting the effect of the Hamaker force and obtained the following expression for a pure system,

$$t_{drainage} = \left( \frac{r_{eq}^3 \rho_l}{16\sigma} \right)^{0.5} \ln \frac{h_0}{h_{crit}} \quad \text{Eq. 2-56}$$

It is worth noting that the film drainage time in Eq. 2-55 and Eq. 2-56 has a form similar to the contact time proposed by Chesters [25] in Eq. 2-62.

### **Compressing force**

In order to apply the above expressions for the determination of the film drainage time, the interaction force  $F$  at the collision requires calculation, which is usually assumed to be proportional to the mean square velocity difference at either ends of an eddy with a size of the equivalent diameter [51] [56] [86]:

$$F \sim \rho_l \varepsilon^{2/3} (d_i + d_j)^{2/3} \left( \frac{d_i d_j}{d_i + d_j} \right)^2 \quad \text{Eq. 2-57}$$

Similarly, Chesters [25] proposed correlations for both viscous and inertial collisions of equal-bubbles in turbulent flows. For the viscous regime, the typical force between two colliding bubbles is expected to be proportional to the turbulent shear rate  $\sqrt{\varepsilon/\nu}$

$$F \sim 6\pi\mu_l r^2 \sqrt{\varepsilon/\nu} \quad \text{Eq. 2-58}$$

On the other hand, for inertial collisions, Chesters [25] pointed out that because of inertia the interaction force  $F$  exerted by one bubble on the other is greater than that calculated by Eq. 2-58. For this case, they used the capillary force exerted on the film, which is induced by variations in the curvature of the gas-liquid interface.

$$F \sim \pi R_a^2 \left( \frac{2\sigma}{r} \right) \quad \text{Eq. 2-59}$$

where  $R_a$  is film radius.

### **Contact time**

For the calculation of the contact or interaction time in a turbulent system, most of the previous studies used the relationship of Levich [87], which is based on dimensional analysis:



$$t_{contact} \sim \frac{d^{2/3}}{\varepsilon^{1/3}} \quad \text{Eq. 2-60}$$

Chesters [25] argued that the duration of a collision is controlled by the external flow in the bulk. By making an analogy to solid particles located in viscous simple shear, they concluded that the contact time of bubbles during a viscous collision in turbulent flows should decrease with an increase in the strain rate in the smallest eddies:

$$t_{contact} \sim (\varepsilon / \nu)^{-1/2} \quad \text{Eq. 2-61}$$

During inertial collisions, there is a conversion process between kinetic energy and surface energy. From this point of view, Chesters [25] stated that the actual contact time for inertial system was less than that obtained by Eq. 2-61. He derived the expression for contact time from a energy balance:

$$t_{contact} \approx \left[ (4\rho_g / 3\rho_l + 1) \rho_l r^3 / 2\sigma \right]^{1/2} \quad \text{Eq. 2-62}$$

By criticizing the simplicity of Levich's expression and the suitability of Eq. 2-61 for unequal-sized bubbles, Luo [58] derived an alternative expression for the interaction time based on a simple parallel film model:

$$t_{contact} = (1 + \xi_{ij}) \left[ \frac{(\rho_g / \rho_l + C_{VM}) \rho_l d_i^3}{3(1 + \xi_{ij}^2)(1 + \xi_{ij}^3)\sigma} \right]^{1/2} \quad \text{Eq. 2-63}$$

where  $C_{VM}$  is the added mass coefficient. Although it was found to be variable during the approaching of bubbles [88],  $C_{VM}$  is normally assumed to be a constant between 0.5 and 0.8 [89].

Kamp and Chesters [88] extended their previous expressions by Chester [25] to unequal-sized bubbles. The interaction time was defined as the interval between the onset of film formation and the moment at which the bubbles begin to rebound. By assuming a balance between the increasing surface free energy and the corresponding reduction in the kinetic energy of the system, they concluded an expression for the interaction time as:

$$t_{contact} = \frac{\pi}{4} \left( \frac{\rho_l C_{VM} d_{eq}^3}{3\sigma} \right)^{1/2} \quad \text{Eq. 2-64}$$

On the other hand, empirical expressions are also often applied in the calculation of interaction time. For example, Tsouris and Tavlarides [51] used the expression of Schwartzberg and Freybal [90], which treated the contact time as the reciprocal of the fluctuation frequency of fluid velocity:

$$t_{contact} \approx \left[ \frac{2.5ND_i^2}{L(T^2H)^{1/3}} \right]^{-1} \quad \text{Eq. 2-65}$$

**Coalescence efficiency calculated by different models**

Based on the combination of different expressions for the contact time and the drainage time, various models for coalescence efficiency were formulated according to Eq. 2-41. The dependence of some typical models on bubble size for the equal-size case is depicted in Figure 2.7. Most of them considered only the inertial collision caused by turbulent fluctuations and were derived based on classical theories of isotropic turbulence, while Chesters [25] divided the collisions in a turbulent flow into viscous and inertial collisions. At the same time, other than turbulence, Prince and Blanch [36], Carrica et al. [91] and Wang et al. [38] took into account buoyancy, laminar shear rate and wake interaction. Furthermore, Prince and Blanch [36] used an identical efficiency for all collision mechanisms while Kolev [92] and Wang et al [37] stated that models for the coalescence efficiency of different collisions might have a different form. Carrica et al. [91] considered the influence of different collision sources on coalescence efficiency by reforming the contact time.

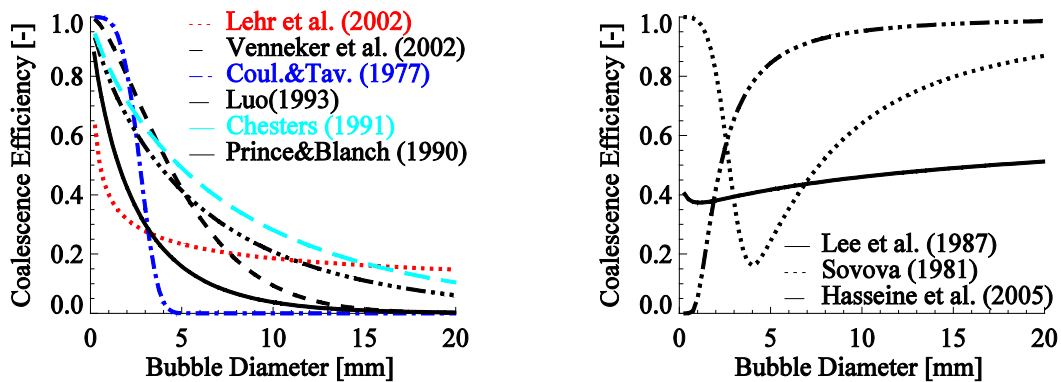


Figure 2.7 Dependence of coalescence efficiency on bubble size  
 $\rho_l=1000 \text{ kg}\cdot\text{m}^{-3}$ ,  $\rho_g=1 \text{ kg}\cdot\text{m}^{-3}$ ,  $\varepsilon=1 \text{ m}^2\cdot\text{s}^{-3}$ ,  $\mu_l=0.001 \text{ Pa}\cdot\text{s}$ ,  $\mu_g=1.8\times 10^{-5} \text{ Pa}\cdot\text{s}$ ,  $\alpha_g=0.3$

From Figure 2.7, one can see that all of the models give a value of between 0 and 1. The models of Coulaloglou and Tavlarides [56] and Venneker et al. [93] predict larger efficiencies for small bubbles than other models, among which Lehr et al. [31] and Prince and Blanch [36] have the smallest value. The model of Coulaloglou and Tavlarides [56] shows a much steeper decreasing trend than others. On the other hand, the models of Lehr et al. [31], Luo [58] and Chesters [25] predict a value considerably larger than zero when the bubble diameter increases up to 20 mm, which will deliver a large coalescence rate for large bubbles. Despite the quantitative difference, the dependence on bubble size of most models is consistent, i.e. decreasing with bubble sizes. However, by using Eq. 2-49, Eq. 2-57 and Eq. 2-60 for the calculation of drainage time, compressing force and contact time, respectively, the model of Hasseine et al. [86] shows an increasing relationship with bubble sizes. Sovová [43] combined the drainage model of Coulaloglou and Tavlarides [56] with the energy model in Eq. 2-35. Therefore, the coalescence efficiency decreases dramatically for small bubbles and then increases with the increase in bubble size due to the contribution of “immediate coalescence”. Finally, Lee et al. [57] argued

that the film thinning together with the rupture of the thin liquid layer control the coalescence rate.

## 2.4 Breakup models

The breakup of bubbles is influenced by the surrounding liquid hydrodynamics and interfacial interactions. The breakup frequency of a bubble is in general determined by the balance between the external stresses (energy) exerted by the surrounding liquid, which acts to distort the stable form of the bubbles, and the restoring surface tension stress (energy) of the bubble. However, to quantify the breakup frequency that one parent bubble breaks up into a daughter bubble with given size, which is used by CFD simulations, e.g.  $\Omega(d_i, d_k)$  in Eq. 2-8, the daughter bubble size distribution of the breakup event has to be determined.

Similar to the case of bubble coalescence, mechanisms and models for droplets are often used for the description of the deformation and breakup of bubbles without further validation. Nevertheless, the work of Müller-Fischer [94] shows that for a single bubble in simple shear flow this approach is justified for deformation but fails in the case of breakup. For example, tip breakup or tip streaming is preferential for bubbles while for droplets different breakup mechanisms can be clearly distinguished. On the other hand, instead of simple shear flow, mature investigations on the difference between bubble breakup and droplet breakup is missing for other cases.

### 2.4.1 Mechanisms leading to bubble breakup

In turbulent gas-liquid flows there are four main categories of external stresses: a) turbulent inertial stresses; b) viscous shear stresses; c) interfacial stresses; d) interfacial instability.

#### **Breakup due to turbulent inertial stresses**

In the turbulent case, the breakup of bubbles is caused by turbulent velocity/pressure fluctuations around the bubble surface. Bubbles are assumed to modify their spherical form with the fluctuation of the surrounding liquid. When the amplitude of the oscillation exceeds that required to make the surface unstable, the bubble starts to deform and stretch in one direction leading to a neck that contracts further and fragments finally into two or more daughter bubbles. Whether or not the bubble will break depends on the extent of the deformation, which can be expressed by the Weber number,  $We$ :

$$We = \frac{\tau_t}{\tau_s} = \frac{\rho_l u_{rel}^2 d}{\sigma} \quad \text{Eq. 2-66}$$

where  $\tau_t$  is the turbulence-induced destroying stress or energy, and  $\tau_s$  is the restoring stress or energy related to the surface tension.

The destroying stress (energy)  $\tau_t$  is defined differently in the literature, for example:

- a) Kinetic energy of the drop transmitted from drop-eddy collisions [56]
- b) Turbulent stresses resulting from velocity fluctuations around the bubble surface [59]
- c) Kinetic energy of hitting eddies of different scales [36] [57] [95]

- d) Dynamic pressure of hitting eddies of different scales [30] [31]

Similarly, the restoring stress or energy  $\tau_s$  is defined inconsistently as:

- a) Surface energy of the parent bubble [57]
- b) Surface stress of the parent bubble [59], which is equal to: (surface energy of the parent bubble)/(volume of the parent bubble)
- c) Critical energy calculated from the critical Weber number [36]
- d) Increase in surface energy during the breakage process, i.e. the difference between the surface energy of all daughter bubbles and that of the parent bubble [95]
- e) Mean value of the increases in surface energy for breakages into two equal-sized daughters and into a smallest and a biggest one [93]
- f) Capillary pressure of the smallest daughter bubble [30] [31]
- g) Combination of criteria d) and f) [96] [97]

### **Breakup due to viscous shear forces**

Aside from the turbulent inertial force, the viscous shear force caused by velocity gradients can also deform the bubble and lead to breakup in high viscosity liquid. In addition, a bubble can experience shear stresses when it locates in a wake region or inside a turbulent eddy. If a bubble has its larger part outside a wake region generated by a leading bubble, the shear stress across the wake boundary may split it via surface indentation and necking. When a bubble is smaller than the length scale of the smallest turbulence eddies, i.e. the Kolmogorov length scale  $\eta$ , it is contained in the smallest eddies, i.e. in the viscous subrange of turbulence. The Kolmogorov length scale denotes the eddy scale where viscous forces begin to have a noticeable effect on the motion of the fluid. Bubbles that are contained within the eddies experience almost laminar flow conditions with a shear rate of  $\sqrt{\varepsilon/\nu}$ .

A mathematical description of bubble breakup due to viscous shear stress is still missing. This is possibly because in most cases of gas-liquid flows, the viscosity of the liquid is usually low, e.g. air-water flow.

On the other hand, the mechanisms for the droplets' breakup in simple shear flow have been widely explored both experimentally [98] ~ [100] and numerically [101] ~ [103]. A spherical droplet will deform and orient in steady simple flow. The steady state shape and orientation depends on the ratio of the viscosity of the dispersed droplet to the continuous liquid and the Capillary number  $Ca$ .  $Ca$  is the ratio of viscous shear stresses to surface tension. For slightly deformed bubbles ( $Ca \ll 1$ ), the deformed droplet has an ellipsoidal shape, and the inclination angle  $\theta$  is about  $45^\circ$  decreasing as  $Ca$  increases. With increasing Capillary number the deformation increases from spherical via ellipsoidal to sigmoidal with pointed ends while the orientation angle approaches  $0^\circ$  for very high shear stresses.

### **Breakup due to interfacial stresses**

As the size of the bubble increases, the breakup mechanisms become further complicated by additional mechanisms such as interfacial stresses and instability. Shearing-off of small bubbles at the rim of large bubbles is one of the most important interfacial breakup mechanisms, which is caused by interfacial forces such interfacial shear force and drag force. The shearing-off process is determined by the balance

---

between the interfacial force and the surface tension at the rim base. When the bubble slip velocity and consequently interfacial force is large enough, the bubble becomes unsteady and stretches downstream, i.e. in the direction of the destroying force. The neck part will further thin and breakup into a number of small bubbles. For this mechanism, there are also no sound theoretical models available. Empirical correlations are often used to determine the size of the small bubbles torn from the large bubbles and the torn-off bubbles are assumed to have identical size [104] [105].

### **Breakup due to interfacial instability**

The breakup mechanisms discussed above all depend on the dynamic characteristics of the flow of the continuous phase. However, in practice it shows that even in the absence of a net flow in the continuous phase, the breakup of a bubble can be caused by interfacial instabilities if its size exceeds the maximum stable size. A correlation for the maximum stable bubble size is given by Ishii and Kojasoy [106]:

$$d_{\max} = 40 \sqrt{\frac{\sigma}{g\Delta\rho}} \quad \text{Eq. 2-67}$$

For air-water systems under normal conditions, the maximum stable size is about 10 cm according to Eq. 2-67. Nevertheless, Wang and his coworkers [37] [38] [107] used a value of 2.7cm to decide whether or not instability is considered.

Two types of surface instability have to be considered: Rayleigh-Taylor instability and Kelvin-Helmholtz instability. The Rayleigh-Taylor instability occurs when a light liquid is accelerated into a heavy fluid, that is, where there is a density difference. The Kelvin-Helmholtz instability can occur when a velocity shear is present in a continuous fluid or the velocity difference across the interface between two fluids is sufficient large. Due to the complexity of the phenomenon, the information about the size distribution of daughter bubbles is still missing. It is usually assumed that two daughter bubbles are of equal size [37] [38]. This simplification is obviously too arbitrary since the instability usually disintegrates a large bubble suddenly into a number of small bubbles. Therefore, the mechanism is excluded in most models.

### **2.4.2 Breakup frequency**

In the last decades, modeling of the breakup process has received considerable effort and a great number of models for the calculation of specific breakup rate, i.e. breakup frequency, were published. According to the four mechanisms discussed in §2.4.1 the classification of representative models is shown in Figure 2.8. Most of the models provide the total breakup frequency of a bubble and an extra function needed to be assumed for the description of daughter bubble size distribution. Models that give the partial breakup frequency, i.e. the breakup frequency of a bubble breaking up into a daughter bubble with given size, are highlighted in blue color. The partial breakup frequency can be used directly in the extended multi-fluid model discussed in §2.2.

Since the continuous flow field is in most applications is a turbulent flow, the study of bubble breakup frequency has focused on the breakup mechanism due to turbulent fluctuations. Actually, this mechanism is usually assumed to be the dominant one and the effects of viscous force, interfacial forces and instability on breakup

---

phenomena are usually neglected without any further validation. Furthermore, models for the calculation of the frequency of bubble breakup due to turbulent fluctuation are formulated on the basis of various criteria, i.e. different definitions for  $\tau_t$  and  $\tau_s$  in Eq. 2-66.

**Models for breakup due to turbulent fluctuation**

For breakup caused by turbulent fluctuation, at least five criteria were adopted, which are explained subsequently by some representative models.

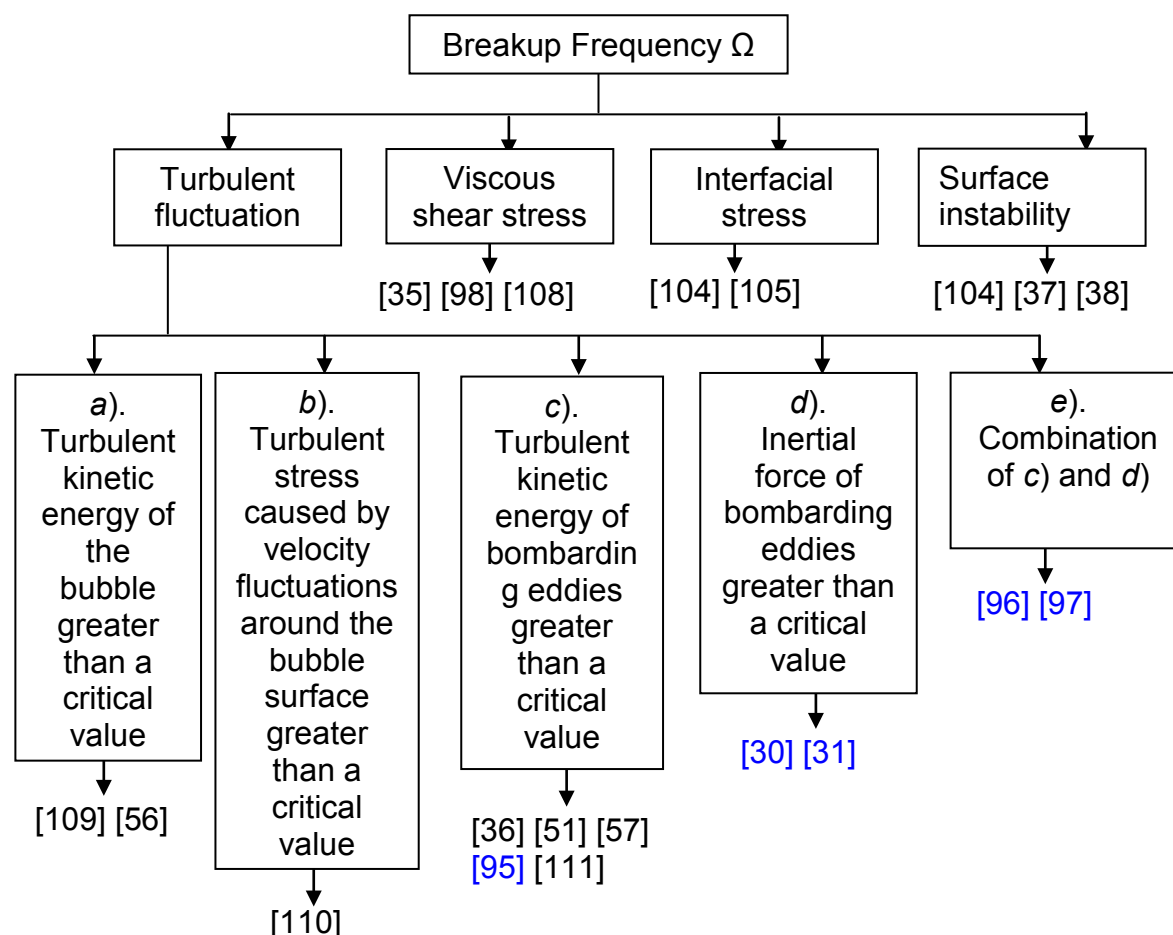


Figure 2.8 Classification of available models for breakup frequency

A pioneering phenomenological model was proposed by Coulaloglou and Tavlarides [56], which was based on the turbulent nature of the liquid-liquid dispersion. The drop oscillates and deforms due to local pressure fluctuations. The basic premise is that an oscillating deformed drop will break if its kinetic energy  $E_d$ , transmitted from drop-eddy collisions, is greater than its surface energy  $E_{crit}$ . The breakup frequency is defined as:

$$\Omega(d_i) = \left( \frac{1}{\text{breakup time}} \right) \cdot \left( \frac{\text{fraction of drops breaking}}{\text{drops breaking}} \right) \tag{Eq. 2-68}$$

The breakup time is determined from the isotropic turbulence theory by assuming that the motion of daughter drops is the same as that of turbulent eddies. The

fraction of drops breaking is assumed proportional to the fraction of drops that have a turbulent kinetic energy greater than their surface tension. With the assumption that the distribution of kinetic energy is a normal function, Eq. 2-68 is expressed as:

$$\Omega(d_i) = C_{12} d_i^{-2/3} \varepsilon^{1/3} \exp\left(-\frac{C_{13} \sigma}{\rho_g \varepsilon^{2/3} d_i^{5/3}}\right) \quad \text{Eq. 2-69}$$

To account for the “damping” effect of droplets on the local turbulent intensities at high holdup fractions, the authors modified the original expression as:

$$\Omega(d_i) = C_{14} d_i^{-2/3} \frac{\varepsilon^{1/3}}{1 + \alpha_g} \exp\left[-\frac{C_{15} \sigma (1 + \alpha_g)^2}{\rho_g \varepsilon^{2/3} d_i^{5/3}}\right] \quad \text{Eq. 2-70}$$

The dependence of “damping” effect on gas volume fraction and dissipation rate is depicted in Figure 2.9.

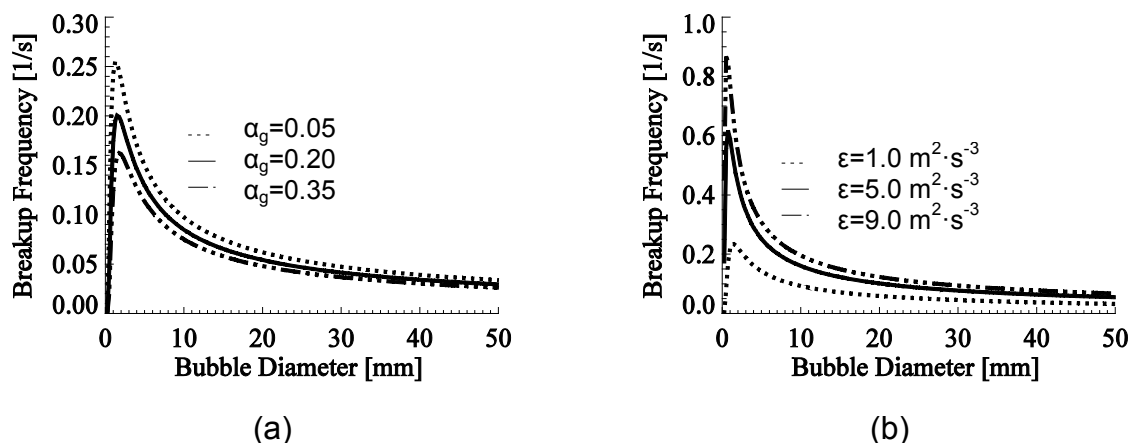


Figure 2.9 Coualoglou and Tavlarides [56] model. (a)  $\varepsilon=1.0 \text{ m}^2 \cdot \text{s}^{-3}$ ; (b)  $\alpha_g=0.1$  ( $C_{14}=0.00481$ ,  $C_{15}=0.08$ )

As pointed out by Prince and Blanch [36], for gas-liquid mixtures, the model of Coualoglou and Tavlarides [56] predicts a breakup rate that is several orders of magnitude lower than the experimental results. This might result from the fact that the density of dispersed phase in a gas-liquid mixture is much lower than that in the liquid-liquid dispersion. Therefore, the density used in the equations of Eq. 2-69 and Eq. 2-70 has to be replaced by that of the continuous phase in order to get reasonable results for gas-liquid flows [108]. This discrepancy indicates that the kinetic energy of turbulent eddies in the continuous phase plays a role in causing the breakup of a bubble or drop instead of the kinetic energy of the bubble or drop itself.

Another similar model was proposed by Chatzi [109] [112]. The unique difference is that they expressed the probability density of the turbulent kinetic energy by Maxwell’s law instead of the normal function. Thus, they published the model in the following form:

$$\Omega(d_i) = C_{16} d_i^{-2/3} \varepsilon^{1/3} \left( \frac{2}{\sqrt{\pi}} \right) \cdot \Gamma \left( \frac{3}{2}, \frac{C_{17} \sigma}{\rho_g \varepsilon^{2/3} d_i^{5/3}} \right) \quad \text{Eq. 2-71}$$

Martínez-Bazán et al. [59] criticized the models, which were derived from an extension of the classical kinetic theory of gases [36] [51] [57] [95]. These models assume the fact that turbulence consists of an array of discrete “eddies” and as a result they rely on physically questionable assumptions about the size and number density of the “eddies”. Therefore, they presented an alternative model based purely on kinematic ideas for fully developed turbulent flows. The premise of the model is that, for a bubble to break, its surface has to deform, and enough energy must be provided by the turbulent stresses in the surrounding continuous liquid. The breakup frequency is assumed to increase with the difference between the turbulent stresses  $\tau_t$  and the surface stress  $\tau_s$ . In other words, the breakup frequency should decrease to zero as this difference vanishes and the turbulent stresses are lower than the surface pressure.

The turbulent stress, which results from the velocity fluctuations existing in the liquid between two points separated by a distance of  $d_i$ , is calculated as:

$$\tau_t = \frac{1}{2} \rho_l u_{ti}^2 = \frac{1}{2} \rho_l C_{18} (\varepsilon d_i)^{2/3} \quad \text{Eq. 2-72}$$

The critical or minimum stress necessary to deform a bubble of size  $d_i$  is defined as:

$$\tau_s(d_i) = \frac{\pi \sigma d_i^2}{\frac{\pi}{6} d_i^3} = 6 \frac{\sigma}{d_i} \quad \text{Eq. 2-73}$$

Thus, the breakup frequency is given by

$$\Omega(d_i) = C_{19} \frac{\sqrt{C_{18} (\varepsilon d_i)^{2/3} - 12 \frac{\sigma}{\rho_l d_i}}}{d_i} \quad \text{Eq. 2-74}$$

The significant feature of this model is that the assumption about turbulence eddies as well as the probability distribution theory of the kinetic energy in eddies is discarded. As a result, there are no integrals involved in the model, which makes it promising for implementation into CFD simulations. The dependence of the breakup frequency on bubble diameter as well as the influence of turbulence dissipation rate is shown in Figure 2.10.



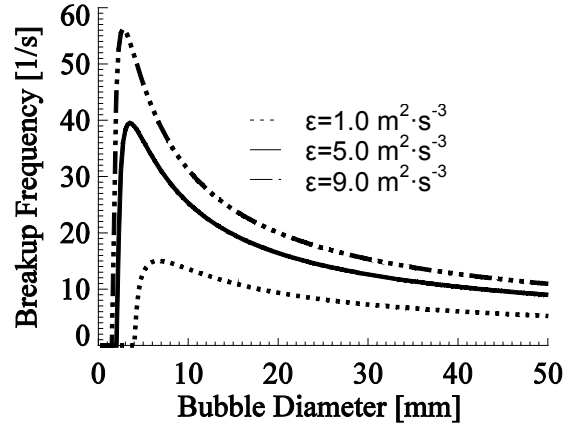


Figure 2.10 Martínez-Bazán et al. [59] model

Narsimhan et al. [111] first proposed a stochastic model for the prediction of breakup frequency in the case that the density and viscosity of the dispersed phase are not far different from that of the continuous phase. They argued that the oscillation and breakage of a drop is induced by the difference in velocity fluctuations between points near the drop surface. This is caused by the arrival of eddies of different scales, which can be described by a Poisson process. The probability distribution of the velocity difference between two points is assumed to be normal, which is given by:

$$P(u) = \frac{1}{\sqrt{2\pi}\sigma} \exp\left(-\frac{u^2}{2\sigma^2}\right) \text{ with the variance } \sigma^2 = u_{ii}^2 = 2(\varepsilon d_i)^{2/3} \quad \text{Eq. 2-75}$$

The critical velocity  $u_{crit}$  or kinetic energy is calculated from the energy balance at equal breakage with the consideration that the increase in the surface energy in this case is the minimum.

$$\frac{1}{2}(\rho_l V_i) u_{crit}^2 = (2^{1/3} - 1) \sigma \pi^{1/3} 6^{2/3} V_i^{2/3} \quad \text{Eq. 2-76}$$

Finally, they derived the breakup frequency  $\Omega$  of a droplet with size  $d_i$  as:

$$\Omega(d_i) = N \cdot P(u^2 \geq u_{crit}^2) = N \cdot \frac{1}{2} \operatorname{erfc}\left(\frac{u_{crit}}{\sigma\sqrt{2}}\right) \quad \text{Eq. 2-77}$$

where  $N$  is the average number of eddies arriving at the surface of a drop in unit time, i.e. the collision frequency, which is regarded as a constant here.

Alopaeus and his coworkers tried to modify the above model by adding a dependence on the turbulence dissipation rate to the eddy-drop collision frequency instead of a constant and by taking into account the viscous force of fluid inside the drop. They ended up with the following expression [113] [114]:

$$\Omega(d_i) = C_{20} \varepsilon^{1/3} \operatorname{erfc} \left( \sqrt{C_{21} \frac{\sigma}{\rho_l \varepsilon^{2/3} d_i^{5/3}} + C_{22} \frac{\mu_g}{\sqrt{\rho_l \rho_g \varepsilon^{1/3} d_i^{4/3}}} } \right) \quad \text{Eq. 2-78}$$

Similar to the idea of Narsimhan, Lee et al. [57] developed a theoretical model for bubble breakup, which was also based on the probabilistic theory. However, they argued that the fragmentation of a bubble will occur if the arriving eddy can provide sufficient energy to overcome a certain ratio of the bubble surface energy. The collision frequency is assumed dependent on both the dissipation rate  $\varepsilon$  and the bubble diameter  $d$ . In a similar fashion to Chatzi et al. [75], they used the Maxwell's law for the distribution of the kinetic energy of eddies. The breakup frequency function has the following form

$$\Omega(d_i) = C_{23} d_i^{-2/3} \varepsilon^{1/3} \left[ 1 - \frac{1}{d_i} \cdot \int_0^{d_i} F(C_{24} \sigma d_i^2 \rho_l^{-1} \varepsilon^{-2/3} d_e^{-11/3}) dd_e \right] \quad \text{Eq. 2-79}$$

where  $F$  is the cumulative chi-square distribution with three degrees of freedom.  $C_{24} = C \cdot (2\pi)^{5/3}$ , where  $C$  is the ratio of the minimal energy required for breakup to the parent bubble surface energy.

With the exception of the density term, Eq. 2-79 is almost the same as Eq. 2-71 if the chi-square distribution is transformed into gamma functions and the effective eddy length scale  $d_e$  assumed approximately equal to the bubble size  $d_i$ . That means that for turbulence-induced breakup the models for bubbles and drops are often transferable to each other. An exception consists in high-viscosity drops. In this case, the viscous force of the drop also plays an important role in the constraining of breakage in addition to surface tension.

The dependence of the breakup frequency predicted by Eq. 2-79 on the dissipation rate  $\varepsilon$  and constant  $C$  is shown in Figure 2.11.

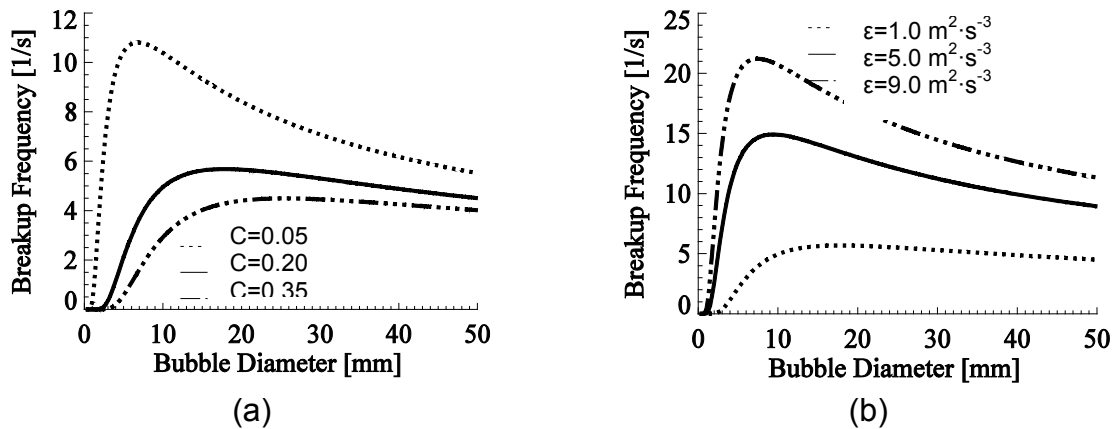


Figure 2.11 Lee et al. [57] model. (a)  $\varepsilon = 1.0 \text{ m}^2 \cdot \text{s}^{-3}$ ; (b)  $C = 0.25$

Lee et al. [57] have made some improvements on the model of Narsimhan et al. [111]. However, using Maxwell's law for the probability density of kinetic energy in turbulent eddies is criticizable since Maxwell's law is only valid for free-gas molecular motion and might be not suitable for imaginary eddies [95]. Furthermore, the breakup

frequency depends strongly on the parameter C, i.e., the minimal required energy, which is still an open question.

Although many previous models considered that the collision between the eddies and bubbles or drops was the dominant reason for breakup, Prince and Blanch [36] first determined the breakup frequency by examining the interaction between the bubble and eddy, and by making an analogy to molecular collisions in ideal gases. They computed the breakup frequency by multiplying the collision frequency  $w$  with a collision efficiency  $P_b$ :

$$\Omega(d_i) = \int_0^{\infty} w(d_i, d_e) P_b(d_i, d_e) dd_e \quad \text{Eq. 2-80}$$

wherein  $d_e$  is the eddy length scale.

The collision frequency  $w(d_i, d_e)$  is defined as the volume swept in unit time by the approaching bubble and eddy, which is equal to the product of the cross-sectional area  $S$ , the relative velocity between bubble and eddy  $u_{rel}$  and the number density of eddies  $n_e$ :

$$w(d_i, d_e) = u_{rel} \cdot S_{ie} \cdot n_e \quad \text{Eq. 2-81}$$

The breakup efficiency  $P_b(d_i, d_e)$  is assumed equal to the probability that turbulent eddies have sufficient energy to rupture a bubble. The critical or minimum energy  $E_{crit}$  is determined from a critical Weber number  $We_{crit}$ , which is considered as a constant for a given system. The random distribution of the turbulent kinetic energy  $E_e$  in the eddy obeys a normal function in Eq. 2-75. Finally, the breakup efficiency  $P_b(d_i, d_e)$  is calculated as:

$$P_b(d_i, d_e) = \exp\left(-\frac{u_{crit}^2}{u_e^2}\right) \quad \text{Eq. 2-82}$$

Prince and Blanch [36] calculated the critical Weber number  $We_{crit}$  from an empirical maximum stable bubble size, and a value of 2.3 was obtained for turbulent air-water system. Therefore, the critical eddy velocity  $u_{crit}$  is given by

$$u_{crit} = \sqrt{\frac{2.3\sigma}{d_i \rho_l}} = 1.52 \sqrt{\frac{\sigma}{d_i \rho_l}} \quad \text{Eq. 2-83}$$

Finally, the integral in Eq. 2-80 can be rewritten as:

$$\Omega(d_i) = \int_{k_{min}}^{k_{max}} \frac{0.14\pi}{16} \left(d_i + \frac{2}{k}\right)^2 \left[ d_i^{2/3} + \left(\frac{2}{k}\right)^{2/3} \right]^{1/2} \varepsilon^{1/3} \exp\left(-\frac{1.18}{2^{2/3}} \frac{\sigma k^{2/3}}{\rho_l d_i \varepsilon^{2/3}}\right) k^2 dk \quad \text{Eq. 2-84}$$

where  $k$  is the wave number of eddies, related to the eddy size by  $k=2/d_e$ .

The influence of energy dissipation rate  $\varepsilon$  and upper limit of the integration on the predicted breakup frequency is depicted in Figure 2.12.

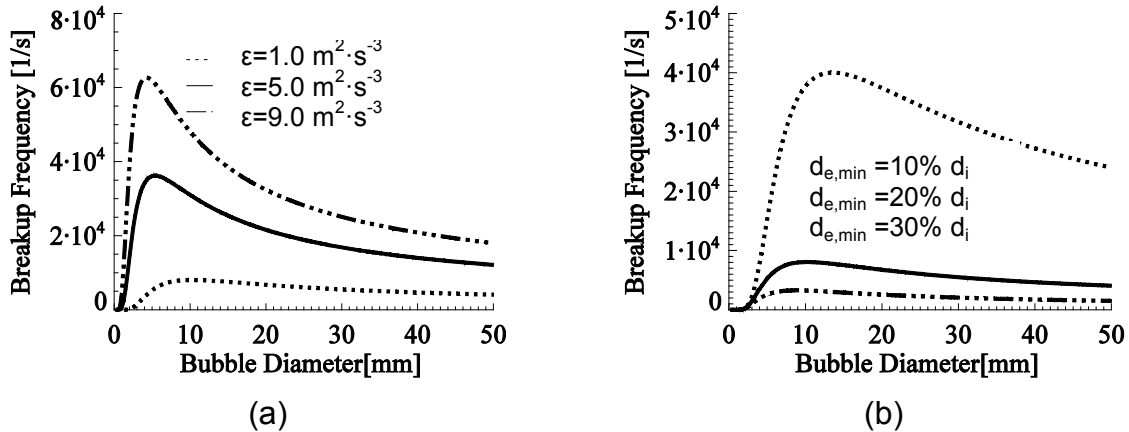


Figure 2.12 Prince and Blanch [36] model. (a)  $d_{e,\min} = 20\% d_i$ ; (b)  $\varepsilon = 1.0 \text{ m}^2 \cdot \text{s}^{-3}$

It must be noted that the upper limit of the integration becomes infinitely large as the eddy size approaches zero. With the premise of the inertial subrange, they set the minimum eddy size arbitrarily to 20% of the bubble diameter. However, Figure 2.12 shows that the results depend sensitively on this limit [108].

Tsouris and Tavlarides [51] criticized their original model of Coulaloglou and Tavlarides [56] by pointing out that it predicts a maximum as the drop size increases, as shown in Figure 2.9. However, the models of Lee et al. [57], Prince and Blanch [36] as well as the model of Martínez-Bazán et al. [59] also exhibit the same behavior especially at high dissipation rates. Tsouris and Tavlarides [51] considered the non-monotonic behavior to be erroneous and proposed a modified model based on the concept of Prince and Blanch [36]. The major difference between two models is the value of the critical energy  $E_{\text{crit}}$ . Tsouris and Tavlarides defined the critical energy as the mean value of the increases in the surface energy of the equal-sized breakage and breakage with a smallest and a biggest daughter. They ended up with the following form for breakup frequency:

$$\Omega(d_i) = \int_0^\infty w(d_i, k) P_b(d_i, k) dk = 0.0118 DF(\alpha_g) \varepsilon^{1/3} \int_{k_{\min}}^{k_{\max}} \left( d_i + \frac{2}{k} \right)^2 \times \left( 1.07 d_i^{2/3} + 8.2 k^{-2/3} \right)^{1/2} \exp\left( -\frac{E_{\text{crit}}}{C_{25} E_e} \right) k^2 dk \quad \text{Eq. 2-85}$$

It can be seen that the modified model has the same problem as its ancestor of Prince and Blanch [36]. That is how to determine the upper and low integration limits. The smallest and largest effective eddy is arbitrarily set to be half the critical drop size  $d_{\text{crit}}$  and the drop diameter, respectively. The influence of the lower integral limit is referred to Lasheras et al. [115].

Luo and Svendsen [95] criticized all previous models by pointing out that experimental costs are needed to determine unknown parameters. Instead of the

total breakup frequency of the mother bubble, they proposed a new theoretical model for the partial breakup frequency,

$$\Omega(d_j, d_i) = \int_0^\infty w(d_i, d_e) P_b(d_i, d_j, d_e) dd_e \quad \text{Eq. 2-86}$$

The collision frequency  $w(d_i, d_e)$  was calculated according to Eq. 2-81 except that the expressions used for velocity and number density of eddies are slightly different.

The computation of breakup efficiency  $P_b(d_i, d_j, d_e)$  is also similar to that of Prince and Blanch [36] and Tsouris and Tavlarides [51]. The unique difference is the critical energy  $E_{crit}$ , which is defined as the increase in surface energy during the breakage event, i.e.

$$E_{crit} = \Delta \bar{E}_i(d_i) = \left[ f_{bv}^{2/3} + (1 - f_{bv})^{2/3} - 1 \right] \pi d_i^2 \sigma = c_{fbv} \pi d_i^2 \sigma \quad \text{Eq. 2-87}$$

The breakage volume fraction,  $f_{bv}$ , can be defined as

$$f_{bv} = \frac{V_j}{V_i} = \frac{d_j^3}{d_i^3} \quad \text{Eq. 2-88}$$

where the subscript i indexes the parent bubble and j indexes one of the two daughter bubbles.

Therefore, the partial breakup frequency is given as:

$$\Omega(d_j, d_i) = 0.923 (1 - \alpha_g) \left( \frac{\varepsilon}{d_i^2} \right)^{1/3} \int_{\xi_{min}}^1 \frac{(1 + \xi)^2}{\xi^{11/3}} \exp \left[ - \frac{\Delta \bar{E}_i(d_i)}{E_e} \right] d\xi \quad \text{Eq. 2-89}$$

where  $\xi = d_e/d_i$  is the size ratio between the bombarding eddy and the bubble. The dependence of the breakup frequency on the dissipation rate  $\varepsilon$  and the gas volume fraction is shown in Figure 2.13.

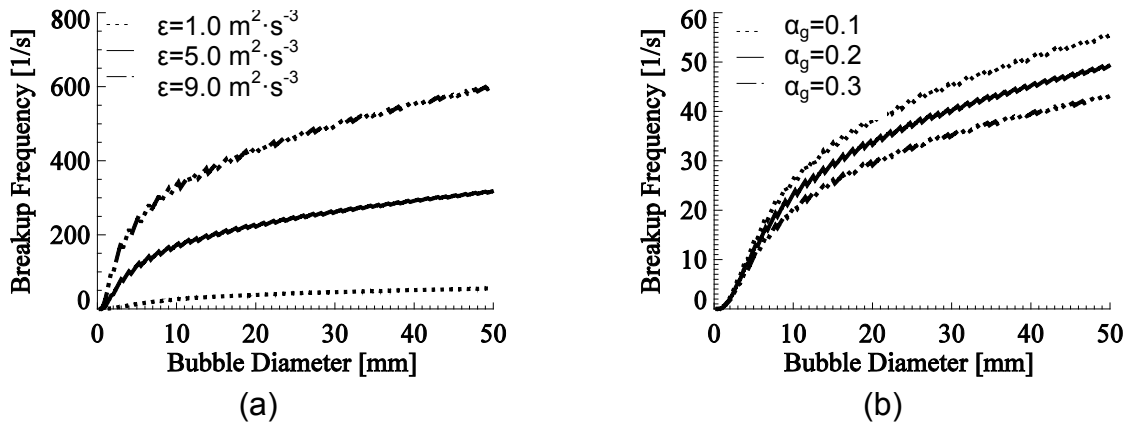


Figure 2.13 Luo and Svendsen [95] model. (a)  $\alpha_g = 0.3$ ; (b)  $\varepsilon = 1.0 \text{ m}^2 \cdot \text{s}^{-3}$

Since no separate daughter distribution function is needed, the model of Luo and Svendsen [95] is widely used in later applications, such as in [2] [116] ~ [118]. However, as pointed by Lasheras et al. [115] the results depend on the lower and upper limits of the integration which is a common feature of the models based on bubble-eddy collisions [36] [51]. The determination of the upper and lower limits includes indirectly two unknowns. On the other hand, the model is found to have no limit for the lower breakup size since the critical energy  $E_{crit}$  in Eq. 2-87 approaches to zero as the size of the smaller daughter bubble  $V_j$  goes to zero [96] [119] [120].

Almost all the above models consider only the energy constraint during the breakup process, namely breakup occurring only if a critical energy is exceeded. Lehr et al. [30] first proposed a model based on a force balance between the inertial force of the arriving eddy and the interfacial force of the smaller daughter bubble, called the capillary constraint by Wang et al. [96]. They claimed that the capillary pressure is the dominant constraint for the breakup of bubbles with radius tending to zero. This is because in such a case, the capillary pressure or interfacial force is very high and thus the arriving eddy may not provide enough dynamic pressure or inertial force to overcome the capillary pressure even though it might contain enough kinetic energy [96].

Lehr et al. [30] calculated the breakup frequency also by multiplying the arrival frequency of the eddy with the corresponding probability density. If a bubble of size  $d_i$  is hit by an eddy of size  $d_e$  and breaks into two bubbles with size  $d_j$  and  $d_i-d_j$ , the breakup frequency  $\Omega$  can be calculated by integrating the product over the whole effective eddy length scale.

$$\Omega(d_j, d_i) = \int_{d_{e,min}}^{d_{e,max}} w(d_i, d_e) P_b(d_i, d_j, d_e) dd_e \quad \text{Eq. 2-90}$$

They assumed that the breakup probability depends on the angle  $\phi$ , under which the eddy hits the bubble. By assuming that it is equal for all steradians, the breakup probability can be calculated from the force balance. The final form for the partial breakup frequency is given by:

$$\begin{aligned} \Omega(d_j, d_i) &= \int_{d_{e,min}}^{d_{e,max}} \frac{3.55 d_i \sigma (1 - \alpha_g)}{\varepsilon^{1/3} d_e^{10/3} \rho_l d_j^4} dd_e \\ &= 1.5 (1 - \alpha_g) \frac{\rho_l^{11/5} \varepsilon^{9/5}}{\sigma^{11/5}} \frac{\hat{V}_i^{1/3}}{\hat{V}_j^{4/3}} \left[ \min \left( \hat{V}_j^{7/6}, \frac{1}{\hat{V}_j^{7/9}} \right) - \frac{1}{\hat{V}_i^{7/9}} \right] \end{aligned} \quad \text{Eq. 2-91}$$

where the normalized volumes of bubble i and j are respectively defined as

$$\hat{V}_i = V_i / \left( \frac{\pi}{6} \frac{\sigma^{9/5}}{\rho_l^{9/5} \varepsilon^{6/5}} \right), \quad \hat{V}_j = V_j / \left( \frac{\pi}{6} \frac{\sigma^{9/5}}{\rho_l^{9/5} \varepsilon^{6/5}} \right) \quad \text{Eq. 2-92}$$

The model has the same advantage as the model of Luo and Svendsen [95]. Arbitrary assumptions about the daughter bubble size distribution can be avoided. However, the upper and lower limits of the integral have to be determined. The upper

---

limit was assumed to be the bubble diameter with the consideration that only eddies of length scale smaller than or equal to the bubble diameter can deform the bubble surface, i.e.  $d_{e,max}=d_i$ . The minimum effective eddy length scale is set as  $d_{e,min}=\max(d_j, d_{min})$ , where  $d_{min}$  is obtained from the force balance by assigning zero to the hitting angle  $\phi$ .

Three years later Lehr et al. [31] put forward with a modified model, which is also based on a force balance. The main difference between the modified and original model is the computation of the breakup probability. Lehr et al. [31] calculated the breakup probability based on the criterion that the kinetic energy of the eddy exceeds a critical energy, which is obtained from the force balance equation.

The Eq. 2-90 is expressed as:

$$\Omega(d_j, d_i) = 1.19 \int_{d_{e,min}}^{d_{e,max}} \frac{\sigma}{\rho_l \varepsilon^{1/3} d_j^4} \frac{(d_e + d_i)^2}{d_e^{13/3}} \exp\left(-\frac{2\sigma}{\rho_l \varepsilon^{2/3} d_j d_e^{2/3}}\right) dd_e \quad \text{Eq. 2-93}$$

In order to enhance computation efficiency, instead of integrating Eq. 2-93 directly, Lehr et al. [31] provided an analytical solution for the breakup frequency  $\Omega(d_i)$  and the corresponding daughter size distribution function by expressing the integral as a sum of incomplete Gamma-functions.

$$\Omega(d_i) = 0.5 \frac{d_i^{5/3} \varepsilon^{19/15} \rho_l^{7/5}}{\sigma^{7/5}} \exp\left(-\frac{\sqrt{2}\sigma^{9/5}}{d_i^3 \rho_l^{9/5} \varepsilon^{6/5}}\right) \quad \text{Eq. 2-94}$$

The influence of the dissipation rate and bubble size on the breakup frequency according to the model of Lehr et al. [31] is shown in Figure 2.14. The breakup frequency increases monotonously with the dissipation rate and the bubble size.

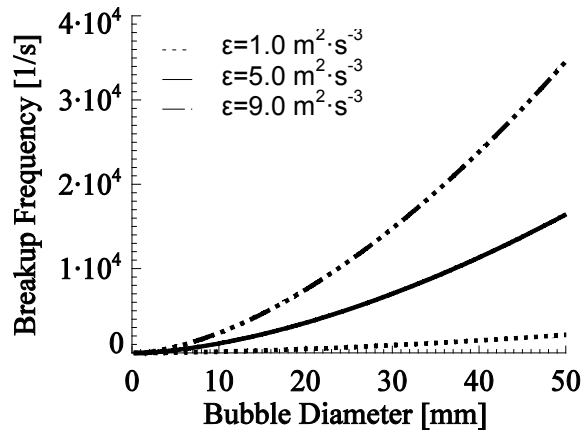


Figure 2.14 Lehr et al. [31] model

Wang et al. [96] argued that the breakup of bubbles should be limited by both the force and the energy constraints. They pointed out that the force balance used by Lehr et al. [30] [31] may not be satisfied during breakage, since during breakup the inertial force of the colliding eddy is usually larger than the inertial force until breakage occurs. On the other hand, they criticized the model of Luo and Svendsen

[95] by pointing out that if the kinetic energy is larger than the critical value defined in Eq. 2-87 it will be possible for the eddy to induce all breakages with one daughter bubble smaller than  $V_i f_{bv}$ . In contrast, Luo and Svendsen [95] considered only the breakage with size  $V_i f_{bv}$ . Here  $f_{bv}$  is the breakage volume fraction defined in Eq. 2-88.

By adding the capillary constraint proposed by Lehr et al. [30] [31], Wang et al. [96] extended the model of Luo and Svendsen [95]. The only difference between the extended model and its ancestor is the breakup probability  $P_b(d_i, d_j, d_e)$ :

$$P_b(d_i, d_j, d_e) = \int_0^\infty \frac{1}{f_{bv,max} - f_{bv,min}} \frac{1}{E_e} \exp\left(-\frac{E_e}{E_c}\right) dE_e \quad \text{Eq. 2-95}$$

where  $f_{bv,max}$  and  $f_{bv,min}$  are determined by the energy and capillary constraints, respectively.

The partial breakup frequency is given as:

$$\Omega(d_j, d_i) = \int_{d_{e,min}}^{d_i} w(d_i, d_e) P_b(d_i, d_j, d_e) dd_e \quad \text{Eq. 2-96}$$

where the collision frequency between bubble and eddy is calculated according to Eq. 2-81.

The dependence of the predicted total breakup frequency on the dissipation rate, gas volume fraction as well as bubble size is depicted in Figure 2.15.

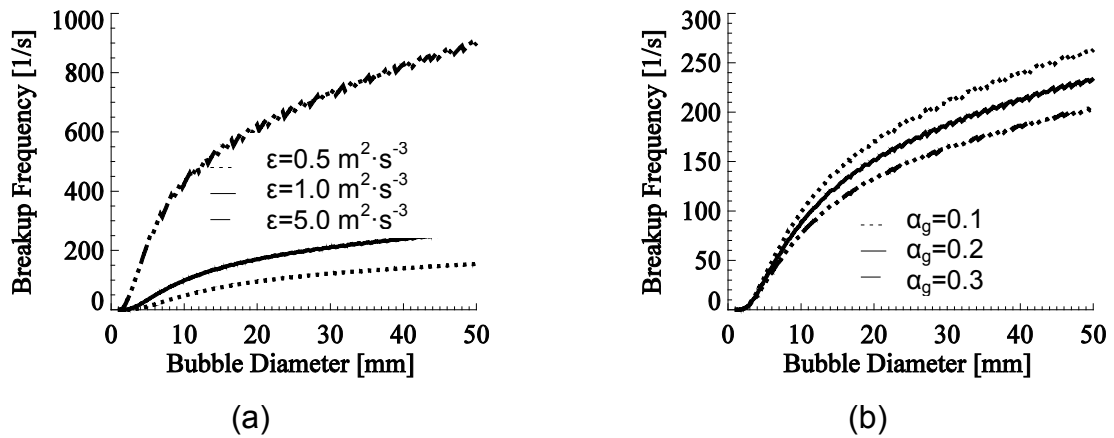


Figure 2.15 Wang et al. [96] model. (a)  $\alpha_g=0.1$ ; (b)  $\epsilon=1.0\text{m}^2 \cdot \text{s}^{-3}$

Since both constraints are considered in the calculation of breakage probability, the model of Wang et al. [96] seems to be most reasonable. However, the calculation of the partial breakup frequency is very time-consuming because a triple integral is involved in Eq. 2-96. Therefore, Wang et al. [121] worked out an efficient numerical algorithm to calculate the triple integral by arbitrarily introducing a cutoff energy and calculating the probability recursively instead of integrating directly. The accuracy of the solution depends severely on the discretization of  $f_{bv}$ .



The last breakup model was published by Zhao and Ge [97], which considers also both the energy constraint and force balance constraint as in Wang et al. [96]. By assuming that one of the two daughter bubbles generated during the breakup process has the same size as the hitting eddy,  $d_e$ , the integral over the eddy size can be avoided.

The breakage probability of a bubble with size  $d_i$  hit by an eddy with size  $d_e$ , is given as:

$$P_b(d_i, d_j = d_e) = P_e(E_e \geq E_{crit}) \quad \text{Eq. 2-97}$$

where  $E_{crit}$  is obtained from the energy and force constraints, i.e.:

$$E_{crit} = \max \left[ \frac{c_{bv} \pi d_i^2 \sigma}{C_e}, \frac{\pi \sigma d_e^3}{3d_i \cdot \min(f_{bv}, 1 - f_{bv})^{1/3}} \right] \quad \text{Eq. 2-98}$$

With the eddy efficiency  $C_e$  the authors tried to describe the situation that energy in the hitting eddy cannot be exhaustively transferred to the bubble.

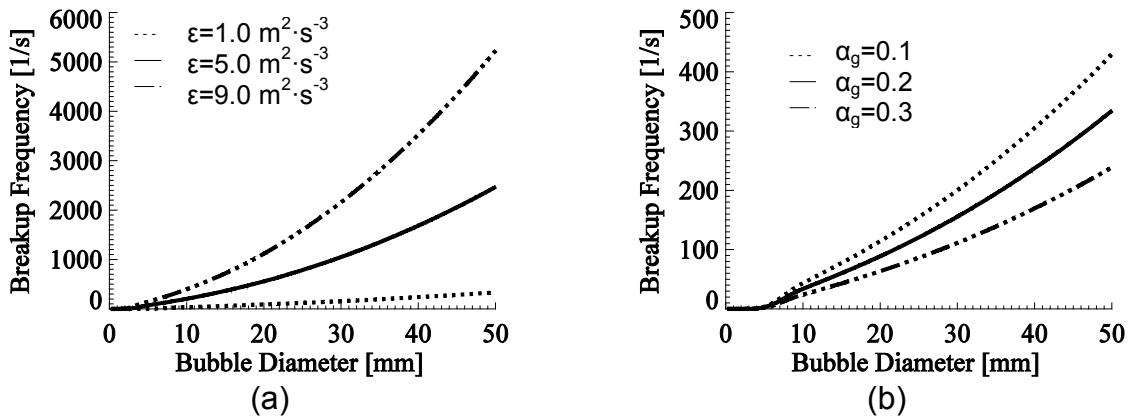


Figure 2.16 Zhao and Ge [97] model. (a)  $\alpha_g=0.3$ ; (b)  $\epsilon=1.0\text{m}^2 \cdot \text{s}^{-3}$

The model seems to be the most general and computationally cheapest one amongst the discussed models. However, the assumption about the size of one daughter equal to the length scale of the eddy should be validated with experimental data and also the determination of the eddy efficiency is worthy of further investigations.

In summary, most of the models discussed so far are based on the bubble-eddy collision mechanism which relies on the assumption that the turbulent continuous flow consists of an array of discrete eddies that can be treated like molecules in classical gas kinetic theory. The imaginary eddy concept is impossible to validate regarding the number density, shape, size of eddies and bubble-eddy interactions. Although the model of Martínez-Bazán et al. [59] avoids the eddy concept, its validation is still restricted to homogeneous and isotropic fully developed turbulent flows and turbulent water jets. The homogeneity of turbulence is well controlled in the experiments, whereas the turbulence dissipation rates are several orders of magnitude larger than bubble columns or pipe flows. Furthermore, almost all models

for turbulent flows are limited to isotropic turbulence and the inertial subrange. On the other hand, the breakup frequencies provided by various models are inconsistent. More recent models such as [51] [95] ~ [97] give a monotonic relation between the breakup frequency and the bubble size, while the older ones, e.g. [36] [56] [57] [59], exhibit a maximum as the bubble diameter increases, which is considered erroneous by Tsouris and Tavlarides [51], whereas the argument is still open to question. The quantitative difference between above models can achieve at least several orders of magnitude, see Figure 2.9 ~ Figure 2.16.

### **Models for breakup due to viscous shear force**

As discussed in section §2.4.1, in turbulent gas-liquid flows, bubbles can be subjected to a variety of destroying forces and breakup in quite different ways. However, compared to the turbulent fluctuations, the influence of viscous shear, shearing-off and surface instability in a turbulent flow is usually neglected and as a result the corresponding models are rare in the literature.

It has been shown that the deformation and breakup of a drop or bubble due to viscous shear force is primarily determined by the Capillary Number  $Ca$ , which is expressed in the ratio of viscous stress to the surface tension:

$$Ca = \frac{\tau_v}{\tau_s} = \frac{\mu_l d \dot{\gamma}}{2\sigma} \quad \text{Eq. 2-99}$$

where  $\mu_l$  is the viscosity of the continuous liquid and  $\dot{\gamma}$  the shear rate.

The criterion used often for the breakup of a bubble due to viscous shear force is  $Ca > Ca_{crit}$ . The critical diameter is therefore determined by:

$$d_{crit} = \frac{2\sigma Ca_{crit}}{\mu_l \dot{\gamma}} \quad \text{Eq. 2-100}$$

Experimental studies show that the critical capillary number  $Ca_{crit}$  depends on the viscosity ratio  $p = \mu_g/\mu_l$  and the flow type [99] [103]. For droplets immersing in simple shear flow, the region of  $Ca_{crit} < Ca < \kappa Ca_{crit}$  is dominated by necking, where the droplet breaks up into two equal-sized fragments and a few much smaller satellite droplets. When the capillary number increases suddenly to a value well above  $Ca_{crit}$ , the droplet is rapidly elongated into a long cylindrical fluid thread, which subsequently breaks into a series of fragments due to the growth of wave like-shape distortions, called capillary instabilities. The deformation prior to breakup decreases as the viscosity ratio  $p$  increases. At viscosity ratios above about 4, breakup in a simple shear flow is virtually impossible [98] [99] [122].

Experimental results of Grace [98] Elemans et al. [108] and Wieringa et al. [4] show that the average breakup time in a simple shear flow can be given by:

$$t_b = \frac{\mu_l d_i}{2\sigma} f(p) \quad \text{Eq. 2-101}$$

where the function  $f(p)$  depends on the flow type and the viscosity ratio.

---

$$f(\rho) = C_{26} \rho^n \quad \text{Eq. 2-102}$$

It is worth mentioning that Lo and Zhang [122] used a different correlation:

$$\log f(\rho) = C_{27} + C_{28} \log(\rho) + C_{29} [\log(\rho)]^2 \quad \text{Eq. 2-103}$$

The breakup frequency is thought inversely proportional to the breakup time defined in Eq. 2-101. This is similar to the concept used by Martínez-Bazán et al.[59].

$$\Omega(V_i) = \frac{C_{30}}{t_b} \quad \text{Eq. 2-104}$$

### **Models for breakup due to interfacial stresses**

As mentioned in section §2.4.1, interfacial stresses can tear small bubbles from a cap bubble rising in water, which is called shearing-off process by Ishii and his coworkers [104] [105]. According to Fu and Ishii [104], the number source of small bubbles sheared-off from the cap/slug bubble is determined by the total sheared-off volume  $V_{so}$  and the generated bubble size  $d_{so}$ . The sheared-off volume  $V_{so}$  can be modeled as a volume related to the gas flow rate across the ring area with an effective thickness  $\delta_{eff}$  of the gas layer that may be sheared off:

$$V_{so} \propto \pi d_i \delta_{eff} u_{rel} \quad \text{Eq. 2-105}$$

where the effective thickness  $\delta_{eff}$  is estimated according to the boundary layer thickness of a turbulent gas flow over a flat plate [69].

The sheared-off bubble size  $d_{so}$  is assumed to be proportional to the maximum stable bubble diameter  $d_{so,max}$ , which is given by the empirical expression derived from the experiment for plunging liquid jet [124] [125]:

$$d_{so,max} = \left( \frac{We_{crit} \sigma}{2\rho_l} \right)^{3/5} \varepsilon^{-2/5} \quad \text{Eq. 2-106}$$

According to Sun et al. [105] the average diameter of the sheared-off bubbles can be determined from the balance between the interfacial friction force and the surface tension force.

$$d_{so} = \frac{2\sigma}{C_s C_{fi} \rho_l u_{rel}^2} \quad \text{Eq. 2-107}$$

where  $C_s$  is a shape coefficient and  $C_{fi}$  is the interfacial frictional factor, which has also a functional dependence on the relative velocity  $u_{rel}$ . In order to determine the final dependence of  $d_{so}$  on  $u_{rel}$ , Sun et al. [105] derived an empirical correlation from their experimental data for confined upward air-water flow by making reference to Eq. 2-106. By considering  $\varepsilon = u_{rel}^3 G^{-1}$ , a dependence of  $d_{so}$  on  $u_{rel}$  is obtained, where  $G$  is the gap of the confined flow channel.

In the work of Fu and Ishii [104], the interfacial drag force is postulated to be effective in such a case that a number of small bubbles are generated at the tail of a slug bubble, whereas its size is lower than the maximum stable size for surface instability. They argued that due to any collision with a turbulence eddy, the slug bubble may deform and propagate downstream along the side interface. The deformed part is subjected to a significant drag force, which is sustained by the surface tension force. When the perimeter of the deformed interface part, reduces to a scale comparable to the eddy size, the surface tension force may be overcome by the drag force and small bubbles may be sheared-off from the interface.

The drag force on the bubble is given as:

$$F_D = \frac{1}{2} k_d C_D \rho_l u_{rel}^2 A_e \quad \text{Eq. 2-108}$$

where  $A_e = \pi d_e^2 / 4$  is the projected area of the bubble and  $d_e$  is the eddy size.

The surface tension force is given as:

$$F_\sigma = \pi d_e \sigma \quad \text{Eq. 2-109}$$

From the balance between  $F_D$  and  $F_\sigma$ , one obtains

$$d_e = \frac{8\sigma}{\rho_l u_{rel}^2 k_d C_D} \quad \text{Eq. 2-110}$$

In the work of Fu and Ishii [104],  $d_e$  has been seen as the critical eddy size that might lead to bubble breakup by this mechanism.

### **Models for breakup due to surface instability**

When the bubble volume exceeds the maximum stable limit, it becomes unstable and disintegrates due to surface instability. Due to insufficient information about the breakup process caused by this mechanism, there are no phenomenological models in the literature. Wang et al. [107] estimate the breakup frequency following the empirical correlation of Carrica and Clause [126]

$$\Omega(d_i) = C_{31} \frac{(d_i - d_{crit})^{C_{32}}}{(d_i - d_{crit})^{C_{33}} + d_{crit}^{C_{34}}} \quad \text{Eq. 2-111}$$

where  $d_{crit}$  is the critical bubble diameter set as 27 mm.

### **2.4.3 Daughter bubble size distribution**

For the calculation of time and space dependent bubble size distributions, in addition to the breakup frequency  $\Omega(d_i)$ , a separate function  $\beta(V_j, V_i)$  has to be proposed for the daughter bubble size distribution. Functions used for daughter bubble size distribution can be classified as three forms: empirical, statistical and phenomenological, see Figure 2.17. An exception that no separate functions are

needed for daughter bubble size distribution is the partial breakup frequency  $\Omega(d_j, d_i)$  directly given by models, e.g. the models highlighted with red color in Figure 2.17.

**Empirical models**

Hesketh et al. [127] compared several different distribution functions with their experimental data [128]. They are Dirac delta function, uniform function and attrition function, which can be described using two Dirac delta functions at  $f_{bv} \rightarrow 0$  and  $f_{bv} \rightarrow 1$ . The results showed that the experimental data is between the values predicted by uniform and attrition breakage. An intermediate function, the so-called 1/X-shaped function, was proposed by the authors:

$$\beta(V_j, V_i) = \left[ \frac{1}{(V_j / V_i + B)} + \frac{1}{(1 - V_j / V_i + B)} - \frac{2}{(B + 0.5)} \right] \frac{I}{V_i} \quad \text{Eq. 2-112}$$

The constant B is added to control the height of the function at  $f_{bv}$  near 0.0 and 1.0. The value of B resulting in the best fit to the measured Sauter mean diameter, and I is the normalization constant.

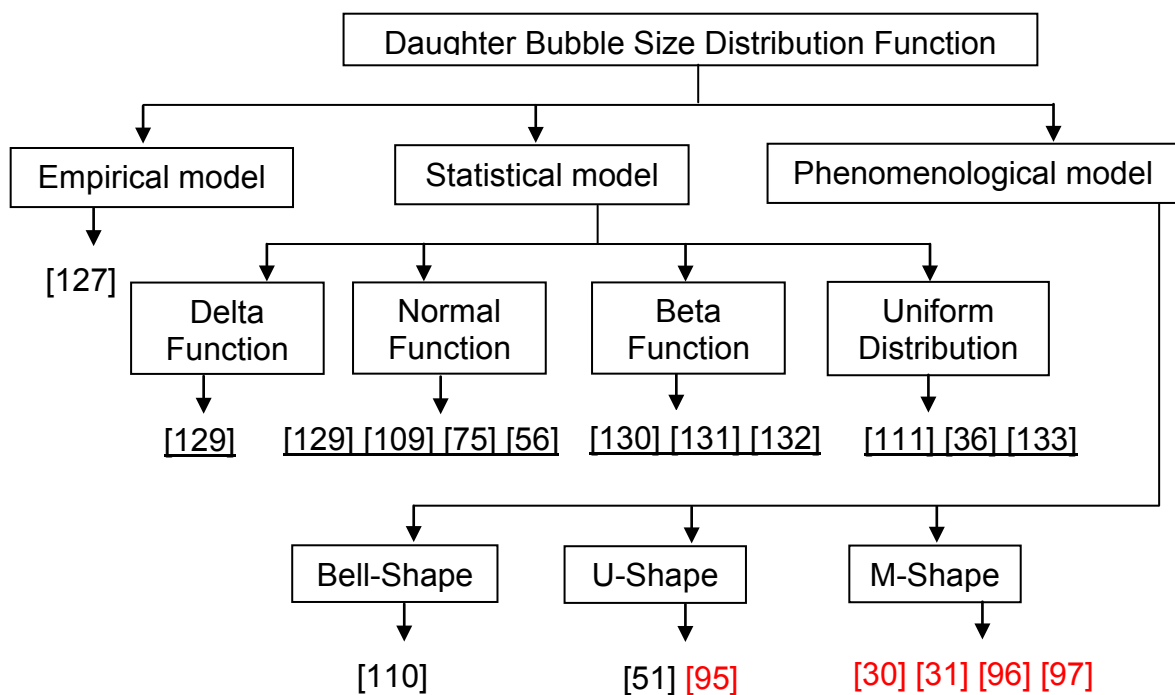


Figure 2.17 Classification of available models for daughter bubble size distribution

**Statistical models**

A statistical model, as the name suggests, assumes that the size of daughter bubble is a random variable and its probability distribution satisfies a simple distribution function. Normal, beta and uniform distribution functions are often used.

A truncated normal function was first used by Valentas et al. [129] for the continuous case, where the size of daughter bubbles is normally distributed about a mean value  $V_{mean}$  with a specified variance,  $\sigma^2$ .

$$\beta(V_j, V_i) = \frac{1}{\sigma\sqrt{2\pi}} \exp\left[-\frac{(V_j - \bar{V})^2}{2\sigma^2}\right], \quad \bar{V} = \frac{V_i}{m}, \quad \sigma = \frac{\bar{V}}{c} = \frac{V_i}{c \cdot m} \quad \text{Eq. 2-113}$$

The dimensionless form is:

$$\beta(f_{bv}, 1) = \beta(V_j, V_i) \cdot V_i = \frac{c \cdot m}{\sqrt{2\pi}} \exp\left[-0.5\left(f_{bv} - \frac{1}{m}\right)^2 (c \cdot m)^2\right] \quad \text{Eq. 2-114}$$

where m is the number of daughter bubbles, usually assumed to be 2, and c is the tolerance of the distribution. For example, c=3 means >99.6% of the daughter bubbles lie in the volume range 0 to  $V_i$ .

Figure 2.18 (a) shows the truncated normal distribution, which has been used in a number of later investigations, such as [56] [75] [109].

Hsia and Tavlarides [130] found that the truncated normal function was unable to predict the results obtained by Ross et al. [76], Verhoff et al. [135] and Ross [134]. Consequently, they modified their earlier work in [56] and assumed the distribution satisfies a beta function rather than the normal function.

$$\beta(f_{bv}, 1) = 30 \cdot \frac{\pi}{6} f_{bv}^2 (1 - f_{bv})^2 \quad \text{Eq. 2-115}$$

Lee et al. [130] also applied a beta distribution for the size of daughter bubbles with the following density function

$$\beta(f_{bv}, 1) = \frac{\Gamma(a+b)}{\Gamma(a)\Gamma(b)} f_{bv}^{a-1} (1 - f_{bv})^{b-1} \quad \text{Eq. 2-116}$$

where a, b are two adjustable parameters. According to Lee et al. [130], for a binary breakage, 2.0 was the best value for them.

Konno et al. [136] proposed a statistical model that includes the distribution of energy in turbulent eddies of different scales and was called a hybrid model by Lasheras et al. [115]. They assumed that the probability to form a daughter bubble of a given size is proportional to the kinetic energy contained in eddies of the same size. However, Konno et al. [131] have shown that their model can be well approximated by the following beta function:

$$\beta(f_{bv}, 1) = \frac{\Gamma(12)}{\Gamma(3)\Gamma(9)} f_{bv}^8 (1 - f_{bv})^2 \quad \text{Eq. 2-117}$$

The dimensionless normal and beta daughter bubble size distribution is depicted in Figure 2.18(a) and Figure 2.18(b), respectively. It shows that both the normal and beta function predict a maximum at equal-sized breakup, i.e., the two daughters

have equal volume, which is contradictory to the experimental findings of Hesketh which show that the equal-sized breakage has the lowest probability [127] [128].

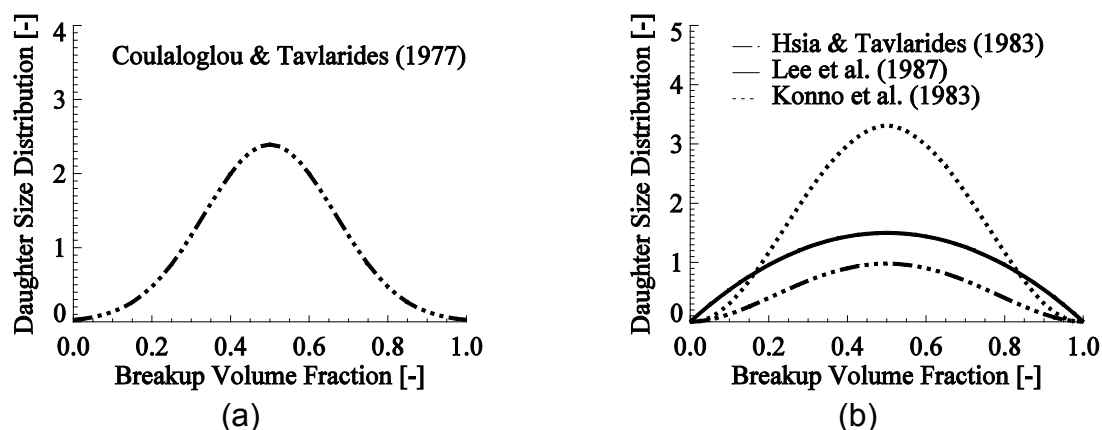


Figure 2.18 (a) Normal function; (b) Beta function

Narsimhan et al. [111] and Randolph [133] argued that a uniform distribution could be used, which was found by Collins and Knudsen [137] to be the best choice by comparing with their experimental data. In the work of Prince and Blanch [36] a uniform distribution was also used since it was assumed that the size of daughter bubbles is a random variable, i. e., daughter bubbles of any size have an equal probability. However, there are no physical reasons to select a uniform model, since turbulent fluctuations are not uniform over all scales [115].

Thus, statistical models might be applicable to systems having stochastic characteristics. That means that if the breakup of a collection of bubbles can be assumed as a large population of independent, random events, the distribution can then be deduced statistically. A presumed density function with more adjustable parameters is of course more flexible and can provide more shapes to fit daughter bubble size distributions. However, the dependence on experimental apparatus increases with the number of free parameters, because the proper selection of adjustable parameters relies heavily on the flow conditions. On the other hand, only through one or two adjustable parameters, the presumed function such as the normal and beta function can hardly reflect the dependence on the underlying turbulence. Therefore, most recent work is based on a phenomenological approach.

### **Phenomenological models**

A phenomenological model is usually a simple algebraic expression, which is formulated for the purpose of relating empirical observations of a phenomenon to each other. It is not directly derived from theory, because the information about the underlying theory of such phenomenon is still insufficient.

According to the shape of daughter size distributions, phenomenological models derived by various researchers can be categorized as three categories, i.e. Bell-shape, U-shape and M-shape.

Martínez-Bazán et al. [110] continued their work on the breakup of air bubbles injected into a fully developed turbulent flow, and presented a model for daughter bubble size distribution on the basis of a force balance. They computed the probability density of a daughter bubble with size  $d_j$  as the product of the probability

that the parent bubble splits into two daughter bubbles with one in the size range  $0 \leq d_j \leq d_i$ ,  $P_1$ , and the probability of the daughter bubble with a given size  $d_j$ ,  $P_2$ . As in Prince and Blanch [36], the size of daughter bubbles is assumed to be a stochastic variable and uniformly distributed on the segment  $[0, d_i]$ , therefore, the distribution probability density of any size falling in  $[0, d_i]$  would always be  $P_1=1/d_i$ . On the other hand, the probability of the parent bubble with size  $d_i$  breaking into a daughter bubble of a given size  $d_j$  should be determined by the difference between the turbulent stresses over a length equal to its size,  $\rho_l \varphi (\varepsilon d_j)^{2/3} / 2$ , and the confinement stresses, i.e. surface pressure stresses of the parent bubble,  $6\sigma/d_i$ . Thus, the probability of the formation of a daughter bubble of size  $d_j$  and its complementary part  $d_k$ ,  $P_2$ , is postulated to be equal to the product of the two surplus stresses corresponding to two daughter bubbles.

Finally, the total probability can be written as:

$$P_b(d_j, d_i) = \frac{1}{d_i} \left[ \frac{1}{2} \rho_l \varphi (\varepsilon d_j)^{2/3} - 6 \frac{\sigma}{d_i} \right] \left\{ \frac{1}{2} \rho_l \varphi \left[ \varepsilon (d_i^3 - d_j^3) \right]^{1/3} \right\}^{2/3} - 6 \frac{\sigma}{d_i} \quad \text{Eq. 2-118}$$

where  $\varphi$  is a constant obtained by integrating the difference between the velocity fluctuations .

Using the normalization condition of the probability density, the dimensionless daughter bubble size distribution is then calculated as:

$$\beta(d_j/d_i, 1) = \frac{\left[ \frac{1}{2} \rho_l \varphi (\varepsilon d_j)^{2/3} - 6 \frac{\sigma}{d_i} \right] \left\{ \frac{1}{2} \rho_l \varphi \left[ \varepsilon (d_i^3 - d_j^3) \right]^{1/3} \right\}^{2/3} - 6 \frac{\sigma}{d_i}}{\int_0^1 \left[ \frac{1}{2} \rho_l \varphi (\varepsilon d_j)^{2/3} - 6 \frac{\sigma}{d_i} \right] \left\{ \frac{1}{2} \rho_l \varphi \left[ \varepsilon (d_i^3 - d_j^3) \right]^{1/3} \right\}^{2/3} - 6 \frac{\sigma}{d_i} d \frac{d_j}{d_i}} \quad \text{Eq. 2-119}$$

From Figure 2.19, one can see that the daughter bubble size distribution predicted by Martínez-Bazán et al. [110] has the same behavior as the above statistical models, i.e. bell-shaped.

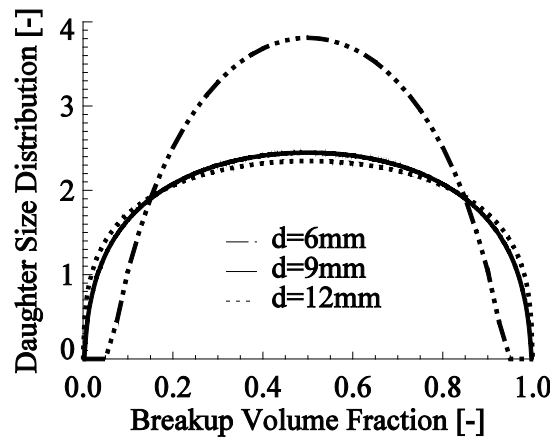


Figure 2.19 Martínez-Bazán et al. [110] model



One of the most popular phenomenological models for the size distribution of daughter bubbles is that in [51] and [93]. This is a bimodal function with high probability density at both ends and low in the middle.

They assumed that the daughter bubble size distribution function is linearly related to the energy requirements for the formation of the daughters. With the expression for the minimal energy required for the bubble breakage proposed by Tsouris and Tavlarides [51] and Venneker et al. [93], the probability density function of daughter bubbles can be written as:

$$\beta(f_{bv}, 1) = \frac{E_{\min} + E_{\max} - E(V_j)}{\int_0^1 [E_{\min} + E_{\max} - E(V_j)] df_{bv}} \quad \text{Eq. 2-120}$$

where  $E_{\min}$  is the energy needed to create the smallest and largest daughter bubbles;  $E_{\max}$  the energy needed to create two equal-sized daughter bubbles;  $E(V_j)$  the energy needed to create two daughters with size  $V_j$  and  $V_i - V_j$ . The results are graphically shown in Figure 2.20(a), and the line goes through zero at  $f_{bv}=0.5$ . However, it is highly unlikely that equal-sized breakage never occurs even though it requires the most energy. Similarly, to the statistical function, the model of Tsouris and Tavlarides [51] is independent of the parent size and flow conditions, which is considered unphysical.

The models discussed above provide only a total breakage rate of the parent bubble  $\Omega(d_i)$  and assume a function for daughter bubble size distribution independently. On the other hand, the following models give the partial breakage frequency  $\Omega(d_j, d_i)$  and the daughter bubble size distribution function is obtained by normalizing the partial breakup frequency by the overall breakage frequency.

$$\beta(V_j, V_i) = \frac{\Omega(d_j, d_i)}{\int_0^1 \Omega(d_j, d_i) dd_j} \quad \text{Eq. 2-121}$$

Therefore, one can get the daughter bubble size distribution directly from the model for breakup frequency  $\Omega(d_j, d_i)$  discussed in §2.4.2, which is also the most attractive point of such models.

The model of Luo and Svendsen [95] is expressed as:

$$\beta(f_{bv}, 1) = \frac{2 \int_{\xi_{\min}}^1 \frac{(1+\xi)^2}{\xi^{11/3}} \exp\left(-\frac{12c_{fbv}\sigma}{\varphi\rho_l \varepsilon^{2/3} d_i^{5/3} \xi^{11/3}}\right) d\xi}{\int_0^1 \int_{\xi_{\min}}^1 \frac{(1+\xi)^2}{\xi^{11/3}} \exp\left(-\frac{12c_{fbv}\sigma}{\varphi\rho_l \varepsilon^{2/3} d_i^{5/3} \xi^{11/3}}\right) d\xi df_{bv}} \quad \text{Eq. 2-122}$$

where  $\varphi$  is about 2.0.

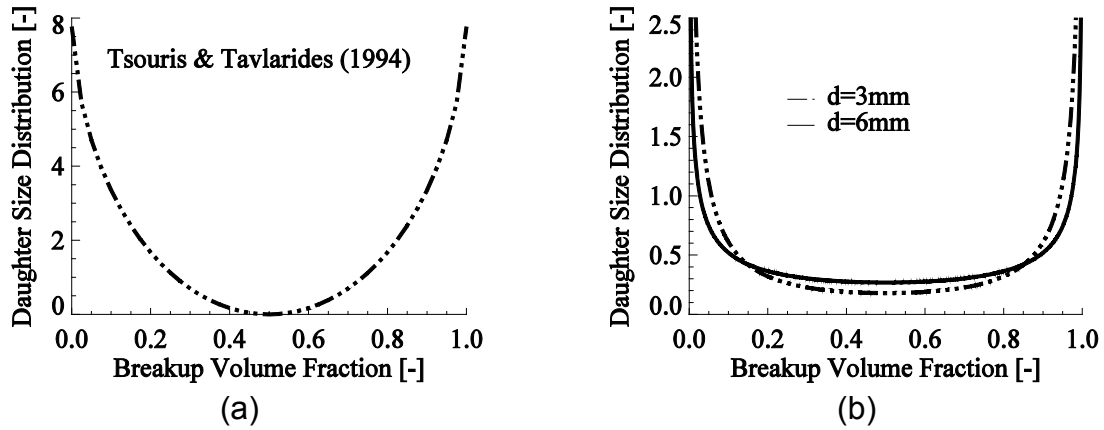


Figure 2.20 (a) Tsouris and Tavlarides [51] model; (b) Luo and Svendsen [95] model

Figure 2.20 shows the U-shape daughter bubble size distributions predicted by two different models. Both have a minimum at equal-sized breakage and maximum when the volume fraction approaches to zero or one, but the model of Luo and Svendsen [95] has a non-zero minimum and exhibits a dependence on the parent bubble size.

Similarly, to the model of Luo and Svendsen [95], Lehr et al. [31] proposed also a correlation for the partial breakup frequency (see Eq. 2-93). However, for efficient computation, they transformed the model back to an overall breakup frequency with a separate daughter bubble size distribution by expressing the integral as a sum of incomplete Gamma-functions. The daughter bubble size distribution has the following form:

$$\beta(f_{bv}, 1) = \frac{1}{\sqrt{\pi} f_{bv}} \cdot \frac{\exp \left\{ -\frac{9}{4} \left[ \ln \left( \frac{2^{2/5} d_j \rho_l^{3/5} \varepsilon^{2/5}}{\sigma^{3/5}} \right) \right]^2 \right\}}{\left\{ 1 + \operatorname{erf} \left[ \frac{3}{2} \ln \left( \frac{2^{1/5} d_j \rho_l^{3/5} \varepsilon^{2/5}}{\sigma^{3/5}} \right) \right] \right\}} \quad \text{Eq. 2-123}$$

The daughter bubble size distribution predicted by the above model is depicted in Figure 2.21. As the parent bubble size increases, the probability of small and large daughter bubbles increases rapidly, and the distribution changes from a monomodal to a bimodal. That means that the equal-sized breakage is more likely for small bubbles than for big bubbles, which is similar to the assumption of Nambiar et al. [138] that bubbles with size of  $d_{\max}$  break always equally, however, no experimental evidence and theoretical support exist.

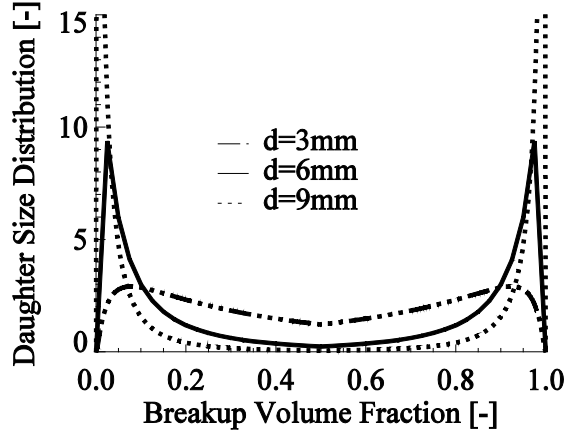


Figure 2.21 (a) Martínez-Bazán et al. [110] model; (b) Lehr et al. [31] model

Similarly, in the model of Wang et al. [96] the daughter bubble size distribution function is also calculated directly from the partial breakup frequency. It has the following form:

$$\beta(f_{bv}, 1) = \frac{\int_{d_{e,\min}}^{d_i} \frac{(d_e + d_i)^2}{d_e^{11/3}} \int_0^\infty \frac{1}{f_{bv,\max} - f_{bv,\min}} \frac{1}{\bar{E}_e} \exp(-E_e / \bar{E}_e) dE_e dd_e}{\int_0^1 \int_{d_{e,\min}}^{d_i} \frac{(d_e + d_i)^2}{d_e^{11/3}} \int_0^\infty \frac{1}{f_{bv,\max} - f_{bv,\min}} \frac{1}{\bar{E}_e} \exp(-E_e / \bar{E}_e) dE_e dd_e df_{bv}} \quad \text{Eq. 2-124}$$

However, the triple integrals in Eq. 2-124 make the application of this model in CFD simulations very time-consuming.

Last, the model of Zhao and Ge [97] is somewhat different from others listed here, since they assumed one of the daughter bubbles having the same size as the bombarding eddy. Therefore, the density probability of a daughter bubble with size  $V_j$  should be the sum of the breakage induced by an eddy with size  $d_e = (6V_j/\pi)^{1/3}$  and with size  $d_e = (6(V_i - V_j)/\pi)^{1/3}$ . Finally, the daughter bubble size distribution is given as:

$$\beta(f_{bv}, 1) = \frac{w(d_i, d_e) P_b(d_i, d_e)}{\int_{f_{bv,\min}}^1 w(d_i, d_e) P_b(d_i, d_e) df_{bv}} + \frac{w(d_i, d_i - d_e) P_b(d_i, d_i - d_e)}{\int_{f_{bv,\min}}^1 w(d_i, d_i - d_e) P_b(d_i, d_i - d_e) d(1 - f_{bv})} \quad \text{Eq. 2-125}$$

where  $w(d_i, d_e)$  and  $P_b(d_i, d_e)$  are the collision frequency and breakup probability, respectively, see section §2.4.2.

The effect of the parent bubble size on the daughter bubble size distribution predicted by the models of Wang et al. [96] and Zhao and Ge [97] is depicted in Figure 2.22(a) and Figure 2.22(b), respectively, which are typical M-shape distributions.

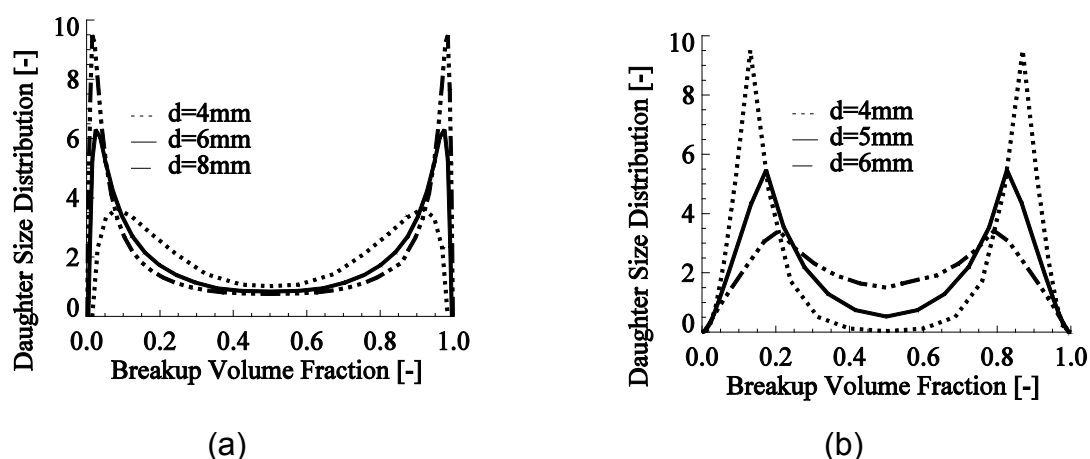


Figure 2.22 (a) Wang et al. [96] model; (b) Zhao and Ge [97] model

According to Wang et al. [96], the daughter bubble size distribution should satisfy four requirements:

- (i) a local minimum but no zero at equal-sized breakup, i.e. at  $fbv=0.5$
- (ii) the distribution function depends on both the parent bubble size and the dynamics in the continuous phase, e.g. the energy dissipation rate
- (iii) the probability density of the daughter particles approaches zero when the breakup volume fraction  $fbv$  approaches zero
- (iv) the function form should not depend on experimental conditions or include singularity

Starting from this point, the phenomenological models are generally more reasonable than the statistical ones, among which the M-shape models in Figure 2.22 seem to be the most reasonable ones.

## 2.5 Conclusions and discussions

By using the extended Eulerian multi-fluid model, time and space dependent bubble size distributions or interfacial area density can be predicted for poly-dispersed flow. Nevertheless, for this purpose, constitutive models are needed for bubble forces, bubble dynamics (such as bubble coalescence and breakup) as well as turbulence. In this chapter, available methods for the extension of the standard multi-fluid model, modelling of bubble coalescence and breakup as well as bubble-induced turbulence are discussed. Since the main objective of this work is to develop a new model for bubble coalescence and breakup, a short discussion about the existing models is given as following.

### 2.5.1 Mechanisms and models for bubble coalescence

For turbulent bubbly flows, it is shown that at least five mechanisms are relevant to cause the relative motion between bubbles and consequently their collision. These mechanisms include turbulent fluctuations, laminar shear stress, capture in turbulent eddies, different rise velocities resulting from body forces, and wake entrainment. On the other hand, most available models assume arbitrarily a dominant mechanism, e.g. turbulent fluctuation, and neglect others without further verification and validation.

The coalescence frequency is calculated by defining collision frequency and coalescence efficiency. For turbulent fluctuation-induced collisions, the general structure of all models is similar to Eq. 2-24. The main difference is in the pre-factors, the value of which is still open. For non-diluted flows, which are normally in the focus of coalescence modeling, the reduction of the free space for bubble movement by bubbles themselves has to be considered by the factor  $\gamma$ . Collisions due to laminar velocity shear and size-dependent bubble rise velocities are obtained by straightforward considerations. They result in Eq. 2-25 and Eq. 2-27, respectively. For the collision of bubbles captured inside a turbulent eddy (see Eq. 2-26), the frequency is calculated by making an analogy to the case of laminar shear-induced collisions. Most open questions arise from the modeling of collision due to wake entrainment, which is especially important for large cap bubbles. Wake entrainment should be the most important mechanism leading to bimodal bubble size distributions, as observed in vertical pipe flows at high void fractions.

In contrast to collision frequency, the formulations of coalescence efficiency are quite different from each other. The widely used film drainage model is based on the statistical theory by assuming the drainage and interaction time to be random variables. The model states that coalescence can occur only when the liquid film ruptures before the bubbles separate again, i.e.  $t_{\text{contact}} > t_{\text{drainage}}$ . However, it has been put into question by recent experimental observations. Doubliez [28] investigated the collision of a single rising bubble with the free liquid surface. He found that film rupture actually occurred when the bubble was already leaving the liquid surface, which was caused by the tension during the departure of the bubble. The experiment of Stewart [67] shows that most of coalescence processes occurred in a short time (1/30 s) and the interface penetration appeared to be instantaneous. On the other hand, the expressions for the drainage and contact time are quite different from one another and depend seriously on simplifying assumptions, e.g. the parallel-film model. However, up to now there are no models available which are qualitatively better than the film drainage model.

In conclusion, the limitation of existing coalescence closure models is clear and further studies on more fundamental and consistent coalescence models are indispensable. These studies must consider all relevant collision mechanisms and they must be applicable to a wide range of flow conditions in the practice.

For the improvement of bubble coalescence modeling, the following topics have to be considered:

- The modeling should be based on physical observations, which shows a dependence on bubble size, liquid property and turbulent parameter.
- All mechanisms have to be included, despite a mechanism being clearly identified as negligible for the case considered.
- The necessity of pre-factors for collision frequency, e.g.  $\gamma$  and  $\Pi$  should be checked. The factor  $\gamma$  considers the reduction of free space for bubble movement due to the existence of bubbles (up to now only discussed for turbulent collisions, it should apply to all kinds of collisions), while the factor  $\Pi$  is only necessary for turbulent collisions, since it is related to the ratio of mean distance between bubbles to the relative turbulent path length.

- According to the film drainage model, the coalescence efficiency should be calculated differently for each mechanism, since the contact time and drainage time of bubble collision related tightly to the mechanism. Up to now for buoyancy or wake interactions, the expression of turbulent collisions is adopted or a constant is assumed.
- The coalescence closures have to be embedded in a model which provides turbulence parameters for the liquid phase correctly, e.g. including the effect of bubbles.
- The model should not rely on open parameters. If an adjustable coefficient is included, a general expression applicable to wide range of flow situations should be proposed.

### **2.5.2 Mechanisms and models for bubble breakup**

Similarly, for bubble breakup, there are various mechanisms that have to be considered. For example, in the case of turbulent gas-liquid flows, turbulence fluctuation, viscous shear stress, interfacial stresses as well as surface instability can cause the deformation and breakup of bubbles. On the other hand, most existing models consider only turbulence-induced bubble breakup, which limits the transferability of these models. Furthermore, various breakage criteria are used in the existing models.

The turbulence parameters such as the turbulent energy dissipation rate  $\varepsilon$ , are essential input parameters for breakup models, which are difficult to estimate with sufficient accuracy by applying a standard turbulent model. Improvements of turbulence models for two-phase flows, especially the bubble-induced turbulence, are of crucial importance for the development of breakage closures.

In a word, for the development of new breakup models, the following aspects need to be contemplated.

- The model should be based on physical observations, and all potential mechanisms should be involved.
- It should be efficient to implement the new model into CFD codes, i.e. no complicated integrals should be included as Eq. 2-96 in the model of Wang et al. [96].
- The model should provide the partial breakage frequency such as by Luo and Svendsen [95] and Wang et al. [96]. That means that additional errors introduced by the arbitrary assumption of a separate daughter size distribution can be avoided.
- The daughter size distribution derived from the partial breakup frequency should have the feature of an M-shape function. That means that the probability of equal-sized breakage is a minimum and the probability is zero as one daughter bubble size approaches zero by binary breakage.

### 3 A generalized model for coalescence and breakup

As discussed in the last chapter, in order to use the extended multi-fluid model for the modeling of poly-dispersed flow further effort needs to be invested in the development of closure models for bubble coalescence and breakup. Although an amount of work has been done in this field, it remains still a weak link in the CFD simulation of gas-liquid flows. Practice shows that it is difficult to transfer the application of the existing models from one case to another. In this chapter, a generally-applied or transferable model based on available knowledge is proposed for the calculation of bubble coalescence and breakup frequency, respectively.

#### 3.1 Coalescence frequency

One major limitation of the existing coalescence models is that they considered usually only one mechanism. In this work, the widespread expression in Eq. 2-12, i.e. coalescence frequency equal to the product of collision frequency and coalescence efficiency, is extended to include all important mechanisms in a turbulent gas-liquid flow.

According to Chesters [25], the modeling concept of bubble coalescence can be split into two parts, i.e. the external flow and the internal flow. The flow dynamics in the external flow, namely, the surrounding liquid phase, leads to the collision of bubbles. Furthermore, it determines important input parameters for the internal flow such as the relative velocity, interaction force and time. The term of internal flow here refers to the thinning process including the flattening and draining of the liquid film captured between two colliding interfaces.

There are various sources in the external flow leading to bubble collisions, which are called collision or coalescence mechanisms following in this work. For example, in the case of a turbulent gas-liquid bubbly flow, turbulence fluctuation, laminar velocity shear, buoyancy, wake entrainment as well as eddy capture might be important mechanisms. These mechanisms are depicted at the right bottom of Figure 3.1 and numbered by (a), (b), (c), (d) and (e), respectively.

##### 3.1.1 Collision frequency

The collision frequency is usually determined by assuming that the collision between bubbles in a locally isotropic turbulent flow field is analogous to that between ideal gas molecules. As shown in Eq. 2-13, the collision frequency of two approaching bubbles is determined by the effective cross-sectional area as they cross each other and the relative velocity between them.

The effective cross-sectional area  $S_{ij}$  for the collision of two bubbles having size  $d_i$  and  $d_j$  can be modeled by using a circle of diameter  $(d_i+d_j)$  to represent a moving bubble's effective collision area while treating the "target" bubbles as point masses (see Figure 3.2). As a result,  $S_{ij}$  can be calculated according to Eq. 2-14 with the exception of wake-entrainment, since it is only effective for bubbles in the wake region behind the leading bubble  $i$ . For the computation of  $S_{ij,wake}$  Eq. 2-14 has to be rewritten as

$$S_{ij,wake} = \frac{\pi}{4} d_i^2 \tag{Eq. 3-1}$$

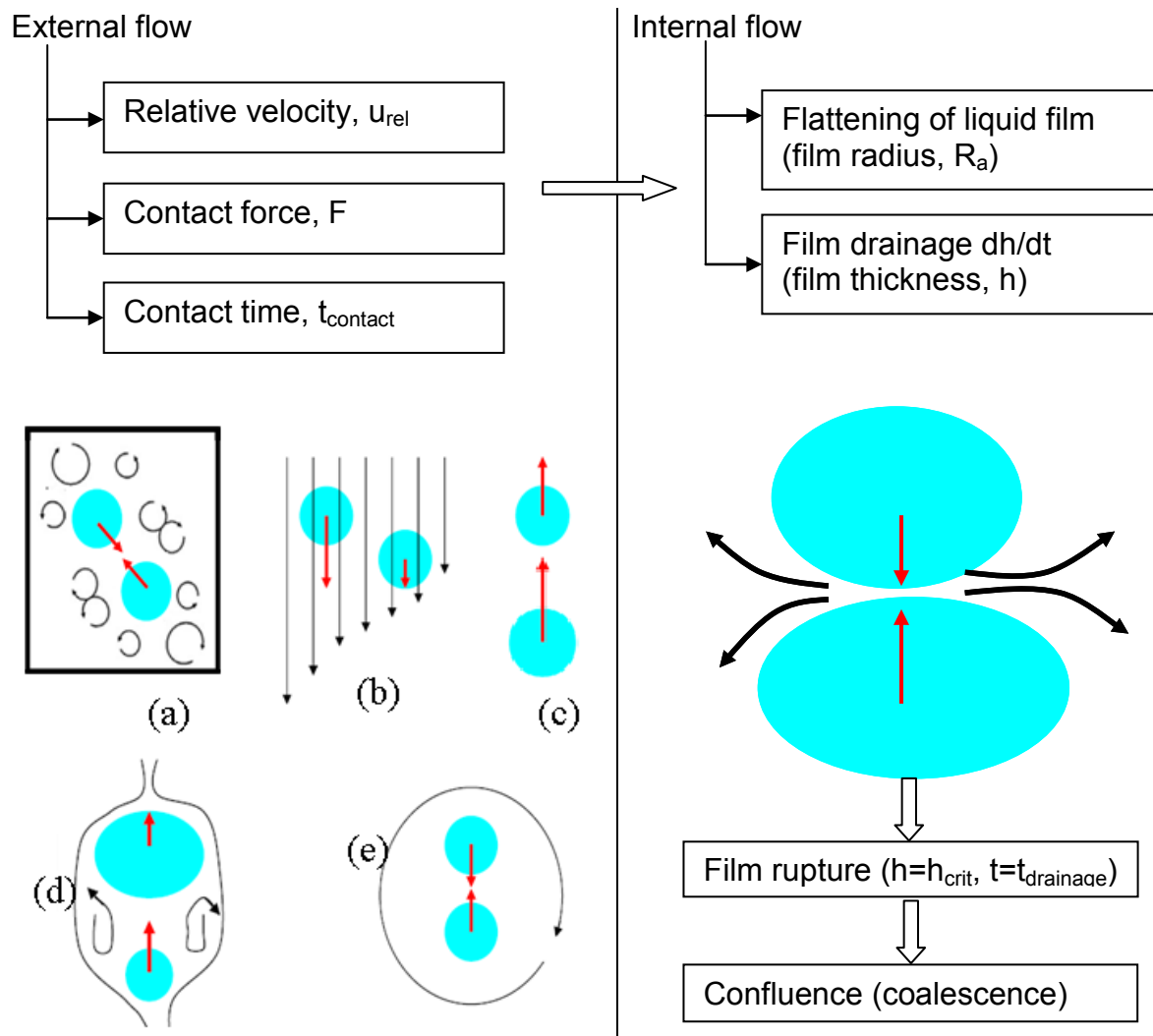


Figure 3.1 Conceptual framework of coalescence process modeling

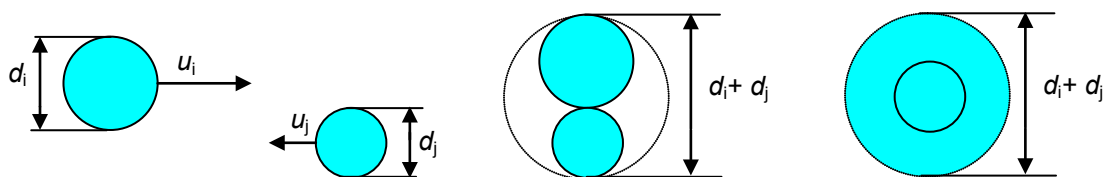


Figure 3.2 Effective cross section for the collision of two bubbles of size  $d_i$  and  $d_j$

Finally, the collision frequency of the two bubbles can be interpreted as the volume swept by the moving bubble per unit time as shown in Figure 3.3.

$$h(d_i, d_j) = S_{ij} \cdot u_{rel} \tag{Eq. 3-2}$$



Note that if Eq. 3-2 multiplied by the number density of “target” bubbles in the collision cylinder,  $h(d_i, d_j)$  is the total collision frequency of a bubble in size group  $i$  and has a correspondent unit of  $s^{-1}$ .

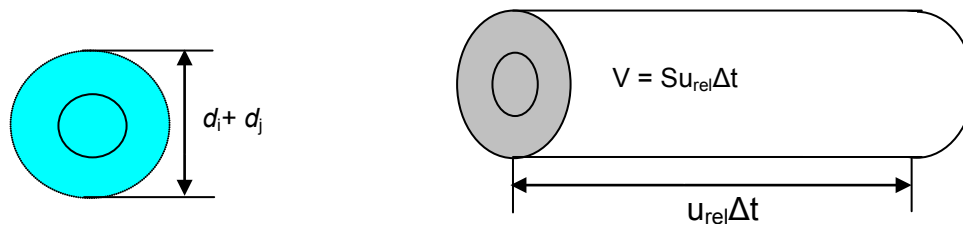


Figure 3.3 Effective volume swept by the two colliding bubbles in a time  $\Delta t$

According to Eq. 3-2, the collision frequency of two approaching bubbles is determined by the bubble sizes and the relative velocity. As discussed above, the relative velocity or relative motion between bubbles in a turbulent poly-dispersed flow can be caused by various mechanisms. Correlations used for the calculation of the relative velocity resulting from different mechanisms are different, which have been discussed in the last chapter. For ease of understanding, those correlations included in the new model are put together here.

**(a) Turbulence fluctuation**

In order to determine the mean approach velocity of bubbles in a turbulence-induced collision, it is assumed that bubble sizes are within the turbulence inertial subrange, i.e.  $\eta < d < l_e$ , and bubbles follow the velocity fluctuation of the liquid. Thus, the average velocity of one bubble with size  $d$  takes the mean turbulent velocity fluctuation between two points distance  $d$  apart, which is calculated by Eq. 2-16. By considering the stochastic inherence of turbulence, bubble velocities are assumed to be statistically non-correlated in space. The relative velocity between bubble  $i$  and  $j$  is determined by the mean square root of the turbulent fluctuations around their surfaces [139]:

$$u_{rel,turb} = (u_{ti}^2 + u_{tj}^2)^{1/2} = 2^{1/2} \varepsilon^{1/3} (d_i^{2/3} + d_j^{2/3})^{1/2} \quad (d_i + d_j > \eta) \quad \text{Eq. 3-3}$$

where  $\eta$  is the Kolmogorov microscale.

**(b) Laminar velocity shear**

The laminar velocity gradient in the bulk flow also gives rise to a relative velocity between the suspended bubbles when they are located at different positions. The shear-induced relative velocity between two adjacent bubbles can be expressed as

$$u_{rel,shear} = 0.5(d_i + d_j) \dot{\gamma} \quad \text{Eq. 3-4}$$

where  $\dot{\gamma}$  is the shear rate in the continuous phase.

**(c) Buoyancy or size-dependent body forces**

Bubble collisions may also result from the difference in size-dependent rise velocities of bubbles caused by buoyancy or other body forces

$$u_{rel,buoy} = |u_{ri} - u_{rj}| \quad \text{Eq. 3-5}$$

where  $u_{ri}$  is the terminal bubble rise velocity of bubble  $i$ . For the calculation of  $u_r$ , a balance between drag and buoyancy forces is assumed.

In addition, it is worth noting that for the case of vertical pipe flow, the shear-induced and buoyancy-induced relative velocity may compensate each other and cannot be regarded as single mechanism.

#### **(d) Wake-entrainment**

A bubble with a size larger than a critical value  $d_{crit}$  could produce strong agitation in the liquid and leave a wake region behind it, where the liquid velocity is higher than that in the bulk flow. The bubbles will be accelerated when they enter such a wake region with the result of collision and coalescence with the leading bubble. Schlichting [69] gave an analytical expression for the dimensionless relative velocity between the trailing and leading bubbles as

$$\frac{u_{rel,wake}(y)}{u_{ri}} = \left( \frac{C_D A}{\beta^2 y^2} \right)^{1/3} \quad \text{Eq. 3-6}$$

where parameter  $A$ ,  $\beta$  and  $y$  is the frontal area of the leading bubble  $i$ , the ratio between the length and the width of the wake, and the distance measured from the center of the leading bubble, respectively.

According to Hibiki and Ishii [62], the average relative velocity between the leading bubble and the bubbles in the wake region, which can be obtained by integrating Eq. 3-6 over the effective wake length, depends on the ratio of the wake length to the leading bubble diameter  $L_w/d_i$ . By treating this ratio as a constant depending on the fluid properties, the average relative velocity can be given by Eq. 3-7.

$$u_{rel,wake} = C_{35} u_{ri} C_D^{1/3} \quad (d_i > d_{crit}) \quad \text{Eq. 3-7}$$

where the constant  $C_{35}$  increases with a decrease in the ratio of  $L_w/d_i$ .

It is noted that the simple treatment of  $L_w/d_i$  as a constant is in principle only reasonable for fully-developed flow and therefore, might introduce error for the flow at the gas entrance, where the average wake length is obviously smaller than the flow far away downstreams and the wake-entrainment is dominant. However, since up to now there is no accurate information about this complicated phenomenon available, this simplification is still adopted in this work

The critical bubble diameter  $d_{crit}$  in Eq. 3-7 is calculated by employing the correlation of Ishii and Zuber [140]:

$$d_{crit} = 4 \sqrt{\frac{\sigma}{g \Delta \rho}} \quad \text{Eq. 3-8}$$

For 25 °C air-water flow system under atmospheric pressure it is about 10 mm.

**(e) Eddy-capture**

For turbulence-induced collision, when the size and relaxation time of bubbles are smaller than the Kolmogorov micro scale  $\eta$ , Eq. 2-26 does not apply to this case any more. Thus, the relative velocity cannot be calculated according to Eq. 3-3. Chesters [25] proposed that the collision of bubbles in such a case is mainly promoted by the viscous shear of turbulence eddies. By making an analogy to the case of laminar velocity shear in Eq. 3-4, the relative velocity between two bubbles inside an eddy, the so-called eddy capture, is given as

$$u_{rel,eddy} = 0.5(d_i + d_j) \sqrt{\frac{\varepsilon}{\nu}} \quad (d_i + d_j \leq \eta) \quad \text{Eq. 3-9}$$

where  $\sqrt{\varepsilon/\nu}$  is the rate of strain characteristic of flow in the smallest eddies.

**3.1.2 Coalescence efficiency**

The coalescence efficiency, which describes the probability of a bubble-bubble collision event resulting in coalescence, is calculated by the most mature model, i.e. the film drainage model (see Chapter 2 for details). According to the film drainage model, the coalescence process essentially consists of three successive steps which are shown in Figure 3.4. As a result, the coalescence efficiency can be calculated from two time scales, i.e. film drainage time  $t_{drainage}$  and contact time  $t_{contact}$ , see Eq. 2-41.

In the literature, it is usual to assign an identical efficiency for collisions caused by various mechanisms. This assumption might be unreasonable since the input parameters such as the relative velocity and the contact time are determined by collision mechanisms, see Figure 3.1. Therefore, in the calculation of coalescence efficiency, the influence of collision mechanisms on the film drainage time and contact time should be considered.

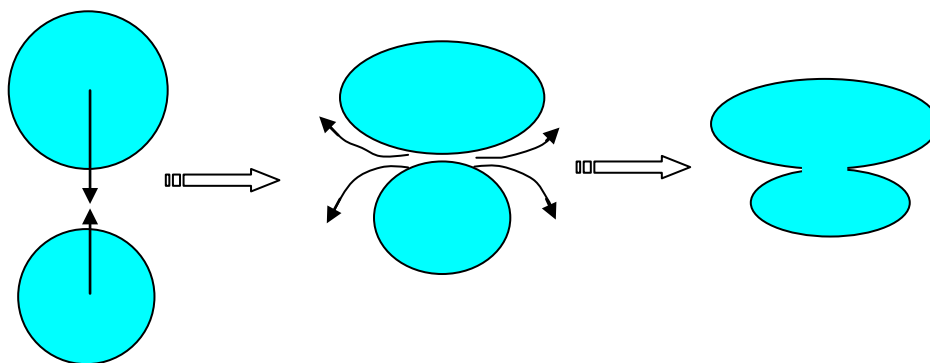


Figure 3.4 Sub-processes of bubble coalescence process

Depending on whether the particle Reynolds number  $Re_d = \rho_l d u_{rel} / \mu_l$  is much smaller or much greater than unity, the respective force governing the collision of bubbles and the film thinning process will be predominately viscous or inertial. In turbulent gas-liquid flows, the viscous and inertial regimes correspond respectively to bubbles much smaller and much larger than the length scale of the Kolmogorov scale  $\eta$  [25].

The coalescence of bubbles much smaller than  $\eta$  is dominated by the viscous force, while for the case of large bubbles the inertial force is predominant.

As discussed above, film drainage time depends heavily on the rigidity and mobility of bubble surface. For fully-mobile deformable interface, e.g. bubbles in pure liquid, the correlation for film drainage time is different for viscous and inertial collisions. For viscous collision, the correlation proposed by Chesters [25] is used for the calculation of the film drainage time, which is given by Eq. 2-51. For collisions controlled by inertial forces, the film drainage time is calculated according to the correlation of Oolman and Blanch [85] in Eq. 2-56. It is noted that both correlations above for film drainage time are proposed for the case of fully-mobile interface and might not be applicable for the case of immobile or partially-mobile such as drops in viscous fluids or bubbles in fluids containing surfacants.

The contact time is determined by the size and the relative velocity of two colliding bubbles, which is given by

$$t_{contact} = \frac{d_i + d_j}{u_{rel}} \quad \text{Eq. 3-10}$$

where the relative velocity  $u_{rel}$  is calculated according to Eq. 3-3 ~ Eq. 3-9.

For viscous collision due to eddy-capture, by making use of Eq. 3-9, Eq. 3-10 becomes

$$t_{contact} = \frac{d_i + d_j}{0.5(d_i + d_j)\sqrt{\frac{\varepsilon}{\nu}}} = \frac{2}{\sqrt{\frac{\varepsilon}{\nu}}} \quad \text{Eq. 3-11}$$

On the other hand, in turbulent gas-liquid flows, inertial collisions can be caused by turbulence, laminar shear as well as buoyancy. The relative motion of bubbles in this case is a combined effect of various collision mechanisms. It is usually difficult to describe the coupling effect between different mechanisms. In the literature, the contribution of each mechanism is usually assumed to be cumulative, which could deliver an overestimation of the coalescence rate. If the mechanisms are comparable, two bubbles after a collision promoted by one mechanism can be separated again by any another mechanism before coalescence could occur. However, if one mechanism is obviously stronger than the others are, it could be the predominately effective disturbance for the contact of two bubbles. In this work, it is assumed that the collision caused by different mechanisms is cumulative while the separation of the bubbles after collision is determined by the strongest mechanism, i.e. the largest relative velocity. Therefore, the contact time in Eq. 3-10 is rewritten as

$$t_{contact} = \frac{d_i + d_j}{\max(u_{rel,k})} \quad \text{Eq. 3-12}$$

wherein the subscript k represents the collision mechanisms of turbulence, laminar shear and buoyancy, and  $u_{rel,k}$  calculated according to Eq. 3-3 ~ Eq. 3-5, respectively.

In addition, the modification factors  $\gamma$  and  $\Pi$  discussed in §2.3 is included in the collision frequency and the correlations proposed by Wang and his coworkers [37] [38] are adopted (see Table 2.1 and Eq. 2-22). The reader is referred to Chapter 2 for details.

### 3.1.3 Final expression for the coalescence frequency

By taking account of the contribution of all mechanisms, the total coalescence frequency is given by

$$\Gamma(d_i, d_j) = \gamma \cdot \left( \begin{array}{l} \Pi \cdot S_{ij,turb} \cdot u_{rel,turb} \cdot \lambda_{turb} + S_{ij,shear} \cdot u_{rel,shear} \cdot \lambda_{shear} \\ + S_{ij,buoy} \cdot u_{rel,buoy} \cdot \lambda_{buoy} + S_{ij,wake} \cdot u_{rel,wake} \cdot \lambda_{wake} \\ + S_{ij,eddy} \cdot u_{rel,eddy} \cdot \lambda_{eddy} \end{array} \right) \quad \text{Eq. 3-13}$$

where the cross-sectional area is calculated by,

$$\begin{aligned} S_{ij,turb} = S_{ij,buoy} = S_{ij,shear} = S_{ij,eddy} &= \frac{\pi}{4} (d_i + d_j)^2 \\ S_{ij,wake} &= \frac{\pi}{4} d_i^2 \end{aligned} \quad \text{Eq. 3-14}$$

The relative velocity between bubbles caused by different mechanisms is given by

$$\begin{aligned} u_{rel,turb} &= 2^{1/2} \varepsilon^{1/3} (d_i^{2/3} + d_j^{2/3})^{1/2}, \quad (d_i + d_j > \eta) \\ u_{rel,shear} &= 0.5 (d_i + d_j) \dot{\gamma} \\ u_{rel,buoy} &= |u_{ri} - u_{rj}| \\ u_{rel,wake} &= C_{35} u_{ri} C_D^{1/3}, \quad (d_i \geq d_{crit}) \\ u_{rel,eddy} &= 0.5 (d_i + d_j) \sqrt{\frac{\varepsilon}{\nu}}, \quad (d_i + d_j \leq \eta) \end{aligned} \quad \text{Eq. 3-15}$$

And the coalescence efficiency is given by

$$\begin{aligned} \lambda_{turb} = \lambda_{shear} = \lambda_{buoy} &= \exp \left[ -\frac{\rho_l^{1/2} r_{eq}^{3/2}}{4\sigma^{1/2} (d_i + d_j)} \ln \left( \frac{h_0}{h_{crit}} \right) \cdot \max(u_{rel,turb}, u_{rel,shear}, u_{rel,buoy}) \right] \\ \lambda_{eddy} &= \exp \left[ -\frac{3\mu_l r_{eq}}{4\sigma} \sqrt{\frac{\varepsilon}{\nu}} \ln \left( \frac{h_0}{h_{crit}} \right) \right] \\ \lambda_{wake} &= 1.0 \end{aligned} \quad \text{Eq. 3-16}$$

In Eq. 3-15, the critical bubble size for wake-entrainment to occur is calculated according to

$$d_{crit} = 4 \sqrt{\frac{\sigma}{g\Delta\rho}}$$

And the Kolmogorov length scale is defined as

$$\eta = \left( \frac{v^3}{\varepsilon} \right)^{1/4}$$

The modification factors  $\gamma$  and  $\Pi$  are determined according to the correlations proposed by Wang et al. [37],

$$\gamma = \frac{\alpha_{max}}{\alpha_{max} - \alpha_g}$$

A value of 0.8 is used for the maximum possible gas holdup  $\alpha_{max}$ .

$$\Pi = \exp \left[ - \left( \frac{h_{b,jj}}{h_{t,jj}} \right)^6 \right] \quad \text{Eq. 3-17}$$

with  $h_{bt,jj} = 0.89(d_i^2 + d_j^2)^{1/2}$  and  $h_{b,jj} = 6.3(n_i + n_j)^{-1/3}$ .

Furthermore, in Eq. 3-13 ~ Eq. 3-16, the subscript *turb* refers to the mechanism of turbulence fluctuation, shear to laminar shear, *buoy* to buoyancy, *eddy* to eddy-capture and *wake* to wake entrainment. The coefficient  $C_{35}$  is dependent on the ratio of wake length scale to the leading bubble size and a constant value of 0.1 used in this work can give a satisfying agreement with the measurement. The initial and critical film thickness  $h_0$ ,  $h_{crit}$  are assumed to be constant. The initial film thickness in air-water systems was estimated by Kirkpatrick and Locket [141] to be  $10^{-4}$  m while the critical film thickness is typically taken as  $10^{-8}$  m [142]. According to the Chesters [25], the initial and critical film thicknesses are different for viscous and inertial collisions.

The coalescence efficiency for collisions caused by wake-entrainment is assumed to be 1, since available information is inconsistent with each other. For example, Hibiki et al. [61] found that the coalescence rate of a spherical bubble entrained by a cap bubble is higher than the entrainment between two cap bubbles. However, the work of Stewart [68] showed that collision and coalescence caused by wake-entrainment can only occur if two bubbles have equivalent sizes. On the other hand, the assumption of 1 means that all entrained bubbles will coalesce with the leading bubbles. This is also reasonable from intuitive insight since it is difficult for a trapped bubble to escape from the wake region.

Finally, it is worth noting that for the case of vertical pipe flow, the effect of the shear-induced collision and the buoyancy-induced collision is combined with each other according to the relative position of the two bubbles.

$$\begin{aligned}
 u_{rel, shear+buoy} &= \pm(u_{ri} - u_{rj}) \pm C_{36} (d_i + d_j) \left| \frac{du_r}{dr} \right| \\
 &\approx 0.25 \cdot \max \left[ u_{ri} - u_{rj} - C_{36} (d_i + d_j) \left| \frac{du_r}{dr} \right|, 0.0 \right] \\
 &\quad + 0.25 \cdot \max \left[ u_{ri} - u_{rj} + C_{36} (d_i + d_j) \left| \frac{du_r}{dr} \right|, 0.0 \right] \\
 &\quad + 0.25 \cdot \max \left[ u_{rj} - u_{ri} - C_{36} (d_i + d_j) \left| \frac{du_r}{dr} \right|, 0.0 \right] \\
 &\quad + 0.25 \cdot \max \left[ u_{rj} - u_{ri} + C_{36} (d_i + d_j) \left| \frac{du_r}{dr} \right|, 0.0 \right]
 \end{aligned} \tag{Eq. 3-18}$$

where  $du_r/dr$  is the shear rate in the radial direction and the constant  $C_{36}$  is dependent on the horizontal mean distance of bubbles.

### 3.2 Breakup frequency

The work of Martínez-Bazán et al. [59] is used as a starting point of the generalized model. The model is based on a pure kinematic idea, and no information about the eddy is needed and no integrals are included. However, in this model only the turbulence mechanism is considered and a separate daughter bubble size distribution function is needed. The daughter bubble size distribution function proposed by Martínez-Bazán et al. [110] is a bell-shape function. As discussed in the last chapter, instead of bell-shape function, the M-shape function is the most reasonable function for the description of breakup progresses in gas-liquid flows. Furthermore, instead of both energy and capillary constraints, in the original work only the energy constraint is used to judge whether the breakup of a bubble can occur or not.

According to the model of Martínez-Bazán et al. [59], by making analogy to the mechanical process, the velocity  $u_b$  at which the breakup process of a bubble takes place can be assumed to increase with the difference between the deformation stress  $\tau$  and the confinement stress  $\tau_{crit}$  exerted on the bubble.

$$u_b = \left( \frac{\tau - \tau_{crit}}{\rho_l} \right)^{0.5} \quad (\tau > \tau_{crit}) \tag{Eq. 3-19}$$

The duration of the breakup process, i.e. the breakup time  $t_b$ , is assumed to be the size of the parent bubble divided by the breakup velocity  $u_b$ .

$$t_b = \frac{d_i}{u_b} \tag{Eq. 3-20}$$

The deformation and confinement stress in Eq. 3-19 is assumed to be the turbulent stress and surface stress of the parent bubble, see Eq. 2-72 and Eq. 2-73. Finally the total breakup frequency of the parent bubble is given by Eq. 2-74.

### 3.2.1 Extensions

#### Breakup constraints

For the determination of the confinement stress or the minimum stress  $\tau_{crit}$  needed for breakage of a bubble to occur, the energy constraint  $\tau_{crit1}$  and capillary constraint  $\tau_{crit2}$  are used in this work, i.e.

$$\tau_{crit} = \max(\tau_{crit1}, \tau_{crit2}) \quad \text{Eq. 3-21}$$

where the energy constraint means that the energy density provided by the velocity fluctuation around the bubble surface should exceed the increase in the surface energy density during the breakage. The increase of surface energy density is determined by the number and the sizes of the daughter bubbles formed in the breakage process, for a binary breakage, a bubble with size  $d_i$  breaking up into two daughter bubbles, which is calculated according to Eq. 2-87.

Therefore, the energy density  $\tau_{crit1}$  caused by turbulent fluctuations around the bubble surface can be obtained from Eq. 2-87,

$$\tau_{crit1} = c_{fbv} \frac{\pi \sigma d_i^2}{\frac{1}{6} \pi d_i^3} = \underbrace{6c_{fbv}}_{\text{Prefactor1}} \frac{\sigma}{d_i} \quad \text{Eq. 3-22}$$

where  $c_{fbv} = f_{bv}^{2/3} + (1-f_{bv})^{2/3} - 1$ ,  $f_{bv}$  is the breakage volume fraction defined in Eq. 2-88.

Nevertheless, as pointed out by Wang et al. [96] the energy constraint, i.e.  $\tau > \tau_{crit1}$ , is still not enough for justifying the occurrence of breakage event, because according to it all bubbles under the disruptive stress will break up since there will always be a daughter size distribution that satisfies  $\tau > \tau_{crit2}$ . This is because the increase of surface energy goes to zero when the size of the smaller daughter bubble  $d_j$  approaches zero in a binary case. On the other hand, when the radius of the daughter bubble approaches zero its capillary pressure becomes very high, which means that the disruptive stress  $\tau$  resulting from the velocity fluctuation in the liquid may not provide sufficient dynamic pressure to overcome the capillary pressure and cause such a breakage [96]. Therefore, the capillary constraint ( $\tau > \tau_{crit2}$ ) is added as a supplement to the energy constraint, which is the surface tension stress of the smaller daughter bubble.

$$\tau_{crit2} = \frac{\sigma \pi d_j}{\pi d_j^2} = \frac{\sigma}{d_j} = \frac{1}{\underbrace{\min[f_{bv}^{1/3}, (1-f_{bv})^{1/3}]}_{\text{Prefactor2}}} \frac{\sigma}{d_i} \quad \text{Eq. 3-23}$$

It is worth noting that the capillary constraint given by Eq. 3-23 has a similar structure as the energy constraint in Eq. 3-22. The main difference lies in the prefactors, i.e.



prefactor1 and prefactor2. The dependence of the two prefactors on the breakage volume fraction,  $f_{bv}$ , is shown in Figure 3.5. It can be seen that for a given parent bubble size  $d_i$  the capillary constraint is much stricter than the energy constraint except for the breakage with a volume fraction  $f_{bv}$  around 0.5, i.e. equal-sized breakage. The capillary surface stress increases steeply as the breakage volume fraction approaches zero or one and suppresses the production of small daughter bubbles.

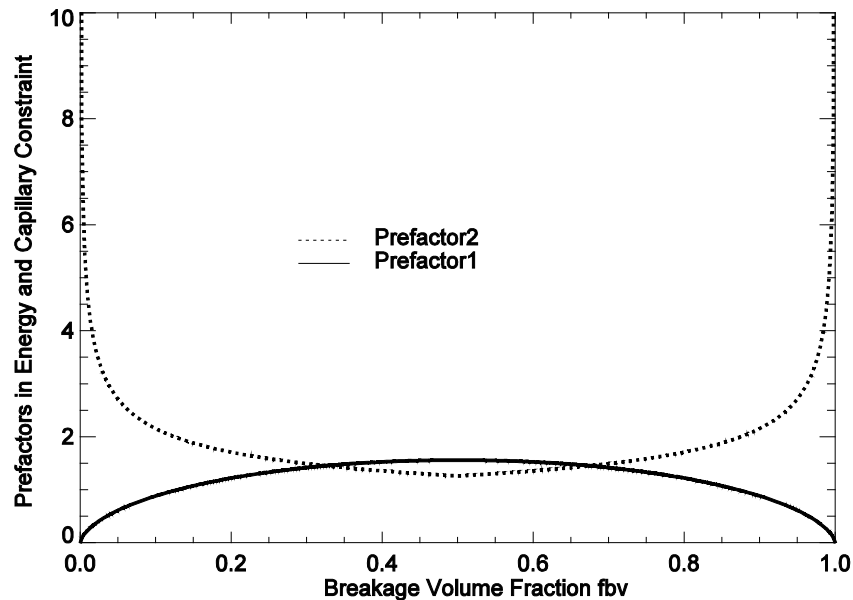


Figure 3.5 Prefactors in Eq. 3-22 and Eq. 3-23

**Various mechanisms**

In general, the breakup of a bubble is the result of a velocity difference between the two points of its surface. The velocity difference can result from three main kinds of sources or mechanisms in a turbulent gas-liquid flow, that is, turbulence fluctuation, velocity shear and interfacial slip, see Figure 3.6(a), (b) and (c), respectively.

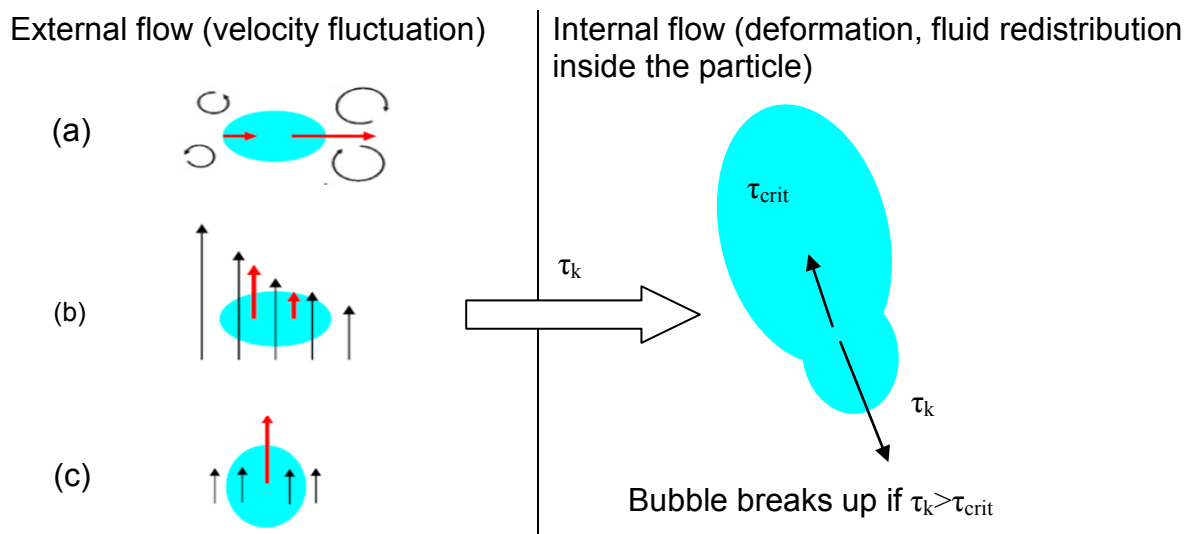


Figure 3.6 Conceptual framework of breakup process modeling

In Figure 3.6, the disruptive stress  $\tau_k$  provided by the velocity fluctuation in the external flow is dependent on the mechanism that causes the fluctuation. The subscript k represents different breakup mechanisms, *inter*: interfacial slip; *turb*: turbulence fluctuation; *shear*: laminar velocity shear; *eddy*: eddy velocity shear.

The deformation force generated by the velocity disturbances can also be distinguished as viscous or inertial. The inertial force is caused by turbulence fluctuation and interfacial slip while the laminar velocity shear and eddy shear of strain give rise to viscous stresses.

The inertial deformation acting on a bubble of size  $d_i$  caused by turbulence fluctuation and interfacial slip can be calculated according to Eq. 3-26 and Eq. 3-25, respectively.

$$\tau_{turb} = \frac{1}{2} \rho_l u_{ti}^2 \quad \text{Eq. 3-24}$$

$$\tau_{inter} = \frac{1}{2} \rho_l u_{ri}^2 \quad \text{Eq. 3-25}$$

where  $u_{ti}$ ,  $u_{ri}$  is the average turbulent fluctuation around the bubble given by Eq. 2-16 and its terminal rise velocity, respectively.

The viscous shear stress due to velocity shear rate in the bulk flow and turbulent eddies is calculated respectively as:

$$\tau_{shear} = \mu_l \dot{\gamma} \quad (\text{mean shear stress}) \quad \text{Eq. 3-26}$$

$$\tau_{eddy} = \mu_l \sqrt{\frac{\varepsilon}{\nu}} \quad (\text{eddy shear stress}) \quad \text{Eq. 3-27}$$

where  $\dot{\gamma}$  is the shear strain rate in the bulk flow.

### **Length scale of the breakup process**

Instead of the parent bubble size, the neck size of the parent bubble before it begins to break up is assumed to be equal to the size of the smaller daughter bubble  $d_j$ . Therefore, for the calculation of the breakup time, the parent bubble size  $d_i$  is replaced by the daughter bubble  $d_j$  in Eq. 3-20.

Finally, the partial breakup frequency  $\Omega(d_i, d_j)$  for a bubble with size  $d_i$  breaking up into two daughter bubbles with size  $d_j$  and  $(d_i^3 - d_j^3)^{1/3}$  is given by

$$\Omega(d_i, d_j) = \frac{1}{t_b(d_i, d_j)} = \sum_k \frac{u_{b,k}(d_i, d_j)}{d_j} \quad \text{Eq. 3-28}$$

The total breakup frequency of bubbles with size  $d_i$  can then be obtained by integrating Eq. 3-28 over the effective range of  $f_{bv}=0.0 \sim 0.5$ , where the breakage volume fraction  $f_{bv}$  is defined by Eq. 2-88.

### **Daughter bubble size distribution obtained directly from the model**

The partial breakup frequency calculated by Eq. 3-28 can be used in the extended Eulerian multi-fluid model directly and no separate functions are needed for daughter bubble size distribution. The daughter size distribution  $\beta$  obtained directly from the partial breakup frequency has an “M-shape”:

$$\beta(d_i, d_j) = \frac{\Omega(d_i, d_j)}{\int_0^{(V_i/2)^{1/3}} 3 \frac{d_j^2}{d_i^3} \Omega(d_i, d_j) dd_j} \quad \text{Eq. 3-29}$$

### **3.2.2 Final expression for the breakup frequency**

By taking into account the contribution of all mechanisms, the total frequency of bubble  $i$  breaking up into bubble  $j$  is given by

$$\Omega(d_i, d_j) = \begin{cases} \sum_k \left( \frac{\tau_k - \tau_{crit}}{\rho_l} \right)^{0.5} \frac{1}{d_j} & (\tau_k > \tau_{crit}) \\ 0 & (\tau_k \leq \tau_{crit}) \end{cases} \quad \text{Eq. 3-30}$$

where the subscript  $k$  refers to the mechanisms leading to bubble breakup such as turbulence, laminar shear, eddy shear and interfacial slip. The destroying stress  $\tau_k$  provided by the breakup mechanisms in the external flow is given by Eq. 3-31.

$$\tau_k = \begin{cases} \tau_{turb} = \frac{1}{2} \rho_l 2^{1/2} (\varepsilon d_i)^{2/3} \\ \tau_{shear} = \mu_l \dot{\gamma} \\ \tau_{eddy} = \mu_l \sqrt{\frac{\rho_l \varepsilon}{\mu_l}} \\ \tau_{inter} = \frac{1}{2} \rho_l U_{ri}^2 \end{cases} \quad \text{Eq. 3-31}$$

and the critical stress or constraint  $\tau_{crit}$  is given by

$$\tau_{crit} = \max \left[ 6C_{fbv} \frac{\sigma}{d_i}, \frac{1}{\min(f_{bv}^{1/3}, (1-f_{bv})^{1/3})} \frac{\sigma}{d_i} \right] \quad \text{Eq. 3-32}$$

### **3.3 Characteristics of the new model**

The characteristics of the new model is studied by plotting the effect of all input parameters such as turbulence dissipation rate and shear rate on the predicted

---

collision frequency, coalescence efficiency and frequency, breakup frequency and daughter bubble size distribution.

### 3.3.1 Collision frequency

An illustration of the influence of turbulence dissipation rate and bubble size on the turbulence-induced collision frequency is shown in Figure 3.7 and Figure 3.8, respectively.

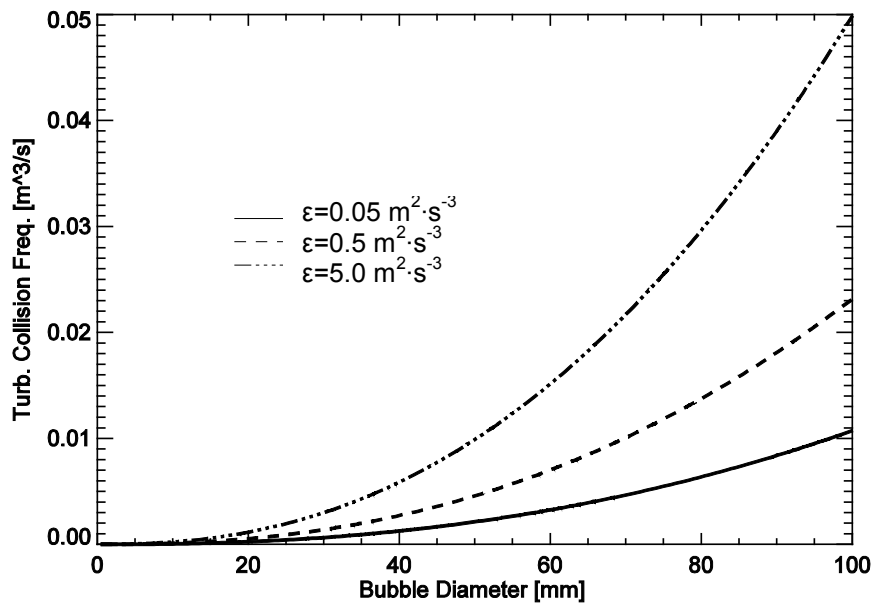


Figure 3.7 Effect of energy dissipation rate on turbulence-induced collision frequency for two equal-sized bubbles

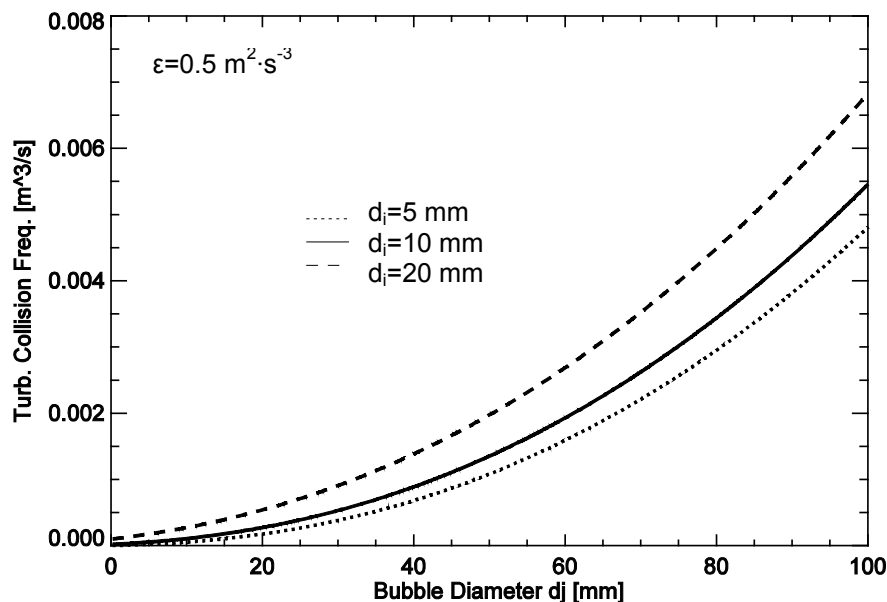


Figure 3.8 Effect of bubble size on turbulence-induced collision frequency

As it can be seen, the frequency of bubble collision due to turbulence fluctuation increases with the dissipation rate and bubble size. This is because in the case of turbulence fluctuation, the approach velocity increases as the dissipation rate  $\epsilon$  and

bubble sizes increase. Furthermore, large bubbles represent a larger cross-sectional area of the “collision tube”.

The collision frequency of two unequal-sized bubbles caused by the difference in their terminal rise velocities (see Figure 3.10) is shown in Figure 3.9.

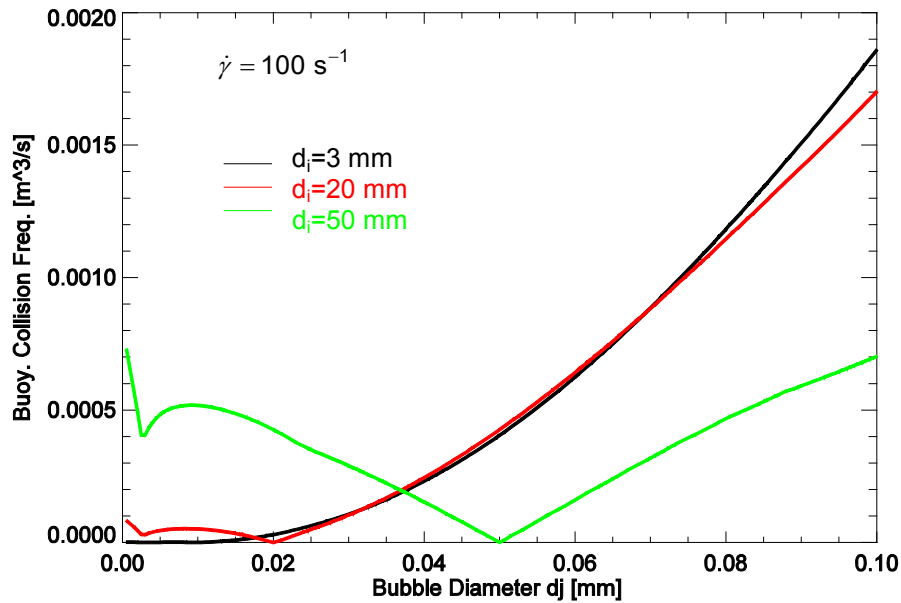


Figure 3.9 Effect of bubble size on buoyancy-induced collision frequency of two unequal-sized bubbles

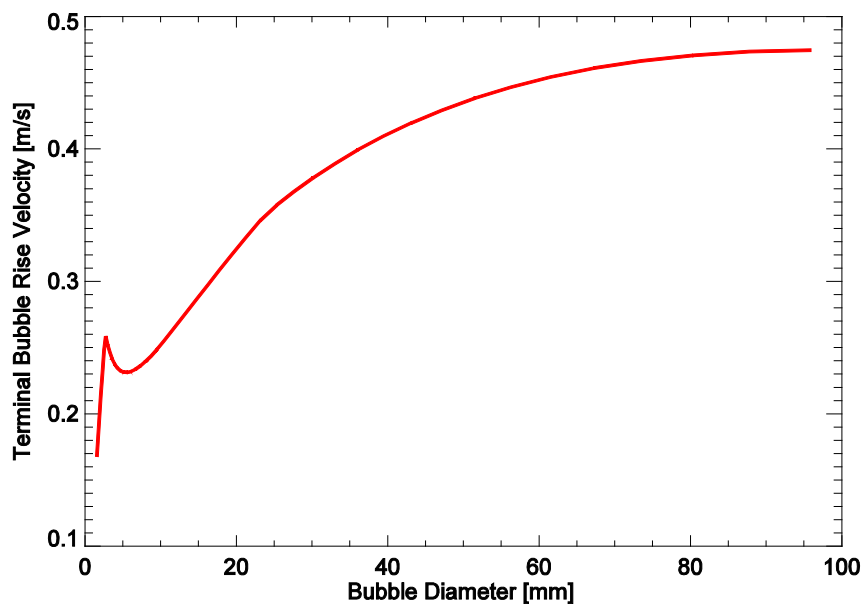


Figure 3.10 Predicted terminal rise velocity of single air bubble in water

The buoyancy-induced collision frequency increases with an increase in the size difference of two colliding bubbles. This is because the terminal rise velocities are purely determined by bubbles’ size. Therefore, the collision frequency of two equal-sized bubbles is zero.

The dependence of shear-induced collision frequency on the shear rate and bubble size is shown in Figure 3.11 and Figure 3.12, respectively.

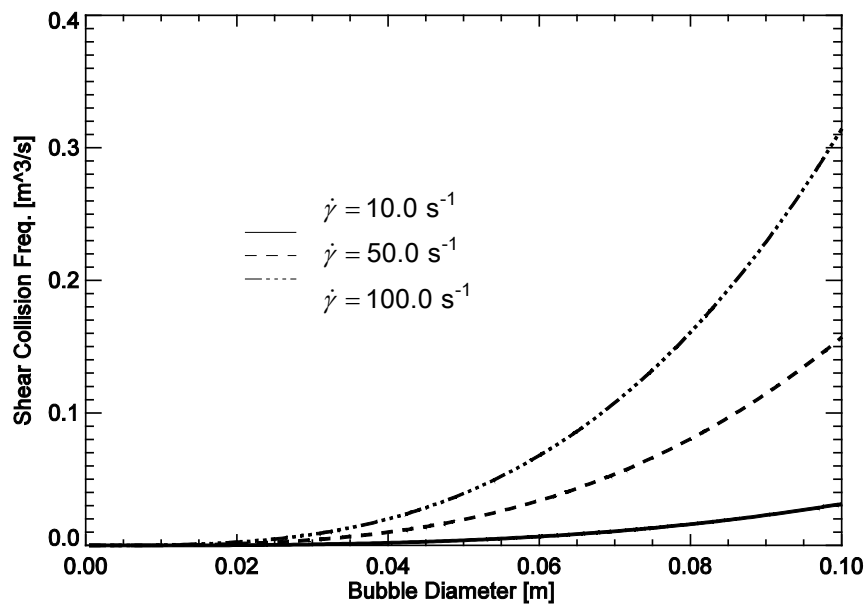


Figure 3.11 Effect of shear rate on shear-induced collision frequency (equal-sized bubbles )

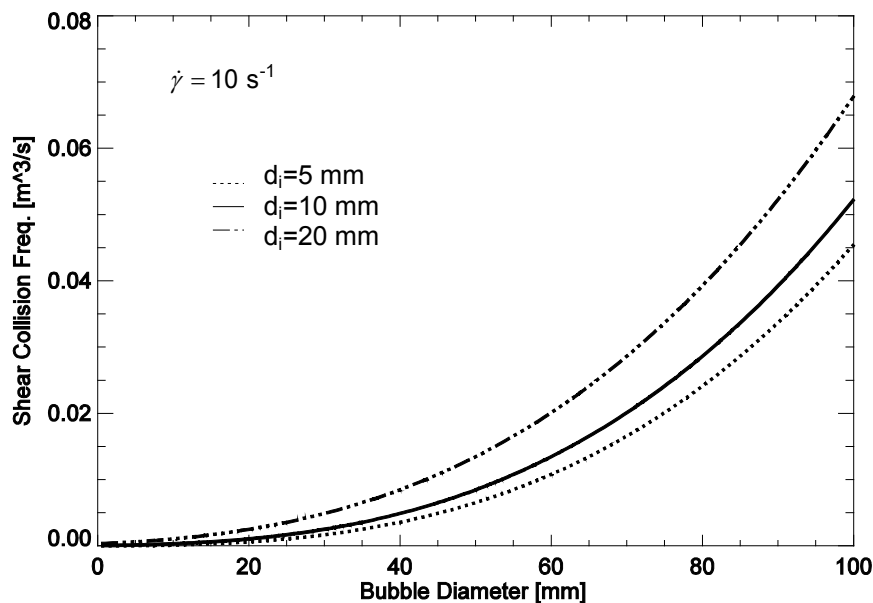


Figure 3.12 Effect of bubble size on shear-induced collision frequency (unequal-sized bubbles)

In this case, the approach velocity of two bubbles is determined by the shear rate and the sum of bubble sizes as shown in Eq. 3-4. Large shear rate and bubble sizes will result in a large relative velocity and consequently a high collision frequency. In comparison to other mechanisms, shear-induced collision frequency of bubbles is high, but with the consideration that the shear rate is almost zero at center region of a pipe flow, the mechanism of laminar velocity shear is only effective in the region near to the wall.

According to Eq. 3-1 and Eq. 3-7, the frequency of bubble collisions caused by wake entrainment is only dependent on the size of the leading bubble, which generates the wake region, as depicted in Figure 3.13.

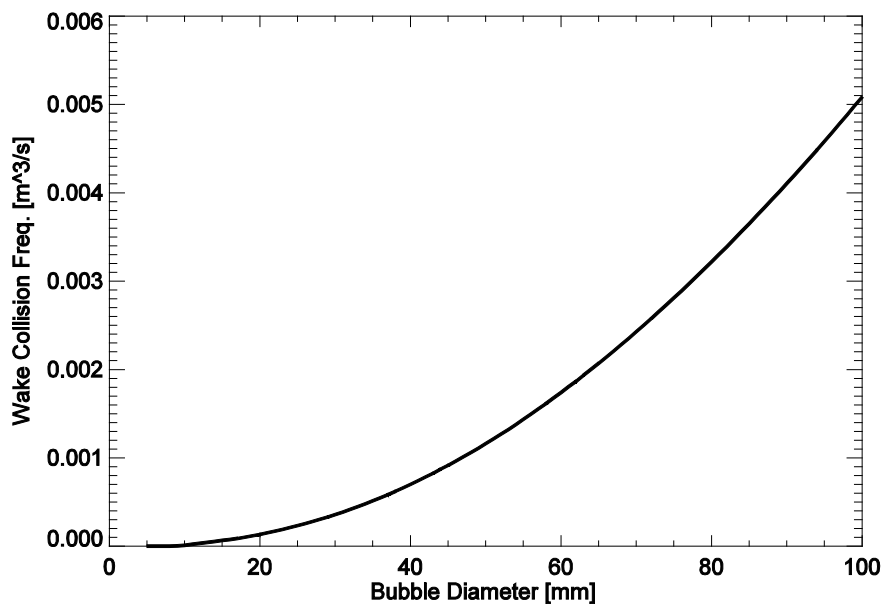


Figure 3.13 Dependence of wake-induced bubble collision frequency on the leading bubble size

The mechanism of eddy capture is only effective for collisions between micro bubbles. As the turbulence dissipation rate increases, the Kolmogorov length scale  $\eta$  decreases. In accordance, the size of bubbles, which can also be captured by eddies, decreases since it is assumed that only bubbles smaller than the Kolmogorov length scale can be captured. The dependency of collision frequency resulting from this mechanism on the turbulence dissipation is shown in Figure 3.14.

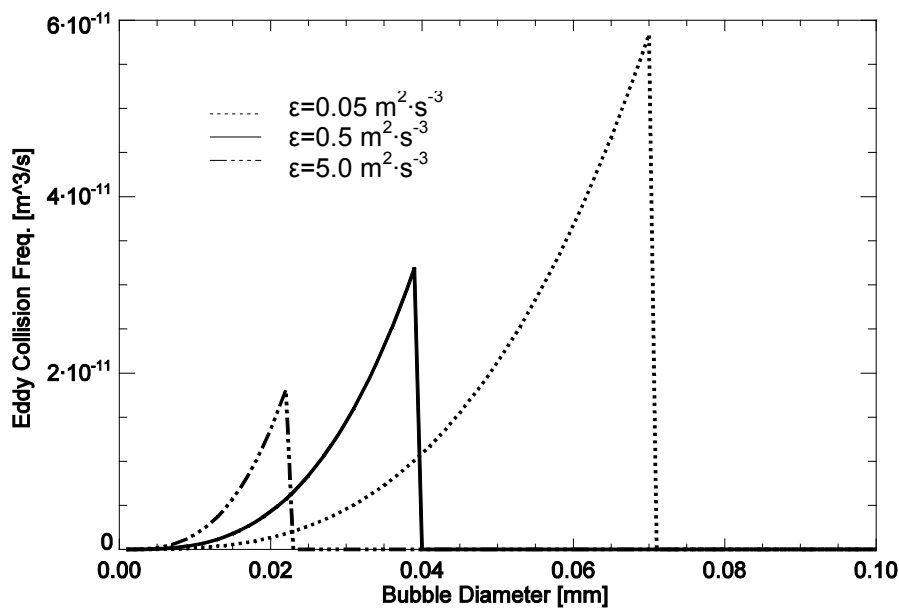


Figure 3.14 Dependence of eddy-capture collision frequency on turbulence dissipation rate

### 3.3.2 Coalescence efficiency

An illustration of the influence of turbulence dissipation rate, velocity shear rate as well as bubble size on the coalescence efficiency of inertial bubble collision caused by turbulence, shear rate and buoyancy is shown in Figure 3.15 ~ Figure 3.17, respectively. The dependence of the coalescence efficiency of each collision between two equal-sized bubbles on the turbulence energy dissipation rate,  $\varepsilon$ , is illustrated in Figure 3.15.

An increase in the energy dissipation rate causes a decrease in the coalescence efficiency. The explanation is that the approach velocity of two bubbles increases with the energy dissipation rate, however, the contact time of the colliding bubbles is inversely proportional to the approach velocity. On the other hand, the coalescence time is independent of the approach velocity according to Eq. 2-56. Therefore, the coalescence efficiency decreases as the turbulence dissipation rate increases.

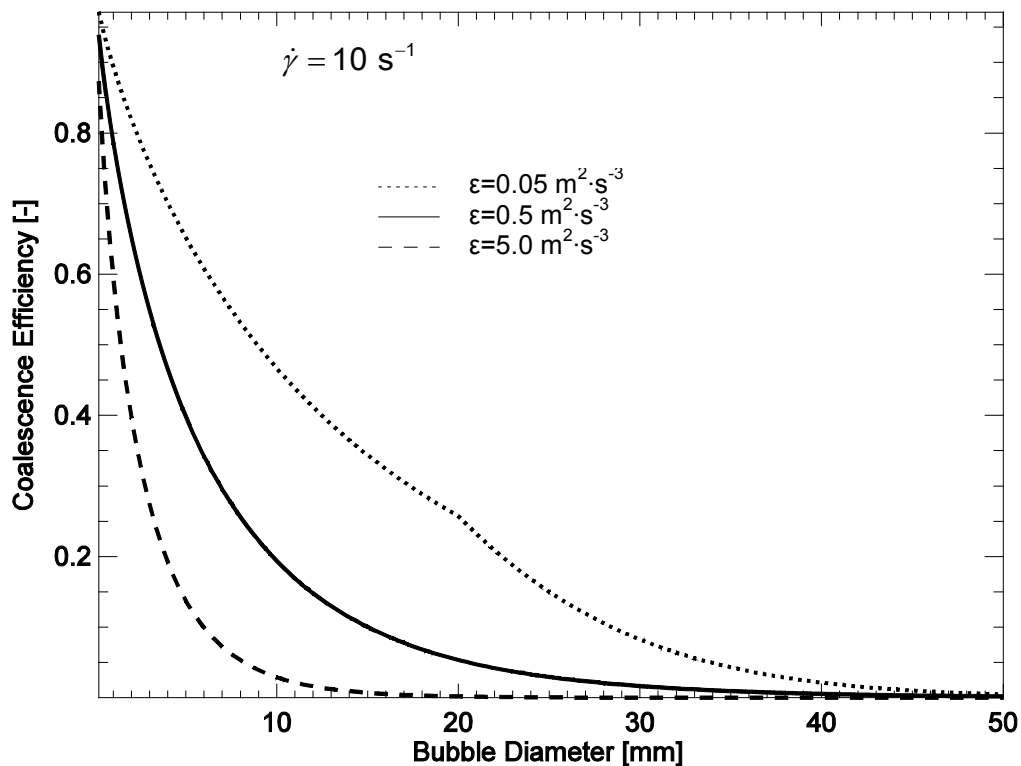


Figure 3.15 Effect of turbulence energy dissipation rate on coalescence efficiency

Similarly, as it can be seen from Figure 3.16, the contact time of two colliding bubbles decreases due to the increase of the shear rate. This effect is especially strong for large bubbles, since the relative velocity between two bubbles caused by velocity gradients in the bulk flow is proportional to the product of the shear rate and the sum of bubble sizes.



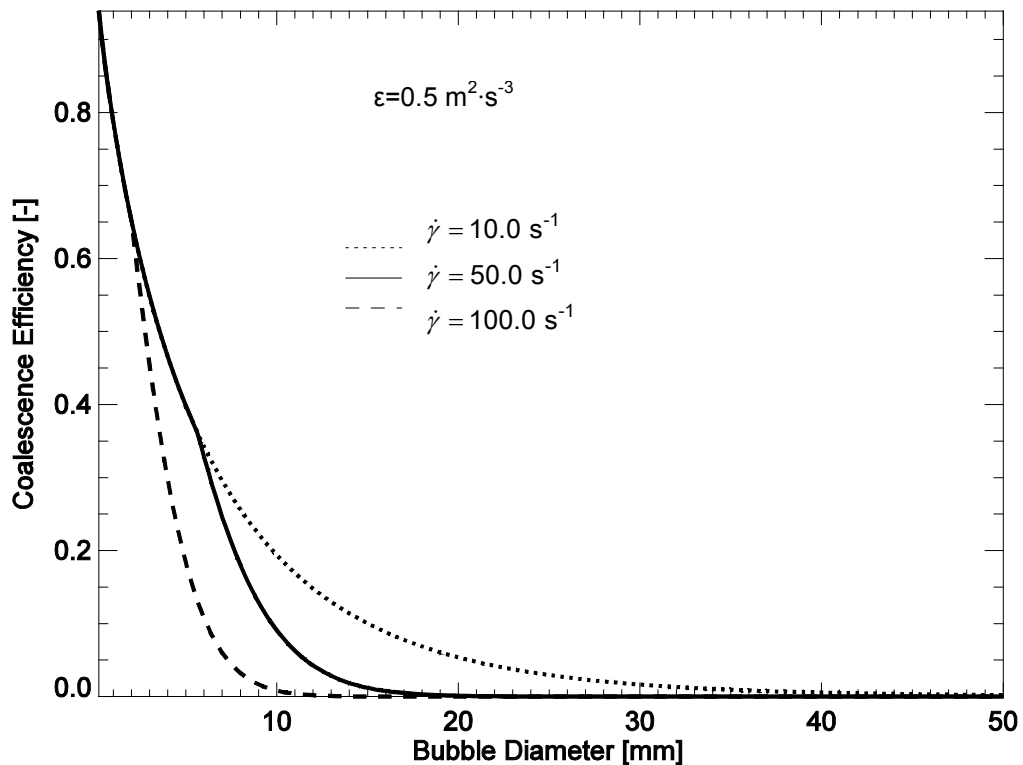


Figure 3.16 Effect of shear rate on coalescence efficiency

If the size of one bubble is kept constant, the influence of the size of the other bubble on the coalescence efficiency of inertial collisions is shown in Figure 3.17. For the collision between two bubbles of size  $d_i$  and  $d_j$ , the coalescence efficiency in general decreases with an increase in bubble size. For a given bubble size  $d_i$ , the efficiency of coalescence with a very small bubble  $d_j$  is very high. However, it decreases rapidly with the increasing of  $d_j$ . This is because the film drainage time expressed by Eq. 2-56, increases much faster than the contact time given by Eq. 3-10. Nevertheless, if one of the two colliding bubbles is small, the liquid film radius is small and the drainage time is always smaller than the contact time, which leads to a very high coalescence efficiency.

The increase of the coalescence efficiency for large bubbles can be explained by a closure evaluation of the contact and the drainage time. The change of contact / drainage time with the increase of bubble size  $d_j$  for two cases with given bubble size  $d_i$  ( $d_i=5 \text{ mm}$  and  $10 \text{ mm}$ ) is shown in Figure 3.18. It can be seen that for these two cases, both contact time and film drainage time increase with the bubble size  $d_j$ . For very small bubble sizes  $d_j$  the drainage time is almost the same for both cases and it is less than the contact time. As the bubble size  $d_j$  increases, the difference in the film drainage times becomes large while the contact time is almost the same for cases  $d_i=5 \text{ mm}$  and  $10 \text{ mm}$ . Therefore, for bubbles larger than  $10 \text{ mm}$ , the contribution of turbulence, shear rate and buoyancy is trivial while the mechanism of wake-entrainment plays a significant role in the coalescence process.

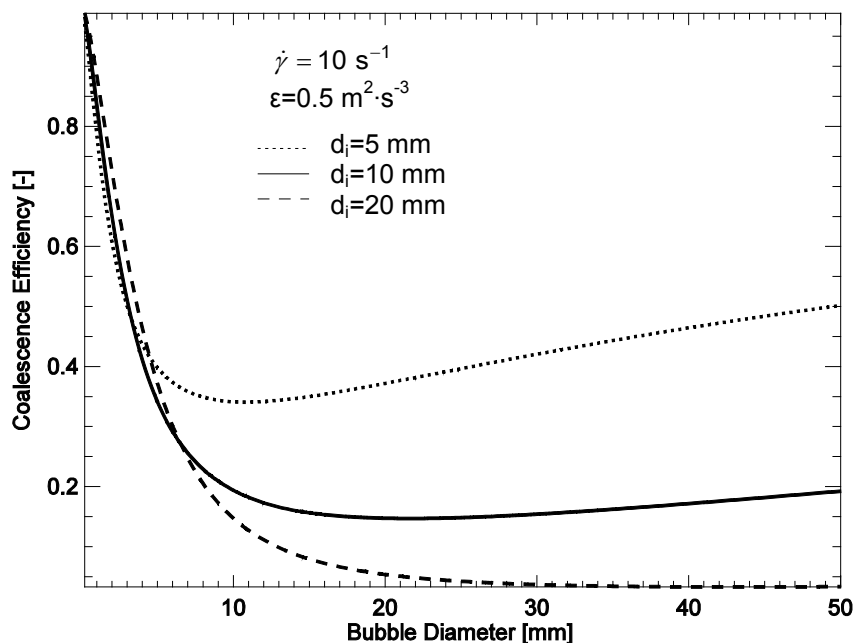


Figure 3.17 Effect of bubble size on coalescence efficiency

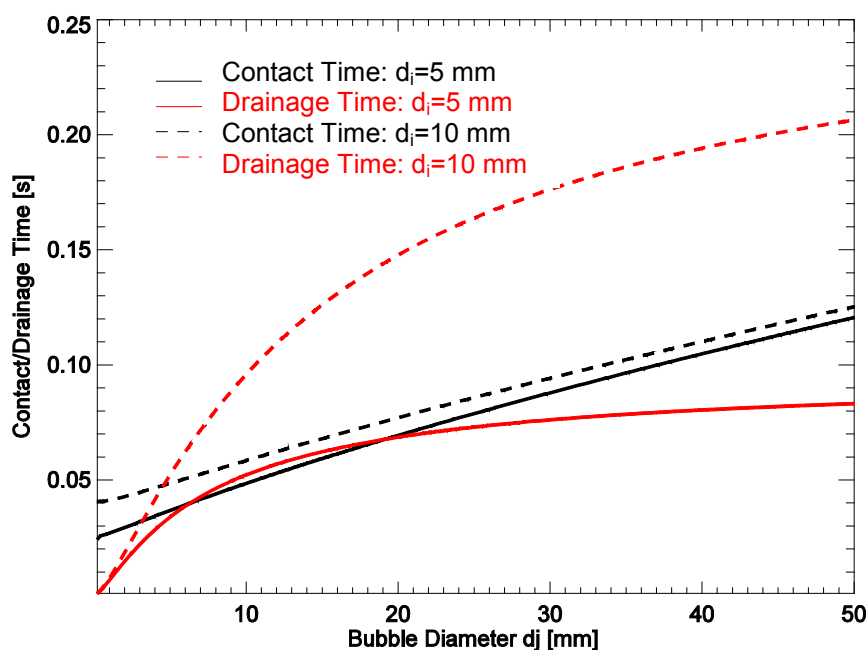


Figure 3.18 Effect of bubble size on contact/drainage time ( $\epsilon=0.5 \text{ m}^2 \cdot \text{s}^{-3}$ ,  $\dot{\gamma}=10 \text{ s}^{-1}$ )

As discussed above, due to low particle Reynolds number, the collision of small bubbles captured inside an eddy is controlled mainly by viscous force. Different from the case of other three mechanisms, i.e. turbulence, shear and buoyancy, the coalescence efficiency is calculated according to the correlation of Eq. 3-16. The influence of turbulence dissipation rate on the coalescence efficiency of two equal-sized bubbles captured inside an eddy is shown in Figure 3.19. For small bubbles that can be captured by eddies, the coalescence efficiency is about 1. In addition, it decreases with the increase of turbulence dissipation rate and bubble size, which is easy to explain by using the definition.

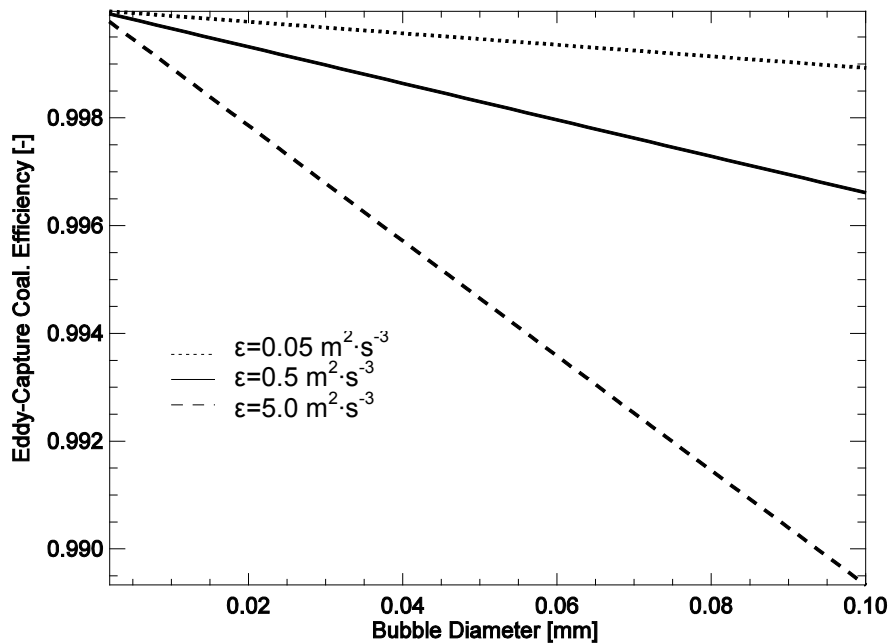


Figure 3.19 Effect of turbulence dissipation rate on coalescence efficiency of two equal-sized bubbles captured inside an eddy

### 3.3.3 Total coalescence frequency

Figure 3.20 ~ Figure 3.22 show the effects of turbulence dissipation rate, shear rate and bubble size on the total coalescence frequency, which is the coalescence rate divided by the product of number densities of bubble size class  $i$  and  $j$ . Here the coalescence caused by wake-entrainment is not included since it depends only on the size of the leading bubble.

The total coalescence frequency of two equal-sized bubbles under three different values of turbulence dissipation rates is depicted in Figure 3.20.

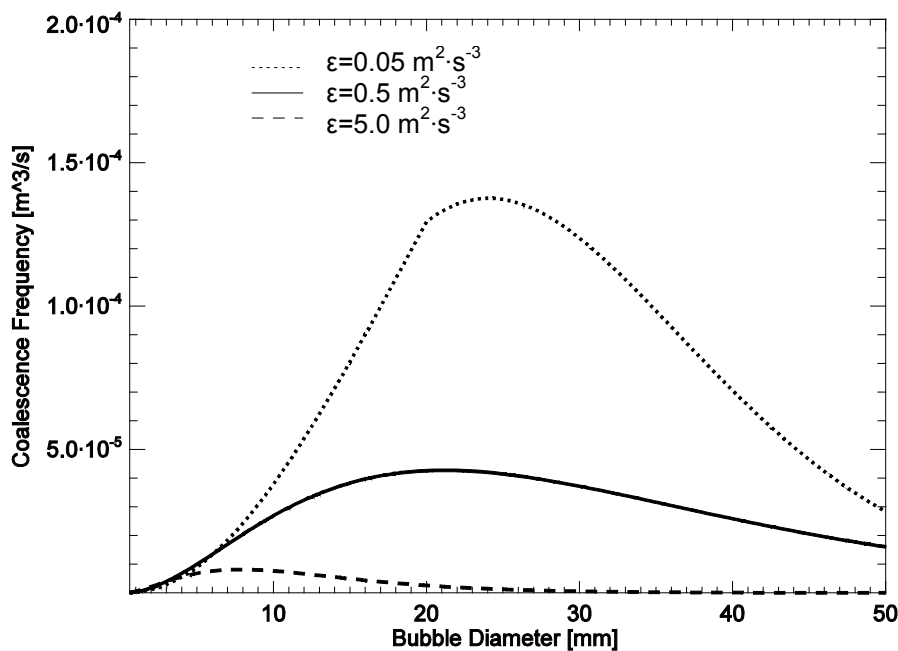


Figure 3.20 Effect of dissipation rate on coalescence frequency ( $\dot{\gamma}=10 \text{ s}^{-1}$ ,  $d_i=d_j$ )

It can be seen that an increase in the dissipation rate will cause a decrease in the coalescence frequency. This is clear since the coalescence efficiency decreases steeply with an increase in the dissipation rate (see Figure 3.15), although the turbulence-induced collision frequency increases with the dissipation rate (see Figure 3.7).

The total coalescence frequency of two equal-sized bubbles under three different shear rates is depicted in Figure 3.21.

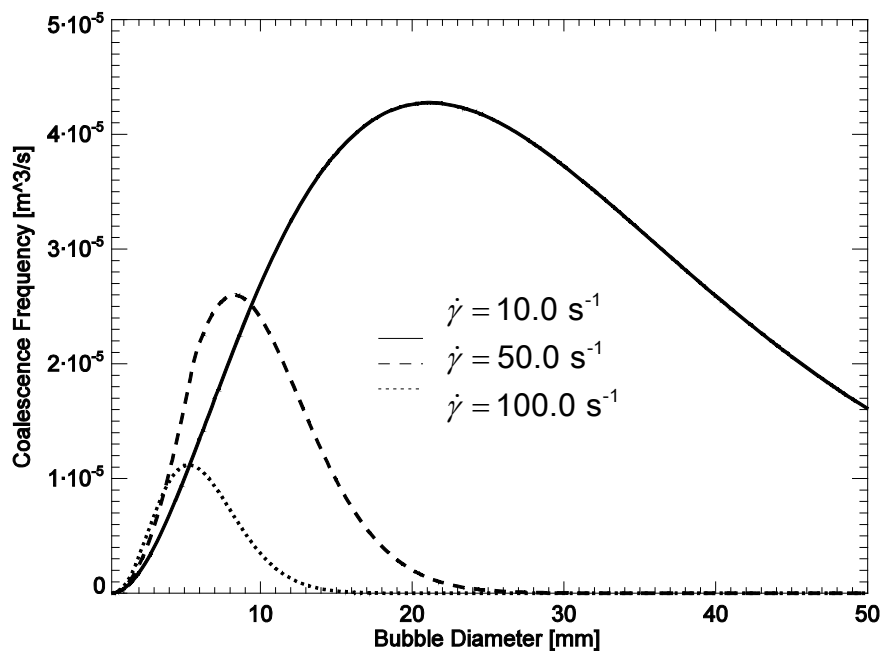


Figure 3.21 Effect of shear rate on coalescence frequency ( $\epsilon=0.5 \text{ m}^2 \cdot \text{s}^{-3}$ ,  $d_i=d_j$ )

Similarly to the case of turbulence dissipation rate, the increase of the shear rate reduces the contact time of two colliding bubbles. If the contact time is smaller than the time needed for the liquid film captured between them to drain out to the critical film thickness, the two bubbles will separate again before the coalescence occurs. Therefore, the coalescence efficiency is low at high shear rate (see Figure 3.16). As a result, the total coalescence frequency will decrease as the shear rate increases, even though the collision frequency increases (see Figure 3.12).

The total coalescence frequency of two unequal-sized bubbles under given shear rate and dissipation rate is shown in Figure 3.22. As discussed above, the collision frequency increases with the bubble sizes while the coalescence efficiency decreases with an increase in the equivalent bubble radius, which is mainly determined by the smaller bubble size (see Eq. 2-43). If the smaller bubble size is kept constant, e.g.  $d_i=5 \text{ mm}$ , the coalescence efficiency will increase with an increase in the larger bubble size  $d_j$  since the contact time is proportional to the sum of the bubble sizes. From Figure 3.22 one can see that if a bubble with a given size  $d_i$  coalesces with a very small bubble  $d_j$ , say  $d_j < 5 \text{ mm}$ , large bubble  $d_i$  results in large coalescence frequency. The explanation is that for these cases the coalescence efficiency is almost 1 for different bubble sizes  $d_i$  and the collision frequency will determine the total coalescence frequency.

As the bubble size  $d_j$  increases, for a large given bubble size  $d_i$ , e.g.  $d_i=20$  mm, the coalescence efficiency decreases steeply due to the fact that the liquid film thickness increases and as a result film drainage time increases. On the other hand, for the case with small  $d_i$ , e.g.  $d_i=5$  mm, the coalescence efficiency decreases at first when  $d_j < d_i=5$  mm and then increases stably, see Figure 3.17. This is because if  $d_j < d_i$  the film drainage time is mainly determined by  $d_j$  and decreases with a decrease in  $d_j$  while for  $d_j > d_i$  the film drainage time remains almost constant for a given  $d_i$  and the contact time increases with an increase in the bubble size  $d_j$ .

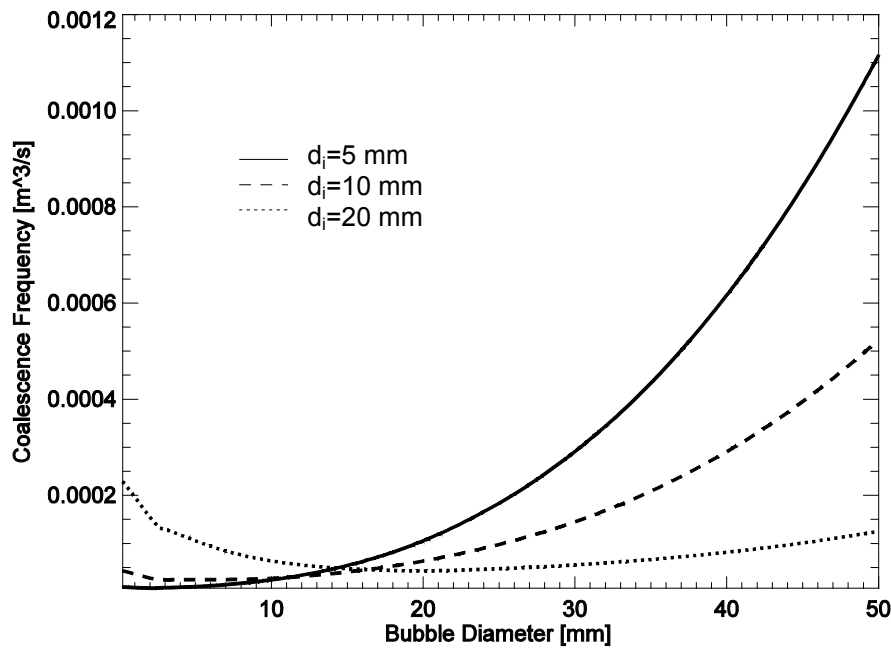


Figure 3.22 Effect of bubble size on coalescence frequency ( $\epsilon=0.5 \text{ m}^2 \cdot \text{s}^{-3}$ ,  $\dot{\gamma}=10 \text{ s}^{-1}$ )

If the contribution of wake-entrainment is considered, the total coalescence frequency of two colliding bubbles larger than the critical bubble size given by Eq. 3-8 is dominated by this mechanism, see Figure 3.23.

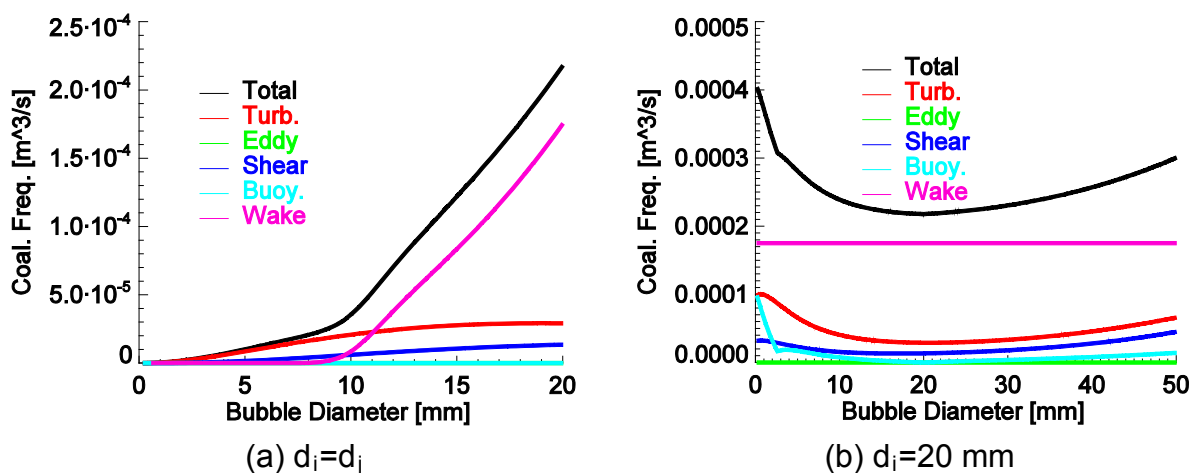


Figure 3.23 Contribution of each mechanism ( $\epsilon=0.5 \text{ m}^2 \cdot \text{s}^{-3}$ ,  $\dot{\gamma}=10 \text{ s}^{-1}$ )

### 3.3.4 Breakup frequency

For the example of air-water systems, the breakup mechanisms of turbulence and interfacial stresses are important since the shear force is negligible due to low viscosity of water.

The influence of bubble size and energy dissipation rate on the turbulence-induced specific breakup rate, which is the total breakup rate divided by the number density of the mother bubble, is shown in Figure 3.24.

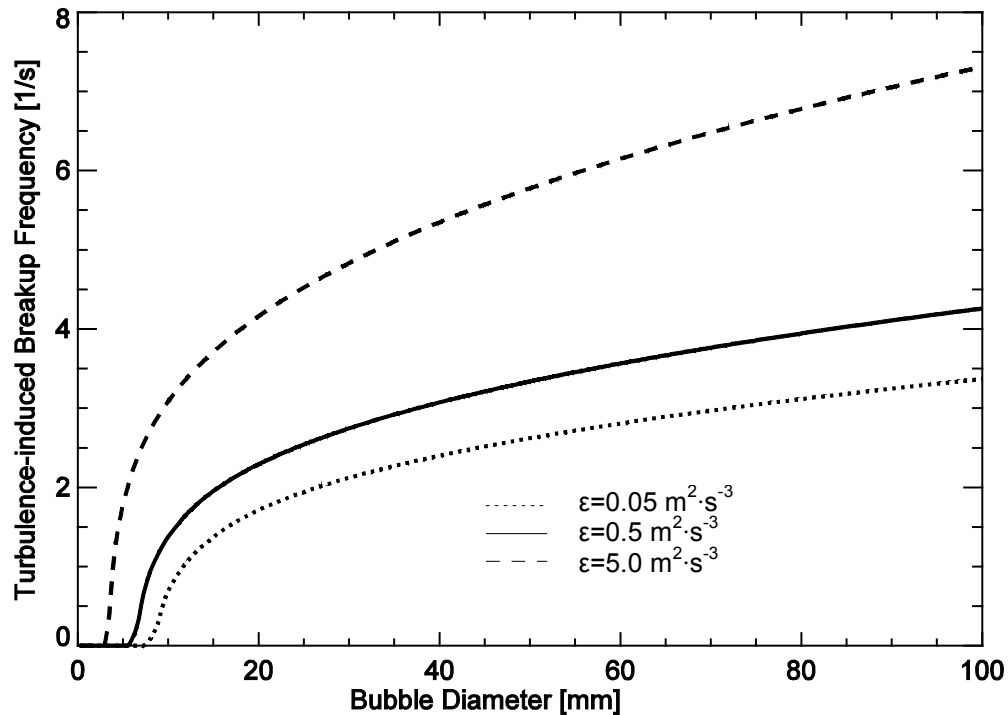


Figure 3.24 Effect of turbulence dissipation rate on turbulence-induced breakup frequency

The larger the bubble size and/or the energy dissipation rate, the higher the breakup frequency. This is reasonable since a large bubble has a low surface tension, which is easy to deform/breakup, and a large dissipation rate can provide a large disruptive stress according to Eq. 3-31. The specific breakup rate of very small bubbles is close to zero, since the turbulence fluctuation around these bubbles is too weak to overcome the surface tension. As the energy dissipation rate increases, the maximum stable bubble size, under which on breakage occurs, decreases.

The specific breakup rate caused by the interfacial slip between air bubbles and water is plotted in Figure 3.25. It depends only on the bubble size and increases with the bubble size since large bubbles have a large slip velocity, which results in a large interfacial stress.

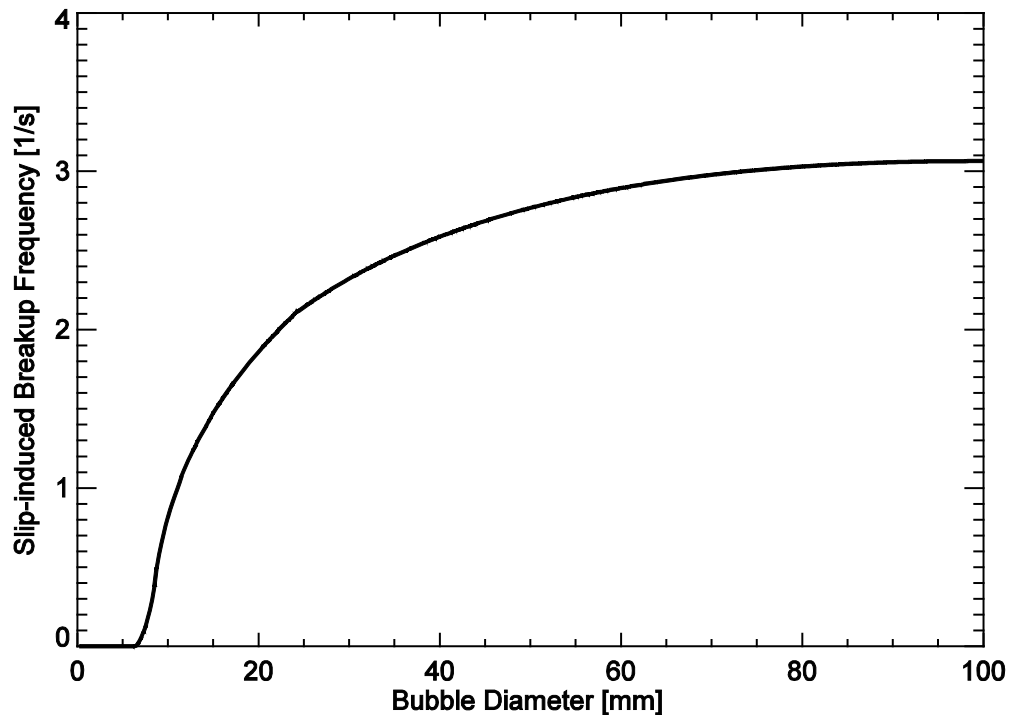


Figure 3.25 Dependence of buoyancy-induced breakup frequency on bubble size

### 3.3.5 Daughter size distribution

The influence of the parent bubble size and the breakage volume fraction on the required minimum stress for breakage is shown in Figure 3.26, which is determined by both energy and capillary constraints (see Eq. 3-21 ~ Eq. 3-23). As discussed above, according to the energy constraint, bubble breakage can occur if the destroying stress around the bubble surface exceeds the increase in surface energy during the breakage. The increase of surface energy has a maximum for equal-size breakage, i.e.  $f_{bv}=0.5$ , and then goes down to zero as the size of the smaller daughter bubble approaches zero, i.e.  $f_{bv}=0.0$ . That means that a bubble can breakup at any point if the size of one of the daughter bubbles is small enough. On the other hand, the capillary constraint limits the size of the smaller daughter bubble, because as the bubble radius curvature tends to zero, its capillary pressure becomes very high. Thus, it is impossible for the external destroying force to overcome the capillary pressure and results into such a breakage. As a result, the highest breakage probability is located at a breakage volume fraction,  $f_{bv}$ , between 0.0 and 0.5 and the corresponding daughter bubble size distribution is the so-called an “M-shape”, see Figure 3.27 and Figure 3.28, which has been shown to be more reasonable than the “U-shape” and “Bell-shape” distributions.

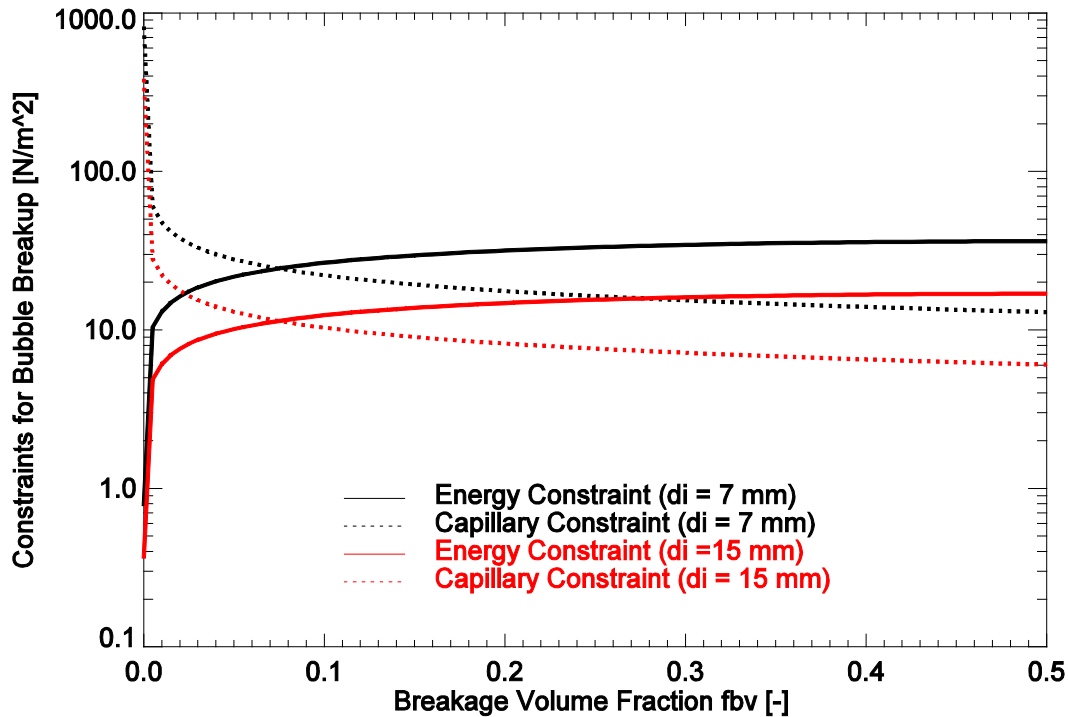


Figure 3.26 Energy and capillary constraints for bubble breakup ( $\varepsilon=1.0 \text{ m}^2\cdot\text{s}^{-3}$ )

In Figure 3.27 the dimensionless daughter size distribution is depicted for four different parent bubble sizes. As it can be seen from Figure 3.26, the larger the parent bubble size is the smaller the required critical stress is, since the critical stress according to the two constraints is inversely proportional to the parent bubble size if the breakage volume fraction is kept constant. Meanwhile, the destroying stress caused by various mechanisms always increases with the bubble size. As a result, the breakup frequency increases with the bubble size (see Figure 3.24 and Figure 3.25) since the time duration of a breakage event decreases as the difference between the destroying stress and the required minimum stress increases. On the other hand, according to the definition (see Figure 3.17 and Figure 3.18), the breakup time is proportional to the size of the smaller daughter bubble. That means that if the difference between the destroying stress and the required minimum stress is the same, it is easier to generate a small and a large daughter bubble than two approximately equal-sized bubbles. Furthermore, the probability of equal-sized breakage will increase with an increase in the parent bubble size. As the parent bubble size increases further, the daughter bubble size distribution will approach approximately to a constant value of 2, i.e. uniform distribution. This is because for large cap bubbles, the breakage is mainly determined by the capillary constraint, which is only very high for the breakage with a small and a large daughter bubbles. In contrast to the case of small daughter bubbles, the critical stress is almost constant for the breakage volume fraction  $f_{bv}$  around 0.5.



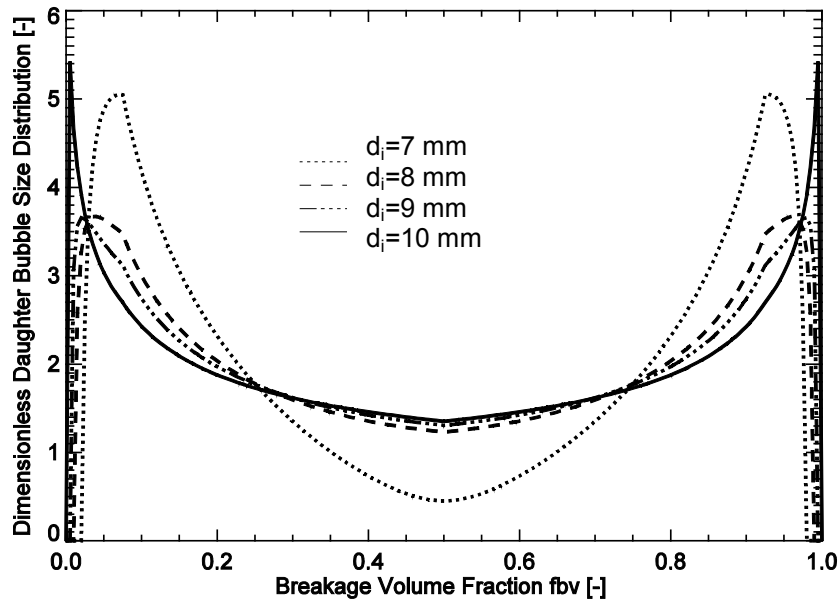


Figure 3.27 Effect of bubble size on daughter size distribution ( $\epsilon=1.0 \text{ m}^2 \cdot \text{s}^{-3}$ )

The influence of turbulence dissipation rate on the dimensionless daughter bubble size distribution is illustrated in Figure 3.28.

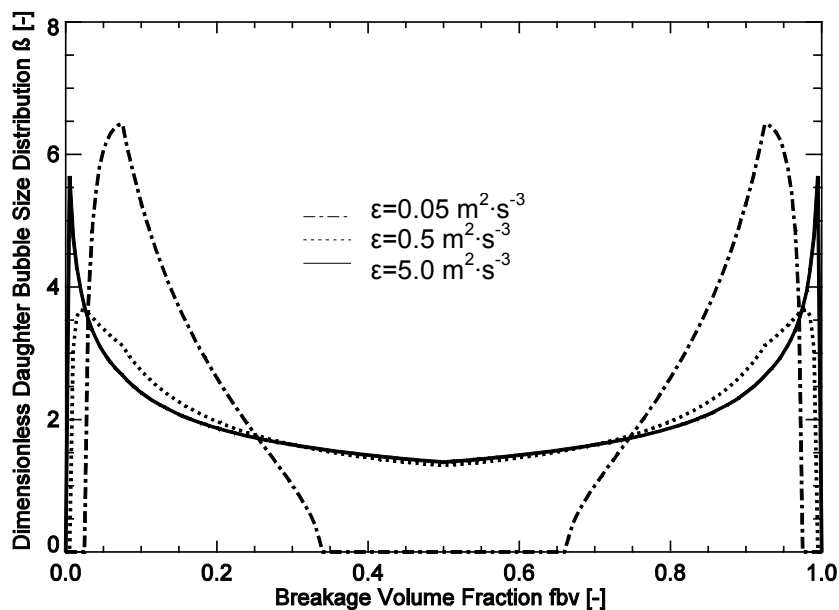


Figure 3.28 Effect of dissipation rate on daughter bubble size distribution

It is easy to understand that the daughter bubble size distribution becomes more flat as the dissipation rate increases from  $0.5 \text{ m}^2 \cdot \text{s}^{-3}$  to  $1.0 \text{ m}^2 \cdot \text{s}^{-3}$ , since large dissipation rates can provide enough destroying stress to overcome the critical stress determined by a wider range of daughter bubble size. When the dissipation rate is small, turbulent inertial stress can only overcome the minimum critical stress which is located at a position between  $f_{bv}$  equal to 0 and 0.5. If the dissipation rate increases further, the number density of very small daughter bubbles increases while the equal-sized breakup rate remains almost constant and the daughter bubble size becomes uneven again. Similarly to the influence of the parent bubble size in Figure

3.27, in the case of a sufficiently large destroying stress, the breakup time for equal-sized breakage remains almost constant while for unequal-sized breakage it is determined by the size and capillary stress of small daughter bubble.

### 3.4 Summary

A theoretical closure model is proposed for the calculation of bubble coalescence and breakup frequency, respectively. In comparison to models available in literature, the advantages of the new model can be summarized as follows:

New model for coalescence frequency:

- a) All potential mechanisms leading to a relative velocity between bubbles in a turbulent gas-liquid bubbly flow are considered
- b) Different correlations are proposed for the calculation of collision frequency and coalescence efficiency in the case of different collision mechanisms
- c) Besides the cumulative assumption, the overlapping of various mechanisms is considered to a certain extent by determining the contact time of two colliding bubbles from the maximum relative velocities, see Eq. 3-12.

New model for Breakup frequency:

- a) All potential mechanisms leading to velocity fluctuations around the bubble surface and result in deformation of bubbles considered
- b) The model is based on pure kinematic analysis so that information about the size and energy of turbulent eddies is not needed. As a result, complicated integrals over the size and/or energy of eddies are successfully avoided
- c) No additional daughter bubble size distribution functions are needed and the directly calculated daughter bubble size distribution obeys the most reasonable 'M-shape'

## 4 Strategy for model test and validation

For the test and validation of the new model for bubble coalescence and breakup, experimental data for different flow situations are needed. Vertical pipe flow under adiabatic conditions is nearly optimal for studying different constitutive models characterizing the dynamic and exchange processes at the gas-liquid interface. In this case, the change of the bubble size distribution due to coalescence and breakup can be observed along the pipe over a long vertical distance, and the gaseous phase travels together with the liquid flow with a stable velocity difference. Another reason that this geometry is selected is that compared to complicated 3D flow fields vertical pipe flow is a much simple case since the radial flow field is almost symmetrical and the boundary conditions are well-defined. For the test of a new model for bubble coalescence and breakup it is ideal to exclude all other uncertainties. However, even for this simple case, there are some obstacles that stand in the way of the test and validation of new models for bubble coalescence and breakup due to the uncertainty of other indispensable constitutive models.

Since it is difficult to measure the coalescence and breakup rates directly, measured bubble size distributions, average bubble size or interfacial area density are usually employed in the validation of new models for the calculation of coalescence and breakup rates. However, the evolution of bubble size distribution in a vertical pipe flow is coupled with that of radial gas volume fraction profiles, which are mainly determined by lateral non-drag forces such as the lift and turbulent dispersion forces. These forces are in turn dependent on the bubble size.

Numerical [143] and experimental [144] investigations have shown that the direction of the lift force changes its sign, if a substantial deformation of the bubble occurs. For air-water systems under atmospheric pressure and room temperature, the lift force coefficient changes its sign around an equivalent spherical diameter of 5.8 mm according to Tomiyama [145], which leads to a demixing of small and large bubbles in the lateral direction. That means that inside upward vertical pipe flow the radial gas volume fraction profile of small bubbles ( $d < 5.8$  mm) has a wall-peak, while large bubbles ( $d > 5.8$  mm) accumulate at the pipe center and cause a core-peak profile in the radial distribution of the volume fraction of gas phase.

On the other hand, both coalescence and breakup rates increase with an increase in the bubble number density. As a result, the evolution of the local bubble size depends on the radial redistribution of the gas volume fraction. Furthermore, large bubbles that accumulate at the pipe center will grow into even larger Taylor bubbles or slugs since the breakup rate is low there due to a small turbulence energy dissipation rate. This is the key mechanism for the transition from bubbly to slug flow, see Figure 4.1.

In both cases of Figure 4.1, small bubbles ( $d < 5.8$  mm) are injected from the bottom; however, a low superficial gas velocity is assumed for the left case. In such a case, small bubbles move along the pipe wall without any interaction and the local gas volume fraction near the wall is higher than the cross-sectional averaged one. Nevertheless, it is still too low for collisions between bubbles to occur and the flow is almost monodispersed. If the superficial gas velocity is further increased, as shown

in the right case, large bubbles are generated by coalescence near the pipe wall and migrate to the pipe center under the effect of lift force.

Finally, uncertainties in the modeling of two-phase turbulence affect directly the evolution of bubble size distribution, since turbulence is one of the important input parameters for coalescence and breakup models.

Therefore, bubble forces and turbulence models for bubbly flow are given in addition below.

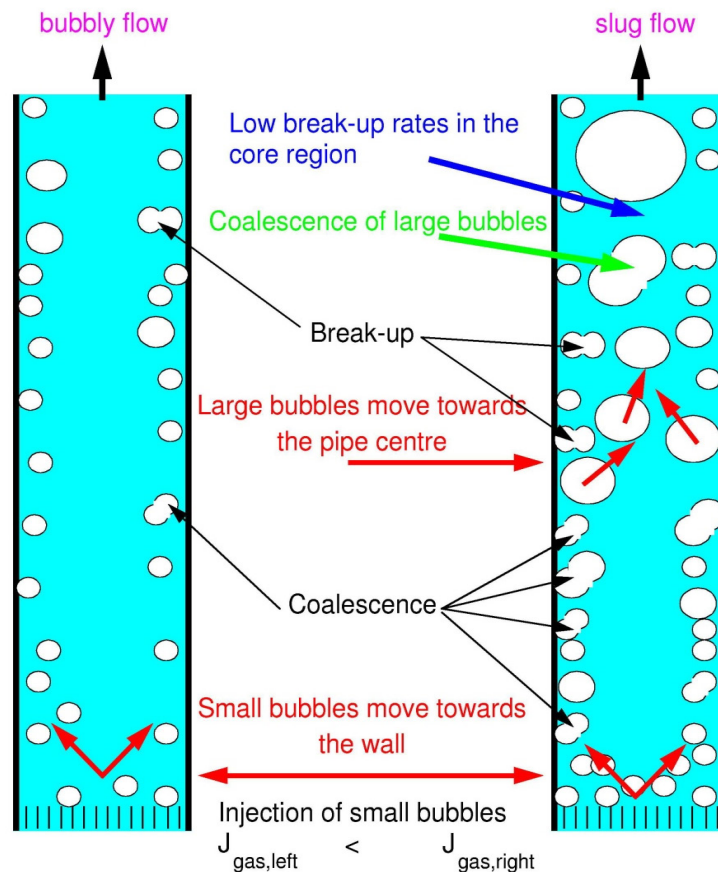


Figure 4.1 Development of bubble size inside a vertical pipe flow [2] [146]

## 4.1 Interfacial force models

### Drag force

The drag force experienced by the dispersed phase  $\beta$  per unit volume is:

$$\bar{F}_{\beta,D} = -\frac{3}{4} \frac{C_D}{d} \rho_l \alpha_\beta |\bar{u}_\beta - \bar{u}_\alpha| (\bar{u}_\beta - \bar{u}_\alpha) \quad \text{Eq. 4-1}$$

where  $\alpha$ ,  $\beta$  indicate the continuous and dispersed phase, respectively.

For the calculation of the drag coefficient  $C_D$ , several correlations that are specific to dispersed flow are available.

Schiller and Naumann [147] proposed a correlation originally for solid particles, which is also suitable for the case of sufficiently small fluid particles or viscous regime.

$$C_D = \frac{24}{\text{Re}_p} (1 + 0.15 \text{Re}_p^{0.687}) \quad \text{Eq. 4-2}$$

where  $\text{Re}_p$  is particle Reynolds number, defined as:

$$\text{Re}_p = \frac{\rho_l |\vec{u}_\beta - \vec{u}_\alpha| d}{\mu_l} \quad \text{Eq. 4-3}$$

The Grace [98] model was formulated originally for flow past a single distorted bubble, which is assumed to be applicable for sparsely distributed fluid particles in the distorted regime:

$$C_D = \frac{4}{3} \frac{gd \Delta\rho}{u_r^2 \rho_l} \quad \text{Eq. 4-4}$$

where  $u_r$  is the terminal velocity. For the case of densely distributed fluid particles, Eq. 4-4 is modified using a power law correction:

$$C_D = C_{D\infty} \alpha_\alpha^p \quad \text{Eq. 4-5}$$

where  $C_{D\infty}$  is the single bubble drag coefficient given by Eq. 4-4 and  $p$  is the volume fraction correction exponent depending on the bubble size.

For the distorted fluid particle regime, the Ishii and Zuber [140] correlation gives:

$$C_D = \frac{2}{3} Eo^{1/2} \quad \text{Eq. 4-6}$$

where  $Eo$  is Eotvos number defined as:

$$Eo = \frac{g \Delta\rho d^2}{\sigma} \quad \text{Eq. 4-7}$$

Similarly, for dense distributed particles, Eq. 4-6 will be modified according to the shape and volume fraction of the particles.

Recently, a correlation of drag coefficient was proposed by Tomiyama [145] for pure systems based on single bubbles rising in a stagnant liquid, which is an extension of the model of Schiller and Naumann [147] in Eq. 4-2:

$$C_D = \max \left\{ \min \left[ \frac{16}{\text{Re}_p} (1 + 0.15 \text{Re}_p^{0.687}), \frac{48}{\text{Re}_p} \right], \frac{8}{3} \frac{Eo}{Eo + 4} \right\} \quad \text{Eq. 4-8}$$

### **Turbulent dispersion force**

The turbulent dispersion force is the result of the turbulent fluctuations of liquid velocity. It has an important influence on the radial gas volume fraction profiles in vertical pipe flows. It causes the transportation of bubbles from regions of high concentration to regions of low concentration, and smoothes the radial gas profiles of gas volume fraction.

In this work, the FAD model proposed by Burns et al. [148], based on the Favre average of the interfacial drag force, is used. By Favre averaging the drag fluctuation term, the turbulent dispersion force per unit volume is derived as:

$$\bar{F}_{\beta,TD} = -C_{TD} \frac{3 C_D v_t}{4 d Pr} \rho_l \alpha_\beta \left| \bar{u}_\beta - \bar{u}_\alpha \right| \left( \frac{\nabla \alpha_\beta}{\alpha_\beta} - \frac{\nabla \alpha_\alpha}{\alpha_\alpha} \right) \quad \text{Eq. 4-9}$$

where  $C_{TD}$  is a user-modifiable multiplier. A value of 1.0 is used in this work.  $Pr$  is the turbulent Prandtl number for continuous phase volume fraction and currently set to be 0.9.

Similar expressions were also obtained by Carrica et al. [92], Drew [149], and Gosman et al. [150]. All these correlations show a proportional dependence on the liquid eddy viscosity  $v_t$ .

### **Lift force**

The lift force considers the interaction of a bubble with the shear field in its surrounding liquid. It acts perpendicularly to the direction of the relative motion of the gaseous and liquid phases. Based on the unit volume it can be calculated as:

$$\bar{F}_{\beta,L} = -C_L \rho_l \alpha_\beta (\bar{u}_\alpha - \bar{u}_\beta) \times (\nabla \times \bar{u}_\beta) \quad \text{Eq. 4-10}$$

Tomiya et al. [151] derived a correlation for  $C_L$  from the experiments on single bubbles rising in stagnant liquids under the conditions of  $-5.5 \leq \log M \leq -2.8$  and  $1.6 \leq \log Eo_d \leq 6$ :

$$C_L = \begin{cases} \min[0.288 \tanh(0.121 \text{Re}), f(Eo_d)] & Eo_d < 4 \\ f(Eo_d) & 4 \leq Eo_d \leq 10 \\ -0.27 & Eo_d > 10 \end{cases} \quad \text{Eq. 4-11}$$

$$\text{with } f(Eo_d) = 0.00105 Eo_d^3 - 0.0159 Eo_d^2 - 0.0204 Eo_d + 0.474$$

Here the modified Eotvos number  $Eo_d$  is calculated according to Eq. 4-7 but using the bubble diameter in horizontal direction,  $d_h$ , instead of the equivalent bubble diameter. It is calculated according to the correlation of Wellek et al. [152] for the ellipsoidal bubble aspect ratio:

$$d_h = d \cdot \sqrt{1 + 0.163 Eo^{0.757}} \quad \text{Eq. 4-12}$$

It is noted that this correlation is only valid for oblate spheroid or ellipsoid bubbles, i.e.  $Eo \leq 40$ .

### **Wall lubrication force**

In the case of bubbly upward flow, the dispersed phase is observed to concentrate in a region close to the wall, but not immediately adjacent to the wall. This effect may be modeled by adding the wall lubrication force, which tends to push the dispersed phase away from the wall. According to the model of Antal et al. [153], the wall lubrication force can be computed as:

$$\bar{F}_{\beta,W} = -C_W \alpha_{\beta} \rho_l \left| \bar{u}_{\alpha} - \bar{u}_{\beta} \right|^2 \bar{n}_W \quad \text{Eq. 4-13}$$

where

$$C_W = \max \left( 0, \frac{C_{W1}}{d} + \frac{C_{W2}}{y_w} \right) \quad \text{Eq. 4-14}$$

The non-dimensional coefficients are by default set to  $C_{W1} = -0.01$  and  $C_{W2} = 0.05$ . Note that the effective distance of the force from the pipe wall is  $y_w = 5d$  with the default values of  $C_{W1}$  and  $C_{W2}$ .

Furthermore, Tomiyama [151] proposed a correlation for the calculation of wall lubrication force:

$$\bar{F}_{\beta,W} = -C_W \frac{d \rho_l}{2} \left[ \frac{1}{y^2} - \frac{1}{(D-y)^2} \right] u_r^2 \bar{n}_W \quad \text{Eq. 4-15}$$

Similarly to the lift force coefficient  $C_W$  proposed by Tomiyama [151] depends on the Eotvos number:

$$C_W = \begin{cases} \exp(-0.933Eo + 0.179) & 1 \leq Eo \leq 5 \\ 0.007Eo + 0.04 & 5 \leq Eo \leq 33 \end{cases} \quad \text{Eq. 4-16}$$

As pointed out by Tomiyama [151], the application of Eq. 4-16 is limited to the case with  $\log M = -2.8$  and the value of  $C_W$  has to be tuned for other Morton number systems.

Recently, Eq. 4-16 was modified by Frank et al. [24] to ensure a continuous dependence on the Eotvos number, which is adopted in this work.

$$C_W = \begin{cases} 0.47 & Eo < 1 \\ \exp(-0.933Eo + 0.179) & 1 \leq Eo \leq 5 \\ 0.00599Eo - 0.0187 & 5 \leq Eo \leq 33 \\ 0.179 & Eo > 33 \end{cases} \quad \text{Eq. 4-17}$$

## 4.2 Two-phase turbulence modeling

Since turbulence is one of the important mechanisms that lead to bubble coalescence and breakup, an investigation on the influence of turbulence modeling is necessary in the test of a new model for bubble coalescence and breakup. However, turbulence modeling is still an open issue in the simulation of gas-liquid flows. In contrast to single-phase flows, the number of terms to be modeled in the governing equations of a two-phase flow is large. This makes the modeling of turbulence in two-phase simulations extremely complex. Two-phase turbulence modeling typically involves two-equation models that are formulated on the basis of single-phase models. For gas-liquid bubbly flow, it is commonly assumed that the motion of gaseous bubbles follows the fluctuations in the continuous liquid phase. Accordingly, turbulence stresses are modeled only for the liquid phase, whereas a simple zero equation model is used for the gaseous phase. In the present study the standard k- $\epsilon$  model or SST model is used for the liquid phase, which belongs to the category of eddy viscosity turbulence models. The production and destruction of liquid turbulence caused by the agitation of bubbles, i.e. the so-called bubble-induced turbulence (BIT), is considered by additional source terms.

### 4.2.1 General approach

There are in general two different approaches to considering bubble-induced turbulence (BIT) discussed in the literature. They are either to add an additional viscosity term or k and  $\epsilon$  source terms.

#### Additional viscosity term

Similarly to the concept of Sato et al. [8], the BIT is described by an additional algebraic viscosity term, which is added to the molecular viscosity of the liquid phase  $\mu_l$  in the same way as the shear-induced turbulence viscosity term  $\mu_t$ :

$$\mu_{eff} = \mu_l + \mu_t + \mu_b \quad \text{Eq. 4-18}$$

where  $\mu_{eff}$  is the effective viscosity and  $\mu_b$  represents the BIT viscosity, which depends on the gaseous phase volume fraction  $\alpha_g$ , the bubble diameter  $d$  and the relative velocity between the phases:

$$\mu_b = C_S \rho_l \alpha_g d |\bar{u}_{rel}| \quad \text{Eq. 4-19}$$

A value of 0.6 was recommended by Sato et al. [8] for the constant  $C_S$ . This expression of Eq. 4-19 is implemented widely in CFD codes such as ANSYS CFX. However, as pointed out by Sato et al. [8] it gives too high a value of  $\mu_b$  near the wall. Therefore, it was further improved by taking into account the damping effect of the wall surface on BIT turbulence.

$$\mu_b = \left[ 1 - \exp\left(-\frac{y^+}{A^+}\right) \right]^2 C_S \rho_l \alpha_g d |\bar{u}_{rel}| \quad \text{Eq. 4-20}$$

where  $\left[ 1 - \exp\left(-\frac{y^+}{A^+}\right) \right]^2$  is the damping factor.



### **Additional source terms for k-ε model**

The most popular approach for the consideration of BIT is to add additional source terms to the transport equations of k and ε / ω such as φ<sub>k</sub> and φ<sub>ε</sub> in Eq. 4-21 and Eq. 4-22.

$$\frac{\partial}{\partial t}(\alpha_l \rho_l k) + \nabla \cdot (\alpha_l \rho_l \vec{u}_l k) = \nabla \cdot \left[ \alpha_l \left( \mu_l + \frac{\mu_t}{\sigma_k} \right) \nabla k \right] + \alpha_l P_k - \alpha_l \rho_l \varepsilon + \varphi_k \quad \text{Eq. 4-21}$$

$$\frac{\partial}{\partial t}(\alpha_l \rho_l \varepsilon) + \nabla \cdot (\alpha_l \rho_l \vec{u}_l \varepsilon) = \nabla \cdot \left[ \alpha_l \left( \mu_l + \frac{\mu_t}{\sigma_\varepsilon} \right) \nabla \varepsilon \right] + \alpha_l \frac{\varepsilon}{k} (C_{\varepsilon 1} P_k - C_{\varepsilon 2} \rho_l \varepsilon) + \varphi_\varepsilon \quad \text{Eq. 4-22}$$

where C<sub>ε1</sub>, C<sub>ε2</sub>, σ<sub>k</sub>, σ<sub>ε</sub> are model constants. The shear-induced turbulence production P<sub>k</sub> is given by

$$P_k = \mu_t |\nabla \vec{u}_l + \nabla \vec{u}_l^T|^2 \quad \text{Eq. 4-23}$$

There are a number of models proposed for the calculation of BIT source terms φ<sub>k</sub> and φ<sub>ε</sub>, which are described in the following section.

#### **4.2.2 BIT source term models**

In most models the production of BIT kinetic energy φ<sub>k</sub> is calculated as the work of interfacial forces (e.g. drag force, added-mass force), i.e. the interfacial force multiplied with the local slip velocity.

$$\varphi_k \propto -\left| \vec{M}_\alpha \right| \cdot \left| \vec{u}_{rel} \right| \quad \text{Eq. 4-24}$$

It is worth noting that the drag force is included in all models, since it is the main source of energy input. Non-drag contributions are considered only in a few models, e.g. the added-mass force considered in the work of Yao and Morel [159].

For the modeling of BIT source term in Eq. 4-21, φ<sub>ε</sub>, the same approach as it was done in the single-phase model is adopted. That is the destruction of BIT is assumed to be proportional to the production divided by a characteristic time scale, τ:

$$\varphi_\varepsilon \propto \frac{\varphi_k}{\tau} \quad \text{Eq. 4-25}$$

If the k-ω model is used instead, the source term for the turbulence eddy frequency ω is calculated according to the transformation ε=β\*ωk,

$$\varphi_\omega = \frac{1}{\beta^* k} \varphi_\varepsilon - \frac{\omega}{k} \varphi_k \quad \text{Eq. 4-26}$$

where β\* = 0.09.

The main difference between the existing models for the BIT source terms is the calculation of the time scale  $\tau$ .

In this study, four different models for BIT production and destruction,  $\varphi_k$  and  $\varphi_\varepsilon$ , are implemented. They are the Morel model [159], Pflieger model [157], Politano model [158] and Troshko model [163].

### **Morel model [159]**

In Morel [159], in the calculation of turbulence produced by the bubble agitation only the work input of the interfacial drag force is considered. The additional source term for the k balance equation is expressed as:

$$\varphi_k = -C_k \bar{F}_{\beta,D} (\bar{u}_g - \bar{u}_l) = C_k \frac{3 C_D}{4 d} \alpha_g |\bar{u}_{rel}|^3 \quad \text{Eq. 4-27}$$

It can be seen that the BIT kinetic energy is proportional to the gas volume fraction.

Accordingly, the source term for energy dissipation balance equation is:

$$\varphi_\varepsilon = C_\varepsilon \frac{\varphi_k}{\tau} \quad \text{Eq. 4-28}$$

In the Morel model [159], a value of 1.0 is used for both constants  $C_k$  and  $C_\varepsilon$ .

The time scale  $\tau$  of the pseudoturbulence destruction was calculated based on a dimensional analysis background. The authors assumed that  $\tau$  is dependent on the bubble diameter  $d$  with the consideration that the wake region behind a bubble is originally of the same size as the bubble. The larger the wake, the longer will be the time required for its energy to cascade to the smallest turbulence eddy scale before it can be dissipated. Therefore, they gave the characteristic time scale as

$$\tau = \left( \frac{d^2}{\varepsilon} \right)^{1/3} \quad \text{Eq. 4-29}$$

### **Pflieger Model [157]**

In the work of Pflieger and Becker [157], the authors proposed a model which is similar to that of Morel [159]. The only difference is the calculation of the time scale  $\tau$ . By making an analogy to the shear-induced turbulence in single-phase flows, Pflieger and Becker [157] calculated the time scale  $\tau$  based on the Kolmogorov's hypothesis that the destruction of turbulence is determined by the time scale of the smallest eddies, which are responsible for energy dissipation, i.e.

$$\tau = \frac{k}{\varepsilon} \quad \text{Eq. 4-30}$$

In addition, a value of 1.44 and 1.92 is used by Pflieger and Becker [157] for the constants  $C_k$  and  $C_\varepsilon$ , respectively.

### **Politano model [158]**

For the calculation of the BIT production,  $\varphi_k$ , Politano et al. [158] proposed a model by extending the model of Lee et al. [160] to the multi-group simulation of poly-dispersed bubbly flow. This model is slightly different from the last two models. According to Lee et al. [160], in an air-water upflow, the increase in the turbulence production of the liquid phase due to the relative motion of bubbles comes from a decrease in the potential energy of the liquid phase when the bubbles displace the same volume of high density liquid from a low pressure to a higher pressure region. As a result, the rate of increase in turbulent kinetic energy per unit mass of the liquid is given as:

$$\varphi_k = -C_k \frac{\alpha_g}{\rho_l} \frac{\partial p}{\partial z} |\bar{u}_{rel}| \quad \text{Eq. 4-31}$$

According to Antal et al. [153] and Lopez de Bertodano et al. [161], the pressure gradient around the bubble surface can be approximated as

$$\frac{dp}{dz} = -\frac{\rho_l |\bar{u}_{rel}|^2}{d} \quad \text{Eq. 4-32}$$

For poly-dispersed flow Politano et al. [158] extended the above model to consider the effect of bubbles of different sizes by using the relative velocity weighted by the gas volume fraction. Therefore, Eq. 4-31 is rewritten as:

$$\varphi_k = C_k \sum_{i=1}^N \frac{\alpha_i |\bar{u}_{rel,i}|^3}{d_i} \quad \text{Eq. 4-33}$$

where  $j$  is the bubble size group.

For the calculation of the characteristic time scale,  $\tau$ , Eq. 4-30 is used. In addition,  $C_k=1.0$  and  $C_\varepsilon=1.92$  were adopted originally in this model.

### **Troshko model [163]**

In a recent work, Lopez de Bertodano [162] found that the time scale of single-phase turbulence destruction in Eq. 4-30 brought unreasonable results for his case of the decay of homogenous two-phase turbulence. In other words, the turbulence decay was shown to depend on the initial dissipation rate. Therefore, he proposed a new expression for the time scale of bubble-induced turbulence destruction, which was used in the BIT model of Troshko and Hassan [163]:

$$\tau = \frac{2C_{VM}d}{3C_D |\bar{u}_{rel}|} \quad \text{Eq. 4-34}$$

where  $C_{VM}$  is the virtual mass force coefficient and a value of 0.5 used in this work. It is worth noting that if the parameters  $C_{VM}$ ,  $C_D$  and  $u_{rel}$  are assumed to be constant for a given bubble size, the time scale predicted by Eq. 4-34 is independent on the radial position, gas volume fraction as well as energy dissipation rate.

### 4.3 Solver

In this work, the models described in the last chapters were implemented and tested in two different solvers, i.e. a 1D simplified Test Solver (the Multi Bubble Size Class Test Solver) and a 3D CFD solver (ANSYS 12.1 CFX solver), respectively. The two solvers especially the simplified one are introduced briefly below.

#### 4.3.1 The Multi Bubble Size Class Test Solver

This is a simplified model for the simulation of gas-liquid flows developing along a vertical pipe, which was proposed and developed originally by Lucas et al. [2]. The aim of this model is to provide an efficient tool for the test of new closure models, which are suitable for their implementation in CFD codes. It considers a large number of bubble size classes, and therefore, is called Multi Bubble Size Class Test Solver. A sufficiently fine discretization of bubble size is usually impossible for a CFD code but desirable for the test of coalescence and breakup models.

For each height position, the Test Solver delivers new radial profiles of the bubble size class resolved gas velocity, gas volume fraction by solving mass and momentum equations of all classes. However, it does not resolve flow parameters of gas and liquid over the pipe height. Instead, the liquid velocity at each height position is calculated by using the Sato [8] correlation from a given gas volume fraction [8], see Eq. 4-35. By assuming that all bubbles perform their upward movement with the average gaseous phase rise velocity, it is possible to transform the time axis to a vertical axis and to evaluate the evolution of flow pattern over the pipe height in the case of stationary flows.

$$\frac{du_l(r)}{dr} = \frac{\tau}{[1 - \alpha_g(r)](\mu_l + \mu_t + \mu_b)} \quad \text{Eq. 4-35}$$

where  $\tau$  is the shear stress and calculated according to following expression, which is derived from the force balance:

$$\tau = \tau_w \left( 1 \mp B \int_0^1 \alpha_g r^* dr^* \right) r^* \pm \frac{B}{r^*} \int_0^{r^*} \alpha_g r^* dr^* \quad \text{Eq. 4-36}$$

where  $B$  and  $r^*$  are dimensionless parameters  $B = gR/u_l^2$  and  $r^* = r/R$ , and  $\tau_w$  is the wall shear stress.

In the Test Solver, bubble size can be discretized uniformly or with a fixed width ratio into  $n$  size classes. In this work, the latter approach is used, i.e.

$$\frac{d_i}{d_{i-1}} = \left( \frac{d_{\max}}{d_{\min}} \right)^{\frac{1}{n-1}} \quad \text{Eq. 4-37}$$

where,  $d_{\max}$ ,  $d_{\min}$  is the maximum and minimum bubble size, respectively.

The influence of the discretization of the bubble size on the predictions is shown in Figure 4.2 for test point 107 at level I. Details about the test points and height levels

will be introduced later in this chapter. It can be seen that if the number of size classes,  $n$ , is equal to or larger than 25, then the influence is negligible especially for gas velocity and volume fraction. A value of 45 is used for  $n$  in this work.

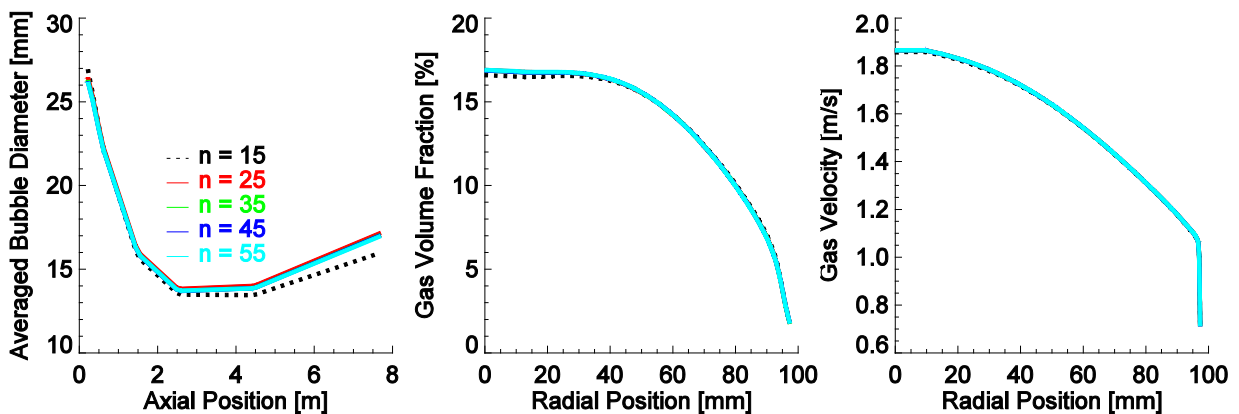


Figure 4.2 Influence of bubble size groups on predicted results (TP107, Level I)

The radial cross-section of the vertical pipe is discretized into  $N$  equal-volume annular rings. The influence of  $N$  on the predicted radial profiles of gas velocity and volume fraction and average bubble diameter is shown in Figure 4.3. The influence of the radial spatial discretization on the results vanishes if the number of discretised annular rings  $N$  is equal to or larger than 120.  $N=150$  is used for all calculations in this work.

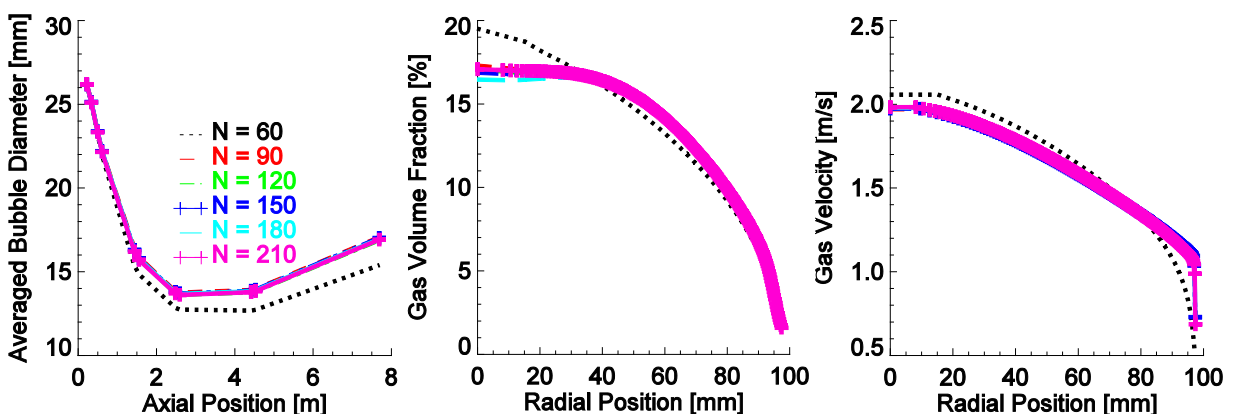


Figure 4.3 Influence of number of radial nodes on predicted results (TP107, Level I)

In the numerical scheme used in the Test Solver, values for gas volume fraction  $\alpha_g$  are given within the radial nodes, while the gradients of gas volume fraction and liquid velocity are given at the boundary of the nodes. For a consistent discrete modeling, partial velocities at the boundaries are introduced according to the scheme shown in Figure 4.4.

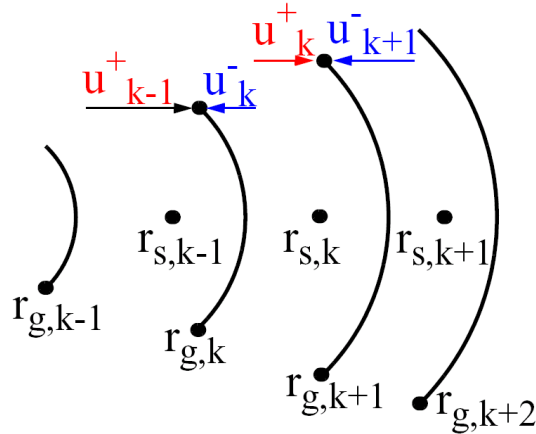


Figure 4.4 Schema of applied discretization method [164]

The velocity  $u_k^-$  is calculated using the node values of node  $k$  and the gradients at the lower boundary of node  $k$  at  $r_{g,k}$ , while  $u_k^+$  results from the node values of node  $k$  and the gradients at the upper boundary at  $r_{g,k+1}$ . Furthermore,  $u_k^-$  is set to zero if positive values are calculated, and  $u_k^+$  is set to zero, if negative values are calculated.

For one time step, at first the change in velocities caused by bubble forces is calculated. Afterwards, the gas volume and momentum are shifted according to the new velocity. It is assumed that the gas volume fraction at one given node is equally distributed within the node width, which forms an annulus in the radial direction. The shift is done in a way in which the center of mass of the annulus is shifted according to  $u\Delta t$ . The centre of mass of an annulus in the case of a constant density is calculated by:

$$r_s = \frac{\int_{r_0}^{r_1} \rho_g r^2 dr}{\int_{r_0}^{r_1} \rho_g r dr} = \frac{2}{3} \frac{r_1^3 - r_0^3}{r_1^2 - r_0^2} \quad \text{Eq. 4-38}$$

with  $r_0$  and  $r_1$  are the inner and outer radii of the annulus.

If a fraction  $\Theta$  of the gas volume is shifted from node  $k$  to node  $k+1$ , the centre of mass of the annulus  $k$  is recalculated according to:

$$r_s^{new} = r_{s,k} + u_k^+ \Delta t = \frac{2}{3} \frac{(1-\Theta_k^+)(r_{g,k}^3 - r_{g,k-1}^3) + \Theta_k^+(r_{g,k+1}^3 - r_{g,k}^3)}{(1-\Theta_k^+)(r_{g,k}^2 - r_{g,k-1}^2) + \Theta_k^+(r_{g,k+1}^2 - r_{g,k}^2)} \quad \text{Eq. 4-39}$$

In the model all radial nodes have an equal volume, i.e.:

$$r_{g,k}^2 - r_{g,k-1}^2 = r_{g,k+1}^2 - r_{g,k}^2 \quad \text{Eq. 4-40}$$

For this special case the following relation applies:

$$\Theta_k^+ = \frac{u_k^+ \Delta t}{r_{s,k+1} - r_{s,k}} \quad \text{Eq. 4-41}$$

In analogy for  $\Theta_k^-$  yields:

$$\Theta_k^- = \frac{u_k^- \Delta t}{r_{s,k} - r_{s,k-1}} \quad \text{Eq. 4-42}$$

These fractions of gas volume are shifted from one node to the other together with their momentum. The source terms in the mass balance resulting from coalescence and breakup are added separately to the gas volume fractions for each node and each bubble class.

The flow chart depicted in Figure 4.5 gives a general schema for the prediction of upward gas-liquid vertical pipe flow with the Test Solver. It can be seen that the calculation terminates if the gaseous phase arrives at the maximum pipe height. The liquid velocity is calculated by adjusting  $\tau_w$  through the iteration between the wall shear stress  $\tau_w$  and the given superficial liquid velocity  $J_l$  according to Eq. 4-35 and Eq. 4-36. If the difference between the calculated and given superficial liquid velocity is lower than a presumed tolerance, the iteration stops,

$$\frac{(J_l^{cal} - J_l^{given})}{J_l^{given}} \leq \Delta \quad \text{Eq. 4-43}$$

### 4.3.2 ANSYS 12.1 CFX-Solver

Since the final goal of the Test Solver is to provide an efficient tool for the preliminary test of new closure models for CFD codes, it is meaningful to validate the simplified model itself and relevant parameters delivered by it with the help of a CFD code. In this work, ANSYS CFX-12.1 is selected to fulfill this requirement, which is a high-performance commercial fluid dynamics program that has been widely applied for over 20 years. Modern extension approaches of the standard multi-fluid model such as the MUSIG and the DQMOM model are available in the CFX-12.1 solver. This makes it possible to use this solver to trace the evolution of local bubble size and to compare the predictions with those delivered by the Test Solver. In this work, the inhomogeneous MUSIG model is employed, whose basic concept is introduced in the section §2.2.5.

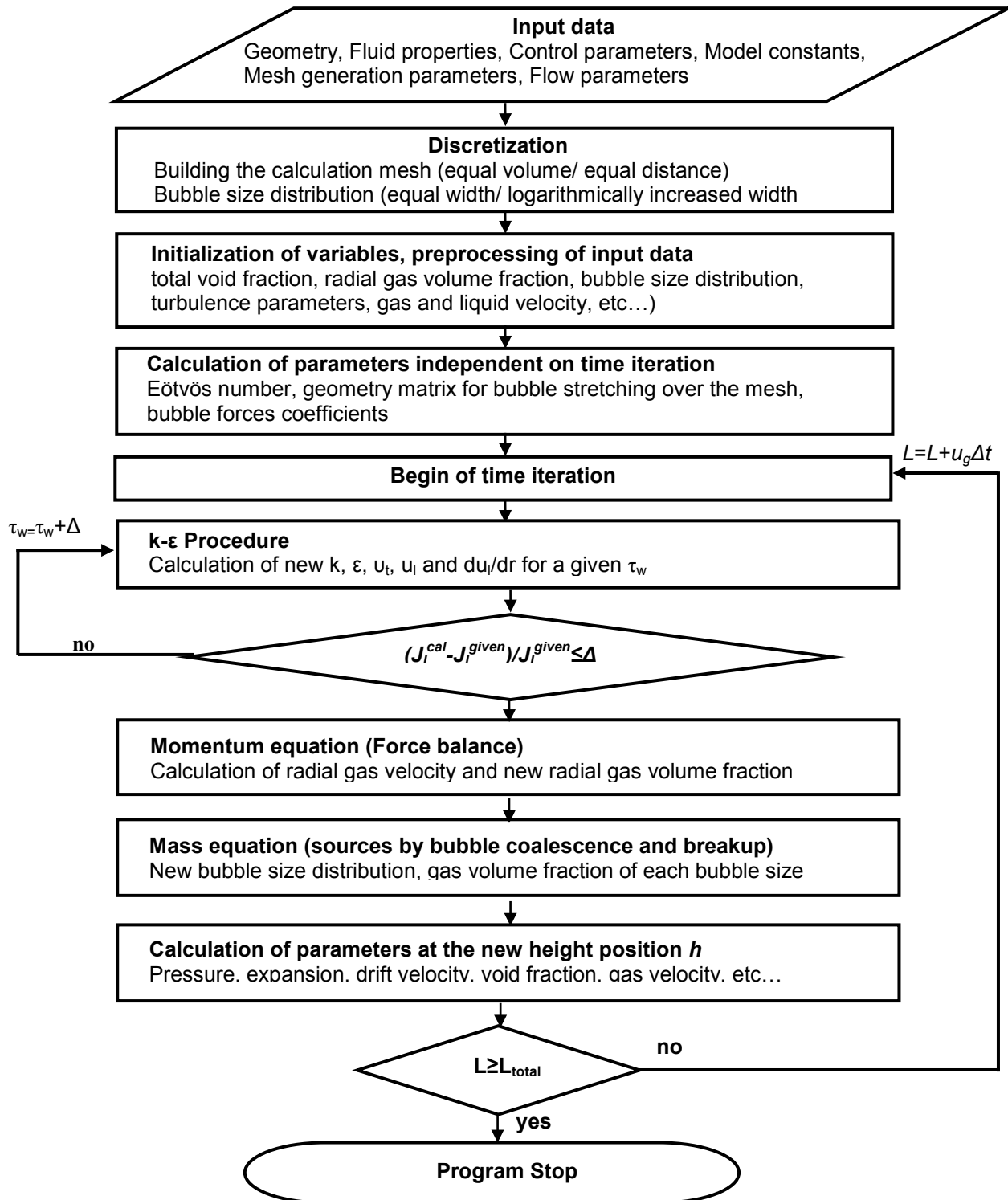


Figure 4.5 Flow chart of 1D Test Solver

#### 4.4 Experimental database

For the validation of the new model discussed in Chapter 3 in a steady-state by using the two solvers discussed above, experimental data for bubble size distributions and radial gas volume fraction profiles at different spatial positions are needed. The following subsections describe the detailed requirements for such a



validation process, limitations of databases available in the literature and the TOPFLOW experiment [9].

### 4.4.1 Requirements

Experimental databases used for the validation of bubble coalescence and breakup models are required to be able to provide the evolution of bubble size distribution for a relatively long time period or over a long distance. The example of vertical pipe flows satisfies the requirement well. In addition, measurements about the bubble size distribution and gas volume fraction should be available for several height positions. A consistent trend regarding the evolution of phase distribution and bubble size distribution along the pipe should be observed.

In the past, many experimental studies have been carried out for turbulent bubbly flows inside vertical pipes or channels, and a number of databases were developed. However, the information provided by these databases is usually incomplete especially for bubble size distributions, which makes it difficult to validate the new model in the two selected solvers by using these data.

Continuous efforts in the development of the IATE method have been made by Ishii and his co-workers analytically and experimentally [53] [165] [166]. Comprehensive databases on the interfacial area concentration have been developed for bubbly flows in vertical pipes. Unfortunately, these data cannot be applied in the solvers selected in this work, since no information about the bubble size distribution is available.

Another well-known database for upward air-water bubbly flow in a vertical pipe was published by Liu and Bankoff [46] [167]. Measurements about liquid and gas velocity, gas volume fraction, probability density function (pdf) of bubble chord length as well as turbulence intensity are available. However, the results are applicable only for fully-developed flow, i.e. measurements done only for one height position ( $L/D=36$ ). In addition, bubble size distribution has to be obtained from the measured chord length pdf, for which the differentiation of the measured irregular curve is required. This operation will magnify any scatter to induce uncertainty [167]. The same problem was encountered by processing the experimental data provided by Liu [168], Ohnuki et al. [169] and Shen et al. [170].

All the databases were achieved from vertical pipes that have an inner diameter of about 50 mm or below with the exception of the last two databases published by Ohnuki et al. [169] and Shen et al. [170], which deliver insights into the flow structure in large diameter pipes ( $D=200$  mm). The use of a large pipe can exclude the dependence of local gas volume fraction distribution on the pipe diameter.

For upward gas-liquid flow in a vertical DN200 pipe ( $D=195.3$  mm), a high-quality database (test series L12) was constructed at the TOPFLOW (Transient two Phase FLOW) test facility, of the Institute of Safety Research at the Helmholtz Zentrum Dresden Rossendorf [9]. This database is finally chosen for the test and validation of the new model in this work mainly based on three considerations.

Firstly, measurements of the bubble size distribution, the radial profiles of gas velocity and the gas volume fraction as well as the decomposition of radial gas

volume fractions according to bubble size are available for several height positions, e.g. for 1 mm inlet orifice data available for 12 height positions (see Table 4.1). Secondly, an extensive range of flow conditions with superficial gas velocity from 0.0625 m/s to 3.185 m/s and superficial water velocity from 0.0405 m/s to 1.611 m/s is covered in the measurement as indicated in Table 4.2. Finally, the quality and plausibility of the measured data was checked extensively. The measured bubble size distribution, radial gas velocity and volume fraction profiles for different heights were compared to each other for all test matrix points.

As a result, a clear and consistent trend regarding their evolution with increasing L/D and superficial gas velocity was found, as depicted in Figure 4.11. In contrast to this test series, discrepancies or inconsistent trends could be found in some published databases as well as the previous measurement series of TOPFLOW. Furthermore, superficial gas velocities have been reconstructed from the measured radial gas volume fraction and velocity profiles. A good agreement with the setting values could be obtained. The evolution of the time and cross-sectional averaged total gas volume fraction along the pipe height was checked with theoretical values predicted by the drift velocity model. As a result the trend along the pipe height is well reflected by the experimental data. In addition, the measurement temperature of the two-phase mixture was kept constant 30°C and the variance is below 1K. This is important for the validation of models for bubble coalescence and breakup because these processes sensitively depend on the temperature due to its effect on surface tension.

### **4.4.2 TOPFLOW air-water experiment in a vertical pipe**

#### **Test facility**

The construction and function of the TOPFLOW facility are described in detail by Schaffrath et al. [171] and Beyer et al. [172]. For this reason, here only the information of the L12 test series that is relevant to the execution of model validation in this work is considered.

To obtain the evolution of the flow along the pipe, a so-called variable gas injection was used. Figure 4.6 shows the geometrical construction of the injection system with six modules which are almost logarithmically distributed over the pipe height. This is because the change of the flow structure, which is mainly caused by the radial redistribution of the gaseous phase, occurs mostly close to the gas injection. Each module (see Figure 4.7) consists of three chambers. In order to analyze the influence of different initial bubble diameters on the development of the flow, the uppermost and the lowest injection chambers are provided with 72x1 mm orifices while the middle chambers have 32x4 mm orifices.

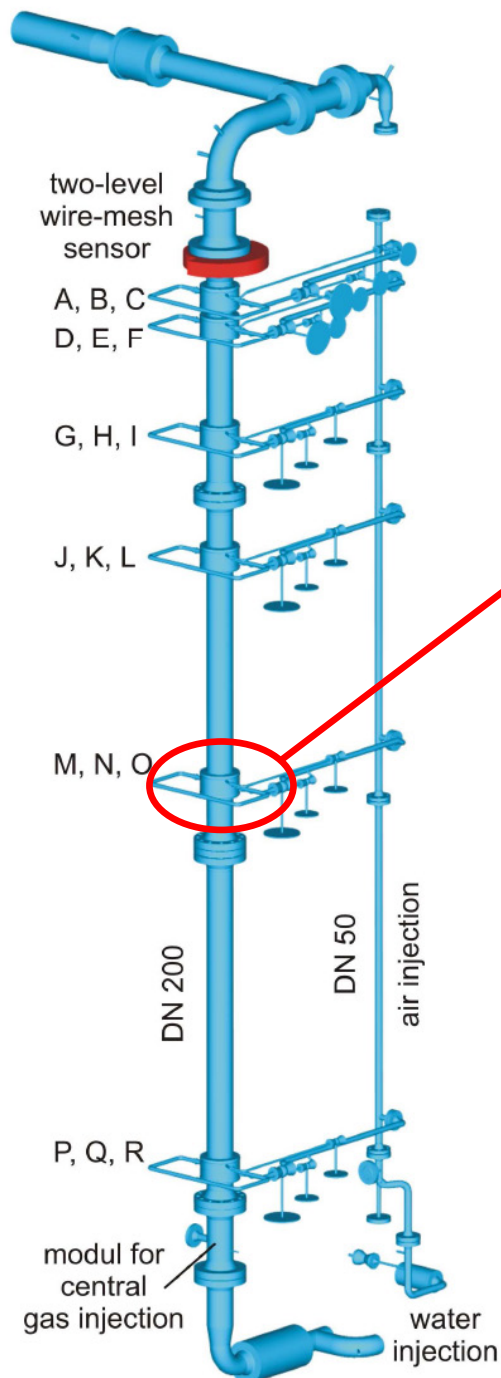


Figure 4.6 Vertical test section of TOPFLOW facility

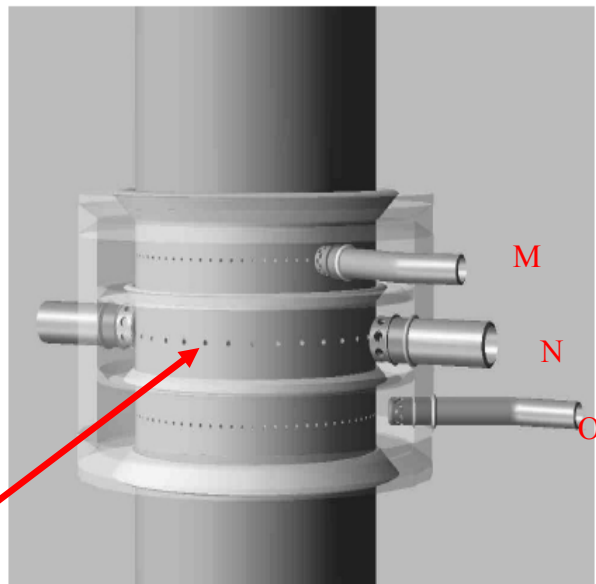


Figure 4.7 Injection module of the variable gas injection

For rotation-symmetric gas injection, all orifices per chamber are equally distributed over the circumference of the pipe. Gas is injected into the pipe through the orifices at the wall. This gas injection offers the advantage that the two-phase flow can smoothly rise up to the measurement plane without being influenced by the feeder within the pipe in other height positions. The supply of the liquid phase is done from the bottom of the test section by means of an isolating valve and a 90° bend. As shown in Figure 4.6, for these experiments, the measurement plane is always situated at the upper end of the test section, where a two level low temperature wire-mesh sensor is used.

Table 4.1 lists the vertical distances between the individual gas injection chamber and the first measurement plane of the wire-mesh sensor located in the flow direction. The experimental data achieved by using 1 mm inlet orifices at different height positions, which are highlighted by bright turquoise, are used in this work.

Table 4.1 Absolute and relative height of injection chambers

injection chamber	position of height	diameter of the inlet orifice [mm]	injection length [m]	L/D ratio
1	A	1	0.221	1.1
1	B	4	0.278	1.4
1	C	1	0.335	1.7
2	D	1	0.494	2.5
2	E	4	0.551	2.8
2	F	1	0.608	3.1
3	G	1	1.438	7.4
3	H	4	1.495	7.7
3	I	1	1.552	7.9
4	J	1	2.481	12.7
4	K	4	2.538	13.0
4	L	1	2.595	13.3
5	M	1	4.417	22.6
5	N	4	4.474	22.9
5	O	1	4.531	23.2
6	P	1	7.688	39.4
6	Q	4	7.745	39.7
6	R	1	7.802	39.9

### **Measurement matrix**

In order to simplify the comparison of individual measurements with each other, a general test matrix was used for all test series of the vertical test section at TOPFLOW facility. Table 4.2 shows the HZDR –Matrix composed of 231 test points. Each matrix point characterizes a combination of superficial velocities for the liquid and gaseous phase. The range of superficial velocities was divided logarithmically and is increased to approximately 4m/s for the liquid phase and to 19m/s for the gaseous phase. The measurement points selected for the present test series are color highlighted in Table 4.2 and different colours indicate different flow regimes such as bubbly flow, churn-turbulent flow and annular flow. They can be grouped in four lines at which the superficial velocity of the liquid or gaseous phase remains constant, respectively. This selection has the advantage that the flow phenomena are only dependent on one variable parameter, which can be evaluated regarding its effect on the flow properties. For investigations on the development of the two-phase flow over the height of the test section, all levels (A-R) shown in Table 4.1 or Figure 4.6 were measured for any point of series <149, respectively. For test points  $\geq 149$ , both injection chambers with 1 mm orifices or 4 mm of injections have to be used to reach the prescribed gas flow rate.

The results of the current test series cover a broad range of flow regimes such as bubbly, churn-turbulent and annular flow. While in the left range of the matrix, the bubbly flow prevails at rather low superficial gas velocity  $J_g$ , the churn-turbulent flow emerges increasingly in the middle and the right range and exclusively at the right edge of the matrix annular flow occurs. For the measurement points 094-107 and 117-119, flow pattern transitions are observed along the bubble height. Thus, the flow pattern changes from bubbly flow at  $L/D=1.1$  into churn-turbulent flow at

L/D=39.9. This is valuable for the validation of new model for bubble coalescence and breakup since they are relevant mechanisms responsible for such a transition.

The circled test points are selected in this work, which covers bubbly flow and churn-turbulent flow as well as the transition range. This is sufficient for the purpose of testing the new model for bubble coalescence and breakup.

Table 4.2 General experimental matrix of HZDR for vertical pipe flows

		Superficial gas velocity $J_G$ [ m/s ]																				
		0.0025	0.0040	0.0062	0.0096	0.0151	0.0235	0.0368	0.0574	0.0898	0.140	0.219	0.342	0.534	0.835	1.305	2.038	3.185	4.975	7.772	12.14	18.97
Superficial water velocity $J_L$ [ m/s ]	4.047	011	022	033	044	055	066	077	088	099	110	121	132	143	154	165	176	187	198	209	220	231
	2.554	010	021	032	043	054	065	076	087	098	109	120	131	142	153	164	175	186	197	208	219	230
	1.611	009	020	031	042	053	064	075	086	097	108	119	130	141	152	163	174	185	196	207	218	229
	1.017	008	019	030	041	052	063	074	085	096	107	118	129	140	151	162	173	184	195	206	217	228
	0.641	007	018	029	040	051	062	073	084	095	106	117	128	139	150	161	172	183	194	205	216	227
	0.405	006	017	028	039	050	061	072	083	094	105	116	127	138	149	160	171	182	193	204	215	226
	0.255	005	016	027	038	049	060	071	082	093	104	115	126	137	148	159	170	181	192	203	214	225
	0.161	004	015	026	037	048	059	070	081	092	103	114	125	136	147	158	169	180	191	202	213	224
	0.102	003	014	025	036	047	058	069	080	091	102	113	124	135	146	157	168	179	190	201	212	223
	0.0641	002	013	024	035	046	057	068	079	090	101	112	123	134	145	156	167	178	189	200	211	222
	0.0405	001	012	023	034	045	056	067	078	089	100	111	122	133	144	155	166	177	188	199	210	221

bubbly flow
churn-turbulent flow
annular flow

### Examples of the results

The evolution of some characteristic parameters of the upward air-water flow along the pipe height is shown below in Figure 4.8 ~ Figure 4.11. It includes the evolution of gas volume fraction, gas velocity and bubble size distribution from L/D=1.1 to 39.9, gas volume fraction decomposed according to the bubble size, and the evolution of the average bubble size and Sauter mean bubble diameter of different test points in the axial direction. As the gaseous bubbles migrate from the pipe wall ( $r=100$  mm) to the pipe center ( $r=0$  mm). The radial profile of gas volume fraction and gas velocity changes stably from a wall-peak to a core-peak (see Figure 4.8). However, for all test points bubbles smaller than 6 mm keep still a wall-peak due to the effect of lift force (see Figure 4.9). For the example of test point 118, the evolution of bubble size distribution from L/D=1.1 to 39.9 is typically bi-directional. The bubble size range at L/D=1.1 is between 0 ~ 60 mm, however, both large and small bubbles are generated by coalescence and breakup as the gas-liquid mixture flows along the pipe (see Figure 4.8). As shown in Figure 4.10, the evolution of the average bubble size along the pipe exhibits a consistent dependence on the superficial gas velocity. It can be seen that for test points 008 ~ 063, the average bubble size increases almost linearly in the axial direction but the increasing rate decreases as the superficial gas velocity increases. From test point 074 on, the evolution of average bubble size is characterized by a breakup trend along the whole pipe height except for a small increase at the beginning. However, as the superficial gas velocity increases further, e.g. test points 118 ~ 140, the breakup trend is again overtaken by the coalescence one at the upper half of the pipe due to the effect wake-entrainment.

The tendency of the Sauter mean diameter evolving along the pipe is similar to that of the average size except that it is smaller especially for those test points with high superficial gas velocities. This difference is mainly caused by the definitions of the average bubble size  $\bar{d}$  and the Sauter mean diameter  $d_{SM}$  (see the nomenclature).

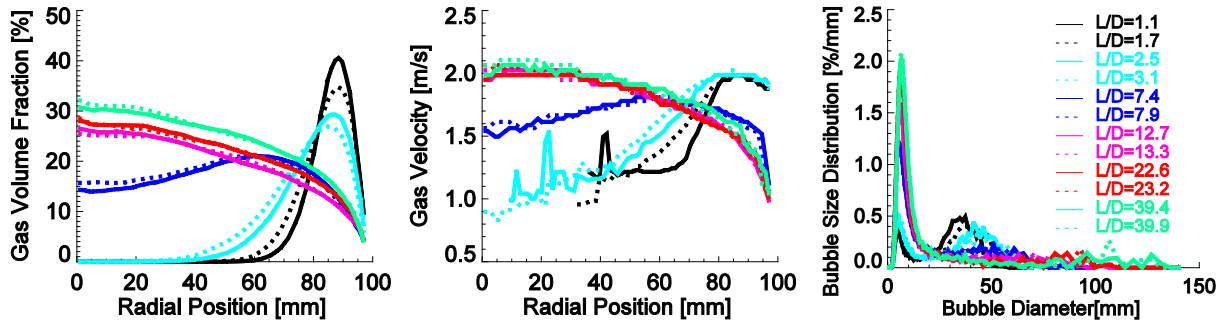


Figure 4.8 Gas volume fraction, gas velocity and bubble size distribution (TP118)

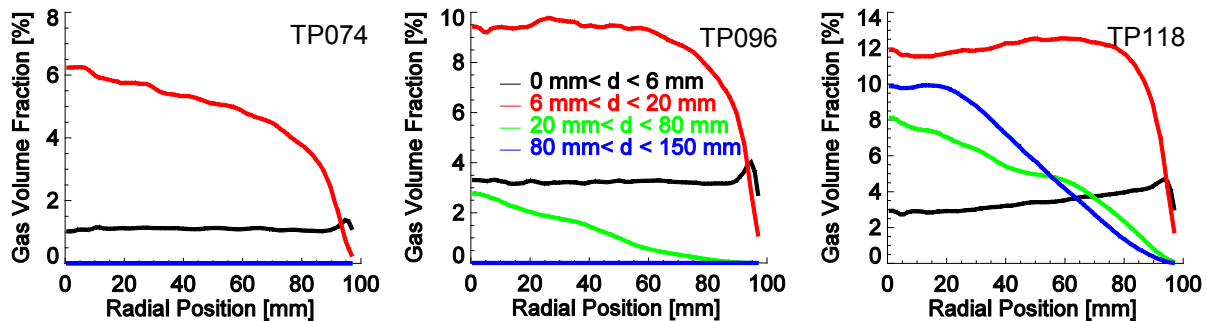


Figure 4.9 Radial profile for gas volume fraction in different size range (Level R)

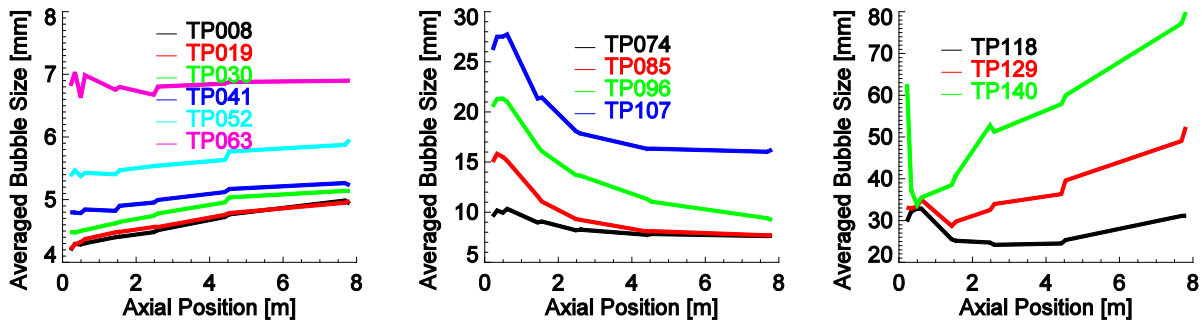


Figure 4.10 Average bubble size of different test points in the axial direction

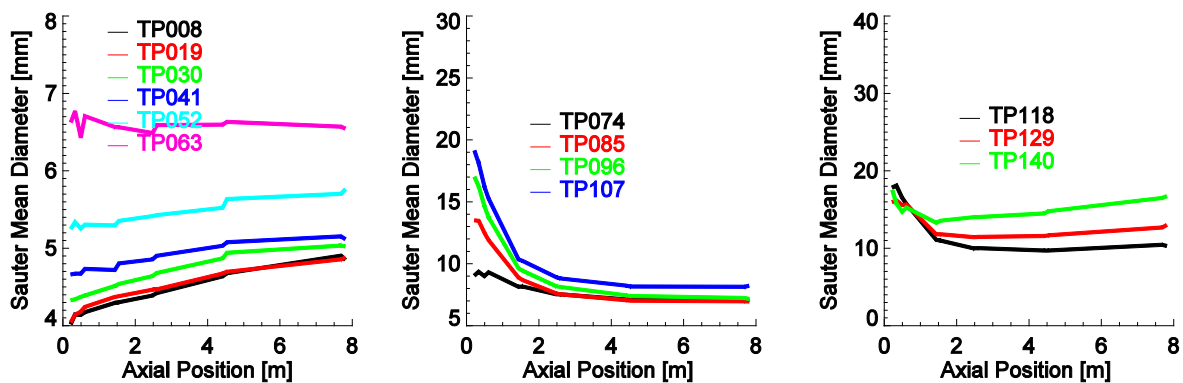


Figure 4.11 Sauter mean diameter of different test points in the axial direction

## 5 Validation of the new model in frame of Test Solver

The new model proposed for bubble coalescence and breakup is extensively tested in the Test Solver, which is at first extended and verified using the CFD code ANSYS CFX.

### 5.1 Extensions of the Test Solver

The original version of the Test Solver proposed by Lucas [2] is extended regarding the calculation of turbulence parameters, cross-sectional averaged gas volume fraction and gas velocity.

#### 5.1.1 Turbulence modeling

Turbulence modeling is one of the important parts in the Test Solver, which provides input parameters for the calculation of bubble coalescence and breakup rates as well as the turbulence dispersion force. In order to investigate the influence of turbulence modeling on the performance of models for bubble coalescence and breakup, it is extended from a one-equation model to a two-equation model including additional BIT source terms. The two-equation k- $\varepsilon$  model is given by Eq. 4-21 and Eq. 4-22 and the BIT source terms described in Eq. 4-27 ~ Eq. 4-34.

In the original version of Test Solver, only one transport equation is solved for the turbulent kinetic energy k. By neglecting the effect of molecular viscosity  $\mu_l$  of the liquid phase and the BIT source production, Eq. 4-21 becomes:

$$\frac{\partial}{\partial t}(\alpha_l \rho_l k) + \nabla \cdot (\alpha_l \rho_l u_l k) = \nabla \cdot \left[ \alpha_l \left( \frac{\mu_t'}{\sigma_k} \right) \nabla k \right] + \alpha_l (P_k - \rho_l \varepsilon) \quad \text{Eq. 5-1}$$

Under steady-state conditions, by considering only the radial dependence of all properties, Eq. 5-1 can be further simplified as:

$$\left( \frac{\mu_t'}{\sigma_k} \right) \frac{d^2(k)}{dr^2} + \left( \frac{1}{\sigma_k} \frac{d\mu_t'}{dr} + \frac{\mu_t'}{\sigma_k} \frac{1}{r} \right) \frac{dk}{dr} - \varepsilon + (\mu_t + \mu_b) \left( \frac{du_l}{dr} \right)^2 = 0 \quad \text{Eq. 5-2}$$

where the shear-induced  $\mu_t$  and the BIT viscosity  $\mu_b$  calculated according to the correlations proposed by Sato [8]

$$\mu_t = \left[ 1 - \exp\left(-\frac{y^+}{A^+}\right) \right]^2 \left[ 1 - \frac{11}{6} \left( \frac{y^+}{R^+} \right) + \frac{4}{3} \left( \frac{y^+}{R^+} \right)^2 - \frac{1}{3} \left( \frac{y^+}{R^+} \right)^3 \right] \mu_l k y^+ \quad \text{Eq. 5-3}$$

$$\mu_b = \left[ 1 - \exp\left(-\frac{y^+}{A^+}\right) \right]^2 0.6 \rho_l \sum_i \alpha_g(r, d_i) d_i u_{ri} \quad \text{Eq. 5-4}$$

where,  $y^+$ ,  $R^+$  are the dimensionless pipe radius and distance from the wall, and  $A^+=16$ ,  $k=0.4$ . Note that Eq. 5-4 is an extension of the original model in Eq. 4-19 to consider the case having multi bubble size classes.

Finally, the turbulence dissipation rate  $\varepsilon$  is calculated inversely from the well-known relation in the two-equation turbulence model:

$$\mu_t' = C_\mu \rho_l \frac{k^2}{\varepsilon} \quad \text{Eq. 5-5}$$

The plots in Figure 5.1 show the predictions of the turbulent kinetic energy, turbulence dissipation rate, eddy kinematic viscosity as well as liquid velocity profile obtained by using the one- and two-equation model, respectively. The results show that the viscosity given by Eq. 5-3 and Eq. 5-4 is in general too low at the pipe center, which is unreasonable and will cause flow instability due to the imbalance between the lift force and turbulence dispersion force (see test point 074, i.e. the plots in the third column of Figure 5.1). Furthermore, according to Eq. 5-1 the additional viscosity term is insufficient to consider the BIT energy production at the pipe center while overestimate the BIT in the high shear rate region, e.g. near the wall. Therefore, the two-equation model is adopted in this work. The BIT source model proposed by Politano [158] is used here in order to compare the performance of the two-equation model with that of the one-equation model. The influence of BIT source models is discussed in detail in the section §5.4.12.

It can be seen in Figure 5.1 that the two-equation model with additional source terms has achieved considerable improvement in contrast to the one-equation model. At low gas volume fractions, e.g. test point 019, the effect of turbulence damping can only be reproduced by the  $k$ - $\varepsilon$  two-equation model. In this case, a lot of small bubbles are accumulated near the pipe wall and thus smoothes the liquid velocity profile. Therefore, the shear production of turbulent kinetic energy  $P_k$  decreases, and at the same time BIT source  $\phi_k$  is negligible for this case. As a result, gas bubbles have an effect of suppressing the liquid turbulence. On the other hand, as superficial gas velocity increases, large bubbles formed near the gas injection at the pipe wall will increase the liquid velocity there so much that the velocity gradient changes from negative to positive. Afterwards, bubbles migrate rapidly to the pipe center and the velocity gradient changes again from positive via zero to negative. As a result, both shear-induced and BIT turbulence increase due to large bubble size and large liquid velocity gradients.

Generally, in comparison to the two-equation model, the one-equation model predicts too large a value for the turbulence parameters in the wall region while too small a kinetic energy and eddy viscosity at the pipe centre. A smaller eddy viscosity means that the turbulent dispersion force is too low. When large bubbles ( $d > 5.8$  mm) move towards the pipe centre under the effect of lift force, the turbulent dispersion force may be not large enough to disperse the bubbles away from the pipe centre. Since the lift force is proportional to the liquid velocity gradient, a positive feedback between the liquid velocity gradient, radial gas volume fraction profile and lift force will occur as it drives large bubbles to the pipe centre. In the one-equation model, the viscosity predicted by Eq. 5-3 and Eq. 5-4 is too low at the pipe center. Therefore, the positive feedback phenomenon is more serious than the case of two-equation model. As a result, the calculation will diverge due to the unreasonable accumulation of large bubbles at the pipe centre, e.g. test point 074 in Figure 5.1. On the other hand, as observed in the experiment, according to the two-equation model the increase of the liquid velocity at Level A caused by bubble injection will reduce liquid

---



velocity gradient or change it to be positive. This will keep the large bubbles near the wall and retard the migration of the whole gaseous phase to the pipe center (see the first and second columns in Figure 5.1).

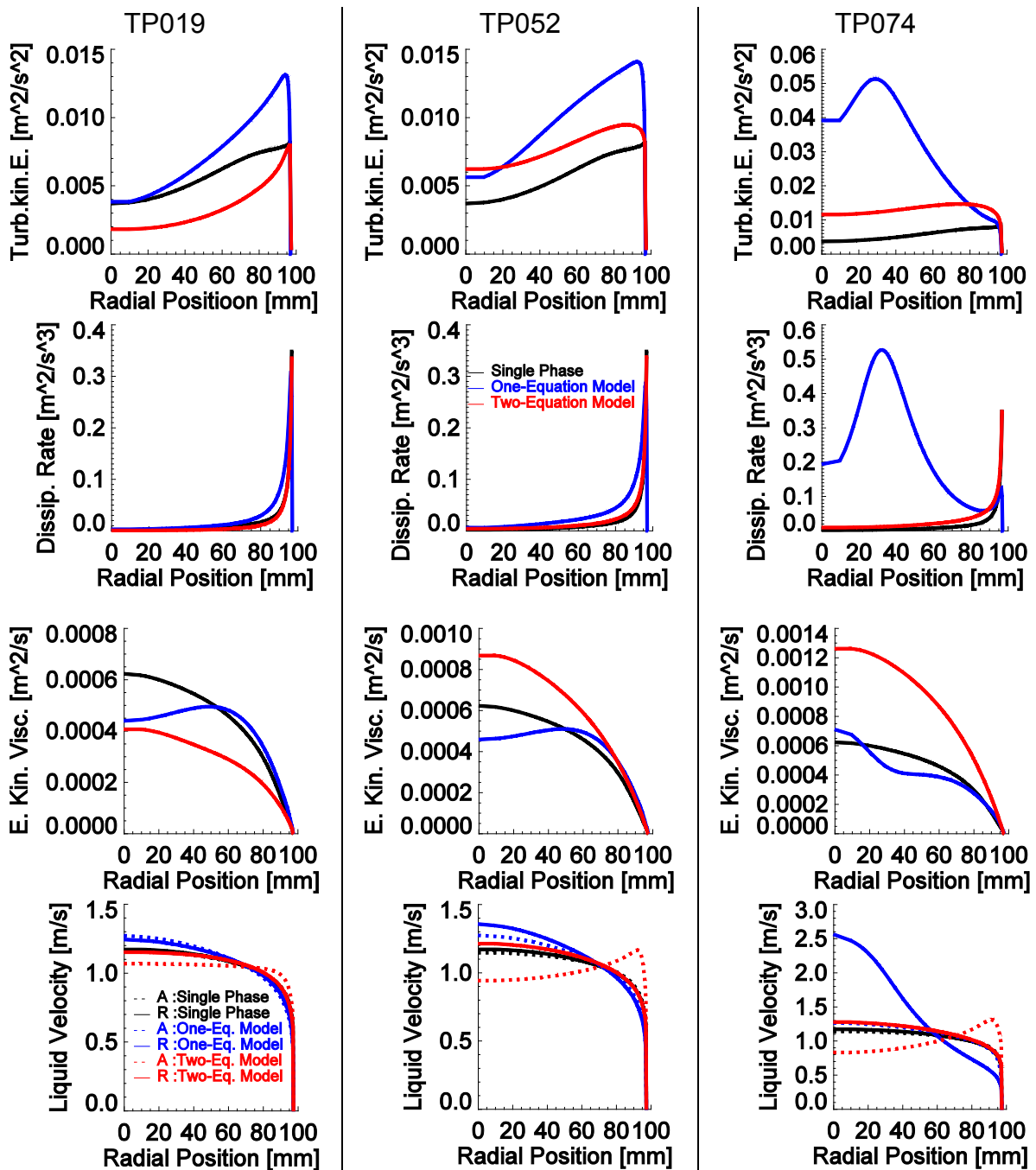


Figure 5.1 Performance of one-equation model and two-equation model with BIT source term (Level R)

Furthermore, the instability effect of the transverse lift force on the radial gas volume fraction profile of test point 074 is illustrated in Figure 5.2. Calculations are done respectively with and without lift force by the one-equation model. It can be seen that in the case without lift force the gaseous phase redistributes stably over the cross section of the pipe under the smoothing effect of turbulent dispersion force. As a result, a smooth profile of gas volume fraction is obtained at Level R and the

unreasonable accumulation of bubbles does not appear at the pipe centre, which is consistent with the experimental observation. In other words, if the one-equation model is used for the calculation of turbulence parameters, lift force calculated by Tomiyama model [151] is too large to deliver a reasonable gas volume fraction profile for this test point.

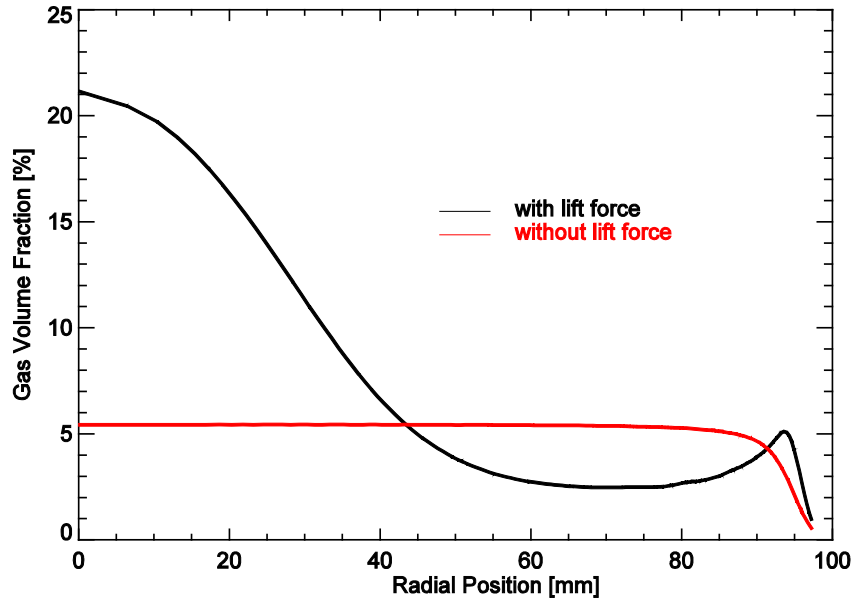


Figure 5.2 Instability effect of radial gas volume fraction profile caused by lift force (TP074, Level R)

### 5.1.2 Cross-sectional averaged gas void fraction

As mentioned in the previous chapter, in order to maintain the simplicity of the Test Solver, it does not resolve the variables over the height of the pipe. Instead, a vertical gas rise velocity that is equal for all bubble size classes and radial positions is assumed.

In the old version of the Test Solver, the cross-sectional averaged void fraction at a certain height position is determined solely by considering the pressure expansion along the pipe. For example, the two-phase mixture flows along the pipe from the height position 1 to position 2, the new total void fraction at position 2 is calculated from:

$$\alpha_{g,2} = \alpha_{g,1} \frac{p_1}{p_2} \quad \text{Eq. 5-6}$$

where  $p_1$ ,  $p_2$  is the absolute pressure at position 1 and 2, respectively.

In order to take into account the influence of relative motion between the gaseous and liquid phase, in this work the drift velocity correlation is used for the calculation of total void fraction along the pipe:

$$\alpha_g = \frac{J_g}{J_g + J_l + u_D} \quad \text{Eq. 5-7}$$

where  $J_g$  and  $J_l$  are the cross-sectional averaged gas and liquid superficial velocities, respectively.

The cross-sectional averaged drift velocity  $u_D$  is calculated according to:

$$u_D = \bar{u}_g - J = (C_0 - 1)J + \bar{u}_{Gl} \quad \text{Eq. 5-8}$$

where  $C_0$  and  $\bar{u}_{Gl}$  is distribution parameter and void-fraction-weighted mean drift velocity, respectively:

$$C_0 = \frac{2}{\langle \alpha_g(r) \rangle R^2 J} \int_0^R j(r) \alpha_g(r) r dr \quad \text{Eq. 5-9}$$

$$\bar{u}_{Gl} = \frac{2}{\langle \alpha_g(r) \rangle R^2} \int_0^R \sum_i u_{D,local}(d_i, r) \alpha_g(r, d_i) r dr \quad \text{Eq. 5-10}$$

where the radial gas volume fraction  $\alpha_g(r)$  and volume fraction of each size group  $\alpha_g(r, d_i)$  can be obtained from the solution of mass conservative equation for each bubble size class.

In addition, for the calculation of  $C_0$  and  $\bar{u}_{Gl}$ , the superficial velocity of the two-phase mixture,  $j(r)$ , and the local drift velocity of the bubble class  $i$ ,  $u_{D,local}(d_i, r)$ , have to be determined:

$$j(r) = u_l(r) [1 - \alpha_g(r)] + u_g(r) \alpha_g(r) \quad \text{Eq. 5-11}$$

$$u_{D,local}(d_i, r) = [1 - \alpha_g(r)] \cdot u_{ri} \cdot f_{swarm}(r) \quad \text{Eq. 5-12}$$

where the swarm factor  $f_{swarm}(r)$  is set to 1.0 in this work. The calculation of radial gas and liquid velocity profiles  $u_l(r)$  and  $u_g(r)$  is given in next section.

The evolution of total void fraction along the pipe height predicted respectively by the old and new methods is illustrated in Figure 5.3.

From the experimental data, one can see that in the case of small superficial gas velocities, for example, test points 019, 042, 063, higher gas fraction values are observed for low pipe heights compared to the linear trend due to decreasing pressure. On the other hand, in the case of large gas fractions, for example, matrix points 096, 107, 129, smaller gas fractions are observed at low pipe heights. This phenomenon of the increase or decrease in gas fractions results from the effect of wall injection of bubbles on the liquid velocity profile.

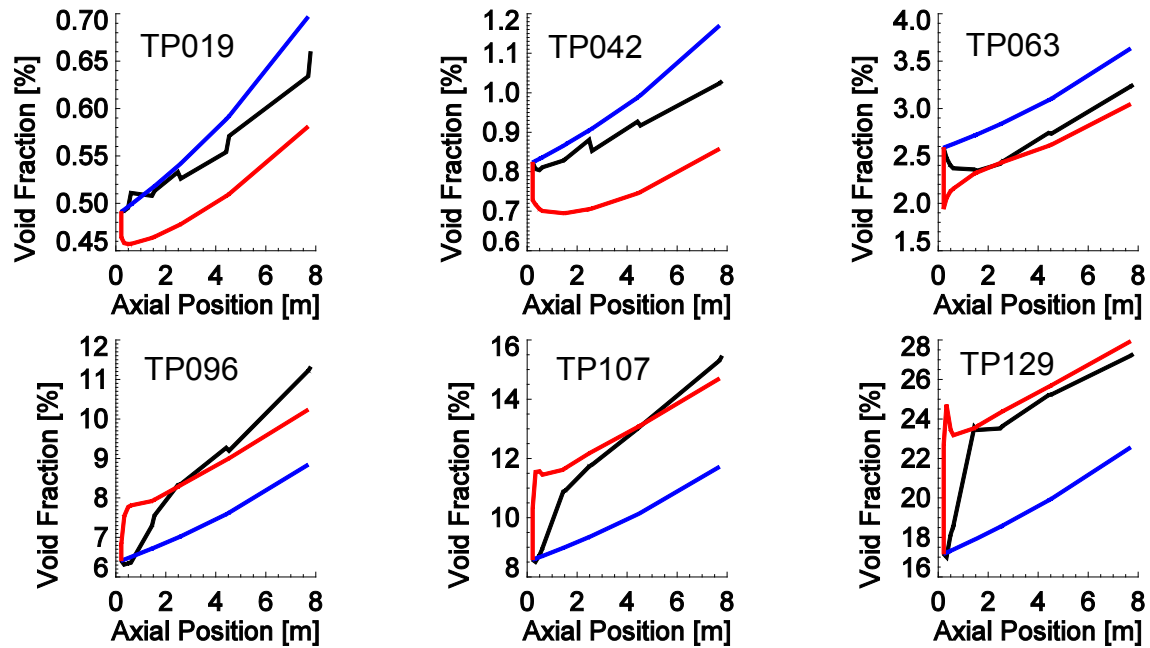


Figure 5.3 Improvement of the prediction of total gas void fraction by the extended model (black line: measurement; blue line: old method; red line: new method)

For the case of small superficial gas velocity or large superficial liquid velocity, small bubbles injected from the pipe wall will smooth the liquid velocity profile, which results in a decrease of the profile parameter  $C_0$  and the average drift velocity  $u_D$ . As the gas-liquid mixture flows along the pipe, the influence of the gas injection disappears quickly and the liquid velocity gradient increases again. That means that the profile parameter  $C_0$  and drift velocity  $u_D$  will be higher than that at the injection position. Therefore, the predicted gas void fraction according to Eq. 5-7 will be higher near the injection position. On the other hand, as the superficial gas velocity increases, the large bubbles injected from the wall will obviously accelerate the liquid phase near the injection. As a result, the liquid velocity gradient is very large but positive at the injection position, which results in a large profile parameter  $C_0$  and drift velocity  $u_D$  according to Eq. 5-9. Therefore, the total void fraction is low at the injection position and then increases as bubbles migrate away from the injection position. As the two-phase mixture flows along the pipe, the liquid velocity profile changes from a wall-peak to a core-peak, and as a result the profile parameter  $C_0$  decreases.

### 5.1.3 Cross-sectional averaged gas velocity

In the Test Solver, the average gas rise velocity is originally calculated by adding the mean liquid velocity  $\bar{u}_l$  with a average relative velocity  $\bar{u}_{rel}$ :

$$\bar{u}_g = \bar{u}_l + \bar{u}_{rel} \quad \text{Eq. 5-13}$$

where  $\bar{u}_l$  and  $\bar{u}_{rel}$  is given by,

$$u_l = \frac{J_l}{1 - \alpha_g} \quad \text{Eq. 5-14}$$

where  $\alpha_g$  is the cross-sectional averaged void fraction.

$$\bar{u}_{rel} = \frac{\sum_i \int_0^R u_{ri} \cdot f_{swarm}(r) r dr \cdot \alpha_g(d_i) \Delta d_i}{\sum_i \alpha_g(d_i) \Delta d_i} \quad \text{Eq. 5-15}$$

In this work, the radial gas velocity  $u_g(r)$  is first calculated from the radial liquid velocity  $u_l(r)$  and the relative velocity  $u_{rel}(r)$ , given by:

$$u_g(r) = u_l(r) + u_{rel}(r) \quad \text{Eq. 5-16}$$

where the radial profile of liquid velocity is calculated according to Eq. 4-35, Eq. 4-36 and Eq. 4-43.

The relative velocity  $u_{rel}$  between the gas and liquid phase in Eq. 5-16 is calculated by averaging the bubble terminal rise velocity of all size classes if the gas volume fraction at the given radial position  $r$  is not zero:

$$u_{rel}(r) = \frac{f_{swarm}(r)}{\alpha_g(r)} \sum_i [\alpha_g(d_i, r) \cdot u_{ri}] \quad \text{Eq. 5-17}$$

Finally, the average velocity of the gaseous phase in the axial direction is calculated as:

$$\bar{u}_g = \frac{\int_0^R u_g(r) r dr}{\int_0^R r dr} = \frac{2}{R^2} \int_0^R u_g(r) r dr \quad \text{Eq. 5-18}$$

The cross-sectional averaged gas rise velocities for different test points calculated respectively by the old and the new method is depicted in Figure 5.4. According to the original method, the average gas velocity is calculated from the mean liquid velocity and the average relative velocity (see Eq. 5-7). This approach is not able to reflect the developing process of the gaseous phase from the injection position at the wall to the whole cross section of the pipe, since both the mean liquid velocity and the average relative velocity have no dependence on the radial position. Therefore, the predicted average gas rise velocity is almost constant over the whole pipe height. On the other hand, the new method calculates the gas rise velocity from the radial liquid velocity profile and the radial relative velocity profile. The increase of average gas rise velocity during the distribution process of the gaseous phase to the whole cross section can be captured well and it delivers a satisfactory agreement with the measurements. Since the average gas velocity determines the corresponding height position at a given time step, it is an important parameter for the prediction of the evolution of flow pattern along the pipe caused by bubble coalescence and breakup.

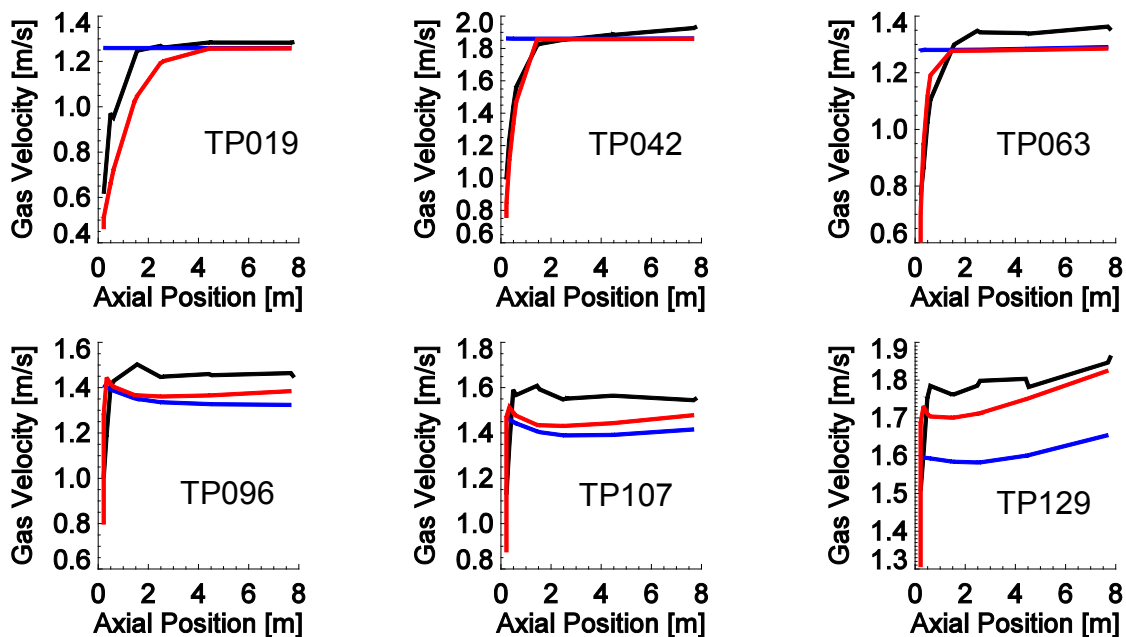


Figure 5.4 Improvement of the prediction for average gas rise velocity by the extended model (black line: experiment; blue line: old method; red line: new method)

From Figure 5.1 to Figure 5.4, one can see that the influence of gas injection on the gas and liquid velocity profile, cross-sectional averaged void fraction and gas rise velocity at low height positions can be well predicted by the extended Test Solver. The agreement with experimental data is considerably improved with comparison to the old version. Therefore, in this work, the extended Test Solver is used for the test of the new model for bubble coalescence and breakup.

## 5.2 Parameter study by using CFD results

Turbulence parameters and liquid velocity predicted by the Test Solver are compared with those by the CFD code CFX for two kinds of upward vertical pipe flows: single-phase (water) and two-phase (air-water). Note that for the two-phase case no models for bubble coalescence and breakup are included.

### 5.2.1 Single-phase flow

As shown below in Figure 5.5, for the case of single-phase flow, constant inlet conditions are given at Level A for turbulent kinetic energy, dissipation rate and liquid velocity, respectively.

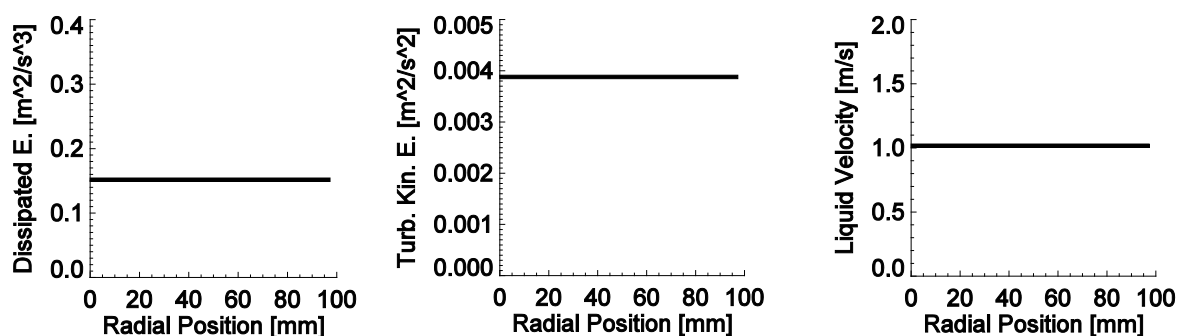


Figure 5.5 Inlet conditions for parameter study of single-phase flow

Predictions about the evolution of the flow along the pipe delivered by the Test Solver and by CFX are compared with each other. Turbulent kinetic energy, dissipation rate, eddy viscosity as well as velocity profile at different height levels are shown in Figure 5.6 ~ Figure 5.9, respectively.

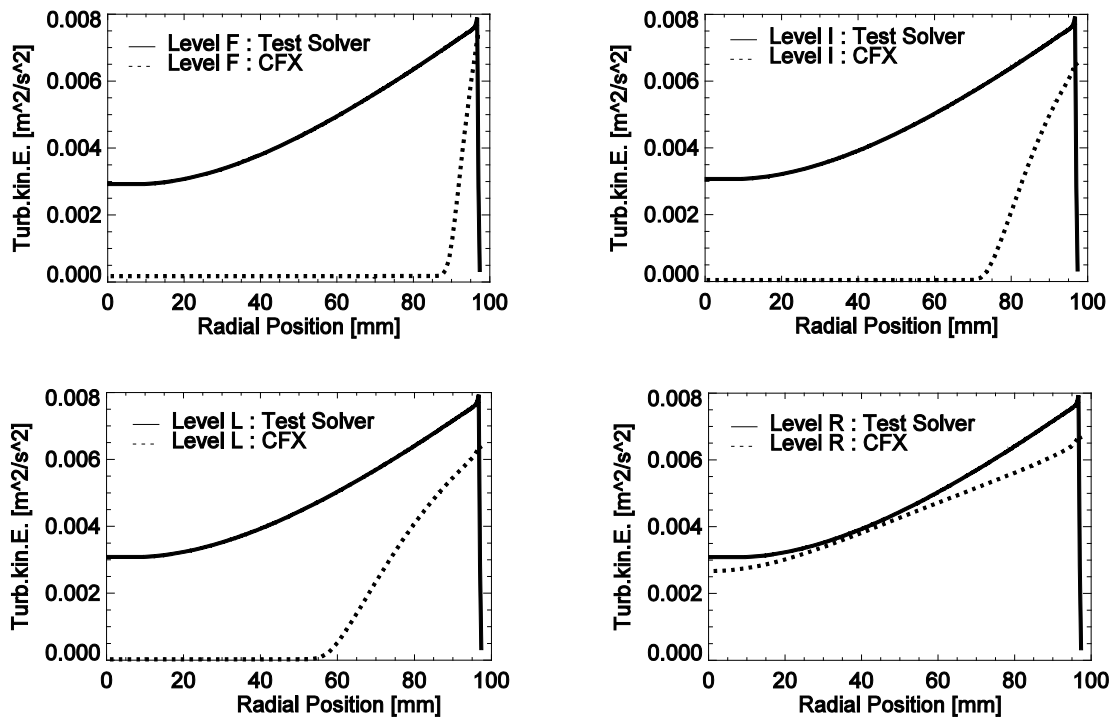


Figure 5.6 Turbulent kinetic energy predicted by Test Solver and CFX

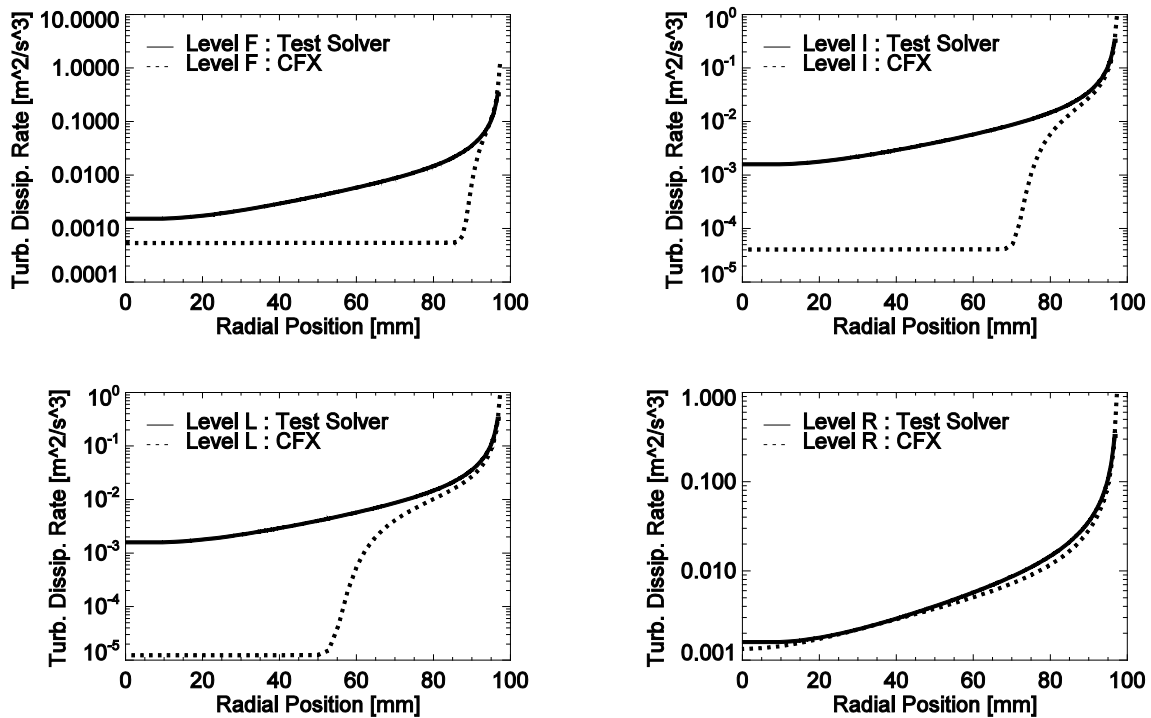


Figure 5.7 Dissipation rate predicted by Test Solver and CFX

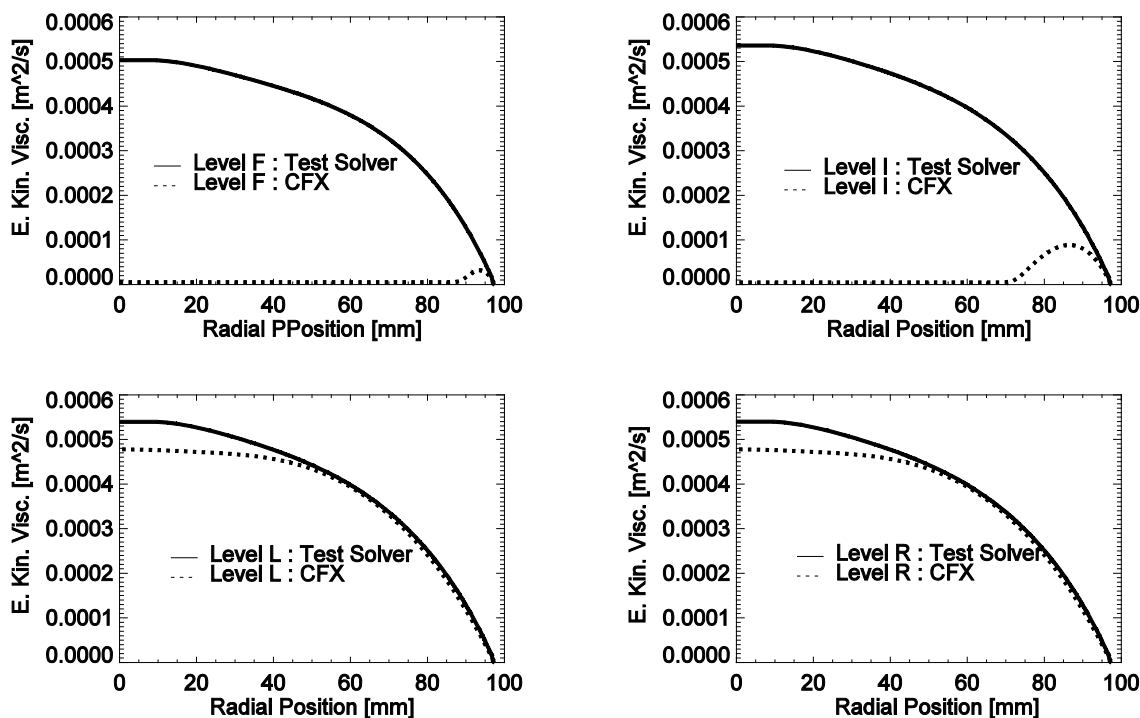


Figure 5.8 Eddy kinematic viscosity predicted by Test Solver and CFX

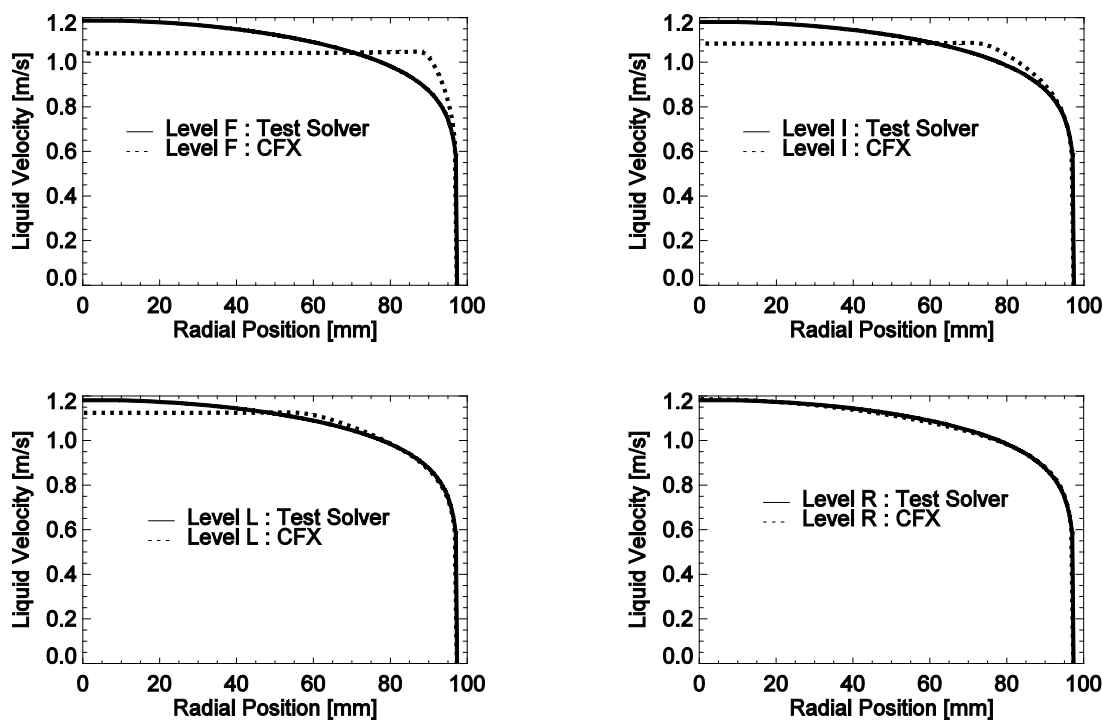


Figure 5.9 Velocity profile predicted by Test Solver and CFX

From the comparison between the predictions provided by the two solvers, considerable difference is to be observed during the development of the flow especially near the gas inlet. However, the agreement gets better as the flow becomes fully developed, e.g. at Level R, where the results achieved in the Test Solver are comparable to those in CFX. According to CFX, under constant inlet



conditions given at Level A, the velocity gradient develops first near the wall and as a result shear-induced turbulence is produced there. Then the development of both the velocity gradient and the turbulence propagates slowly to the pipe center. On the other hand, the flow develops almost immediately into a fully developed profile after the gas inlet according to the Test Solver although the given inlet profiles are constant. That means that the inlet conditions at Level A have marginal influence on the development of the flow downstream, which is quite questionable. The discrepancy might be caused by the inherent characteristics of the Test Solver such as no transport equations solved in the axial direction. Instead, the vertical liquid velocity is calculated by using the Sato [8] model in Eq. 4-35 and Eq. 4-36, which was originally developed for fully-developed flows. As a result, the developing process of liquid velocity profile and turbulence parameters from a constant profile to a fully-developed one can hardly be captured by the Test Solver.

## 5.2.2 Two-phase flow

For the parameter study of two-phase flow, the test point 118 is chosen as an example. The same inlet conditions are given at Level A for the Test Solver and CFX calculations. Inlet liquid turbulence parameters are determined by assuming a fully-developed single-phase flow with equal liquid volumetric flow rate, which is provided by CFX calculations. Inlet conditions for gas volume fraction and gas velocity profile are taken from measurement data. The liquid velocity is derived from the gas velocity by assuming a constant difference (see Figure 5.10), which has to conform the given liquid volumetric flow rate.

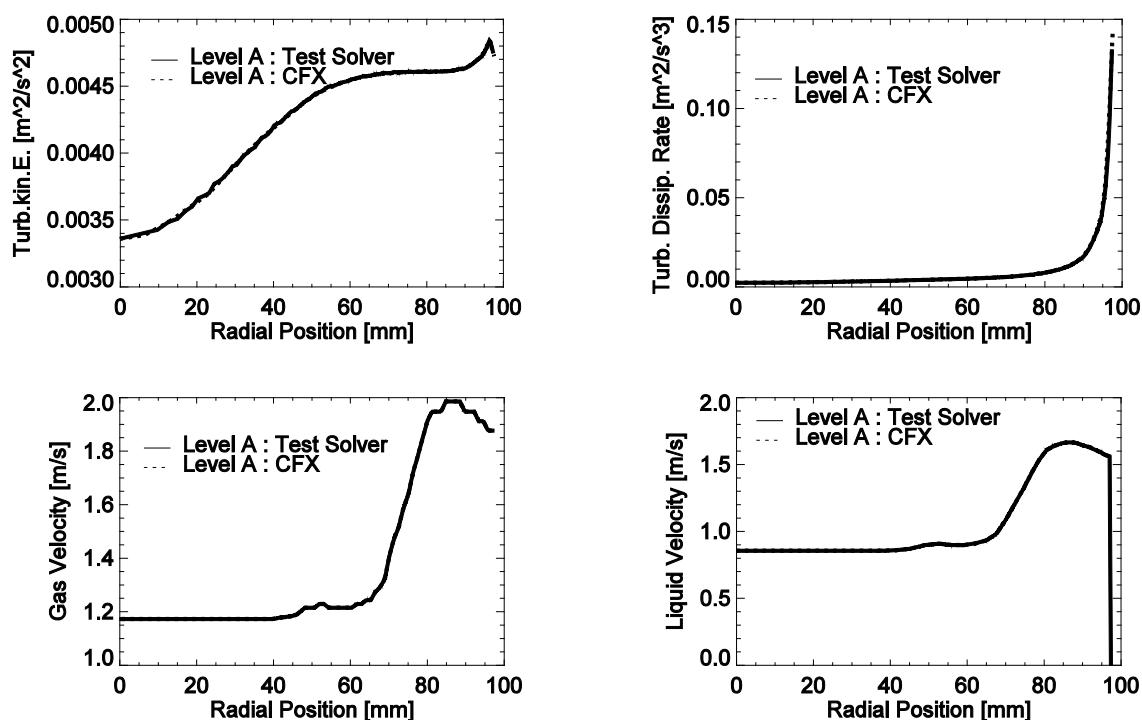


Figure 5.10 Inlet conditions for parameter study of two-phase flow

In order to test the performance of the  $k-\epsilon$  turbulence model in Test Solver, models for bubble coalescence and breakup as well as additional BIT source terms are excluded here. Comparison between the results obtained in the two solvers for

turbulent kinetic energy, dissipation rate, eddy kinematic viscosity as well as liquid eddy velocity are shown below in Figure 5.11 ~ Figure 5.14.

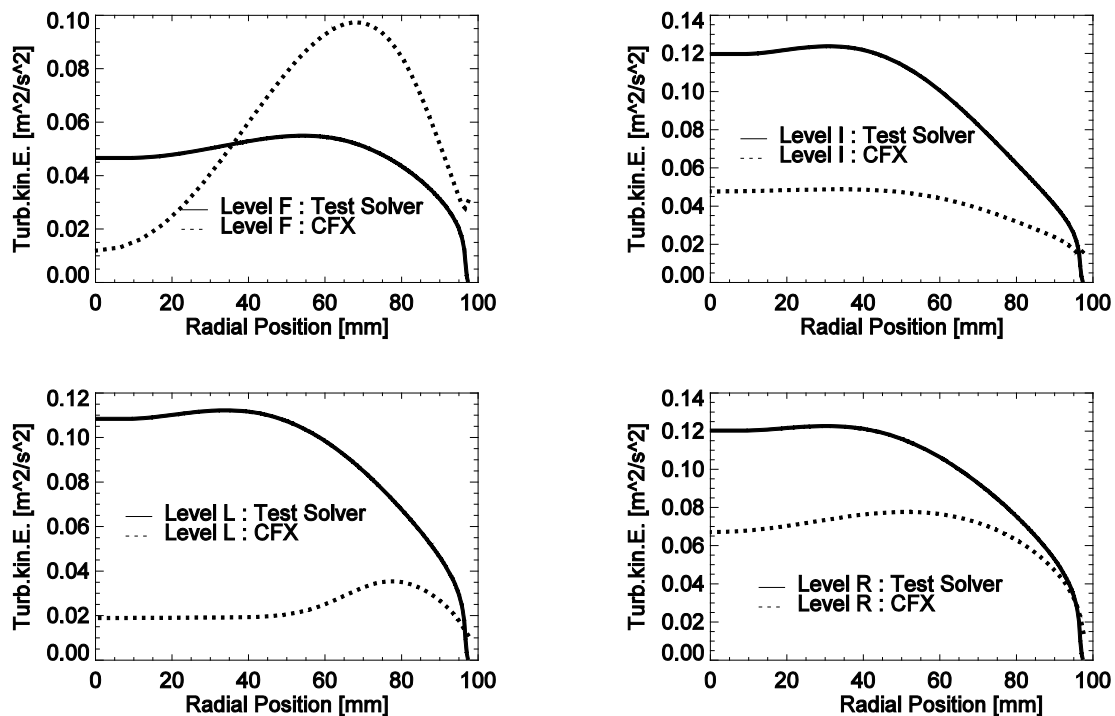


Figure 5.11 Turbulent kinetic energy predicted by Test Solver and CFX

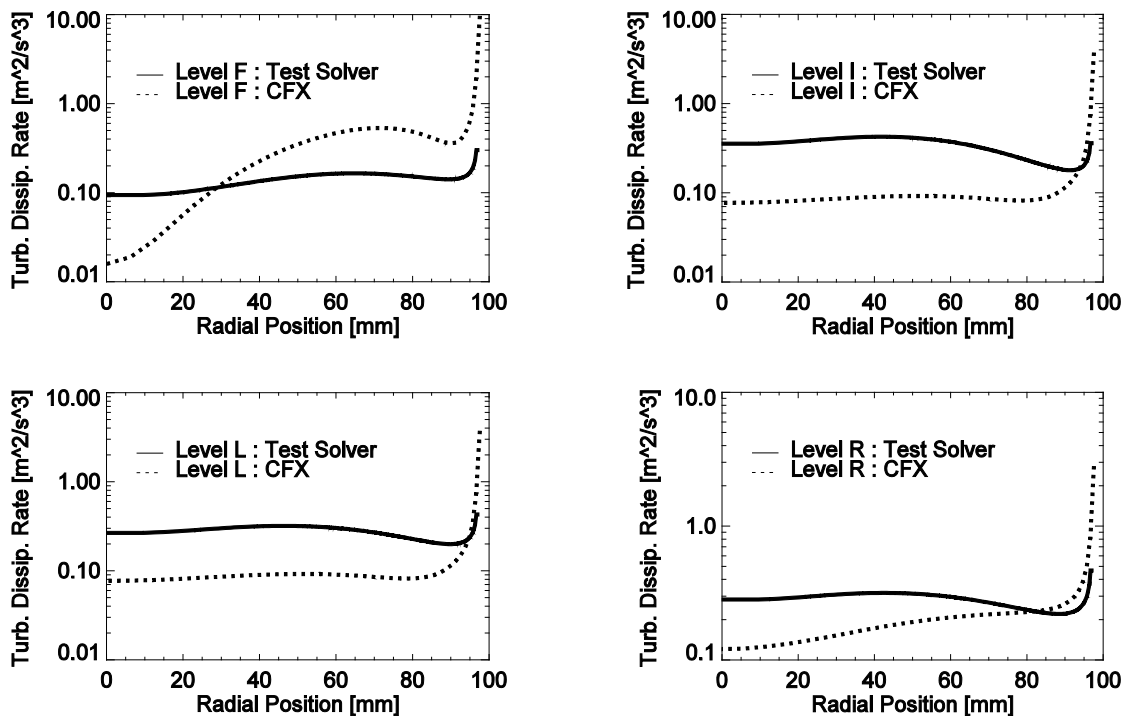


Figure 5.12 Dissipation rate predicted by Test Solver and CFX

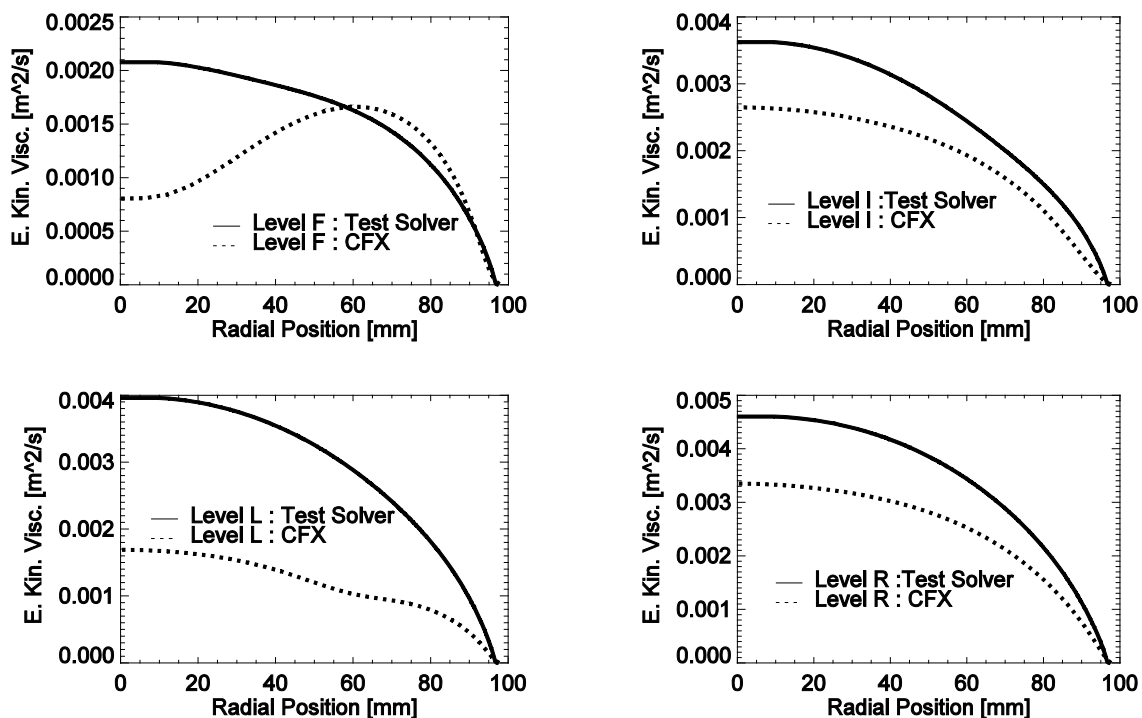


Figure 5.13 Eddy kinematic viscosity predicted by Test Solver and CFX

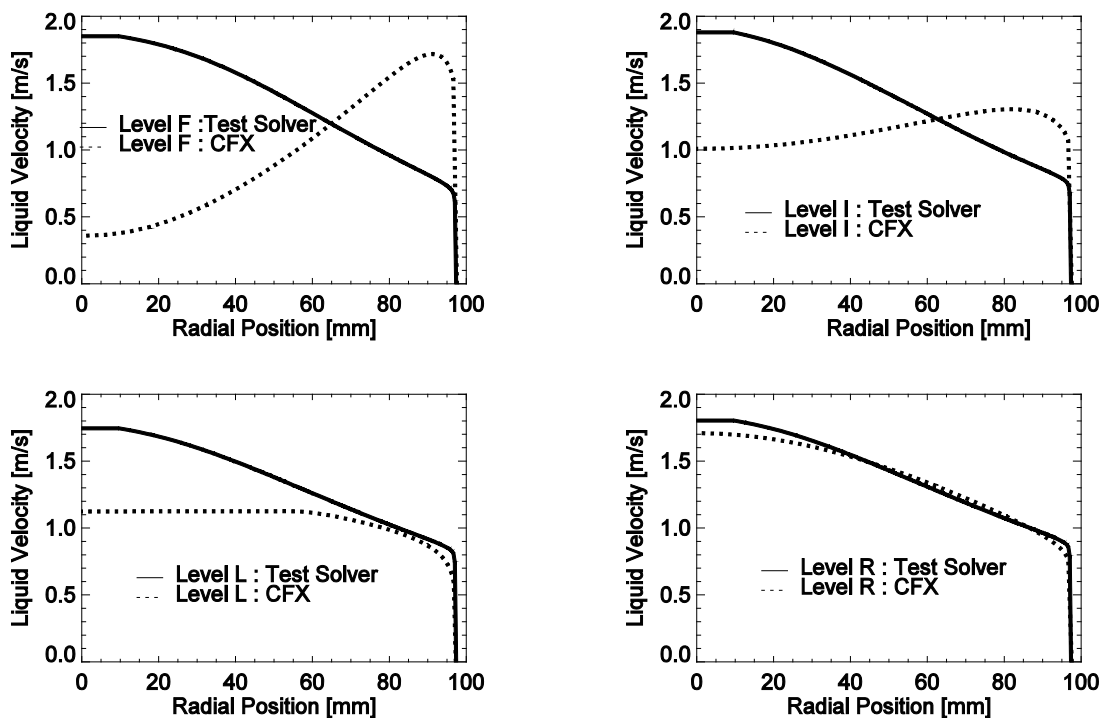


Figure 5.14 Liquid velocity profile predicted by Test Solver and CFX

In contrast to the case of single-phase flow, the agreement between the results of the Test Solver and those of CFX seems much better in this case. This is because with the developed inlet profiles the propagation process of the flow predicted by CFX is much faster than that in the last case with constant inlet conditions. However, the development of the flow is still too fast according to the Test Solver. In other

words, the change of turbulence parameters and liquid velocity profiles from Level F to Level R is negligible, which indicates again that the influence of inlet conditions on the development of flow structure cannot be captured correctly in the Test Solver. According to the Test Solver the liquid velocity profiles change suddenly from a wall-peak profile given at Level A to a core-peak profile at Level F, which is much faster than that in the CFX predictions (see Figure 5.14). As a result, the evolution of shear-induced turbulence predicted by the Test Solver is faster than that by CFX. Furthermore, a wall-peak liquid velocity profile will produce a positive lift force for large bubbles and help to suppress their migration towards the pipe center. In other words, the redistribution of gaseous phase from the injection position at the pipe wall to the center will be overestimated by the Test Solver. In addition, turbulence parameters calculated by the Test Solver are in general larger than those by CFX, which can also accelerate the redistribution process of the gaseous phase due to large turbulent dispersion force.

Finally, from Figure 5.11 to Figure 5.13 one can see that the turbulent parameters predicted by CFX decrease suddenly at Level L in comparison with those at Level I. This is caused by the transition of the liquid velocity profile from a wall-peak to a core-peak. During the transition, the velocity gradient changes from positive via zero to negative and at Level L the absolute velocity gradient reaches its minimum, see Figure 5.14. Since at low absolute velocity gradient the shear-induced turbulence is also low, the turbulence parameters are correspondingly minimal at Level L. However, in the Test Solver calculations, this effect cannot be observed since before it reaches Level F, the liquid velocity profile already has a core-peak.

### **5.3 Implementation and test of available models**

As shown in Chapter 2, there are a large number of models and theories available in the literature. Nevertheless, since all of them were adjusted under certain conditions in the original work, they should be verified for the applied case such as vertical pipe flow before their application. Many comparative studies have been done for poly-dispersed gas-liquid flows with various coalescence and breakup models [38] [173] [174]. However, most of the study cases focus on bubble columns [38] [173] or two-phase jets [174].

In this work, three couples of the most popular models developed by different researchers are implemented in the Test Solver. They are models of Lehr et al. [31], Luo and Svendsen [95] [175] and Prince and Blanch [36]. These models are chosen with the consideration that these authors proposed both coalescence and breakup models simultaneously.

Note that in all the calculations run in this work, measurements of the gas volume fraction and the bubble size distribution at Level A are used as inlet conditions. As the air-water mixture flows along the pipe, predicted results such as the bubble size distribution and the gas volume fraction at different height levels are compared with measurements.

#### **5.3.1 Test cases**

A comparative study of available models is performed for the case of upward vertical pipe flow. Cross-sectional averaged bubble size distributions as a function of the

axial location are examined for four test points with different combinations of gas and liquid superficial velocities. Breakup and coalescence rates estimated by various models can only be compared with each other qualitatively, since it is impossible to separate the coalescence and breakup processes. Nine different combinations of bubble breakup and coalescence models listed in Table 5.1 are examined in this study.

Table 5.1 A list of cases

Cases	Coalescence model	Breakup model
1	Lehr et al. [31]	Lehr et al. [31]
2	Lehr et al. [31]	Luo and Svendsen [175]
3	Lehr et al. [31]	Prince and Blanch [36]
4	Luo and Svendsen [95]	Lehr et al. [31]
5	Luo and Svendsen [95]	Luo and Svendsen [175]
6	Luo and Svendsen [95]	Prince and Blanch [36]
7	Prince and Blanch [36]	Lehr et al. [31]
8	Prince and Blanch [36]	Luo and Svendsen [175]
9	Prince and Blanch [36]	Prince and Blanch [36]

### 5.3.2 Results

At low gas volume fractions, e.g. test point 041, the inlet bubble size at Level A is smaller than 10 mm. Bubbles are sparsely dispersed and both coalescence and breakup is weak. The change in bubble size distribution is nearly negligible. With the increase of superficial gas velocity, the inlet bubble size becomes large. The evolution of bubble size from Level A to Level R is breakup dominant, e.g. for test point 085, the average bubble diameter decreases from about 16 mm to 8 mm. The last case of test point 107 with  $J_{\text{f}}=1.017$  m/s and  $J_{\text{g}}=0.219$  m/s is an example of flow regime transition. The characteristic of the evolution of bubble size distribution is that besides the growth of the peak of small bubbles, remarkable formation of large bubbles ( $d>40$  mm) is observed at the upper pipe section.

As shown in Figure 5.15 and Figure 5.16 for test point 041, the coalescence model of Lehr et al. [31] with their own breakup model or with that of Luo and Svendsen [175] provides the best agreement with experimental data for the evolution of bubble size distribution and mean bubble diameter (cases 1, 2). On the other hand, the Prince's [36] breakup model delivers an overestimation of the volume fraction for small bubbles (case 3). Furthermore, Prince's [36] and Luo's [95] coalescence models overestimate the coalescence rate in contrast to the breakup rate calculated by the model of Lehr [31] and of Luo [175] (see cases 4, 5, 7, 8). With the combination of the powerful coalescence and breakup models (cases 6, 9), the number densities of both small and large bubbles are overestimated. The average bubble diameter goes first steeply down and then increases continuously due to the generation of large bubbles, see Figure 5.16.

In Figure 5.16 the predictions of average bubble size are ordered by coalescence model or by breakup model, respectively, e.g. cases 1, 2 and 3 having an identical coalescence model. The comparison between the cases 1, 2, 3 shows that the average bubble size predicted by the Prince's [36] breakup model is much smaller than that by the other two models, and the breakup model of Luo [175] is slightly

stronger than that of Lehr et al. [31]. However, if the Lehr's [31] coalescence model is replaced by that of Luo [95] (cases 4, 5, 6) or of Prince [36] (cases 7, 8, 9), the breakup rate predicted by Lehr's [31] model exceeds that by Luo's [95] model, but both of them underpredict the breakup rate. In these cases, the breakup model of Prince [36] delivers a better agreement with the experimental data. On the other hand, coalescence rate predicted by Prince's [36] model is generally larger than that by the other two models, see cases 1, 4, 7 and 2, 5, 8. However, if the model of Prince and Blanch [36] is used for the determination of breakup rate, coalescence rate predicted by Luo's [95] model overtakes that by Prince's [36] model (see cases 3, 6, 9). That means that as bubble size decreases coalescence efficiency predicted by Prince's [36] model decreases faster than that by Luo's [95] model. In addition, the average bubble size decreases steeply near the inlet of the flow if the breakup of Prince [36] is adopted.

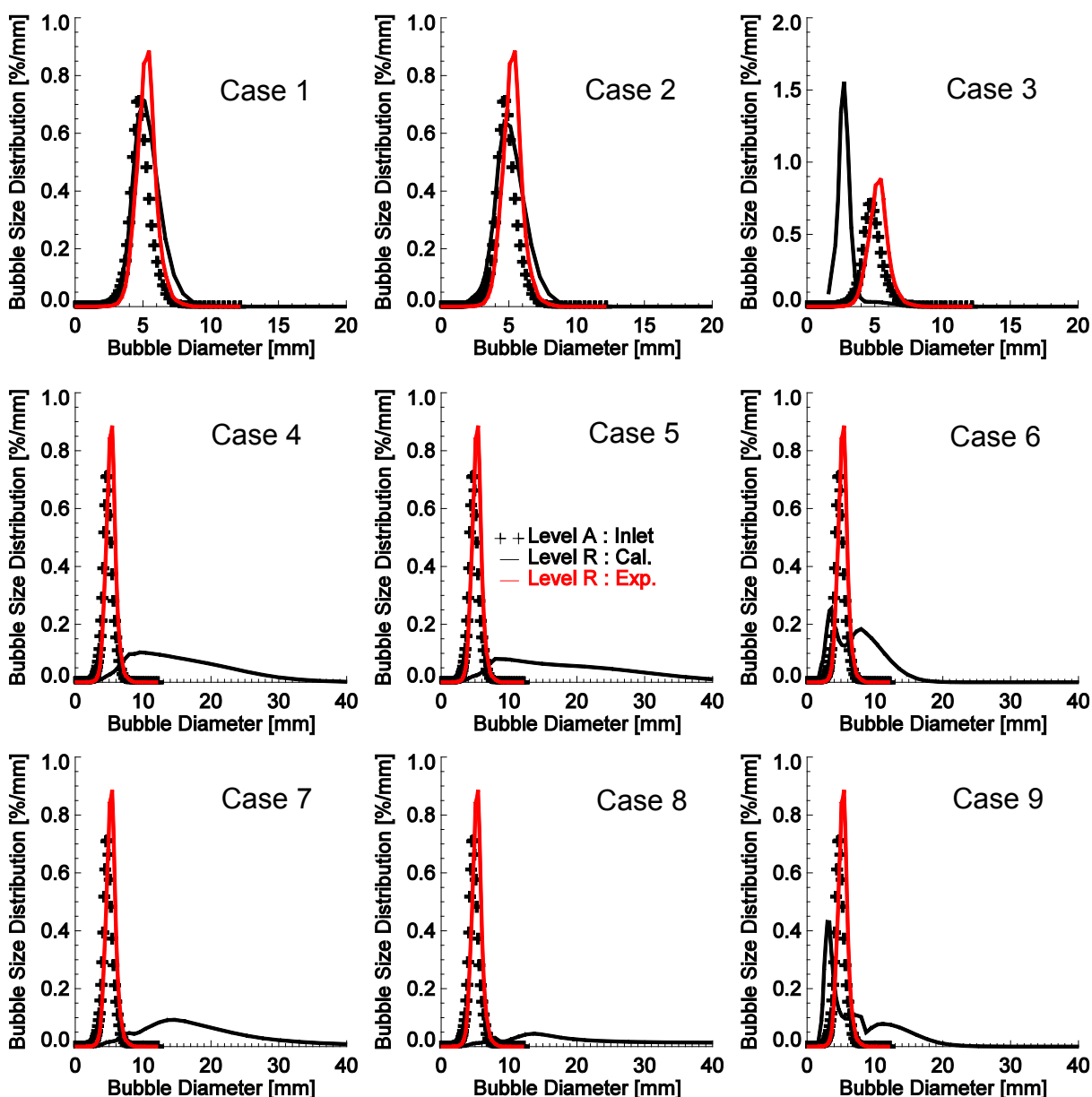


Figure 5.15 Prediction about bubble size distribution at Level R (TP041)

In conclusion, from Figure 5.15 and Figure 5.16 one can see that in general:

Breakup rate: Prince's [36] model > Lehr's [31] model > Luo's [175] model  
 Coalescence rate: Prince's [36] model > Luo's [95] model > Lehr's [31] model

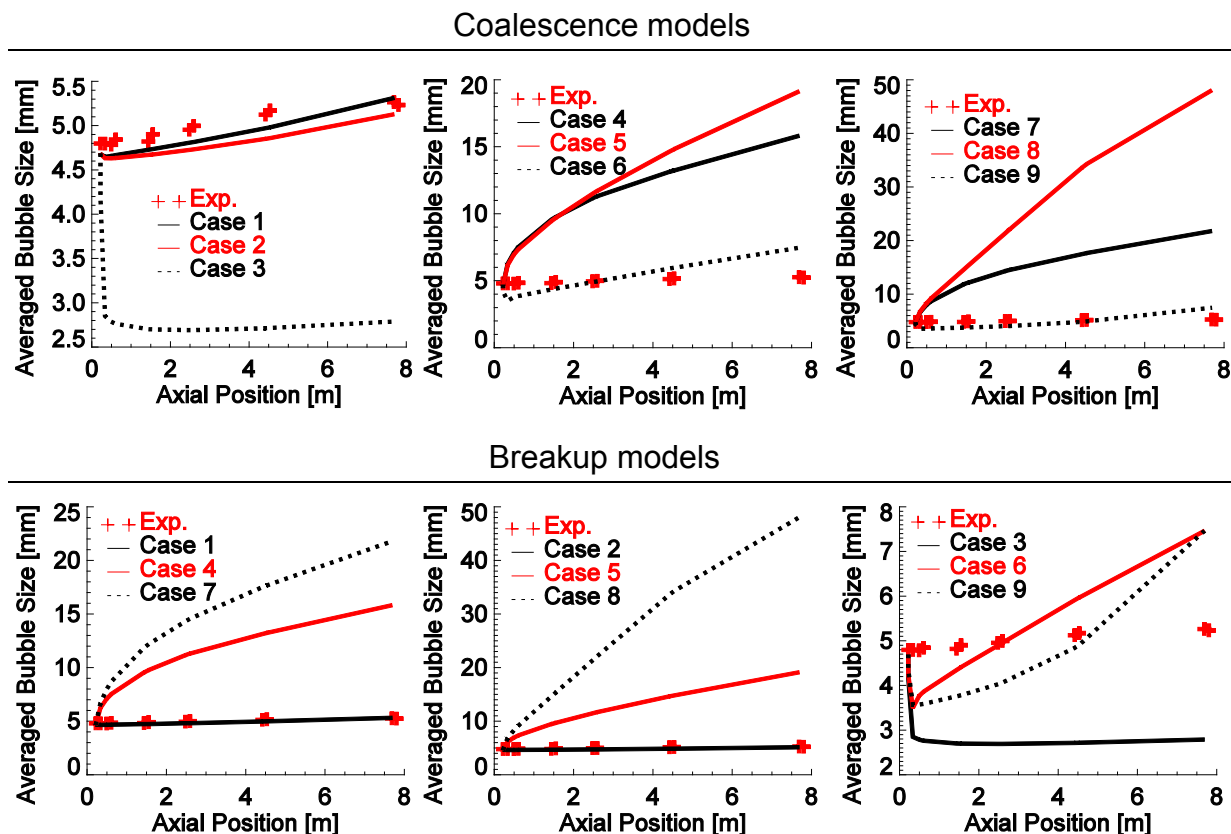


Figure 5.16 Prediction of the evolution of average bubble size in the axial direction (TP041), ordered by either coalescence model or by breakup model

For test point 063, predictions about the evolution of bubble size distribution and average bubble diameter with different combinations of models are shown in Figure 5.17 and Figure 5.18, respectively. The information that one can obtain from the results about the performance of different models is similar to the previous case except that the predicted bubble size is larger in all cases due to the higher superficial gas velocity.

As shown in Figure 5.17, the agreements achieved by cases 1 and 2 are still the best one. At the same time, the performance of cases 6 and 9 is improved in comparison to the example of test point 041. Furthermore, the breakup model of Prince and Blanch [36] is too strong in contrast to the Lehr's [31] coalescence model, while the coalescence rates given by the model of Prince [36] and of Luo [95] are too large, if the breakup model of Lehr [31] and of Luo [175] are used (see cases 4, 5, 7, 8).

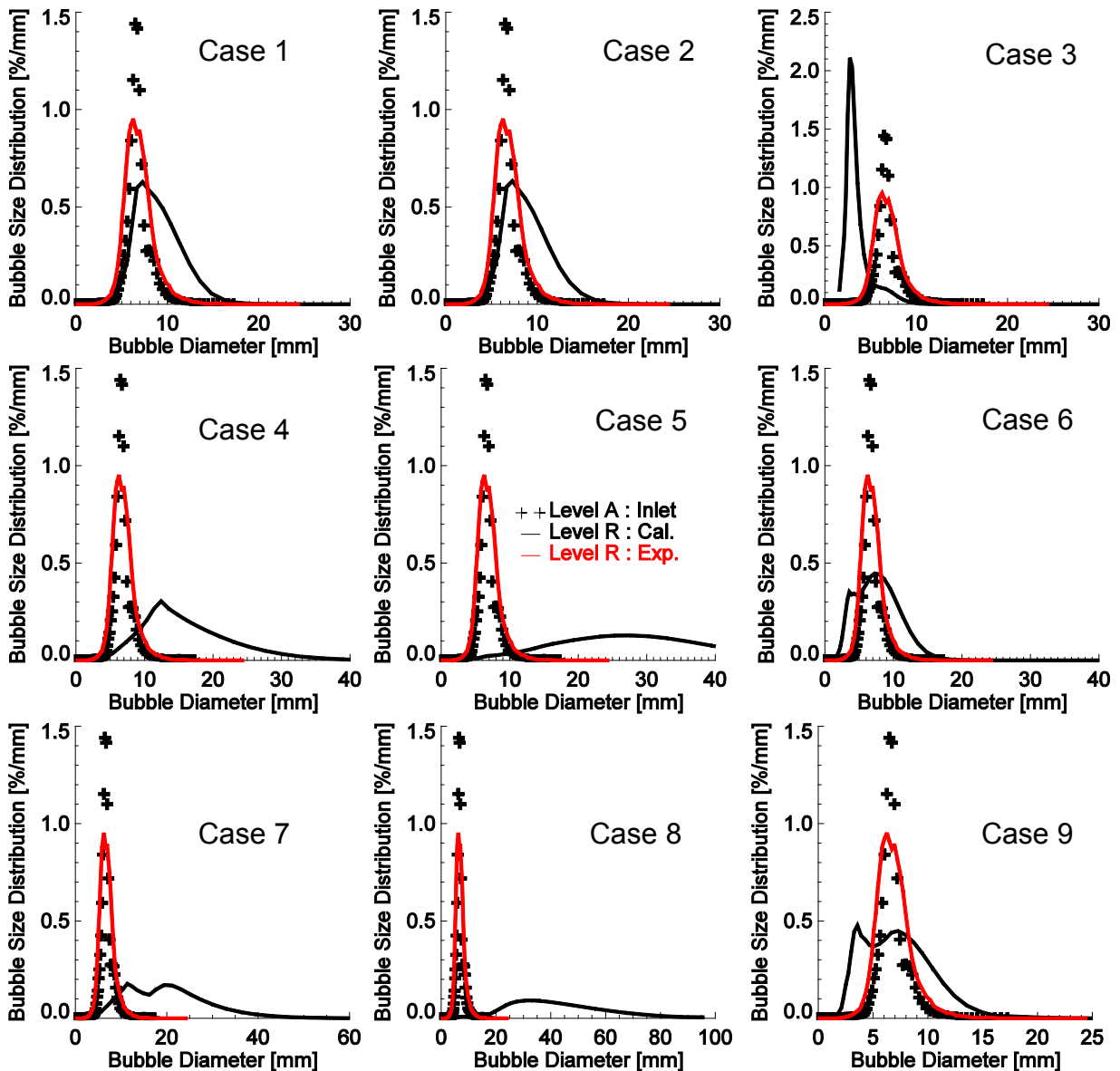
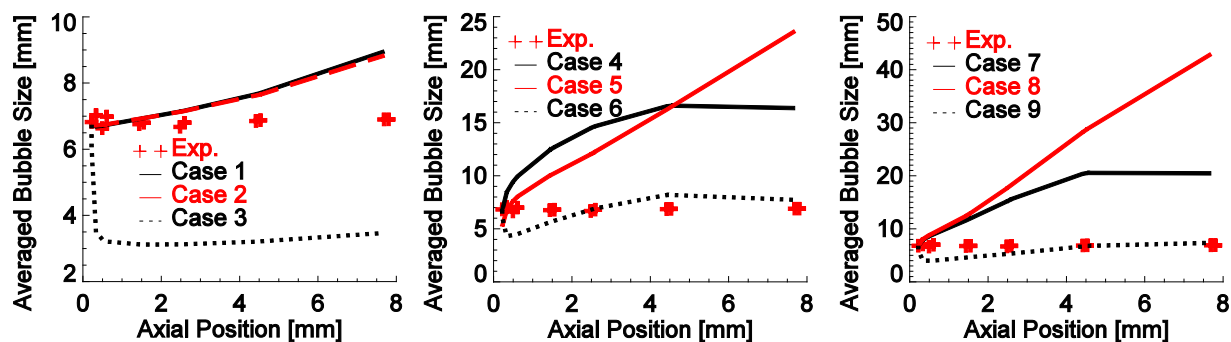


Figure 5.17 Prediction of bubble size distribution at Level R (TP063)

From Figure 5.18 one can see that unlike the monotonous increasing tendency of bubble size along the pipe in test point 041, in some cases such as 4, 6, 7 and 9 the average bubble size decreases slowly at the upper section of the pipe. It implies that the coalescence efficiency predicted by the model of Lehr [31] and of Prince [36] decreases as the bubble size increases while the coalescence model of Luo and Svendsen [95] has no such an effect.



## Coalescence models



## Breakup models

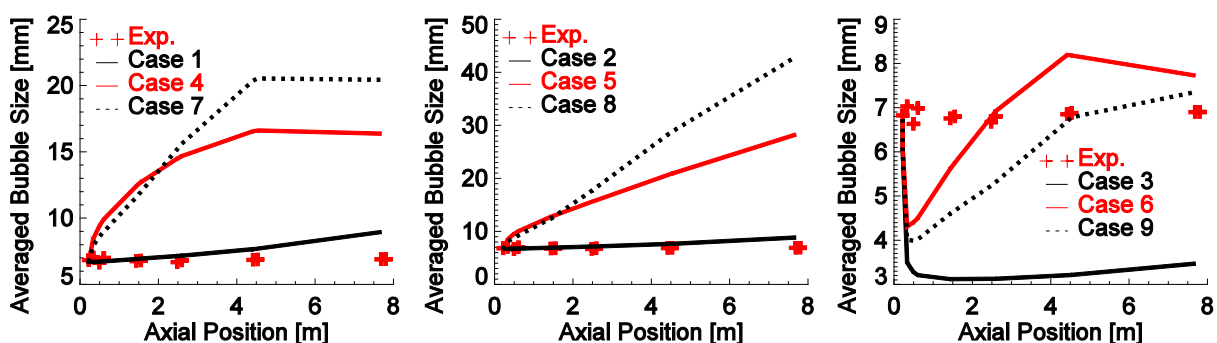


Figure 5.18 Prediction of the evolution of average bubble size in the axial direction (TP063), ordered by either coalescence model or by breakup model

The evolution of bubble size distribution and average bubble diameter predicted by all combinations of models is depicted in Figure 5.19 and Figure 5.20 for test point 085, respectively. For this test point, bubbles at the inlet level are of medium size and bubble breakup plays a more important role than the last two cases. The agreements between bubble size distributions predicted by cases 3, 6, 9 and experimental data are most satisfying, where the breakup model of Prince and Blanch [36] is used. That means that the breakup rate predicted by Prince's [36] model gives a minimum deviation while that by the other two models is too small. Although the Prince's [36] model gives an overestimation for the breakup rate at the beginning of the flow, it seems that it is the best option for this combination of gas and superficial liquid velocity. If the Prince's [36] model is chosen to calculate the breakup rate, the influence of various coalescence models is trivial such as for cases 3, 6, 9. In contrast, the other two models give too small a breakup rate. As a result, the bubble size is overestimated for all cases with different coalescence models, especially for the case 8, since the coalescence rate given by Prince's [36] model is the largest.

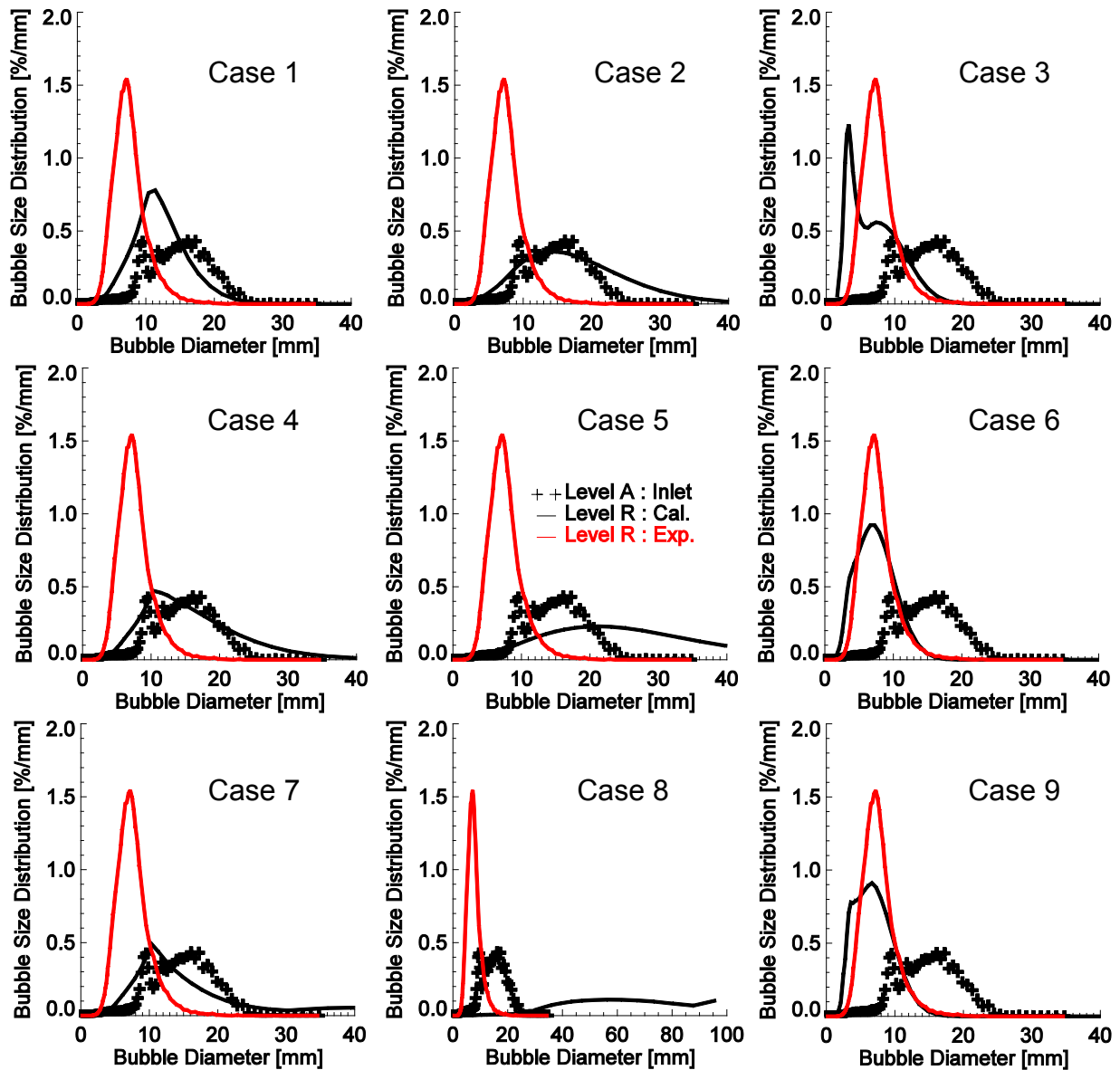


Figure 5.19 Prediction of bubble size distribution at Level R (TP085)

Predictions about the evolution of average bubble size provided by different combinations of coalescence and breakup models are illustrated in Figure 5.20. The decreasing trend of the average bubble size along the pipe observed in the measurement can only be reproduced by the breakup model of Prince and Blanch [36] while other two models are too weak to do that. Furthermore, the experimental data exhibit a continuous decrease of the average bubble size in the axial direction while according to the breakup model of Prince [36] the average bubble size decreases steeply only at a short distance away from the inlet and afterwards increases stably. At the outlet of the pipe, a good agreement between the simulation and experiment is reached.

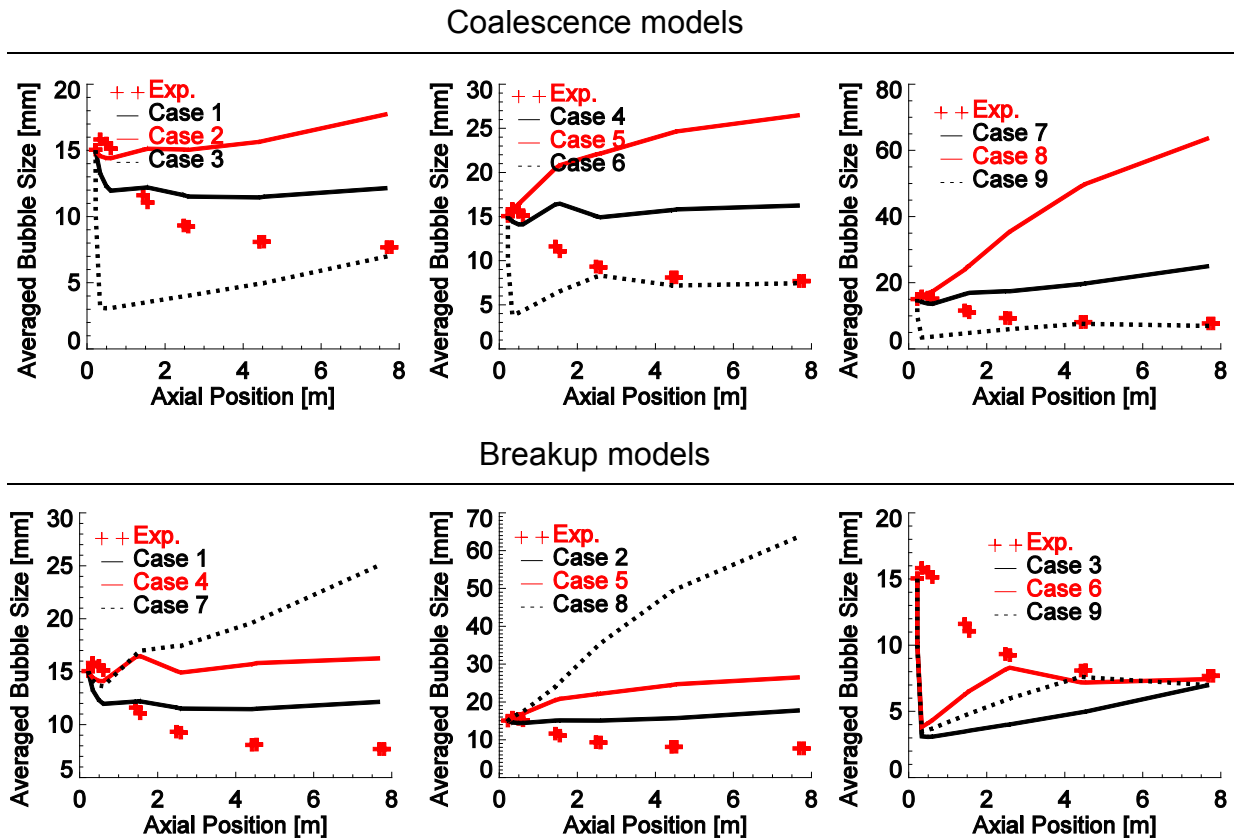


Figure 5.20 Prediction of the evolution of average bubble size in the axial direction (TP085), ordered by either coalescence model or by breakup model.

A comparison of the predicted bubble size distribution and the average bubble size with the measurement for test point 107 is shown in Figure 5.21 and Figure 5.22, respectively. In this case a transition of flow regime is observed as the bubble size distribution evolves along the pipe. That means that the flow changes from a bubbly flow at Level A to a churn-turbulent flow at Level R.

As it can be seen in cases 3, 6, 9, the breakup model of Prince and Blanch [36] delivers a good agreement for the peak of small bubbles generated by breakup but fails to predict the formation of large bubbles by coalescence. As a result, the predicted cross-sectional averaged bubble diameter is in general lower than the measured one, see Figure 5.22. On the other hand, the altitude of the peak of small bubbles is underpredicted and the peak located at a relatively larger bubble size in the other two cases using the breakup model of Lehr [31] and of Luo [175]. Furthermore, a small peak of very large bubbles can be observed in cases 7 and 8. However, this is caused by the overestimation of total coalescence rate and not by the effect of wake-entrainment since the mechanism is not included in the coalescence model of Prince and Blanch [36]. Therefore, for cases 7 and 8 the predicted average bubble diameter is much larger than the measured one, see Figure 5.22.

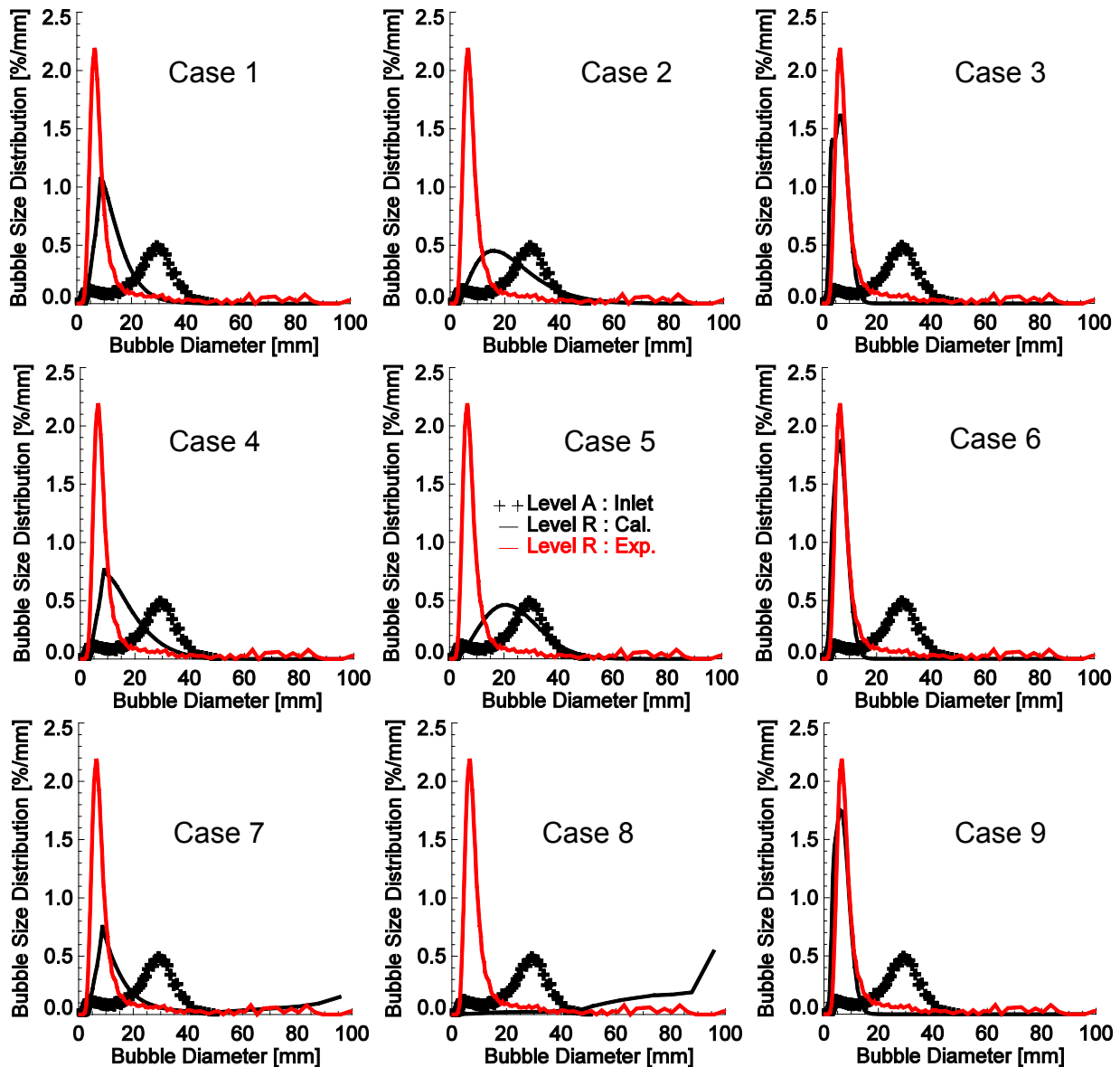


Figure 5.21 Prediction of bubble size distribution at Level R (TP107)

The comparison between the predicted average bubble sizes in Figure 5.22 shows that the cases 1 and 4 give the best agreement for the evolution along the pipe, although they fail to predict a reasonable bubble size distribution. On the other hand, the average bubble size delivered by the Prince's [36] breakup model is obviously smaller than the measured one and moreover, the coalescence models have scarce influence.

In conclusion, although a number of models for the calculation of bubble coalescence and breakup are available in the literature, the application range of these models is limited. The test of some typical models in the Test Solver for the case of upward vertical pipe flow shows that there are no models, which are able to deliver reasonable predictions about the evolution of the bubble size distribution and the average bubble size for all test points. Therefore, further effort is required in the development of new models for bubble coalescence and breakup.

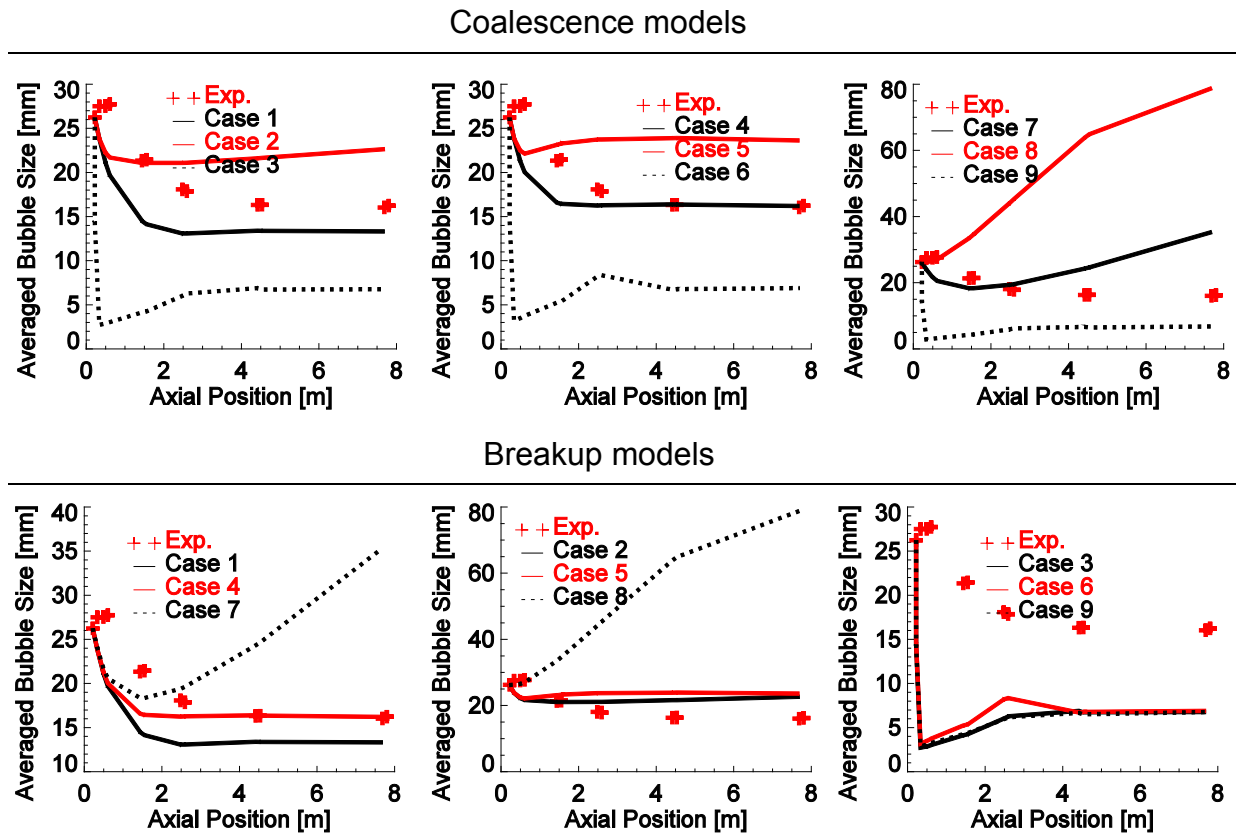


Figure 5.22 Prediction of the evolution of mean bubble size in the axial direction (TP107), ordered by either coalescence model or by breakup model.

## 5.4 Implementation and test of the new model

Predictions delivered by the new model about the evolution of bubble size distribution, average bubble size, gas velocity and gas volume fraction are depicted below in Figure 5.23 ~ Figure 5.32, respectively. For the calculation of BIT source terms the model proposed by Pflieger and Becker [157] is adopted, which was introduced in Chapter 4, and constants  $C_k=1.44$  and  $C_\epsilon=1.92$ .

### 5.4.1 Cross-sectional averaged bubble size distribution at Level R

The comparison between the predicted and measured bubble size distributions at Level R for different test points is shown in Figure 5.23 and as reference the inlet bubble size distribution at Level A is also depicted. For very low gas volume fractions such as test points 041 and 052, the change in bubble size distribution from Level A to Level R is determined mainly by coalescence, but it is not noticeable. With the increase in superficial gas velocity, bubble breakup begins to play a role. Bubble size distribution evolves from Level A to Level R in the direction of small bubble diameter. The tendency becomes more obvious as the superficial gas velocity increases further such as test points 085 and 096. On the other hand, from test point 107 on, bubble size distribution evolves in both directions to small and large bubble diameters simultaneously. That means that with an increase in the peak of small bubbles, new large bubbles are generated due to coalescence by wake-entrainment, whose contribution is more and more important as the superficial gas velocity increases.

A good agreement is in general achieved for all test points except that the volume fraction of small bubbles is slightly overpredicted for breakup-dominant cases such as test points 063 and 074, while an overestimation of the generation of large bubbles due to wake-entrainment is found at test points 107 ~ 129.

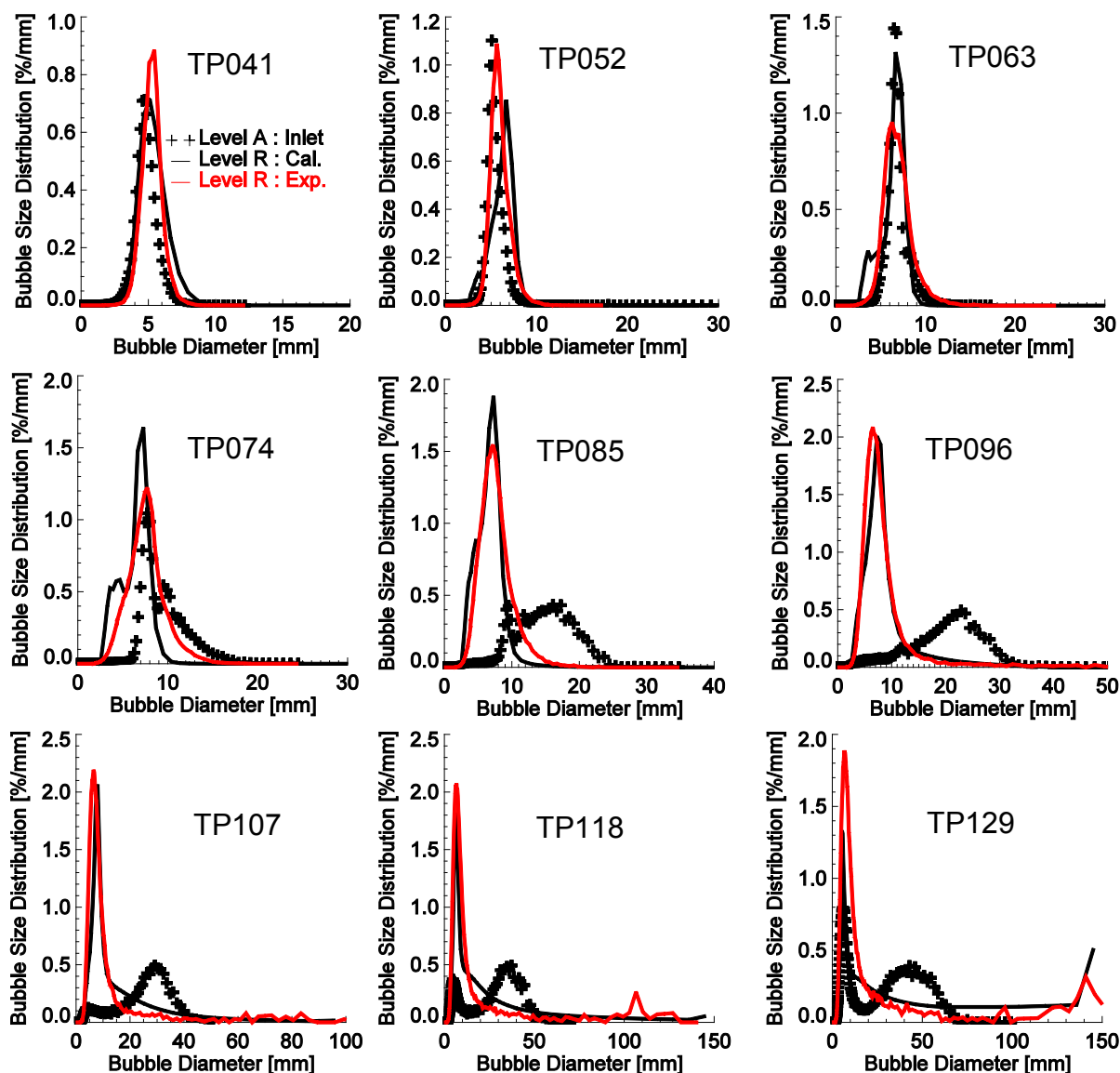


Figure 5.23 Bubble size distribution at Level R for different test points

#### 5.4.2 Evolution of bubble size distribution along the pipe

In order to keep track of the whole evolution process of bubble size distribution along the pipe, i.e. from Level A to Level R, the predicted bubble size distribution at different height levels are depicted below in Figure 5.24 and Figure 5.25 for test points 107 and 129, respectively.

As shown in Figure 5.24, the evolution tendency of bubble size distribution along the pipe observed in the experiment is well captured by the Test Solver with the new closure model. Bubble size distribution from Level A to Level F evolves in the directions of both small and large bubble diameters, i.e. bimodal development. However, in the simulation, breakup is too strong while coalescence is

underestimated, especially at the beginning of the flow. Due to this imbalance effect, the peak of small bubbles increases too fast at the beginning. However, after Level O the increase of small bubbles slows down while a simultaneous formation of very large bubbles by wake entrainment is observed.

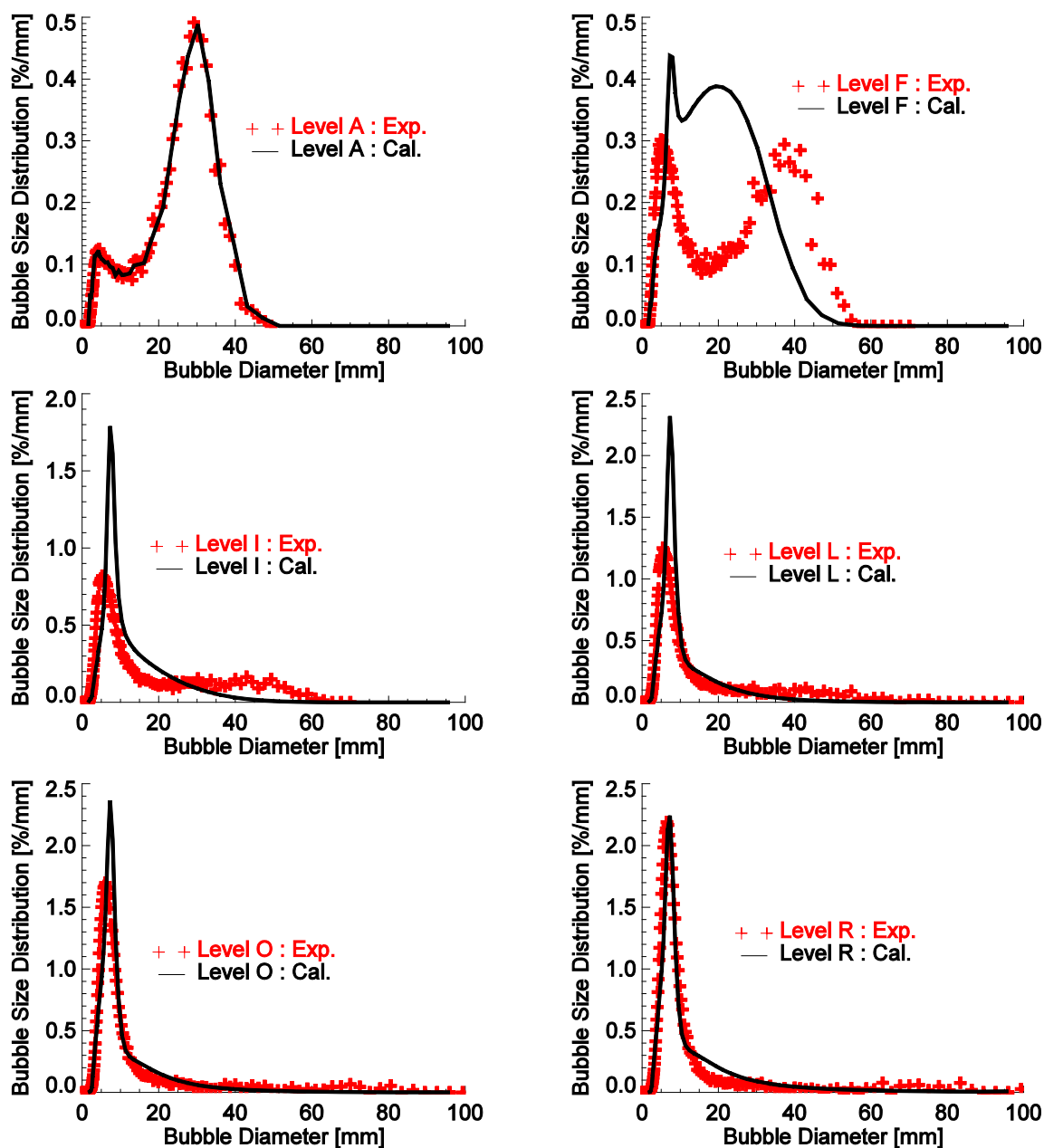


Figure 5.24 Evolution of bubble size distribution along the pipe for TP107

With the increase in the superficial gas velocity, the overestimation of breakup rate at the beginning of the flow is obviously alleviated, e.g. test point 129. As shown in Figure 5.25, the increase of the peak of small bubbles generated by breakup as well as the bimodal development of size distribution is well reproduced by the new model. The explanation for the difference between these two test cases is that in the last case the coalescence mechanism of wake-entrainment plays a role at the upper part of the pipe while in this case it has already a contribution from the beginning due to a large inlet bubble size. Nevertheless, the coalescence caused by this mechanism is

too strong so that at the upper part of the pipe, the predicted volume fraction of large bubbles is too large, while that of small bubbles is too small. As a result, the predicted average bubble size at Level R is considerably larger than the measured value, see Figure 5.26. The contribution of wake-entrainment can be reduced by using a smaller value for coefficient  $C_{35}$  or a larger value for the critical bubble size  $d_{crit}$ , see Eq. 3-15.

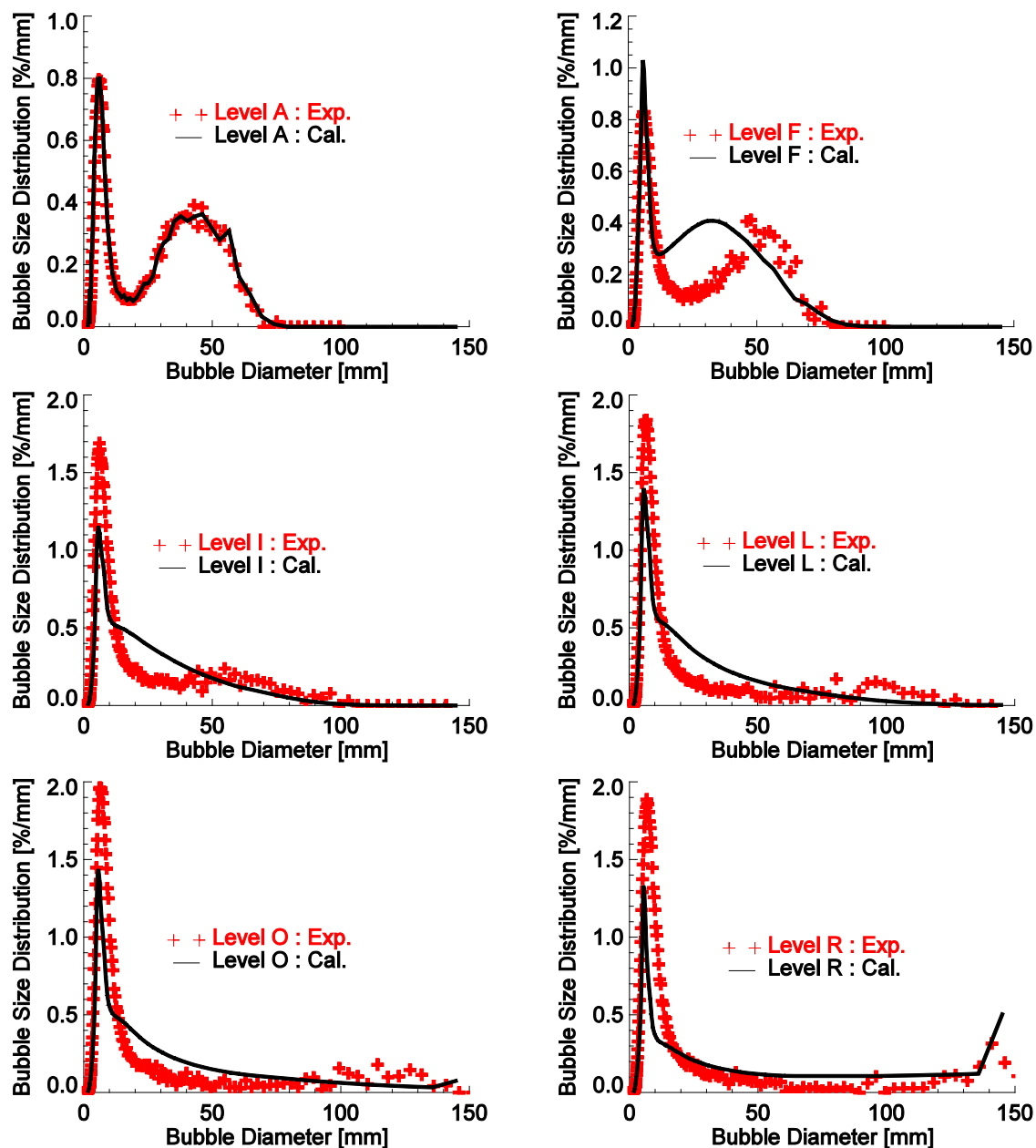


Figure 5.25 Evolution of bubble size distribution along the pipe for TP129

### 5.4.3 Evolution of average bubble size along the pipe

The comparison between the predicted and the measured cross-sectional averaged bubble sizes for several test points is depicted in Figure 5.26.



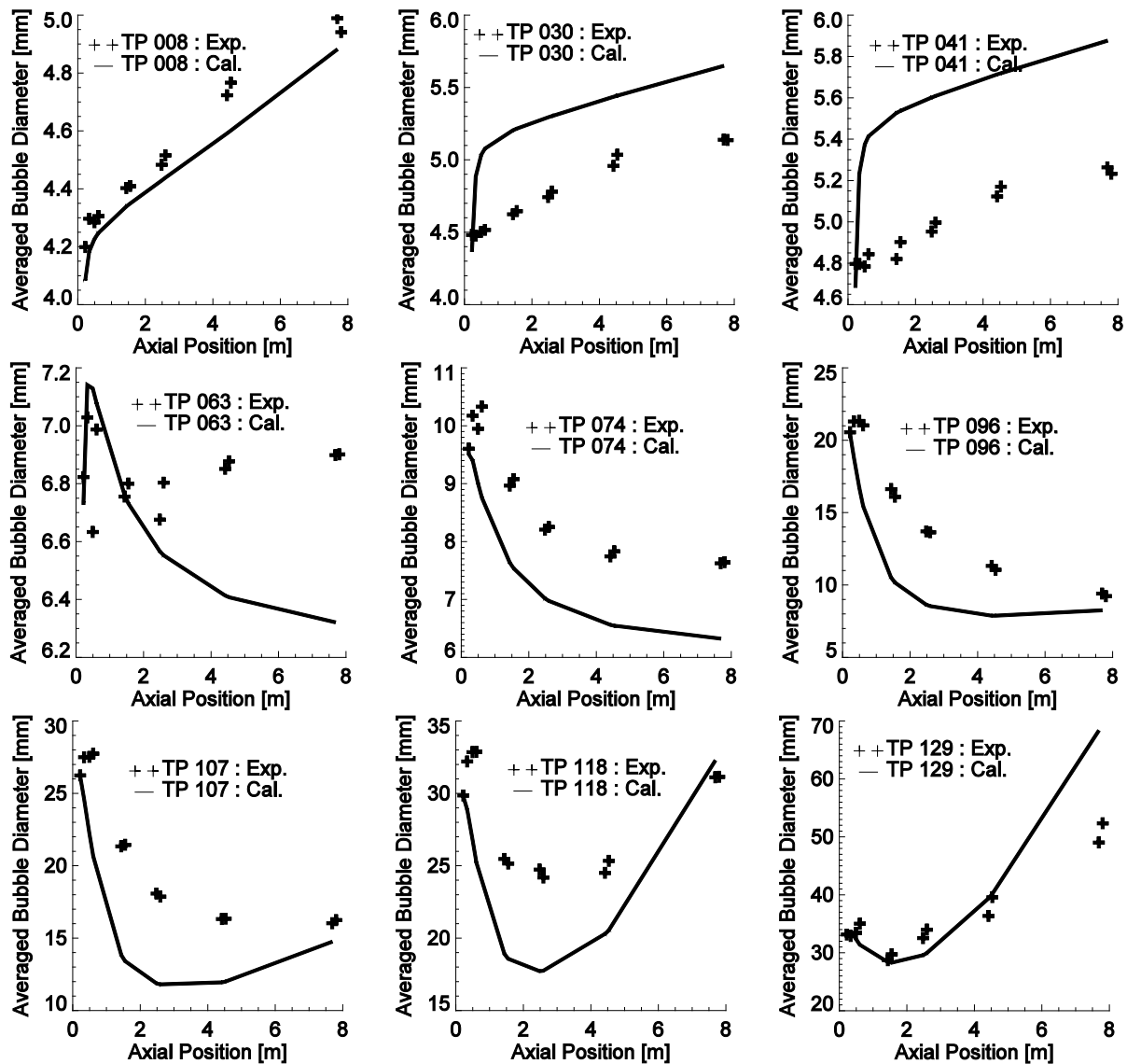


Figure 5.26 Evolution of mean bubble size along the pipe for different test points

As it can be seen, the evolution tendency of the average bubble size in the axial direction as well as with the increase in the superficial gas velocity is well reproduced by the new model. For test point 008, there is almost no coalescence and breakup of bubbles to be observed due to low gas volume fraction. With an increase in the superficial gas velocity, the bubble size increases first due to coalescence, see test points 030 and 041. However, for these coalescence-dominant cases, the predicted mean bubble size is slightly larger than the measured value due to the overprediction of coalescence rate. On the other hand, for breakup-dominant cases at higher superficial gas velocity, e.g. test points 074 and 096, the predicted average bubble size is smaller than the experimental data due to an overestimation of breakup rate. As the superficial gas velocity increases further, e.g. test points 107, 118 and 129, the increasing trend of average bubble diameter at the upper end of the pipe caused by wake-entrainment is overestimated in the simulation.

The comparison between the predicted radial profiles of Sauter mean bubble diameter and the corresponding measurements for different height levels, i.e. Level F, I, L, O and R, is shown in Figure 5.27.

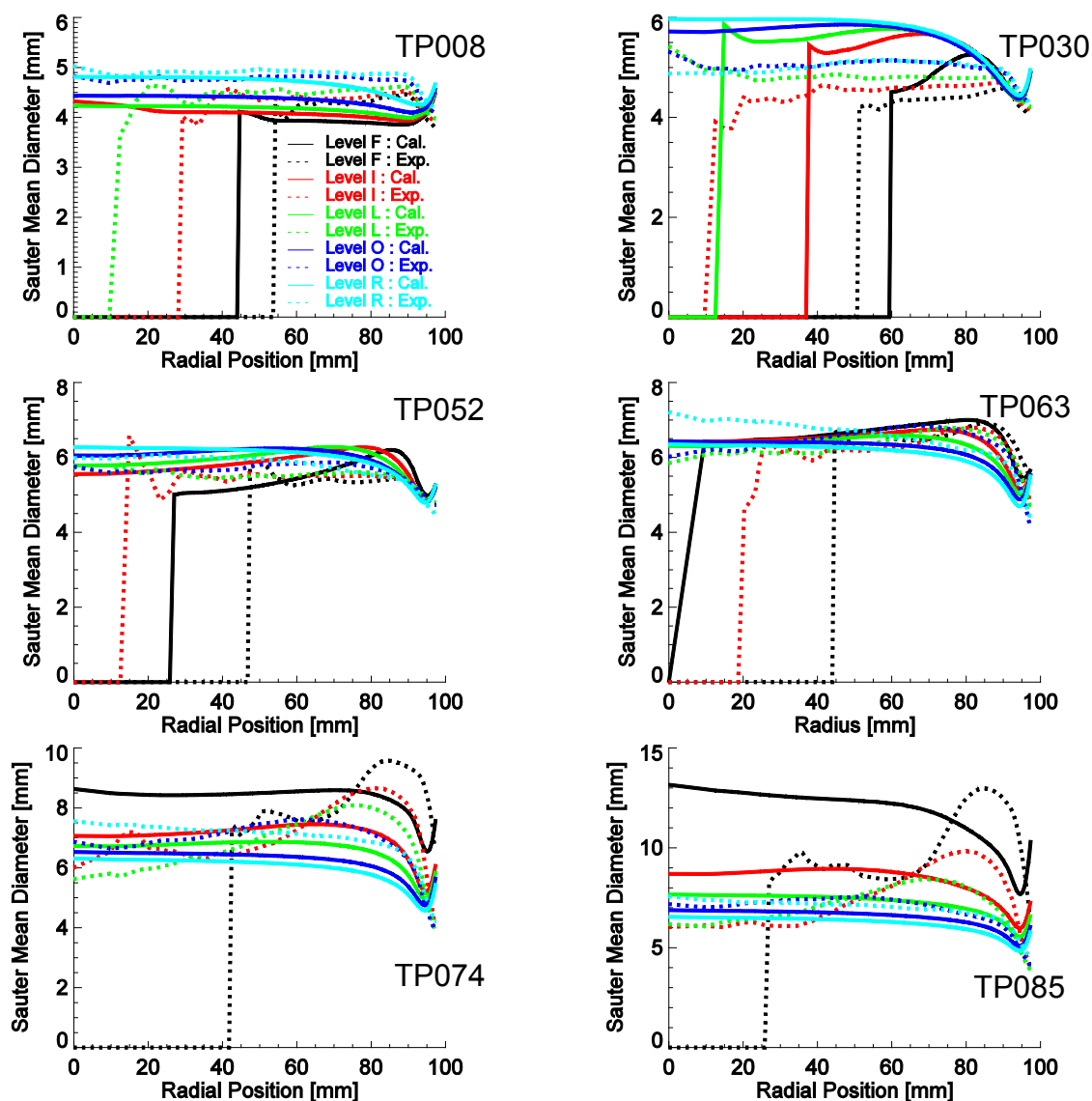


Figure 5.27 Radial profile of Sauter mean bubble diameter for different levels and test points

Again for test point 008 there are almost no coalescence and breakup events observed. The slight increase of bubble size from Level F to Level R is purely due to the pressure expansion, which is slightly underestimated in the simulation. Test point 030 is one example where coalescence is more important than breakup. However, according to the new model, the coalescence rate is too large especially at the beginning of the flow, e.g. Level F. In the case of test points 052 and 063, coalescence is almost in equilibrium with breakup. The change of the bubble size from Level F to Level R is the smallest. Nevertheless, as the superficial gas velocity increases further, e.g. test points 074 and 085, breakup becomes more important than coalescence. The mean bubble size decreases from Level F to Level R. The predicted bubble size is in general smaller than the measured one, especially at Level F. In addition, bubbles migrate more rapidly to the pipe center and the deviation between the simulation and measurement increases with superficial gas velocity.

Finally, note that simulated results exhibit a small increase near the pipe wall, which might be caused by too strong a wall lubrication force for small bubbles. In this work, the correlation of Tomiyama [151] is adopted.

The influence of the Tomiyama [151] and of Antal [153] wall force correlations on the predicted Sauter mean diameter and the gas volume fraction of small bubbles is illustrated in Figure 5.28. It can be seen that if the Antal [153] correlation is used for the calculation of wall force, the Sauter mean bubble diameter agrees well with the measured one in the near-wall region, see Figure 5.28 (a). As shown in Figure 5.28 (b), the Tomiyama [151] model delivers too strong a repelling force for small bubbles in the near-wall region so that the volume fraction of small bubbles ( $d \leq 6$  mm) is too low and the mean bubble diameter is then overestimated. Furthermore, the mean bubble diameter calculated by using the Antal correlation is in general larger than that by the Tomiyama [151] model. This is caused by the fact that more small bubbles accumulate long in the near-wall region, which will result in a higher coalescence rate.

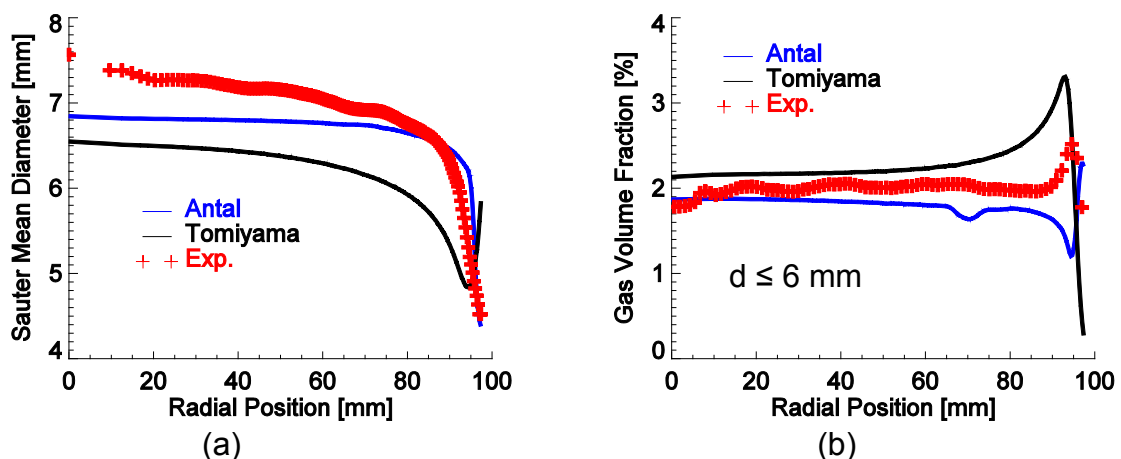


Figure 5.28 Influence of wall lubrication force on Sauter mean diameter and gas volume fraction of small bubbles (TP085, Level R)

#### 5.4.4 Radial gas volume fraction profile at Level R

The predicted and measured radial profiles for gas volume fraction at Level R are depicted in Figure 5.29 for several test points. The comparison indicates a good agreement with the measurement. However, for wall peak cases with low superficial gas velocities such as test points 041 and 052, the predicted peak near the wall is generally lower than the measured one. This discrepancy might be caused by too large a wall lubrication force for small bubbles given by the Tomiyama [151] correlation. On the other hand, for the core-peak cases with large superficial gas velocities such as test points 107 and 129, the predicted peak at the pipe center is slightly higher than the experimental data, which is caused by the imbalance between the lift force and turbulent dispersion force. The influence of bubble forces on the radial gas volume fraction profile will be shown in Figure 5.33 ~ Figure 5.35.

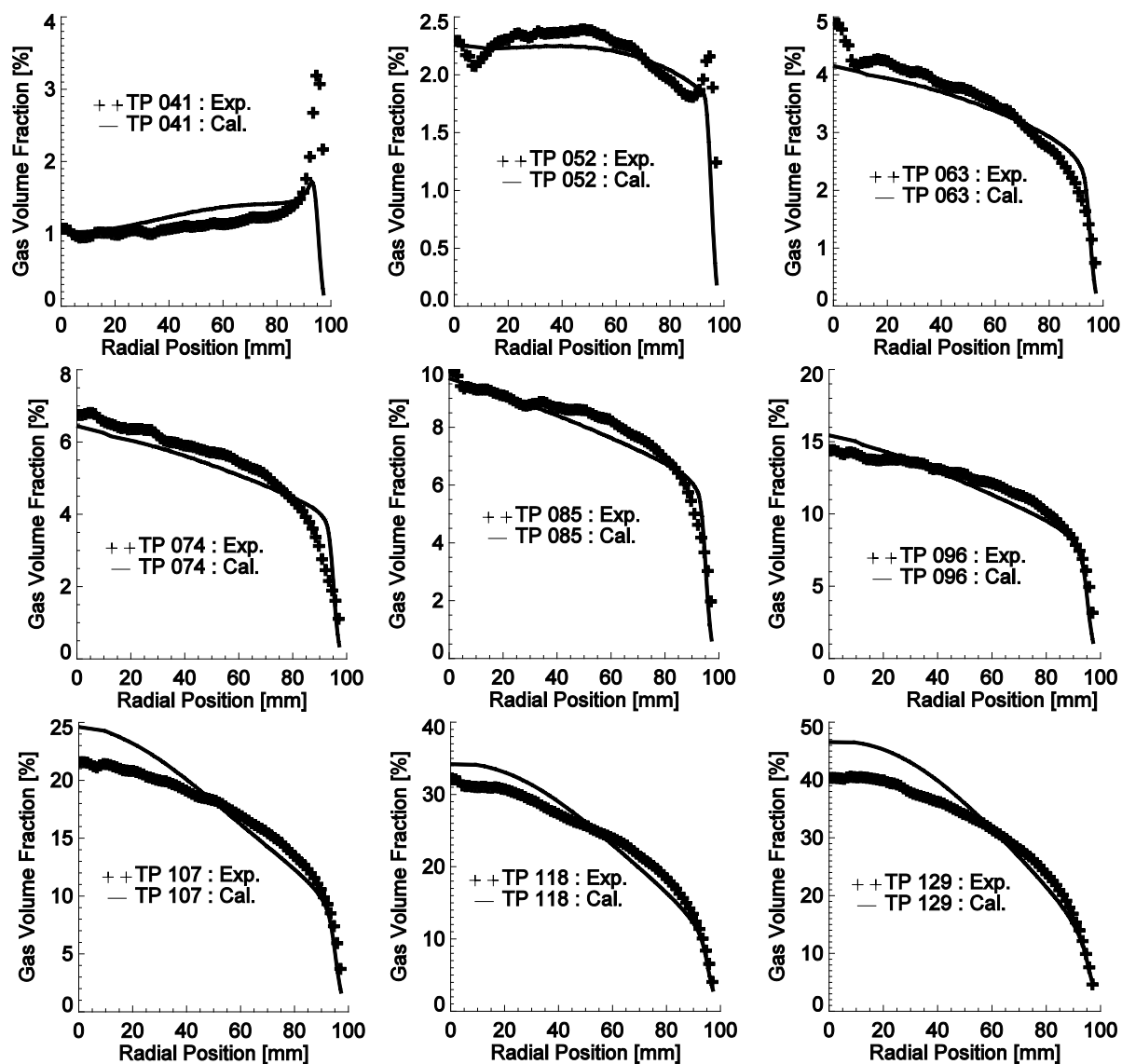


Figure 5.29 Radial gas volume fraction profiles at Level R for different test points

#### 5.4.5 Evolution of radial gas volume fraction profiles along the pipe

In order to explain clearly the migration or redistribution process of gaseous bubbles from the injection position at the pipe wall to the pipe center, the radial gas volume fraction profiles at different height levels are shown in Figure 5.30 and Figure 5.31 for two test points, respectively.

As shown in Figure 5.30, for the case of test point 085, the predicted gas volume fraction at all levels is similar to the measured one except that the migration velocity is slightly overestimated.

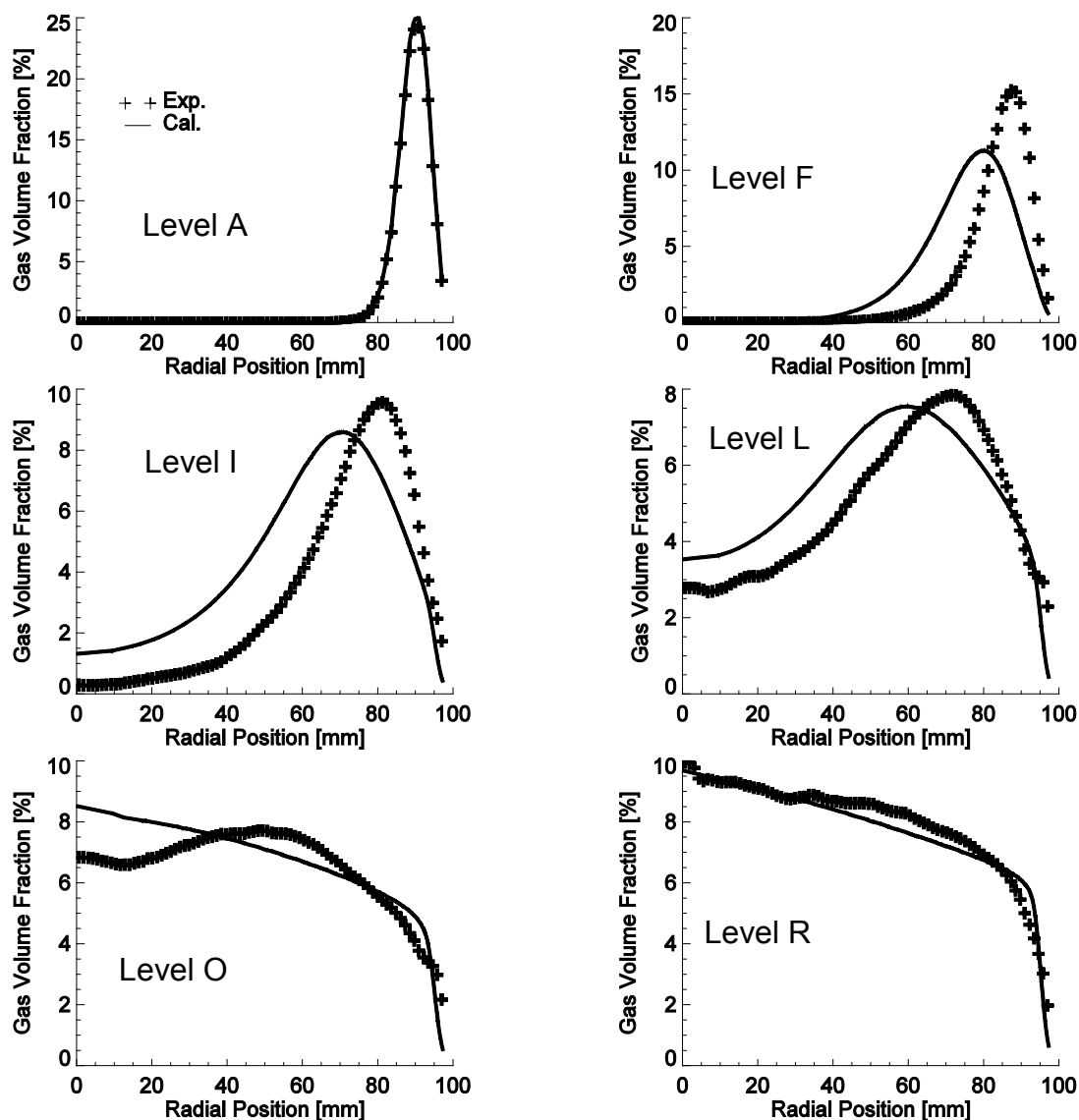


Figure 5.30 Evolution of radial gas volume fraction from Level A to Level R (TP085)

As indicated in Figure 5.31, the problem of the overprediction of bubble migration velocity becomes more serious as the superficial gas velocity increases. For the test point 118, the profile of the gas volume fraction at Level I is already similar to that at Level R. For this discrepancy, there might be three main reasons, i.e. errors in bubble forces, inlet conditions for the liquid phase as well as bubble aspect ratios. That means that bubble forces acting toward the pipe center such as lift force for large bubbles are too large for high superficial gas velocities. Due to the lack of experimental data, the inlet liquid velocity is calculated for a given gas volume fraction profile by using Sato [8] model given by Eq. 4-35 and Eq. 4-36, which was developed originally for fully developed bubbly flows and might give an overestimation at the entrance. This is also proved by the parameter study in §5.2. Finally, the bubble aspect ratio is calculated according to the Wellek correlation (see Eq. 4-12), which is only valid for the ellipsoidal shape. As a result, the horizontal extension of spherical-cap or Taylor bubbles will be dramatically overestimated according to Eq. 4-12.

The rapid redistribution of large gaseous bubbles from the injection position at the pipe wall to the whole pipe cross section will result in an overestimation of the bubble coalescence, as shown in Figure 5.23 and Figure 5.26. As the bubble size increases due to the overestimated coalescence rate, the bubble force or migration velocity will increase in turn. That means that there is a positive feedback between the bubble size and the gas redistribution velocity.

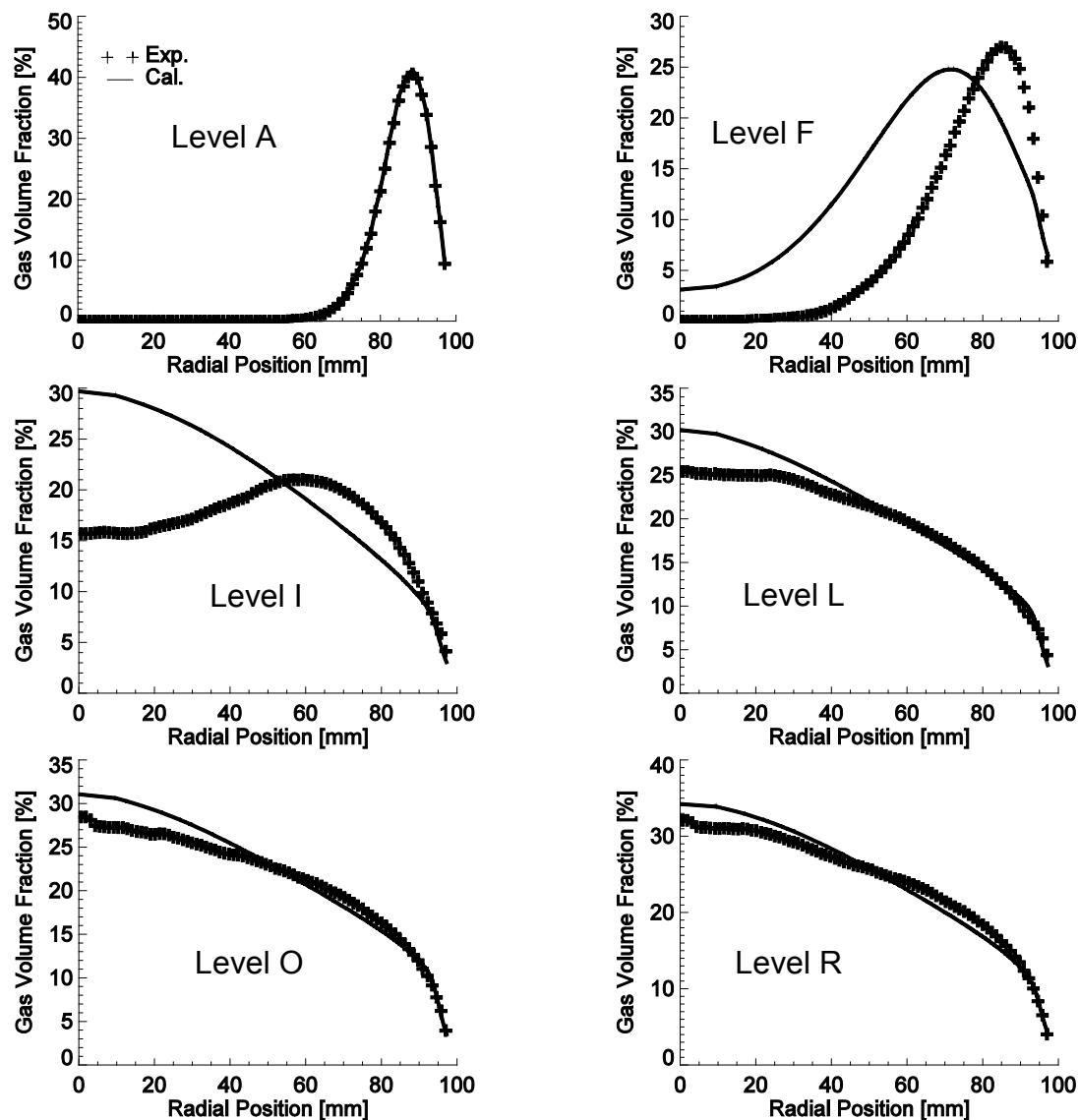


Figure 5.31 Evolution of radial gas volume fraction from Level A to Level R (TP118)

#### 5.4.6 Radial gas velocity profile

The radial profiles for gas velocity at Levels A, F, I are depicted in Figure 5.32 for different test points.

It can be seen that the agreement between the calculation and the measurement is in general very satisfying. However, for almost all test points the predicted velocity at Level A is larger than the measured value, especially for the test points with low superficial gas velocities. This proves further that the liquid velocity calculated by the Sato [8] model given in Eq. 4-35 is too large since the relative velocity between the

gas and liquid phase is almost constant. Another discrepancy is that for large superficial gas velocities such as test points 118 and 129, the velocity profile changes much faster from a wall-peak to a core-peak than in comparison to measurements. This is coupled with the overprediction of the redistribution of the gas volume fraction from the pipe wall to the pipe center discussed above.

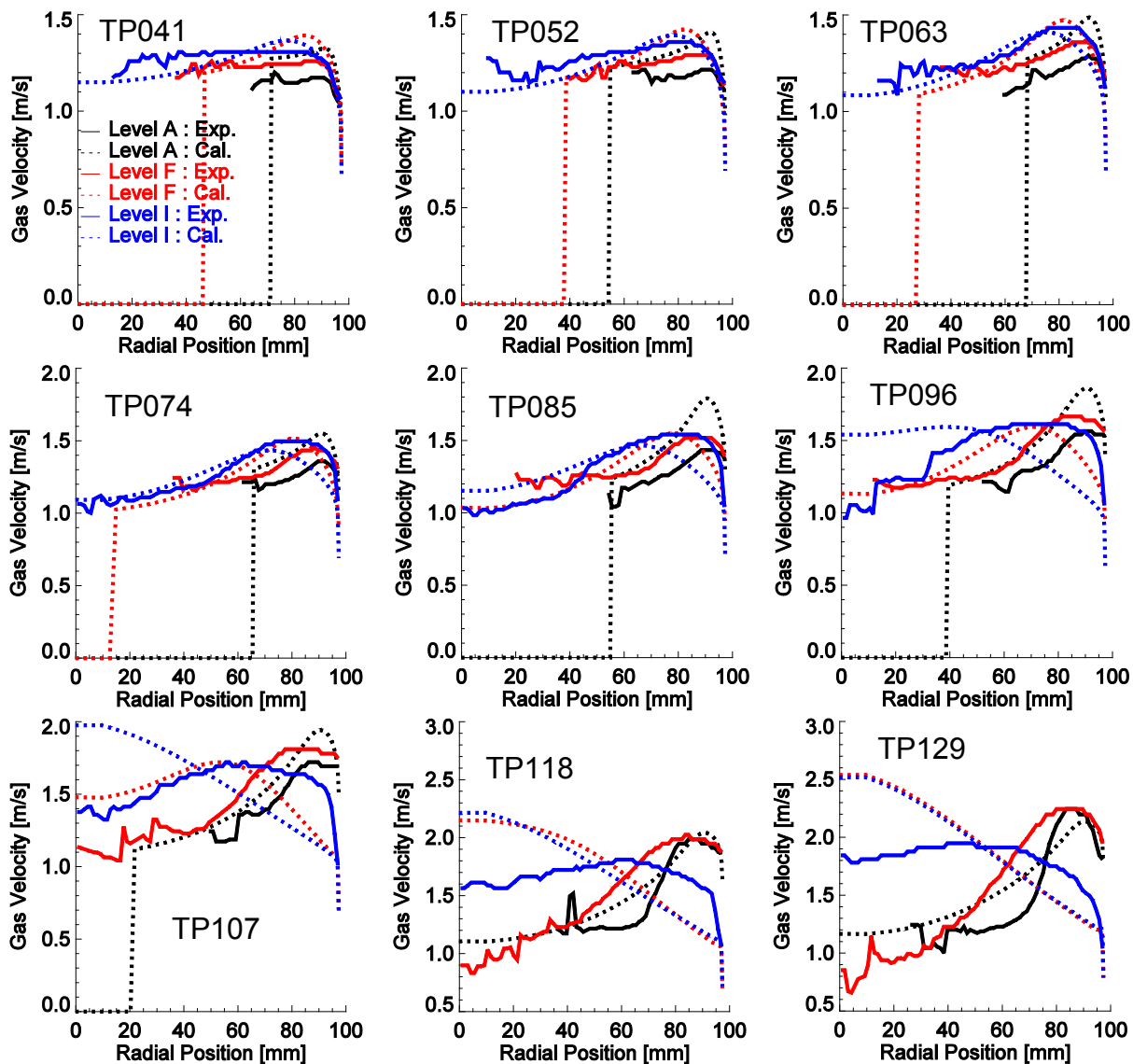


Figure 5.32 Radial profile of gas velocity at Level A, F and I for different test points

#### 5.4.7 Influence of turbulent dispersion force

The influence of turbulent dispersion force on the radial gas volume fraction profile is shown in Figure 5.33. It can be seen that by reducing the coefficient of turbulent dispersion force to a half ( $C_{TD}=0.5$ ), the migration of bubbles from the pipe wall to the center is obviously slowed down, see Level I. However, for such a low turbulent dispersion force, the gas volume fraction at the pipe center is too high by comparison with the measurement at the upper section of the pipe such as Levels L and O. As discussed before, this is caused by the fact that the smoothing effect of turbulent dispersion force is too weak to overcome the accumulation effect of lift force.

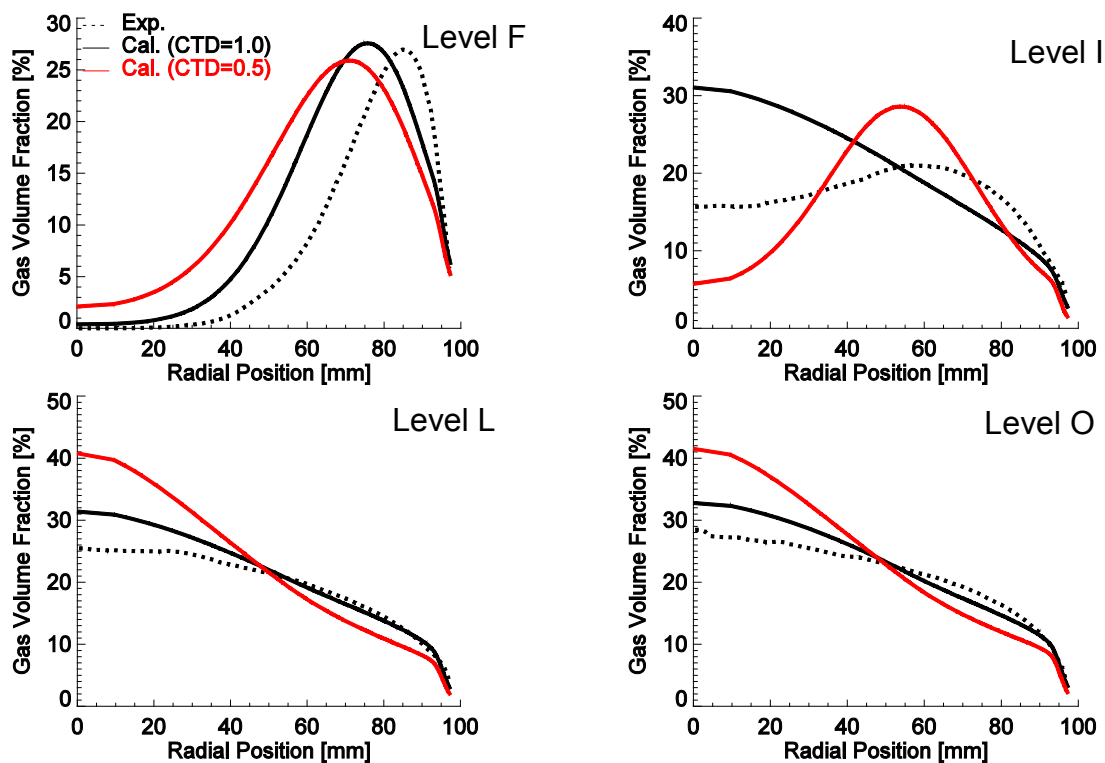


Figure 5.33 Influence of turbulent dispersion force on radial gas migration velocity (TP118)

#### 5.4.8 Influence of lift force

The influence of lift force on the evolution of gas volume fraction is depicted in Figure 5.34.

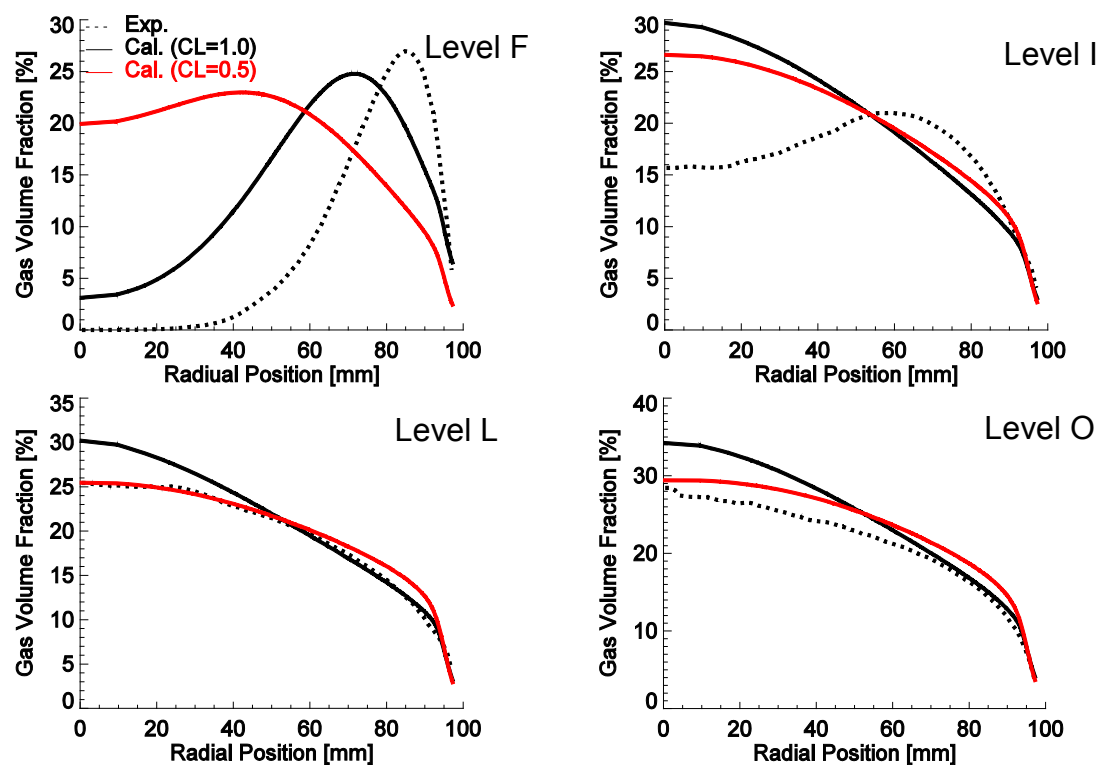


Figure 5.34 Influence of lift force on radial gas migration velocity (TP118)



As it shows if the amplitude of transverse lift force decreases to one half ( $C_L=0.5$ ), the velocity of bubbles migrating from pipe wall to the pipe center will increase dramatically at the beginning, e.g. at Level F. This is because for this case due to the effect of gas injection, the velocity gradient is positive at the beginning (see Figure 5.32). That means that large bubbles ( $d>5.8$  mm) will migrate towards the pipe wall, while small bubbles ( $d<5.8$  mm) move to the pipe center according to the lift force correlation of Tomiyama [151]. On the other hand, for the case of TP118, the injected average bubble size is much larger than 5.8 mm (ca. 30 mm). That means that under the effect of lift force most of the bubbles will accumulate in the near wall region. Therefore, under positive velocity gradients reducing the lift force will increase the migration velocity of the gaseous phase to the pipe center. However, after Level I the liquid velocity gradient changes again to negative, which means under the effect of lift force large bubbles will migrate to the center while small bubbles to the wall. In this case, a smaller lift force coefficient will suppress the accumulation of large bubbles at the pipe center.

#### 5.4.9 Influence of wall lubrication force

Beside the turbulent dispersion force and lift force, the wall lubrication force is also included in the radial momentum equation for the gaseous phase.

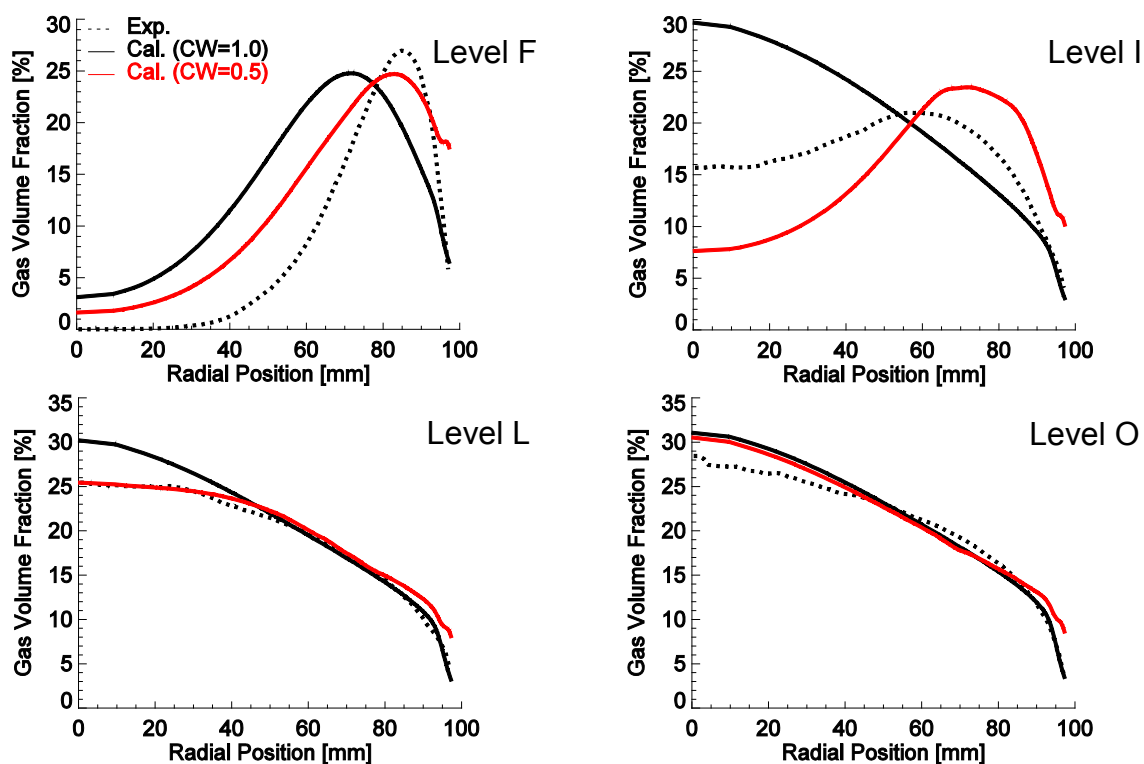


Figure 5.35 Influence of wall lubrication force on radial gas migration velocity (TP118)

From Figure 5.35 one can see that the influence of wall lubrication force on the radial gas velocity is noticeable although it in principle should be only active in the thin layer adjacent to the wall [153]. In other words, the wall lubrication force computed according to the correlation of Tomiyama [151] given in Eq. 4-15 and Eq. 4-16 has a considerable influence on the gas volume fraction at the pipe center. It is clear that the migration of bubbles to the pipe center is decelerated over the whole pipe height

by reducing the wall lubrication force since it acts always towards the pipe center. As a result, the gas volume fraction at the pipe center decreases for a low wall lubrication force coefficient which is similar to the effect of lift force. In addition, the coefficient calculated according to Eq. 4-16 is dependent on the Eotvos number or bubble diameter, which is too large for small bubbles as indicated in Figure 5.28.

#### 5.4.10 Contribution of each coalescence and breakup mechanism

As introduced in Chapter 3, the new model for bubble coalescence and breakup includes different mechanisms. The breakup mechanisms compass turbulence, eddy-shear, laminar-shear and interfacial stresses. The contribution of each breakup mechanism to the evolution of bubble size distribution is depicted Figure 5.36. The red plus sign is the measured bubble size distribution at Level A. The black solid line is the bubble size distribution at Level R predicted by the model only including turbulence-induced breakup. Similarly, the other three lines represent the prediction of bubble size distribution at Level R with only one breakup mechanism of eddy-shear, laminar-shear and interfacial stresses, respectively.

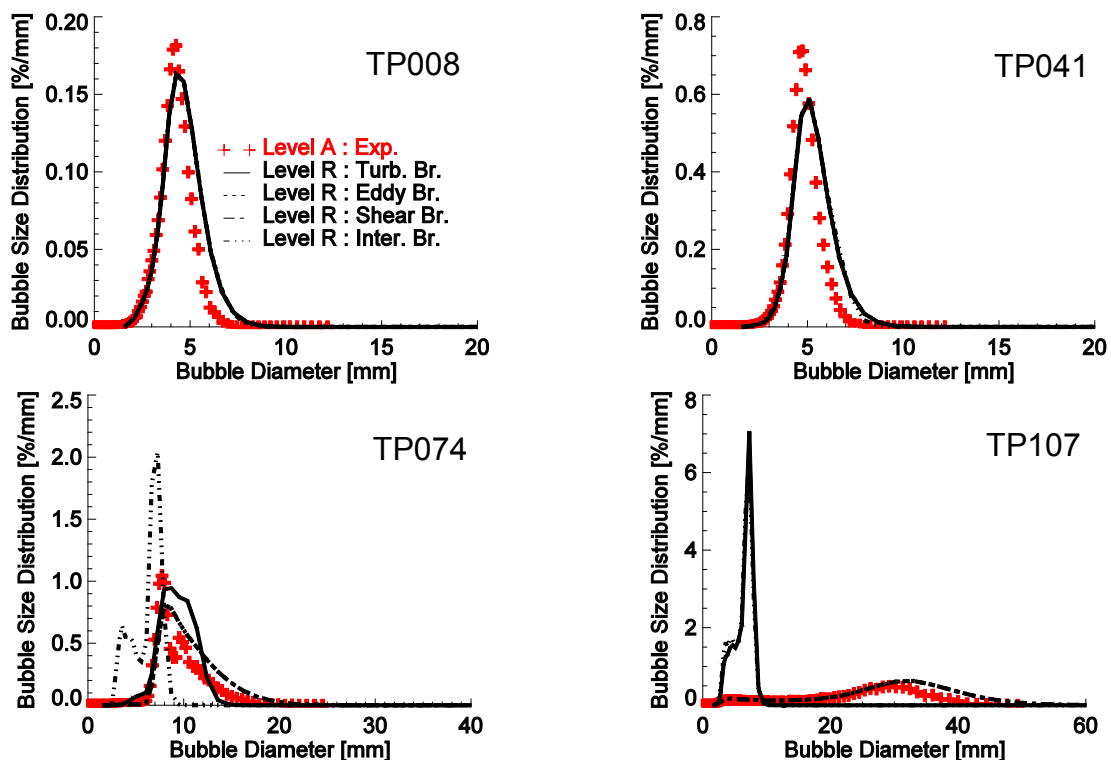


Figure 5.36 Contribution of each breakup mechanism for different test points (coalescence not included)

It can be seen that for test cases with low superficial gas velocity, e.g. test points 008 and 041, no breakup events are observed as the bubble size distribution evolves from Level A to Level R, since the bubble size distribution at Level R predicted by different mechanisms is almost the same. The increase of bubble size is caused purely by pressure expansion. From test point 074 on, breakup begins to play a role in the evolution of bubble size distribution. The mechanism of interfacial stresses is the most important mechanism and followed by the turbulence-induced breakup while the other two mechanisms, i.e. eddy-shear and laminar shear stress, have no effect due to the low viscosity of water. Therefore, the mechanism of interfacial

stresses might be responsible for the overestimation of breakup rate for the breakup-dominant cases such as test point 074, see Figure 5.23. On the other hand, as the superficial gas velocity increases the turbulence-induced breakup of bubbles becomes more important, since the dissipation rate increases with the increase in the superficial gas velocity. For the case of test point 107, the two breakup mechanisms have an almost equivalent contribution.

Similarly, the coalescence mechanisms of turbulence, eddy-capture, laminar shear rate, interfacial slip and wake-entrainment are taken into account in the new model. The bubble size distribution at Level R predicted by including only one of the mechanisms and the measurement at Level A is shown in Figure 5.37. For test point 008, all mechanisms have no effect on the bubble size distribution at Level R, which means no coalescence is observed in this case. However, from test point 041 on, the turbulence-induced coalescence begins to occur, which is responsible for the overestimation of coalescence rate in these cases. For test point 074, three mechanisms except the eddy-capture have an influence on the bubble size distribution at Level R, especially the mechanism of wake-entrainment. Furthermore, with the increase of superficial gas velocity, the contribution of wake-entrainment becomes more remarkable, which is the most important mechanism for the cases with high superficial gas velocity such as test point 107.

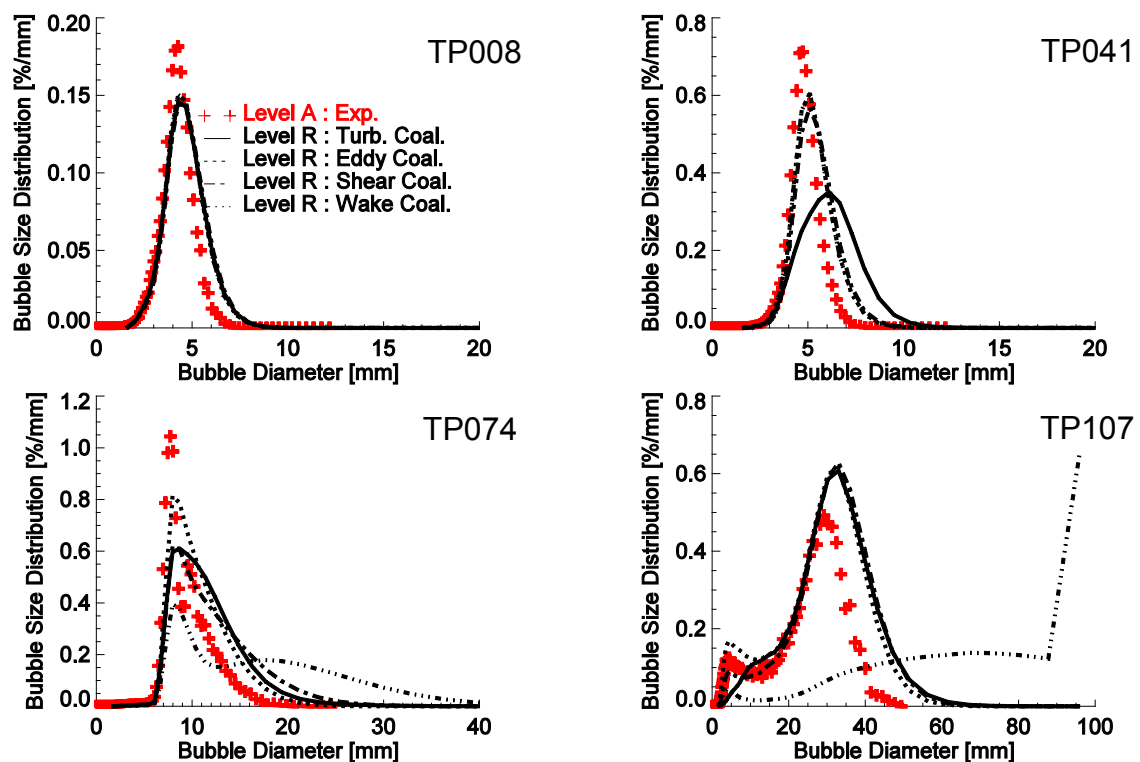


Figure 5.37 Contribution of each coalescence mechanism for different test points (breakup not included)

#### 5.4.11 Contribution of the mechanism of wake-entrainment

The influence of the coefficient  $C_{35}$  in Eq. 3-15 on the evolution of average bubble size in the axial direction of the pipe is depicted in Figure 5.38. Three different values are used for the coefficient  $C_{35}$ , which affects the coalescence rate caused by wake-entrainment. As it can be seen for the simulations at test point 074, predictions about

the average bubble size with the coefficient of 0.3, 0.1 and 0.05 are all smaller than the measurement. This indicates that the breakup rate caused by interfacial stresses (see Figure 5.36) is too large or that the contribution of other coalescence mechanisms is underpredicted. On the other hand, for test points with higher gas volume fractions, e.g. 107, 118 and 129, the value of  $C_{35}$  has a considerable influence on the evolution of average bubble size. In other words, wake-entrainment is the most important coalescence mechanism for these test points. The coefficient of 0.1 used for  $C_{35}$  delivers the best agreement with the experiment for the three cases.

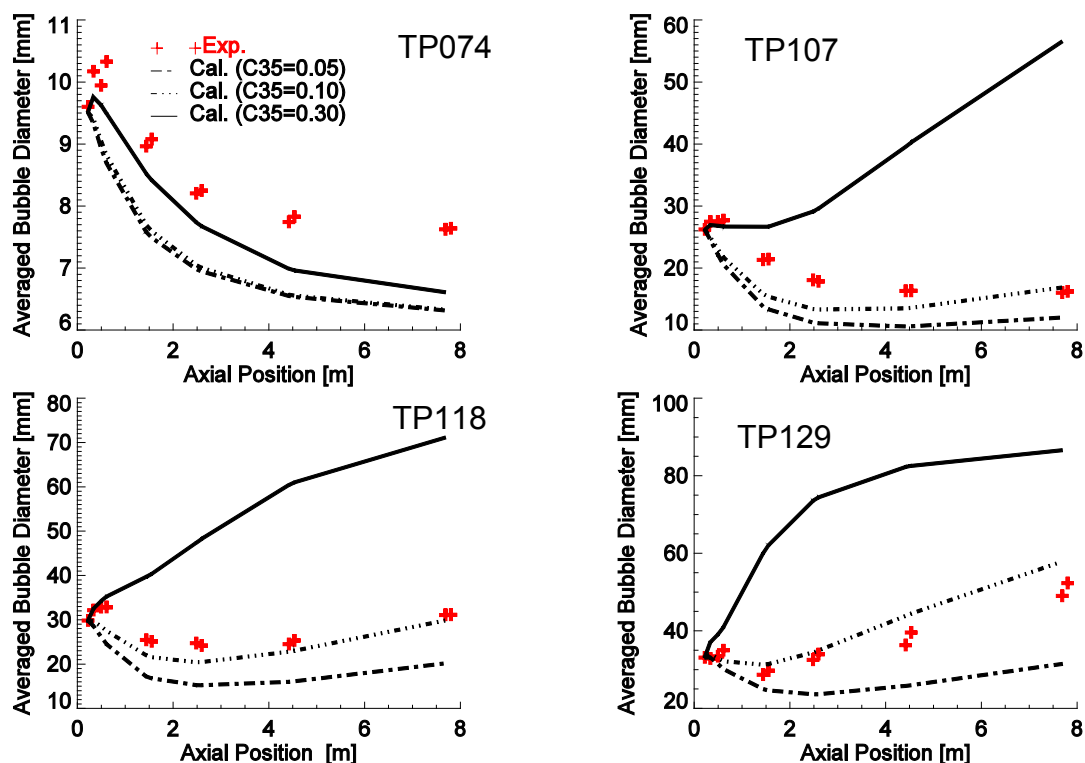


Figure 5.38 Influence of the coefficient for coalescence caused by wake-entrainment on the evolution of average bubble diameter in axial direction

#### 5.4.12 Influence of two-phase turbulence modeling

Turbulence is one of the most important mechanisms that lead to bubble coalescence and breakup in a turbulent gas-liquid flow. Turbulence parameters such as turbulence dissipation rate are important input parameters for bubble coalescence and breakup models. Therefore, it is necessary to study the influence of different two-phase turbulence modeling methods.

As discussed in §4.2, turbulence modulation induced by bubbles has to be considered in the turbulence modeling of bubbly flows. It may be taken into account by adding additional viscosity term or source terms to the  $k$  and  $\varepsilon/\omega$  transport equations. Various models for BIT source terms are implemented in the Test Solver and calculations are done for several test points with different superficial gas velocities. Since BIT turbulence is directly dependent on bubble size, for the first step models for bubble coalescence and breakup are not included to exclude the influence of bubble size. Some examples of the predicted turbulence parameters

such as turbulent kinetic energy, eddy dissipation rate and eddy viscosity as well as liquid velocity profile are shown below in Figure 5.43 ~ Figure 5.46.

### Time scale calculated by different BIT models

As discussed previously, the main difference between available models for BIT source terms lies in the adopted characteristic time scale  $\tau$ , which is shown in Figure 5.39 for different test points. It can be seen that the time scale computed by Eq. 4-29 and Eq. 4-30 is dependent on radial position as well as gas volume fraction. It decreases with an increase in the superficial gas velocity or in the dissipation rate  $\varepsilon$ . The average bubble size is used in Eq. 4-29 and Eq. 4-34. In addition, the time scale provided by the Troshko [163] model is independent on the radial position.

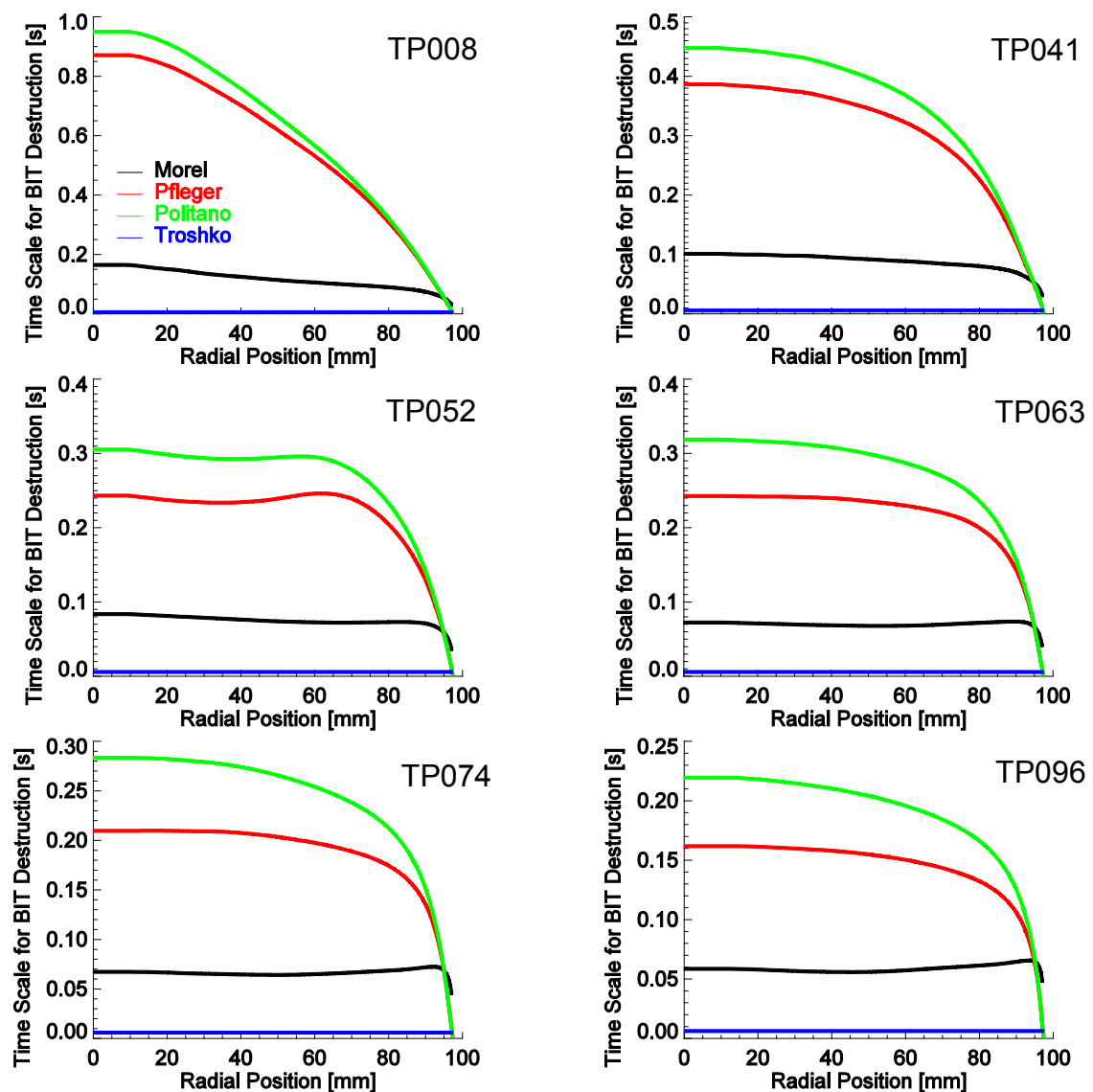


Figure 5.39 Time scale  $\tau$  for the destruction of BIT kinetic energy predicted by different BIT models (Level R)

Furthermore, the time scale calculated by the Morel [159] model is distinctly smaller than that by the models of Pflieger [157] and Politano [158]. That means that the additional energy dissipation rate introduced by bubbles is high and as a result the liquid eddy viscosity is low if the BIT energy production is comparable. As discussed

above, since the occurrence of low eddy viscosity or dispersion force will result in an unreasonable accumulation of bubbles at the pipe center, a BIT model with a small time scale might bring instability during the calculation. Therefore, as shown in Figure 5.40, for the case using the BIT model of Morel [159], one has to adjust the coefficient  $C_\varepsilon$  to a smaller value in order to achieve reasonable results, e.g. instead of 1.0 suggested by Morel [159] a value of 0.6 used in this work. For cases with small bubbles or low gas volume fractions the time scale predicted by the Troshko [163] model is even smaller than that by the Morel [159] model. As a result, in such a case the coefficient  $C_\varepsilon$  has to be adjusted to a value smaller than that used in the Morel [159] model to stabilize the calculation, e.g. a value of 0.06 used in this work. Figure 5.40 shows the influence of the coefficient  $C_\varepsilon$  on the radial profile of gas volume fraction calculated by the Morel [159] model. It can be seen that a small value of coefficient  $C_\varepsilon$  can help to dampen the unreasonable accumulation of large bubbles at the pipe center or the positive feedback between the gas volume fraction profile and the shear lift force.

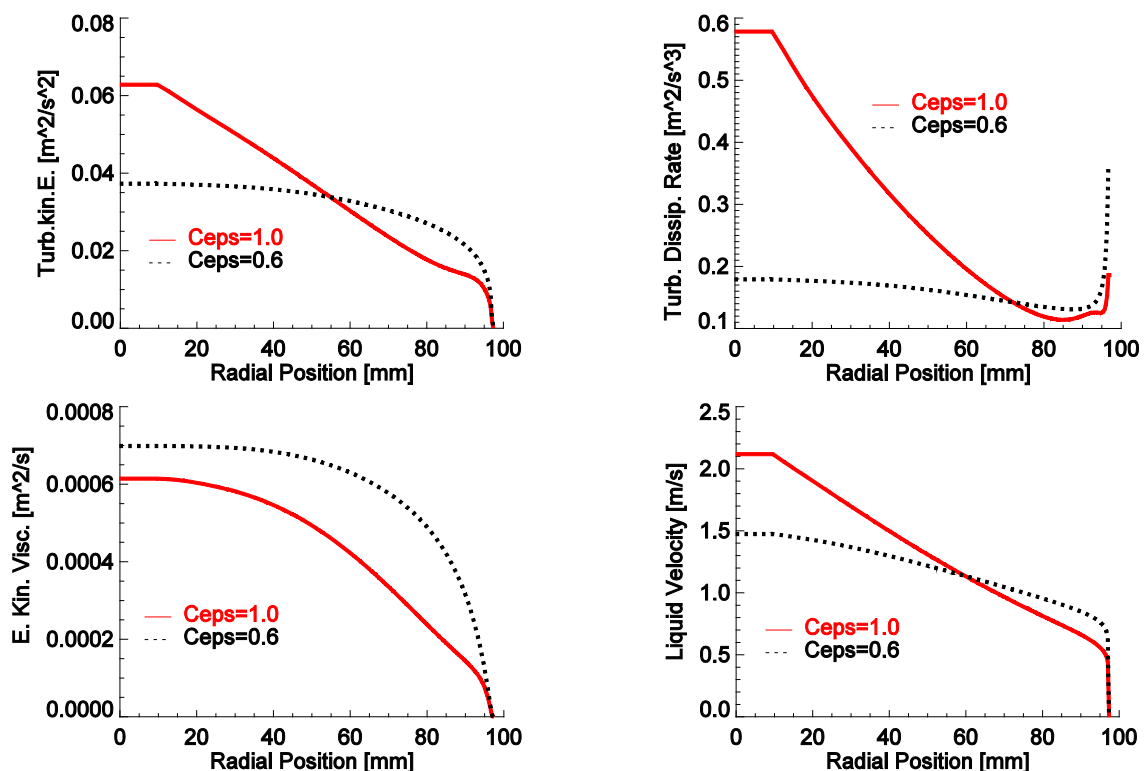


Figure 5.40 Influence of the coefficient  $C_\varepsilon$  on the turbulence parameters and liquid velocity profile (Morel [159] BIT model, Level R, TP063)

As shown below in Figure 5.41, the BIT kinetic energy according to different models has a similar dependence on the radial position for different test points. The fact that the absolute value calculated by the Pflieger [157] model is higher than that by the other models is caused by the coefficient  $C_k$  used in Eq. 4-27. The difference between the Politano [158] model and others becomes larger as the superficial gas velocity increases. This is caused by the fact that the drag coefficient is not included in the Politano [158] model (see Eq. 4-33), which increases with the bubble size. In addition, BIT kinetic energy provided by the model of Morel [159] is equal to that given by the Troshko [163] model.

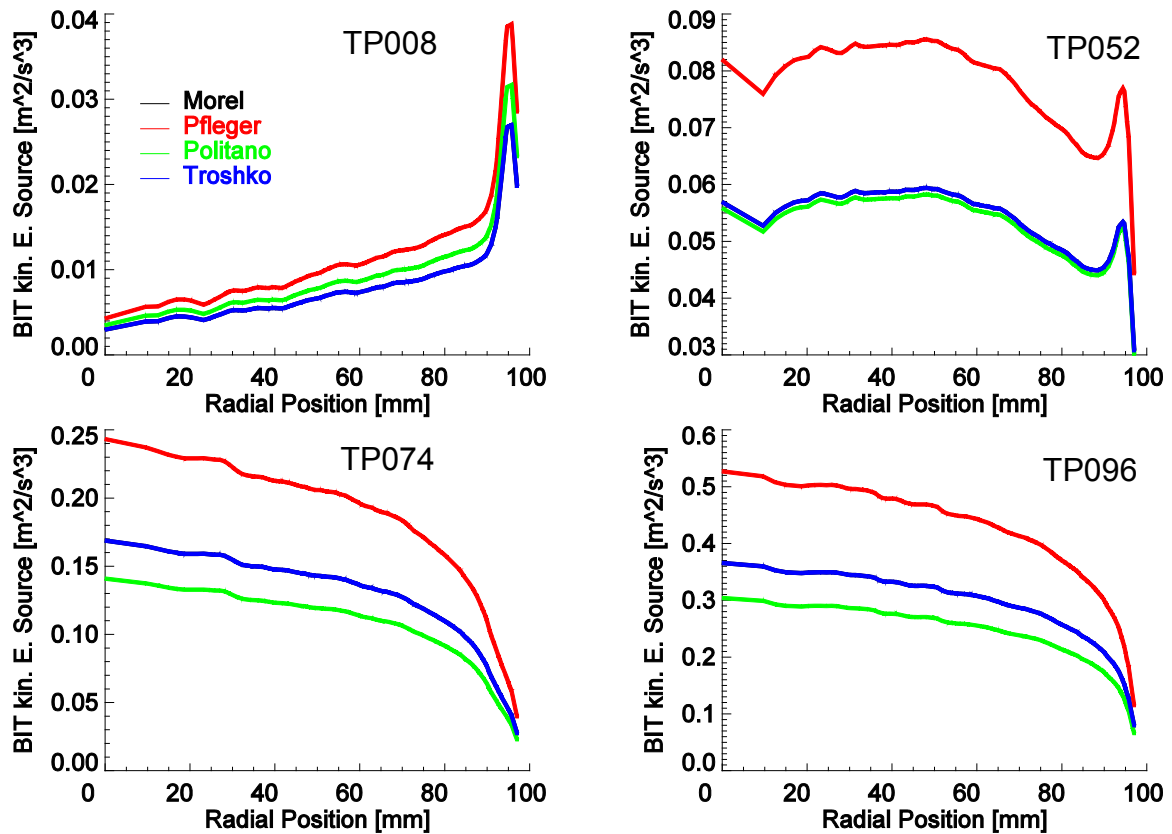


Figure 5.41 BIT source of kinetic energy predicted by different models (Level R)

Unlike the case of BIT kinetic energy, BIT dissipation rate is quite different from each other due to the time scale used by different models, see Figure 5.42. Generally speaking, the model of Pflieger [157] and of Politano [158] have a similar performance with a high peak at the near-wall region since the time scale calculated by Eq. 4-30 in this region is very small in comparison to that at the pipe center, see Figure 5.39. On the other hand, the BIT dissipation rate according to other two models of Morel [159] and Troshko [163] has a similar shape as the kinetic energy source shown in Figure 5.41 and the influence of time scale is trivial for a reduced  $C_\varepsilon$ .

### **Without bubble coalescence and breakup**

The turbulent kinetic energy of liquid phase calculated according to different BIT source models is depicted in Figure 5.43 for different test points. In general, at low gas volume fractions, turbulence is mainly generated by the classical shear production which increases with the eddy viscosity and velocity gradients while the additional BIT production source is negligible. For upward bubbly flow inside a vertical pipe, at low superficial gas velocity, liquid velocity profiles are more uniform than the profile of a single-phase with equal superficial liquid velocity, see Figure 5.46. Therefore, a suppression of shear-induced turbulence due to the existence of bubbles is observed in these cases such as test points 008, 041 and 052. The shear-induced turbulence is the lowest for test point 041 since its liquid velocity gradient is the smallest, see Figure 5.46. With the increase of the superficial gas velocity, the gas volume fraction turns into a core-peak profile, and bubbles at the pipe center will increase the velocity gradient in comparison to the case of single-phase flow. As a result, the shear-induced turbulence in the liquid phase increases as bubbles are introduced into the flow (see the comparison between the prediction without BIT

models and single-phase profile). Similar phenomena were observed in the experimental work of Shawkat et al. [177].

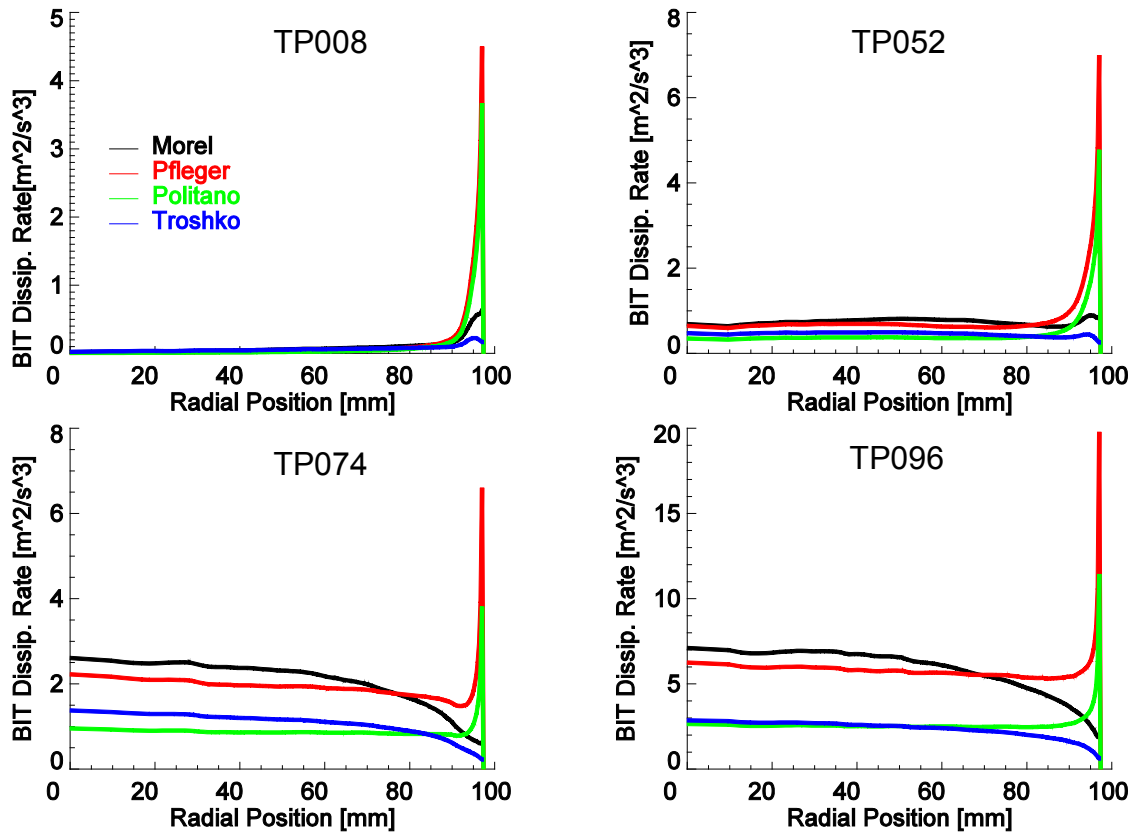


Figure 5.42 BIT source of dissipation rate predicted by different models (Level R)

On the other hand, as the number of bubbles introduced into the flow increases, e.g.  $\alpha_g > 1.0\%$ , the BIT source cannot be neglected any more. For example, from test point 041 on, the contribution of BIT to the overall turbulence is larger than that of the shear-induced turbulence and moreover, increases as the superficial gas velocity increases. However, the performance of different BIT models is quite different in the capture of the influence of BIT. For wall-peak cases, the Sato [8] model overpredicts the turbulent kinetic energy especially at the wall region because it considers the BIT turbulence by an additional viscosity term which directly influences the shear-induced turbulence while in the core-peak cases where the BIT turbulence is the most important the model gives an underprediction for the contribution of bubbles. In summary, the Sato [8] model can hardly describe the influence of bubbles on the liquid turbulence correctly.

As discussed above, the main difference of BIT models with additional source terms for  $k$  and  $\epsilon$  transport equations, e.g. models of Morel [156], Pflieger and Becker [157], and Politano et al. [158], lies in the characteristic time scale  $\tau$ . At the test points where the BIT begins to be important, e.g. test points 063 and 074, the turbulent kinetic energy predicted by the Morel [159] model is the largest at the pipe center and the liquid eddy viscosity is the lowest compared to other three approaches, see Figure 5.45. The low eddy viscosity will be a source of instability during the calculation by recalling the positive feedback between the lift force and gas volume fraction profiles due to insufficient dispersion. However, as the superficial gas



velocity increases further, both turbulent kinetic energy and dissipation rate will increase, but the kinetic energy increases more rapidly so that the liquid eddy viscosity increases. This will suppress the positive feedback and reduce the unreasonable peak of gas volume fraction at the pipe center. If this effect is successfully damped, the difference between the three BIT models with additional source terms for  $k$  and  $\varepsilon$  equation is only caused by the coefficients  $C_k$  and  $C_\varepsilon$ . For example, in the case of test point 096, the turbulent kinetic energy predicted by the Pflieger [157] model is larger than that by Morel and Politano [158] models. That is because  $C_{k,Morel}=C_{k,Politano}=1.0$  while  $C_{k,Pflieger}=1.44$ , and meanwhile the drag coefficient  $C_D$  is not included in the Politano [158] model, which is larger than 1.0. On the other hand, the Sato [8] model with additional viscosity term predicts the smallest BIT turbulent kinetic energy for test cases with large superficial gas velocities, and delivers a profile similar to that of neglecting BIT source.

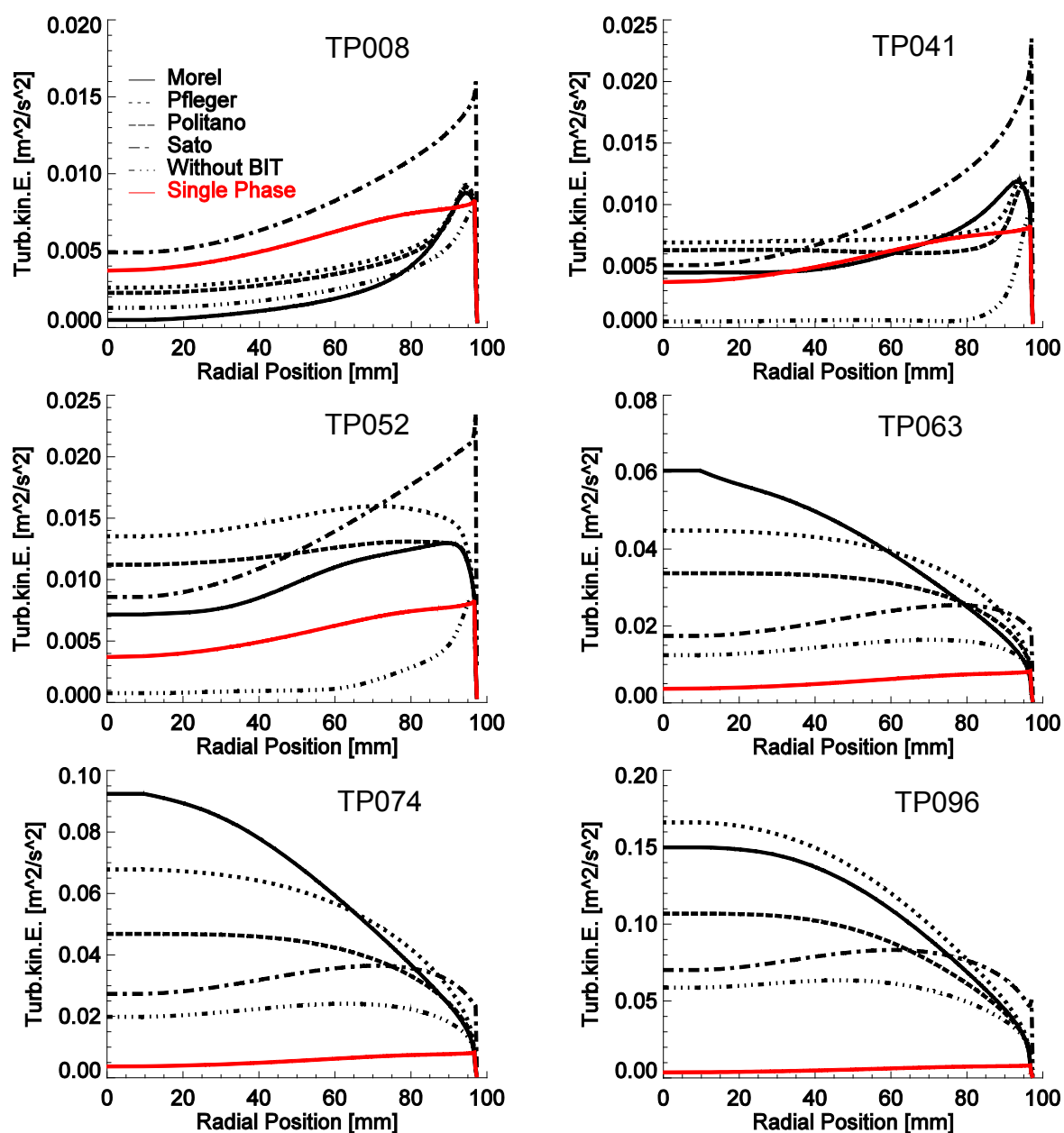


Figure 5.43 Turbulent kinetic energy predicted by different BIT models (Level R)

The turbulence dissipation rate predicted by different BIT models for several test points at Level R is shown in Figure 5.44. The influence of BIT models as well as superficial gas velocity is similar to the case of turbulent kinetic energy illustrated in Figure 5.43. At test point 008, the contribution of bubbles is negligible. From test point 041 on, the additional BIT dissipation rate has a significant contribution to the overall one, which is even higher than the classical shear-induced dissipation. As the superficial gas velocity increases further (e.g. test point 063), shear-induced dissipation rate also increases due to an increase in the shear-induced production at high liquid velocity gradients. For test points 063 and 074, the accumulation of large bubbles at the pipe center, which is caused by the positive feedback due to a surplus of the lift force compared to the turbulence dispersion, results in a higher dissipation rate by the Morel [159] model. For test point 096, the dissipation rates predicted respectively by the Morel [159] and the Pflieger [157] models are similar to each other and larger than that by the Politano [158] model. The difference is mainly caused by the time scale  $\tau$ , the turbulent kinetic energy  $k$  as well as the prefactor  $C_\varepsilon$ . Again, the Sato [8] model gives an overprediction of dissipation rate in the near wall region due to the additional viscosity term described in Eq. 5-4.

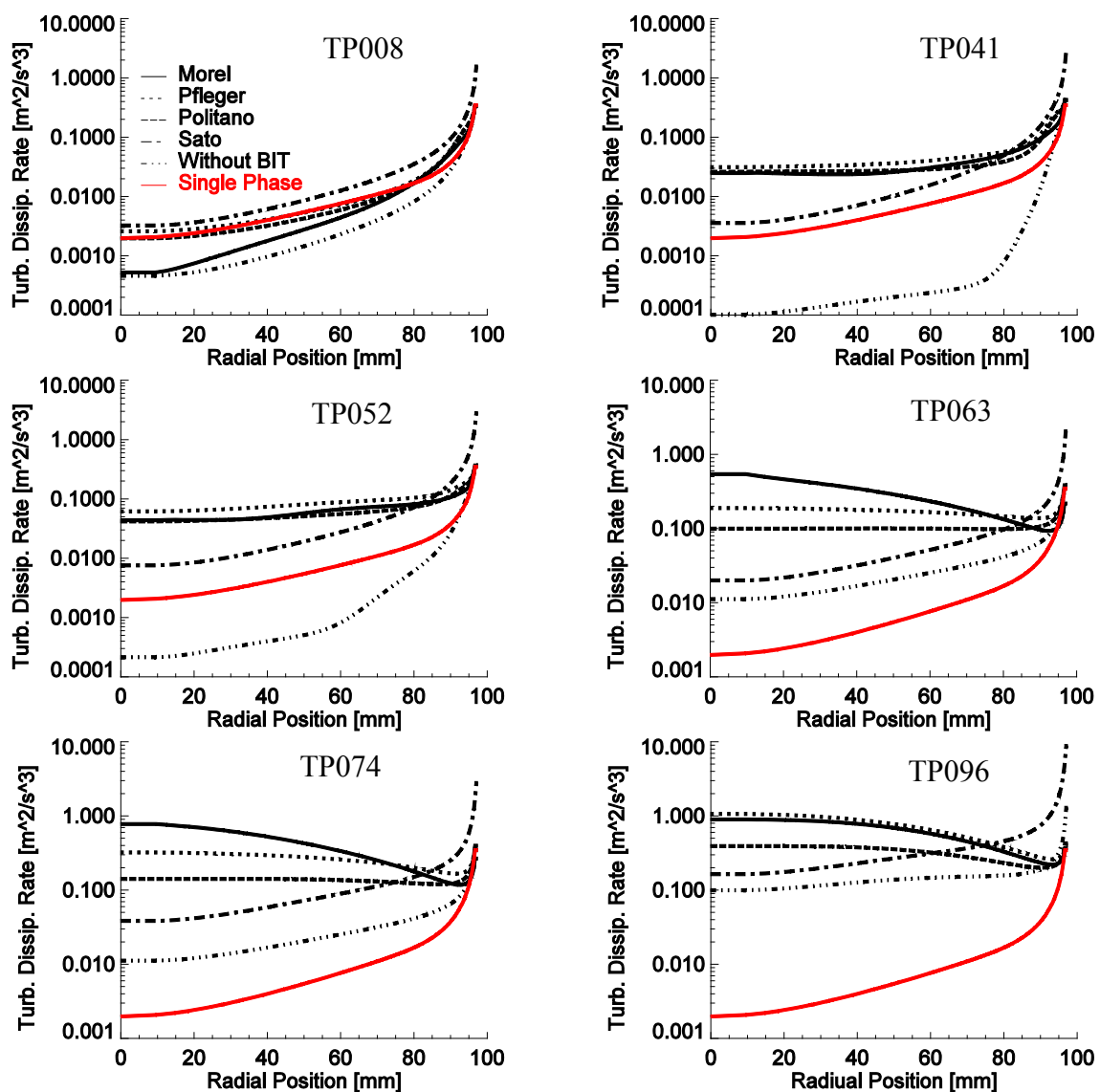


Figure 5.44 Turbulence dissipation rate predicted by different BIT models (Level R)

As it shows in Figure 5.45, the Sato [8] model gives a maximum viscosity for all cases while the Morel [159] model always has the smallest value for the chosen test points, but its difference to other models decreases at the superficial gas velocity increases. At low gas volume fractions, e.g. test points 008, 041 and 052, the approach with additional source term for  $k$  and  $\epsilon$  shows a suppression of eddy viscosity by the introduction of bubbles which is already proved experimentally [177]. On the other hand, the Sato [8] model with an additional viscosity term cannot reproduce this effect, while it always delivers a viscosity larger than that of single-phase flow. Furthermore, it is reasonable to observe that the liquid eddy viscosity increases with the superficial gas velocity or gas volume fraction, since it is proportional to the square of the turbulent kinetic energy, which increases with the gas volume fraction. Furthermore, the increasing speed according to the Sato [8] model is the largest followed by the Morel [159] model. The eddy viscosity calculated by the Pflieger [157] and Politano [158] models increases more slowly with an increase in the gas volume fraction than that by the Morel [159] model. That means that the energy dissipation rate predicted by the two models increases more rapidly.

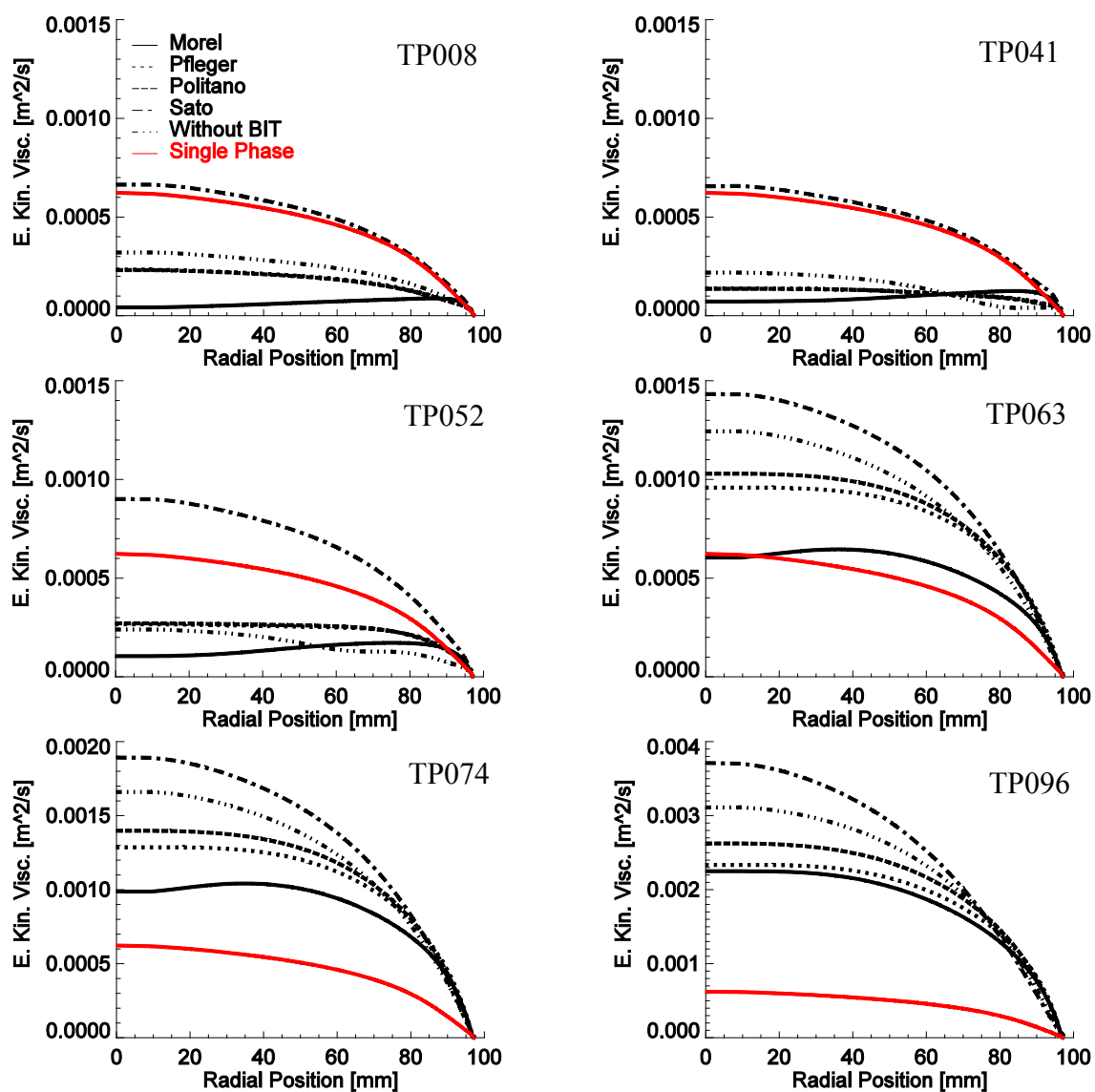


Figure 5.45 Liquid eddy viscosity predicted by different BIT models (Level R)

Liquid velocity profile predicted by different BIT models is shown in Figure 5.46. For the test points with low superficial gas velocities, where the bubble size is small, bubbles locate preferably in the near wall region. This will smooth the liquid velocity profile and dampen the turbulence intensity. As the bubble size increases with the superficial gas velocity, large bubbles will migrate to the pipe center under the effect of the lift force, and increase the liquid velocity gradient and thus the turbulence intensity.

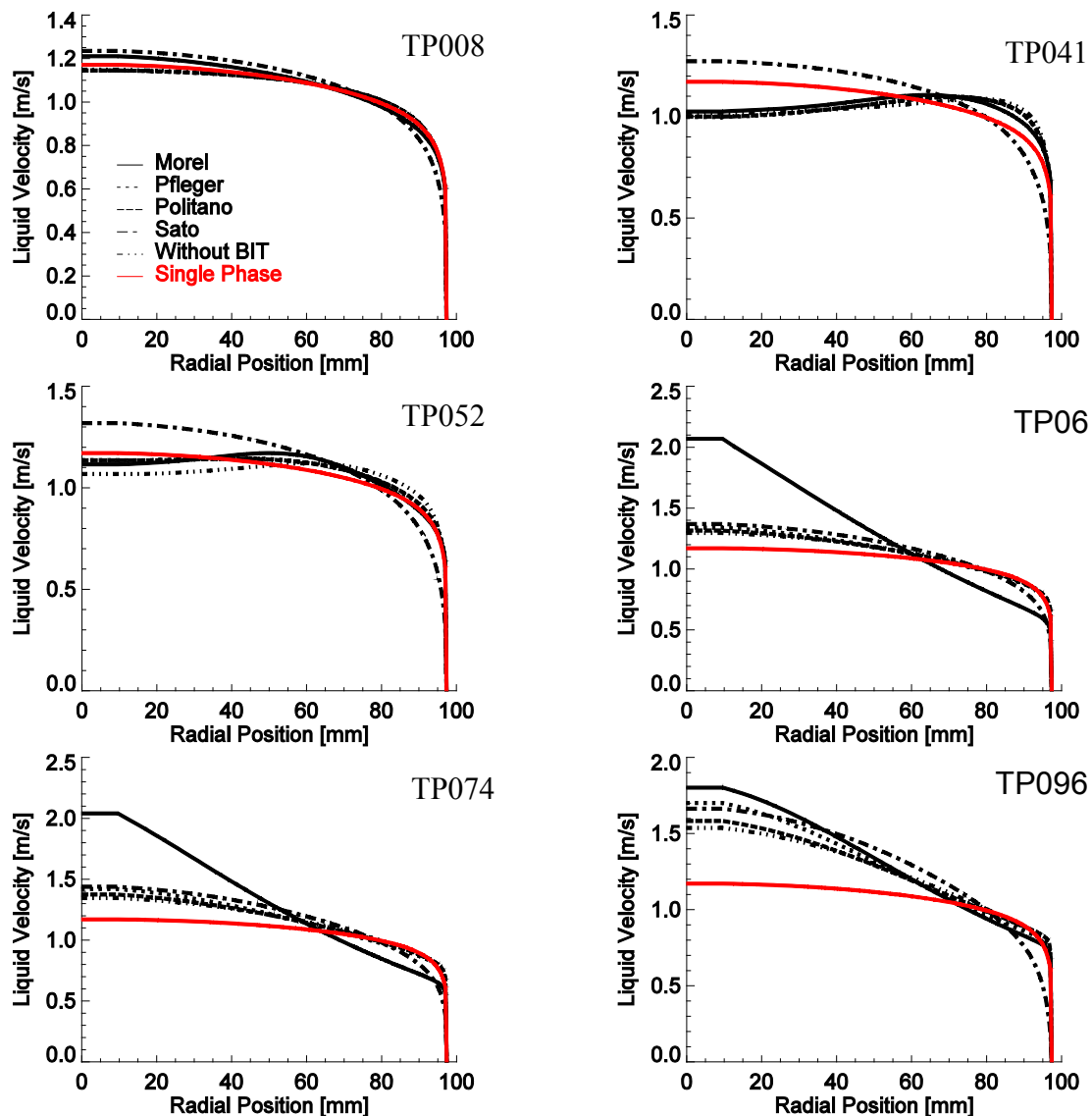


Figure 5.46 Liquid velocity profile predicted by different turbulence models (Level R)

### **With bubble coalescence and breakup**

By including bubble coalescence and breakup models, predictions with different BIT models are performed for four different test points. The influence of the BIT models on the evolution of average bubble size is shown in Figure 5.47. As it can be seen from the comparison between different test points, the influence of BIT is trivial for the test points with small superficial gas velocity and increases with an increase in the superficial gas velocity. This is reasonable since the BIT turbulence increases with the gas volume fraction. Moreover, the main contribution of turbulence to the

evolution of bubble size is to increase the breakup rate, which begins to take effect at a high superficial gas velocity, see Figure 5.37 and Figure 5.38.

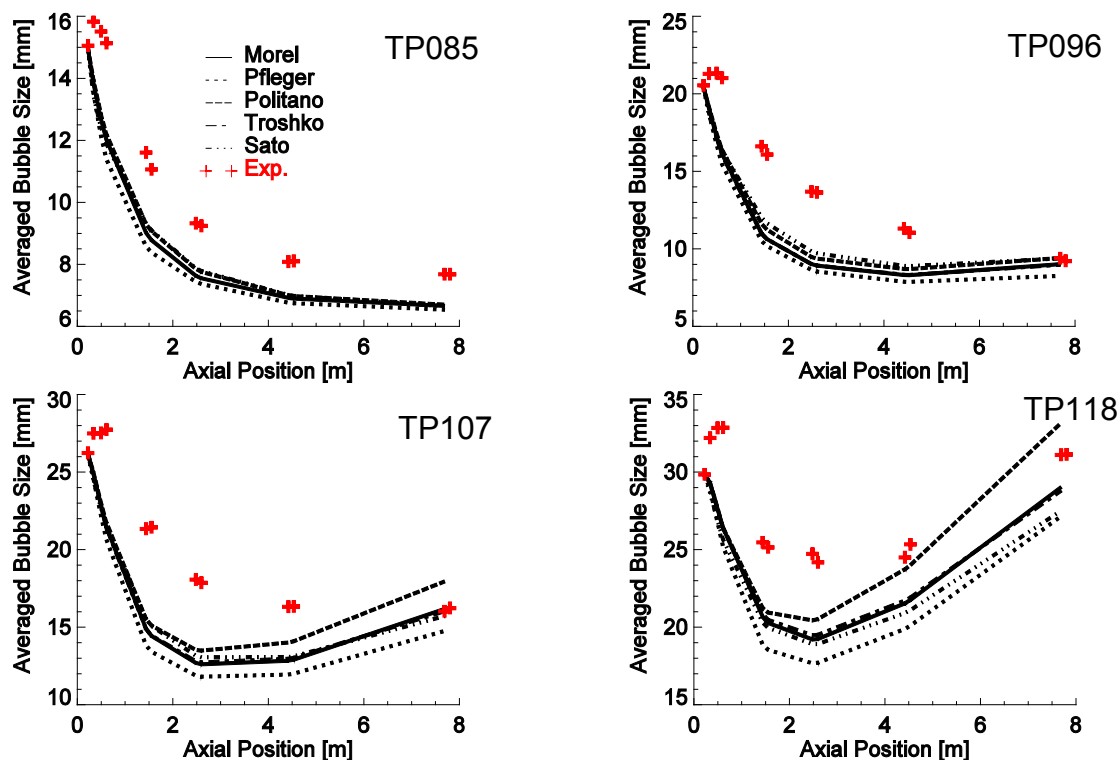


Figure 5.47 Influence of BIT models on average bubble size

For the test point 118, the average bubble diameter is the largest if the Politano [158] BIT model is used, while it is the smallest if the Pflieger [157] model is used. That means that the turbulence dissipation rate predicted by the Pflieger [157] model is larger than that by the Politano [158] model, since the turbulence-induced breakup rate is directly determined by the dissipation rate. The results predicted by the model of Morel [159] and of Troshko [163] are similar to each other if the value of 0.6 and 0.06 is used for  $C_\epsilon$  in two models, respectively. On the other hand, at low gas volume fractions, the Sato [8] model delivers a slightly large mean bubble size with comparison to other three models. However, the bubble size, which is predicted by using the Sato [8] BIT model, decreases more rapidly than the other models, as the superficial gas velocity increases. That means that the dissipation rate calculated by Sato [8] model increases more rapidly than the other kind of models with the increase of superficial gas velocity.

In Figure 5.48 and Figure 5.49, the radial profiles of gas volume fraction and gas velocity are predicted by different BIT models. In comparison to the case of bubble size shown in Figure 5.47, the influence of BIT models on gas volume fraction and velocity is more intuitive, since the turbulence models directly influence the turbulent dispersion force, which determines the radial migration of bubbles. Firstly, as shown in Figure 5.49 the Sato [8] model delivers a low value of liquid velocity near the pipe wall, which implies a large profile parameter  $C_0$  and average drift velocity in the drift-flux model. As a result, the cross-sectional average of the gas volume fraction calculated by the drift-flux model is lower than that by other models.

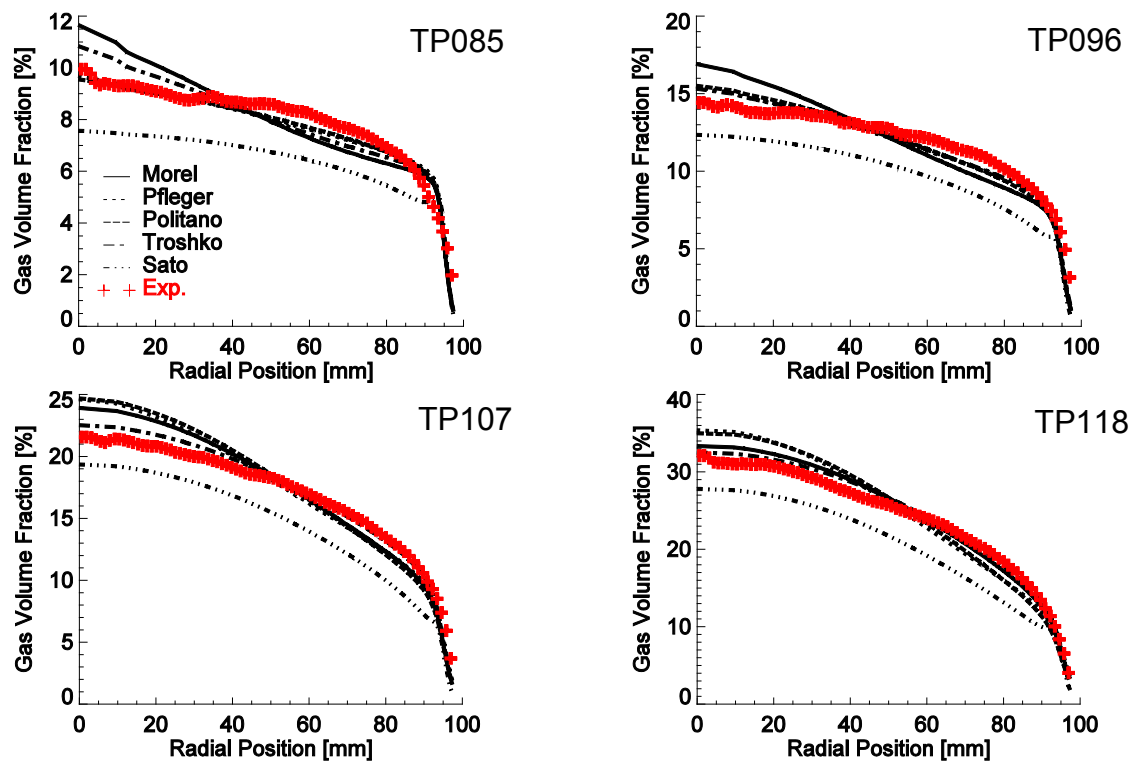


Figure 5.48 Influence of BIT models on radial gas volume fraction profile(Level R)

On the other hand, for cases with low superficial gas velocity, e.g. test point 085, the gas volume fraction at the pipe center predicted by Morel's [159] and Troshko's [163] model is higher than the measurement, while the models of Pflieger [157] and Politano [158] achieve a better agreement. This is because for this test case, the turbulent dispersion calculated by the first two models is a little bit too weak as shown in Figure 5.52. However, as the superficial gas velocity increases the eddy viscosity predicted by the Morel [159] model and Troshko [163] model increases more rapidly than that by the other two models and overtakes it at the test point 107. As a result, for this case, the radial gas volume fraction is more flat than that given by the Pflieger [157] and Politano [158] models.

The influence of BIT models on the radial gas velocity profile is shown in Figure 5.49. For the chosen test points, the influence of different BIT models is negligible except that the Sato [8] model predicts too low a velocity in the near wall region. This is because according to the Sato [8] model bubbles are dispersed far away from the pipe wall by the turbulent dispersion force due to a large viscosity, see Figure 5.52. The Morel [159] and Troshko [163] models overpredict the fractions at the pipe center for test points with low gas fractions such 085 and 096. For test points with high gas volume fractions such as 107 and 118, the overprediction occurs when the Pflieger [157] and Politano [158] models are used. The explanation is the same as that used for the radial gas volume fraction profile in Figure 5.48, i.e. too weak a turbulent dispersion force, but the root cause is the definition of time scale adopted by different models.

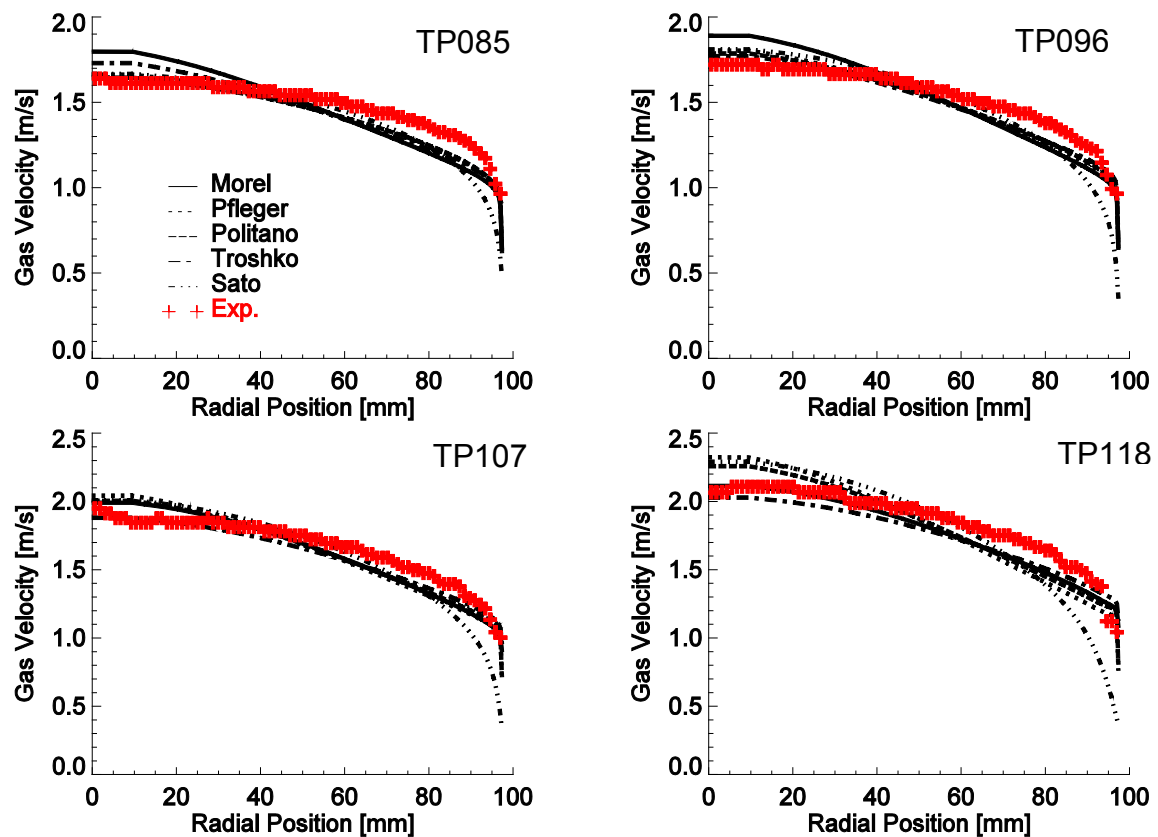


Figure 5.49 Influence of BIT models on radial gas velocity profile (Level R)

The turbulence parameters, i.e. turbulent kinetic energy, dissipation rate and eddy viscosity calculated by using the  $k-\varepsilon$  model with additional BIT source or additional viscosity terms are depicted in Figure 5.50 ~ Figure 5.52, respectively.

The influence of BIT models on the turbulence parameters is more intuitive than that on bubble size and gas volume fraction. As shown in Figure 5.50, the turbulent kinetic energy predicted by using the BIT model of Pflieger [157] is the largest for all chosen test points while the smallest if the Sato [8] model used. The results given by the Morel [159] and Troshko [163] models are similar to each other and larger than those by the Politano [158] model. For test points with low gas volume fractions, the prediction delivered by the Morel [159] and Troshko [163] models are close to that of Politano [158] model while for high gas volume fractions cases they are close to that of Pflieger [157] model. That means that the kinetic energy predicted by the former two models increases more rapidly than that by the latter two ones as the superficial gas velocity increases from 0.0574m/s to 0.219m/s. The main reason is that the dissipated energy increases more rapidly according to the Politano [158] and Pflieger [157] models, see Figure 5.51.

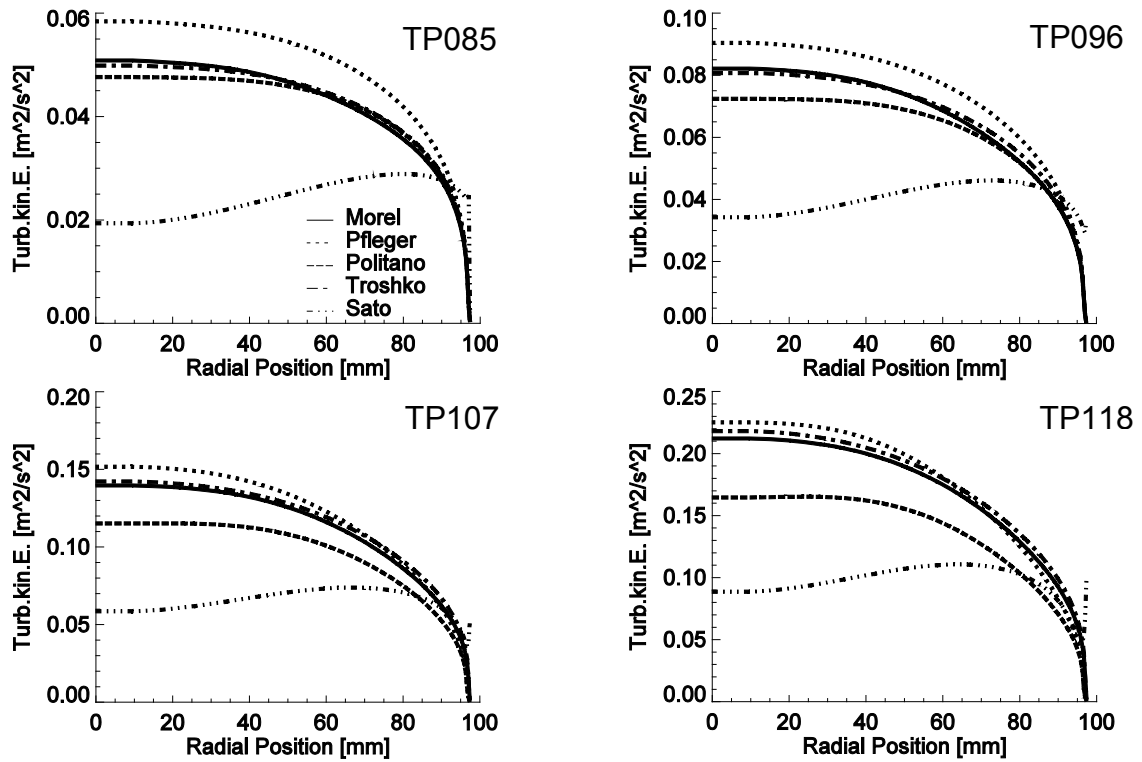


Figure 5.50 Influence of BIT models on the turbulent kinetic energy (Level R)

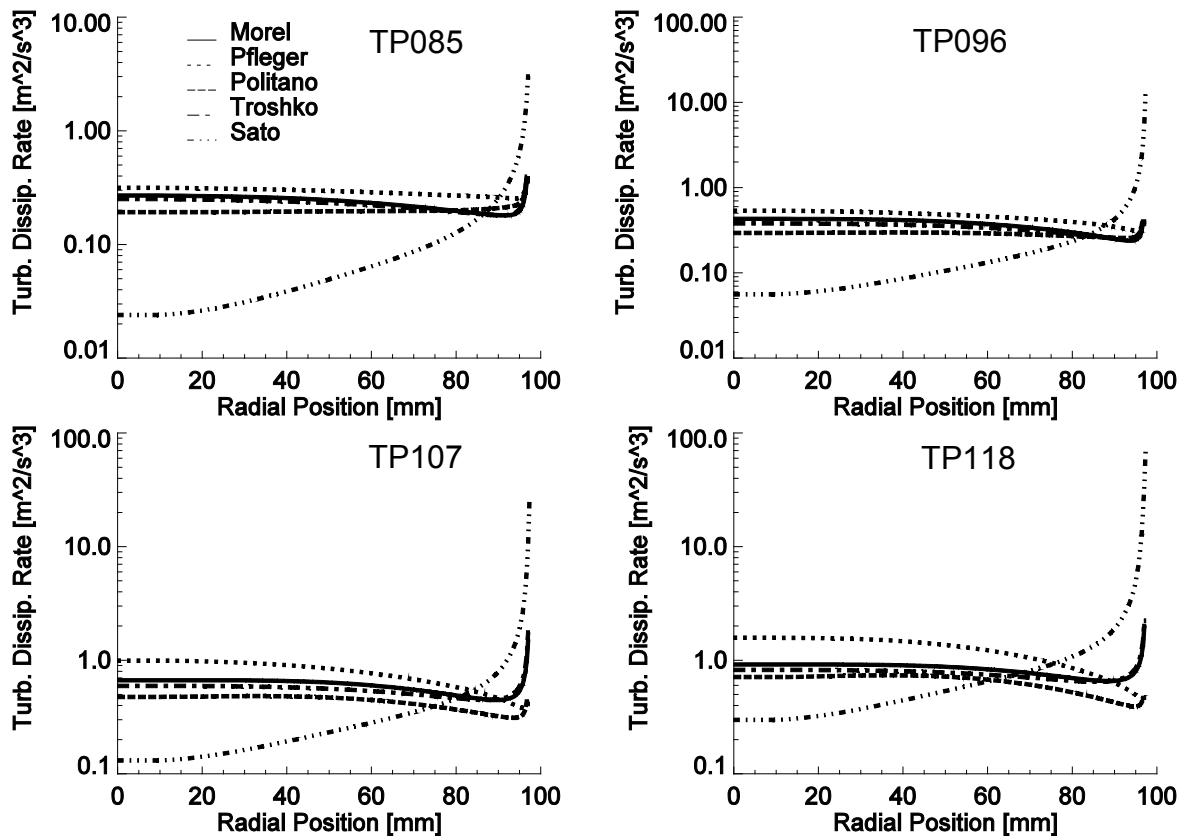


Figure 5.51 Influence of BIT models on liquid turbulence dissipation rate (Level R)



From Figure 5.51 one can see that in comparison to other four models, the model of Sato [8] gives too small a value at the pipe center while too large a one in near-wall region. That is because that according to the Sato [8] model, the influence of bubbles on the turbulent kinetic energy and dissipation rate is only considered by the viscosity in the turbulence production term, which might be not enough for the pipe center since there the velocity gradient is almost zero, while it is too strong for the high shear region. In addition, the predicted dissipated energy increases with the superficial gas velocity, but the increasing speed according to the Sato [8] model is the largest and followed by the Pflieger [157] model. On the other hand, the dissipation rate calculated respectively by the model of Morel [159] and of Troshko [163] increases more slowly as the superficial gas velocity increases. Therefore, at test point 118 the liquid eddy viscosity predicted by the two models exceeds that by the model of Pflieger [157] and Politano [158], see Figure 5.52.

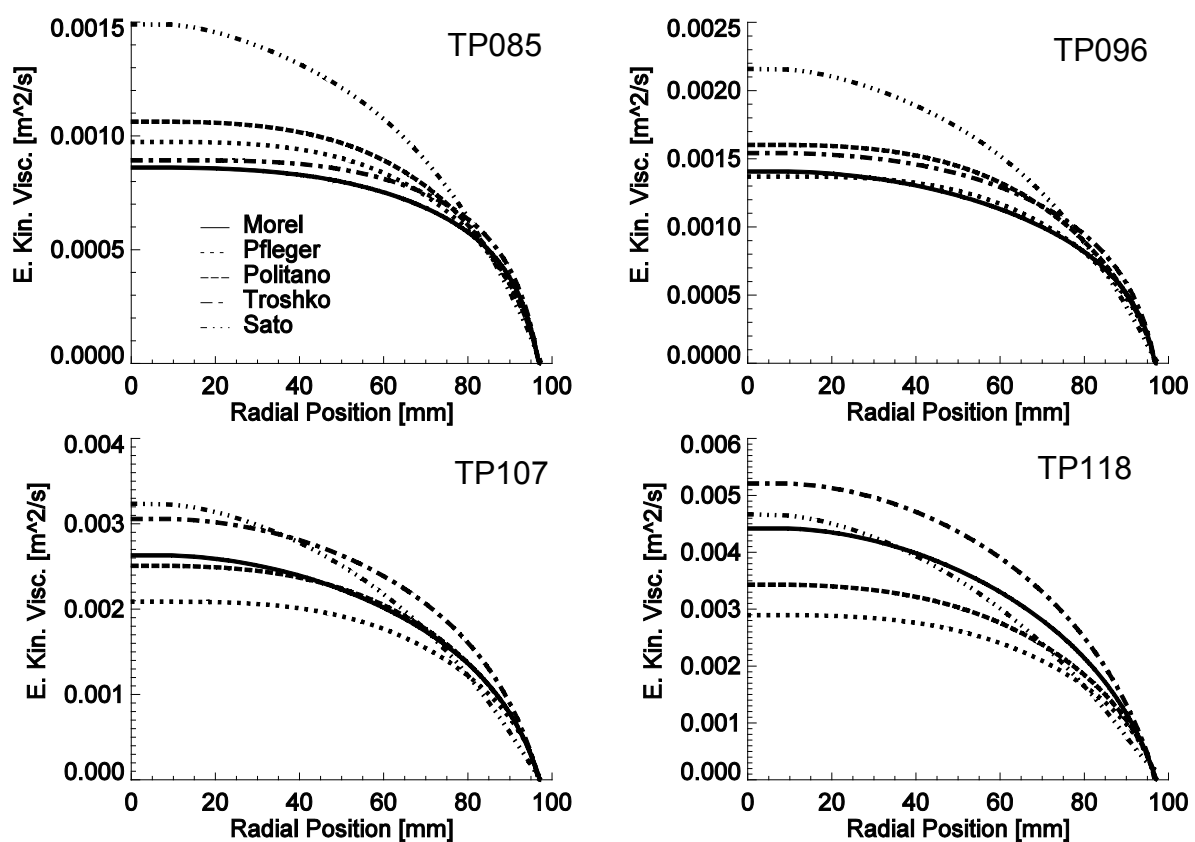


Figure 5.52 Influence of BIT models on liquid eddy kinematic viscosity (Level R)

As discussed above, too low a viscosity will result in an overprediction of gas volume fraction at the pipe center while too large a viscosity will cause a uniform distribution. As shown in Figure 5.52, for test points with low gas volume fractions such as TP085, the eddy viscosity calculated according to the Sato [8] model is in general the largest while that by the Morel [159] model is the smallest. However, as the superficial gas velocity increases from the test point 085 to 118, the viscosity provided by the model of Morel [159] and of Troshko [163] increases much faster than that by the Politano [158] and the Pflieger [157] models. As a result, the viscosity calculated by the Pflieger [157] model is the smallest while that by the Troshko [163] model is the largest for the test point 118.

## 5.5 Discussions

By using the simplified Test Solver, a comparative study of available bubble coalescence and breakup models is carried out for the case of upward vertical pipe flow. The bubble size distribution as well as the average bubble diameter as a function of axial position is studied by nine different combinations of three couples of the most popular models. Since under adiabatic conditions bubble coalescence and breakup is the single source or sink responsible for the change of bubble size distribution, the position of the peak of the bubble size distribution as well as the cross-sectional averaged bubble diameter can affect the equilibrium between bubble coalescence and breakup. With a higher breakup rate, the peak moves from a larger bubble size to a smaller bubble size since there are more breakup events. As a result, the average bubble diameter decreases. With higher coalescence rates, the peak moves from a smaller bubble size to a larger bubble size since there are more coalescence events, and the average bubble diameter increases. Therefore, from Figure 5.15 ~ Figure 5.22, one can see that the breakup rate predicted by Prince and Blanch [36] is much higher than that by Lehr's [31] and Luo's [95] models. For small bubbles, the breakup rates predicted by the latter two models are comparable with each other but the breakup rate predicted by Luo's [95] model increases more slowly as bubble size increases so that for large bubbles the breakup rate predicted by the Lehr's [31] model is larger than that by the Luo's [95] model. On the other hand, the coalescence rates given by the model of Prince and Blanch [36] and of Luo and Svendsen [175] are much higher than that by Lehr et al. [31]. For large bubbles, the coalescence rate given by Prince's [36] model is larger than that by Luo's [175] model. However, the coalescence rate predicted by Luo's [175] model decreases more slowly as bubble size decreases so that for small bubbles the coalescence rate predicted by Luo's [175] model is slightly larger than that by Prince's [36] model.

In summary, the performance of various models for bubble coalescence and breakup is quite inconsistent for different combinations of gas and liquid superficial velocities. The predicted results severely depend on the chosen models, and the dependence on bubble size is inconsistent. That means that some models give good predictions for small bubbles, while others are more suitable for large bubbles.

Finally, the new model for bubble coalescence and breakup is extensively examined in the Test Solver. Simulations are performed for a large number of test points with different combinations of gas and liquid superficial velocities. Predictions about the evolution of bubble size distribution, average bubble size, radial gas volume fraction and velocity profile are compared with the measurement correspondingly. In addition, the influence of bubble forces (turbulence dispersion, lift and wall lubrication force) and BIT turbulence models on the predicted bubble size and gas volume fraction is analyzed. Furthermore, the contribution of each coalescence / breakup mechanism to the evolution of bubble size distribution of different test points is studied in detail. Generally speaking, a relatively good agreement between the prediction and the measurement is achieved for all test points.

However, as it can be seen from Figure 5.23 and Figure 5.26, for the coalescence-dominant cases such as test points 008 ~ 052, the predicted bubble size is larger than the measured one while for breakup-dominant cases with higher superficial gas velocity, the predicted bubble size is smaller than that in the measurement. From the

analysis of the contribution of each of coalescence / breakup mechanisms, see Figure 5.36 and Figure 5.37, it can be supposed that the mechanism of turbulence could introduce deviations in the coalescence-dominant cases, since the turbulence-induced coalescence is the most important one for these cases. On the other hand, the mechanism of interfacial stresses might be responsible for the overestimation of breakup rate in breakup-dominant cases. In addition, the bubble size is in general overestimated at the upper section of the pipe for the cases where the mechanism of wake-entrainment plays an important role. Furthermore, the deviation with the experimental data increases as the superficial gas velocity increases. That means that the coalescence rate predicted by wake-entrainment is overpredicted by the new model for high superficial gas velocities.

On the other hand, the peak of the predicted gas volume fraction at Level R for wall-peak cases, see Figure 5.29, is lower than the measured one. This discrepancy indicates that the wall lubrication force calculated according to the correlation of Tomiyama [151] is too large for small bubbles. In addition, the redistribution process of gaseous phase from the injection position at the pipe wall to the whole cross section is overestimated, especially for cases with large gas volume fractions (Figure 5.31). The bubble migration velocity is found to be dependent on the bubble forces, i.e. turbulent dispersion, lift and wall lubrication forces (see Figure 5.33 ~ Figure 5.35). Generally speaking, the turbulent dispersion force has an effect of smoothing the radial distribution of gaseous phase. For small coefficients, the redistribution of gaseous bubbles will be retarded. However, this will result in an unreasonable peak of gas volume fraction at pipe center in comparison with the experiment. This is caused by the accumulation effect of the lift force under the negative velocity gradient in an upflow. For a small lift force, the spread of the gas volume fraction will be accelerated in the immediate vicinity of the injection position for large superficial gas velocities. This is because the injection at large superficial gas velocities will cause an increase in the liquid velocity near the pipe wall and result in a positive velocity gradient in the radial direction. In this case, large bubbles will be kept in the near-wall region under the effect of lift force. On the other hand, as the two-phase mixture flows away from the injection position, the liquid velocity profile forms a core-peak, i.e. negative velocity gradient. In this case, a smaller lift force will suppress the accumulation of large bubbles at the pipe center and smooth the radial profile of gas volume fraction. Finally, if the wall lubrication force is too strong, most of bubbles are pulled far away from the wall and the force has a remarkable influence on the redistribution of the gaseous phase over the whole cross section. By reducing the wall lubrication force by one-half, the migration of the gas can be decelerated and at the same time the agreement with measurement is improved at the pipe center. In addition, Eq. 4-12 proposed by Wellek [152] used for the calculation of the horizontal extension of a deformed bubble will contribute to the overestimation of the migration of spherical-cap or Taylor bubbles from the pipe wall to the center, since this correlation is only valid for ellipsoidal bubbles.

## 6 Validation of the new model in ANSYS 12.1 CFX-Solver

In this work, the generalized new model for bubble coalescence and breakup is implemented in the commercial CFD code ANSYS CFX-12.1 through user FORTRAN subroutines. They serve to supplement the inhomogeneous MUSIG approach, which is available in CFX as a beta feature, with alternative closure models. Simulations are carried out for air-water flows in a large upward vertical pipe under steady-state conditions. Both air and water are considered as isothermal. In order to take into account the pressure expansion of gas volume fraction with the increasing pipe height, air is considered as a compressible ideal gas. All simulations are computed with fluid-specific turbulence models, i.e. k- $\epsilon$  or SST turbulence model for the continuous phase whereas zero-equation dispersed phase turbulence model for the gaseous phase.

Simulations are carried out for several TOPFLOW test cases with different combinations of gas and liquid superficial velocities, e.g. test points 072, 074, 083, 085, 094, 096 and 118 (see the test matrix in Table 4.2). The results are compared with the experimental data as well as the results provided by the Test Solver and the standard closure models in CFX. The new model is shown to be capable of capturing the evolution of the bubble size distribution and the gas volume fraction along the pipe and notable improvements are observed with comparison to the results provided by the standard closures.

### 6.1 Setups

For swifter computations, a mesh of a 1 m long pipe is used for the mesh study and simulations in the first phase. Further simulations are also run on an 8m pipe in order to obtain the comparison between the predicted results and the measured ones over the whole test section of TOPFLOW facility.

#### 6.1.1 Mesh details

By assuming that the flow inside the pipe is axisymmetric, a 2D geometry mesh is chosen for the calculation. It is a small sector of the cylindrical pipe geometry with an opening angle of 5 degrees consisting of one layer of cells in the circumferential direction. The details of the mesh resolution are shown in Table 6.1 and non-uniform distribution of mesh cells is adopted (see Figure 6.1). In order to study the influence of space discretization on the numerical results, four different meshes are used for the mesh study of 1 m pipe flow and the results can provide a reference for the 8m pipe simulations.

Table 6.1 Mesh information

Mesh No.	Height of the Pipe [m]	Total nodes	$\Delta x_{\max}$ [mm]	$\Delta x_{\min}$ [mm]	$\Delta z_{\max}$ [mm]	$\Delta z_{\min}$ [mm]
1	1.0	25x50x2	9.49556	1.2	52.608	5
2	1.0	36x50x2	6.2682	0.9	52.608	5
3	1.0	50x50x2	5.08147	0.5	52.608	5
4	1.0	25x100x2	9.49556	1.2	39.062	3
5	8.0	36x500x2	6.2682	0.9	41.531	4

x: radius direction; z: axial direction

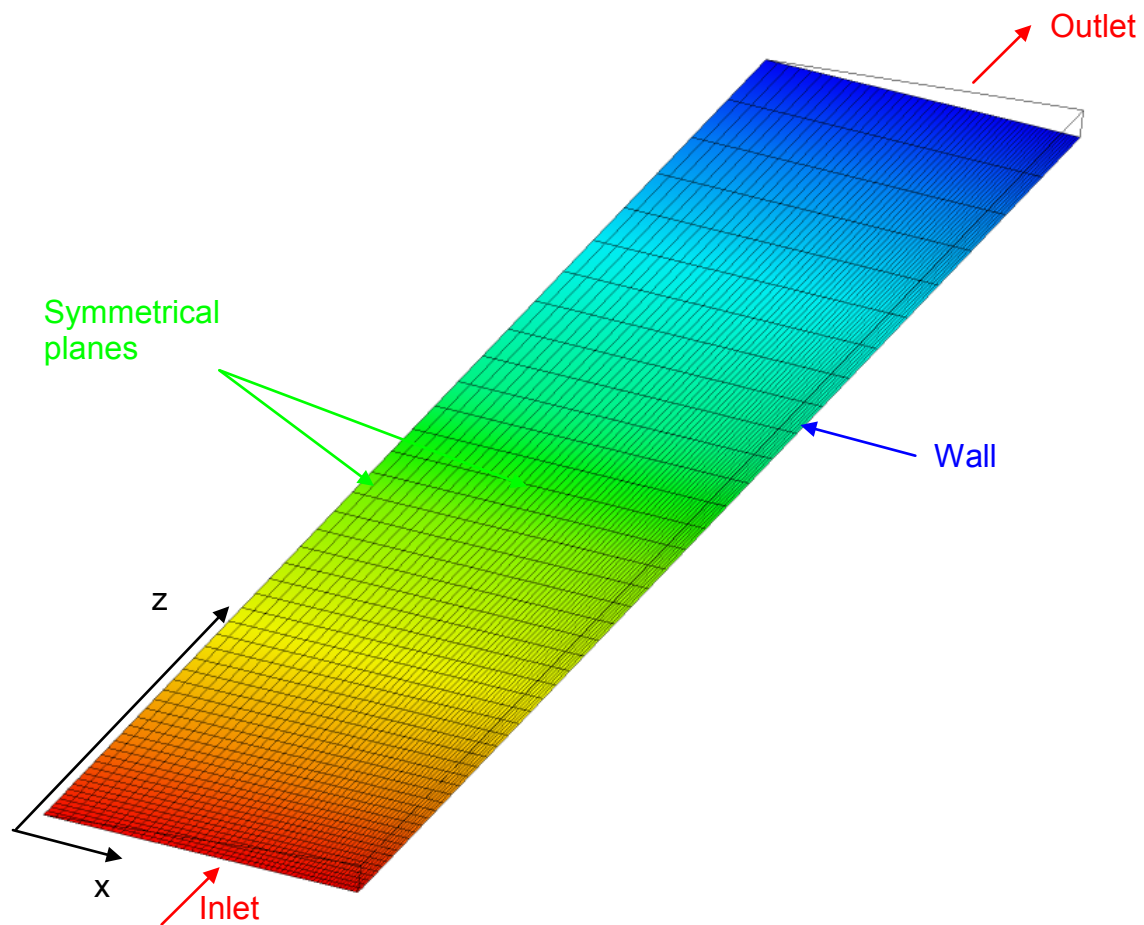


Figure 6.1 2D mesh for a 5° axial-symmetric sector of the vertical pipe geometry

The results of mesh study are shown in Figure 6.2. The influence of meshes 1, 2, 3 and 4 described in Table 6.1 on the prediction of bubble size distribution, average bubble size, gas volume fraction, gas velocity as well as turbulence parameters is illustrated. It can be seen that all the four meshes deliver almost identical results except for a small deviation at the near-wall region. For example, mesh 1 and mesh 4 with 25 nodes in the radial direction give a smaller value for the turbulence dissipation rate near the wall than the other two meshes. The results show that the number of nodes in the radial direction has a stronger effect than that in the axial direction. A mesh with  $\Delta x_{\max} \leq 6.2682$  mm and  $\Delta x_{\min} \leq 0.9$  mm can provide mesh-independent predictions. According to the conclusion, the mesh 3 and mesh 5 are used in this work for the 1 m and 8 m pipe simulations, respectively.

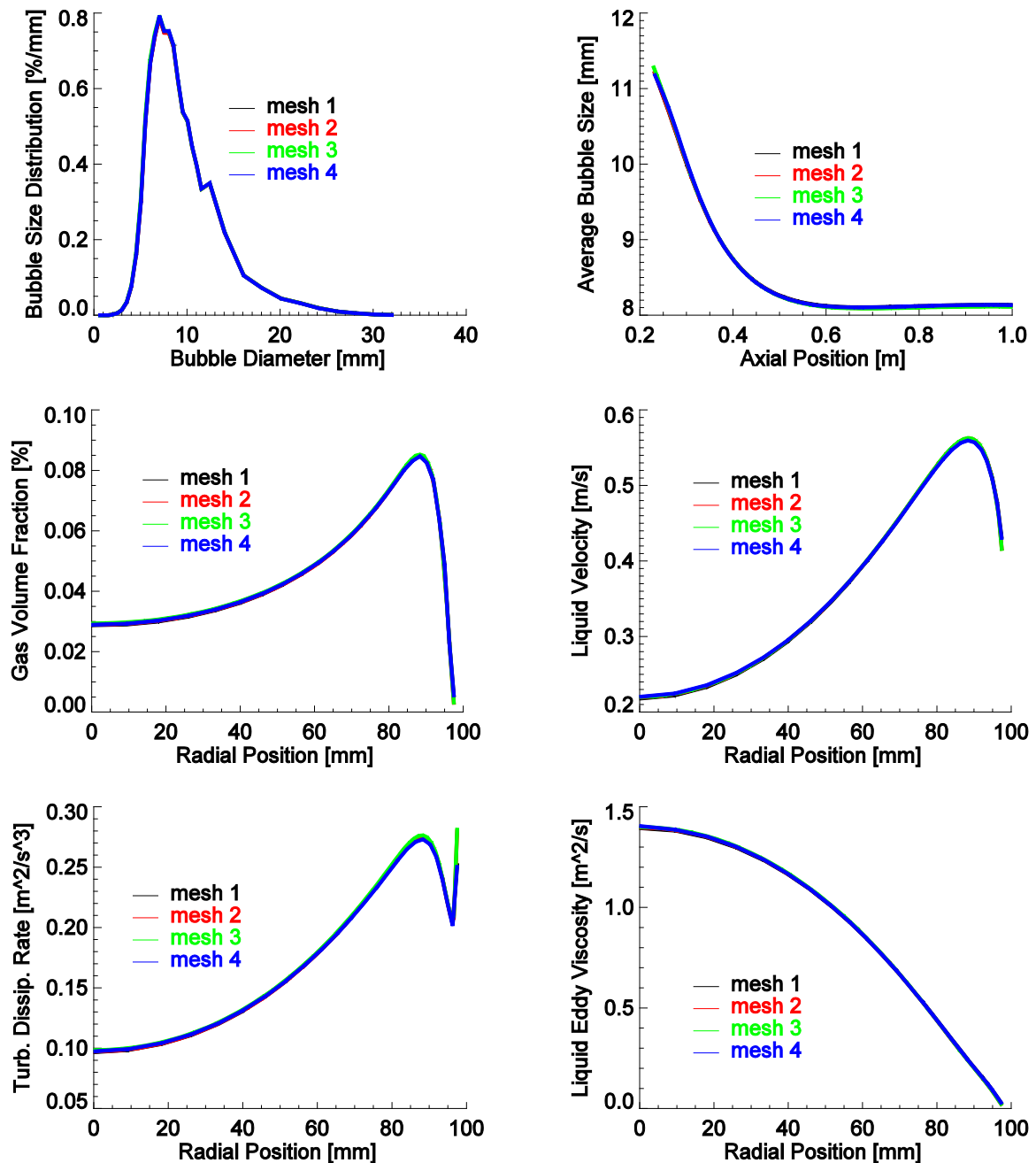


Figure 6.2 Influence of different meshes on the results (TP072, Level F)

### 6.1.2 Boundary conditions

Four kinds of boundary conditions (wall, outlet, symmetry and inlet) are applied to the quasi 2D mesh used in this work:

#### Wall

With the consideration of the viscosity difference of air and water, the outer wall of the vertical pipe has been set as hydraulically smooth walls with a non-slip boundary condition applied for the continuous liquid phase and a free-slip boundary condition for the gaseous phase. With a non-slip condition it means that the fluid has the same velocity as the wall, and in this work it is zero. A free-slip condition means that the gas velocity is tangent to the wall and not retarded by the existence of the wall.

### **Outlet**

The upper boundary condition is set to be an outlet boundary condition. The use of 'artificial walls' by the solver to stop the flow entering the domain is suppressed by expert parameter settings. The average static pressure is selected which means that the static pressure is allowed to vary locally on the outlet boundary such that the average pressure is constrained in a specified manner. In this work, the option of averaging over the whole outlet is used. The reference average pressure at the outlet is calculated according to the experimental condition that 0.25Mpa is fixed at the injection position ( $z=0.0\text{m}$ ) and to the hydrostatic pressure drop along the pipe, i.e.  $\Delta p = \rho g L$ .

### **Symmetry**

Two symmetry boundary conditions are applied to the front and rear planes of the computational domain, see Figure 6.1. At a symmetrical boundary, the gradient of all variables is equal to zero.

### **Inlet**

The inlet boundary of the computation domain is located at  $z=0.221\text{ m}$ , which means that the measurement for injection at Level A can be used as inlet conditions (see Table 4.1 and Figure 4.6). For the gaseous phase a mass flow rate related to the prescribed superficial gas velocity is applied while a velocity inlet condition is used for the liquid phase. The gas volume fraction profile and bubble size distribution are taken from the experimental data. The gaseous phase is divided into two velocity groups in the MUSIG model ( $d_1 < 6\text{ mm}$ ,  $d_2 > 6\text{ mm}$ ) corresponding to the sign change of lift force. The volume fraction of each group is obtained by multiplying the total measured gas volume fraction profile with a corresponding fraction of each group. One major difficulty in the setup of inlet conditions is that no measurement information is available for the liquid phase. Two methods are adopted in this work for the determination of liquid conditions at the inlet, i.e. assuming a fully-developed single-phase flow (single-phase) or using the corresponding results from Test Solver (two-phase). For the first method, the liquid inlet conditions have been shown in Figure 5.10.

#### **6.1.3 Initial conditions**

The velocity fields and volume fractions of air and water are in principle initialized with the given profiles at the inlet. The initial distribution of hydrostatic pressure  $p_{ini} = \rho g(L-z)$  is applied as an initial guess for the whole pressure field in the pipe.

#### **6.1.4 Convergence criteria**

The criteria for the judging of convergence are based on the maximum normalized residuals of each conservative equation and the overall flow balances (overall conservation). If all the maximum residuals are less than  $10^{-4}$  and the imbalance is less than 0.01, the simulation is regarded to be converged.

#### **6.1.5 Discretization of bubble size**

Two different approaches are used for the discretization of bubble size, i.e. equal and unequal discretization. For the 1 m pipe calculations, the bubble size is discretized unequally. With the consideration that there is a narrow peak of the bubble size distribution between  $d=0 \sim 12\text{ mm}$ , a fine discretization with  $\Delta d=0.5\text{ mm}$

is used for the first 24 MUSIG sub-size groups while the width of other groups is fixed to 2 mm. For the 8m pipe case, the bubble size is discretized equally with a width of 2 mm. The influence of the discretization approaches on the predicted bubble size distribution of test points 072 and 074 is shown in Figure 6.3. It can be seen that the equal discretization with an interval less than 3 mm is comparable to the unequal approach.

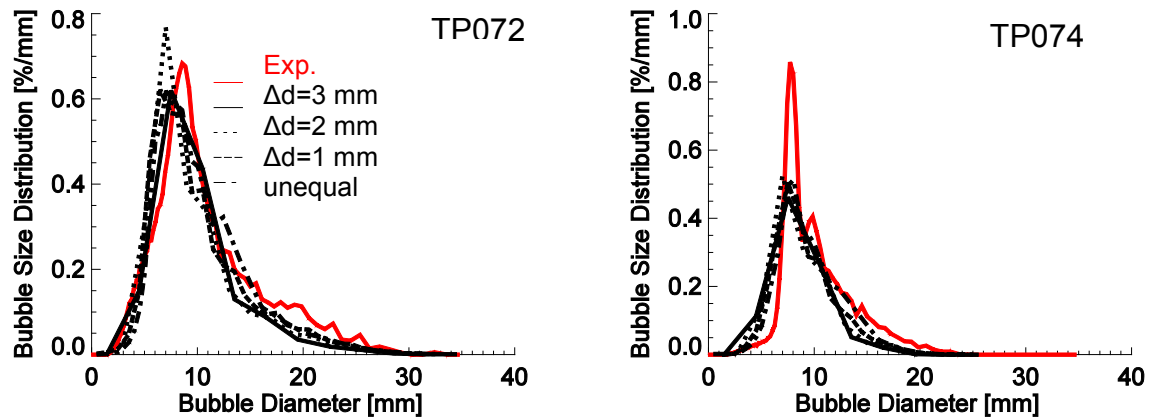


Figure 6.3 Influence of discretization on the predicted bubble size distribution at Level F (SST model+Morel [159] BIT model,  $C_k=C_\epsilon=1.0$ , two-phase liquid inlet)

## 6.2 Results

Predictions about the evolution of bubble size distribution, gas velocity and volume fraction along the pipe as well as the influence of liquid inlet conditions and bubble forces are shown below in Figure 6.4 ~ Figure 6.36, respectively.

### 6.2.1 Evolution of bubble size distribution along the pipe

From the test matrix (see Table 4.2) one can see that test points 072, 074, 083 and 085 are in the bubbly flow regime while 094, 096 and 118 are the transition cases between bubbly flow and churn-turbulent flow. The first 6 cases are simulated by using the 1 m mesh while simulations for the 8m long pipe are carried out only for the test point 118 due to the high computational cost.

With the consideration that lift force changes its sign for bubble diameter of around 6 mm according to the correlation of Tomiyama [178], in the calculation the gaseous phase is divided into 2 velocity groups in the MUSIG approach, i.e.  $N=2$ . Each of them is further subdivided into  $M$  sub-size groups ( $M_1, M_2$ ), see Figure 2.1.

#### 1 m pipe

The predictions of 1 m pipe for bubble size distributions at Level A ~ F are shown in Figure 6.4 ~ Figure 6.9 for different test points, respectively.

The evolution of bubble size distribution of the test point is depicted in Figure 6.4. In the simulation, the whole bubble size range is divided into 30 sub-size classes ( $M_1=12, M_2=18$ ). The inlet bubble size range is between 1 ~ 20 mm and the initial average bubble size is about 9.5 mm. For this case the change of bubble size distribution from Level A to Level F is not noticeable. In other words, coalescence and breakup rates of bubbles are almost in equilibrium. The amplitude of the peak



around 8 mm decreases along the flow and the size distribution becomes slightly broader. That means that as the two-phase mixture flows along the pipe there are a few small bubbles torn from large bubbles and there is simultaneous coalescence of large bubbles. This tendency is also predicted by the new model, but the small bubbles generated due to breakage are a little bit more prevalent than that observed by the measurement, which is consistent with the results provided by the Test Solver.

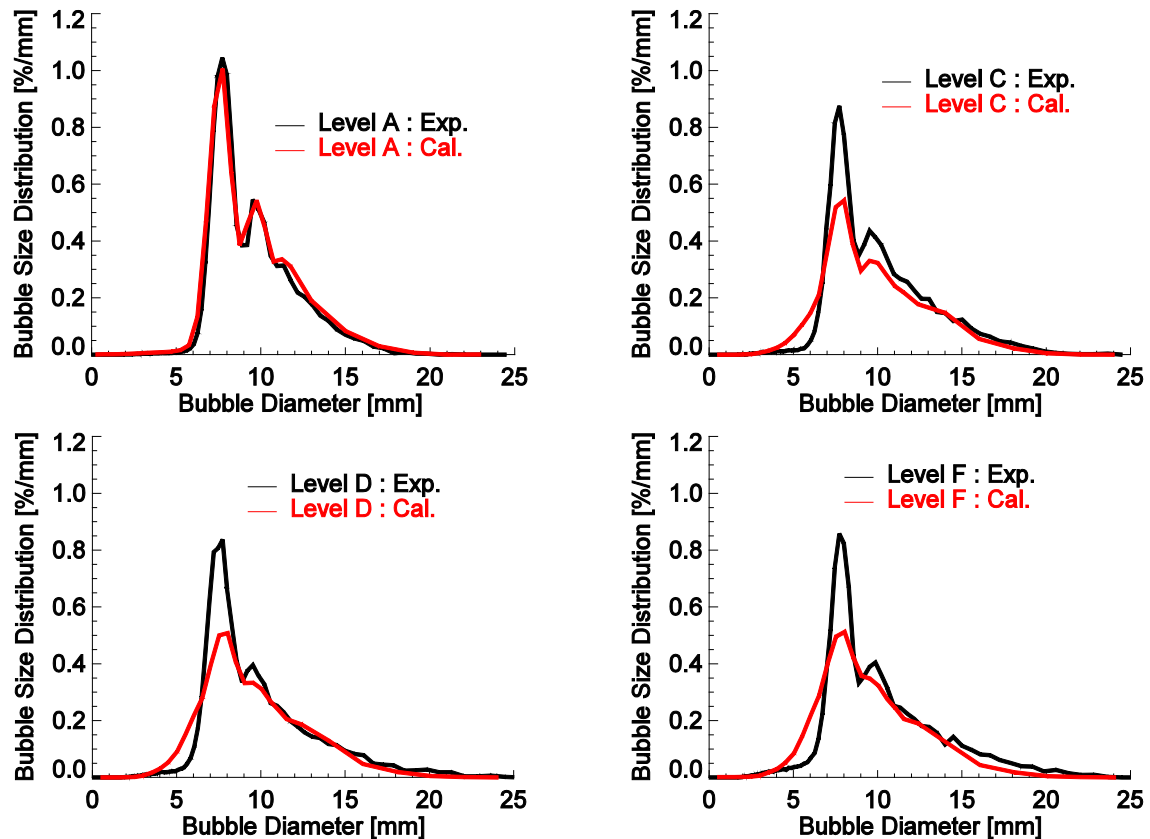


Figure 6.4 Evolution of bubble size distribution along the pipe height (TP074, SST model+Morel [159] BIT model,  $C_k=C_\epsilon=1.0$ , two-phase liquid inlet)

The evolution of bubble size distribution of test point 085 from Level A to Level F is depicted in Figure 6.5. In comparison to the case of TP074, due to an increase in the superficial gas velocity, the percentage of large bubbles increases and the initial bubble size exhibits a transitional bimodal distribution. The initial average bubble size is about 15 mm. As a result, the breakup rate is larger than that in the last case. In the simulation the whole bubble size range is divided into 34 size classes ( $M_1=12$ ,  $M_2=22$ ). Bubbles larger than 10 mm are not stable and disappear rapidly due to simultaneous coalescence and breakup. In the prediction the generation of small bubbles due to breakup is faster than that in the experimental due to an overestimation of breakup rate or an underestimation of coalescence rate. This trend is also to be observed in the predictions of the Test Solver.

As the amplitude of the peak of large bubbles increases further with the superficial gas velocity, the distribution of the initial bubble size becomes again monomodal, e.g. test point 096. However, the peak moves to a large bubble diameter around 22 mm, and the initial average bubble size increases to 20.5 mm, see Figure 6.6. In the simulation, the bubble size range is divided into 38 size classes ( $M_1=12$ ,  $M_2=26$ ).

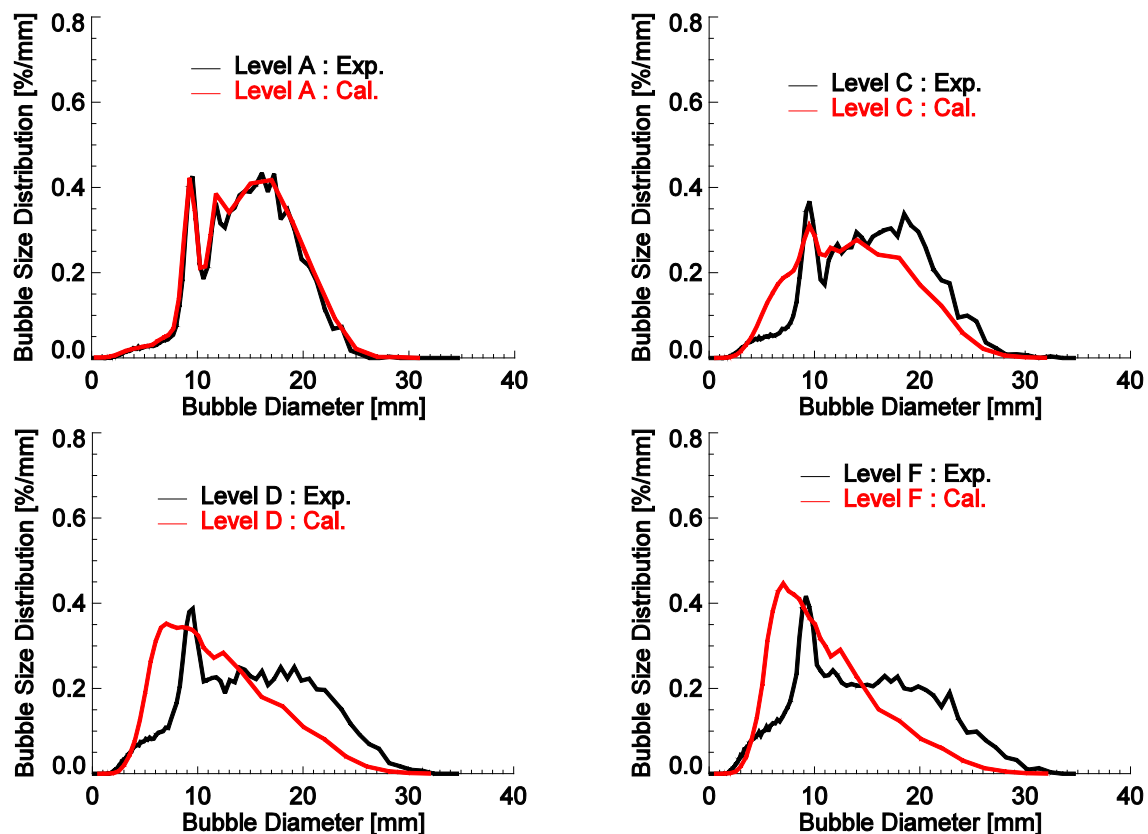


Figure 6.5 Evolution of bubble size distribution along the pipe height (TP085, SST model+Morel [159] BIT model,  $C_k=C_\epsilon=1.0$ , two-phase liquid inlet)

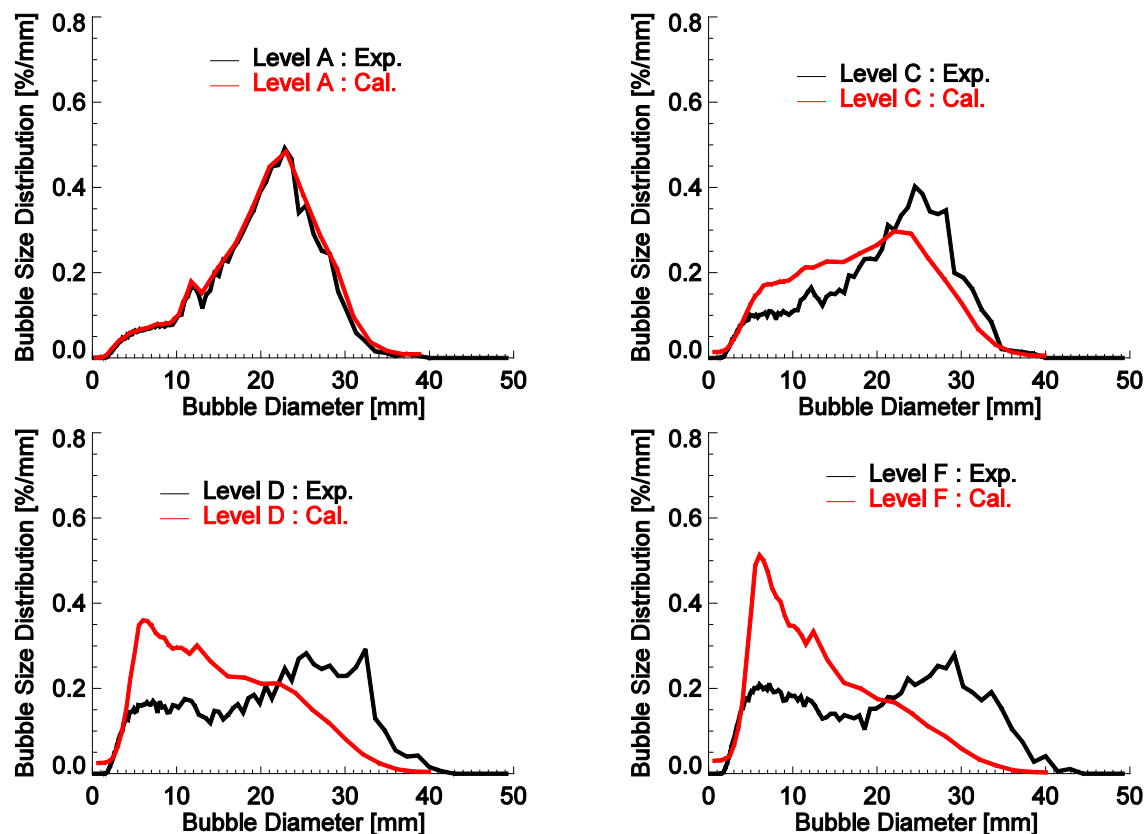


Figure 6.6 Evolution of bubble size distribution along the pipe height (TP096, SST model+Morel [159] BIT model,  $C_k=C_\epsilon=1.0$ , two-phase liquid inlet)

One can see from Figure 6.6 that as the mixture flows upward along the pipe a peak of small bubbles around  $d=6$  mm appears while the peak of large bubbles decreases from about 0.5(%/mm) to 0.3(%/mm). On the other hand, the position of large bubbles moves from about 22 mm to 29 mm, which means that there are large bubbles generated by coalescence as the flow goes from Level A to Level F, even though the whole tendency is breakup dominant. In general, the predicted breakup tendency and the size of daughter bubbles agree well with the experimental data. However, the peak of small bubbles grows too fast, which is similar to the conclusion of the simulation done by Test Solver.

The bubble size distributions at different height levels of test point 072 are shown in Figure 6.7. As shown in Table 4.2, the superficial gas velocity of test point 072 is the same as that of test point 074 (see Figure 6.4), but the superficial liquid velocity is reduced by about one half. As a result, the inlet bubble size is larger than that of the test point 074 and the average bubble size is about 15 mm. The inlet bubble size distribution at Level A is weakly bimodal and has a small peak around 9 mm and 18 mm, respectively. In the simulation the whole bubble size distribution is divided into 34 size classes ( $M_1=12$ ,  $M_2=22$ ).

Due to the breakage of large bubbles, the amplitude of the peak of small bubbles grows as the mixture flows from Level A to Level F. The evolution of bubble size distribution along the pipe is well predicted by the new model.

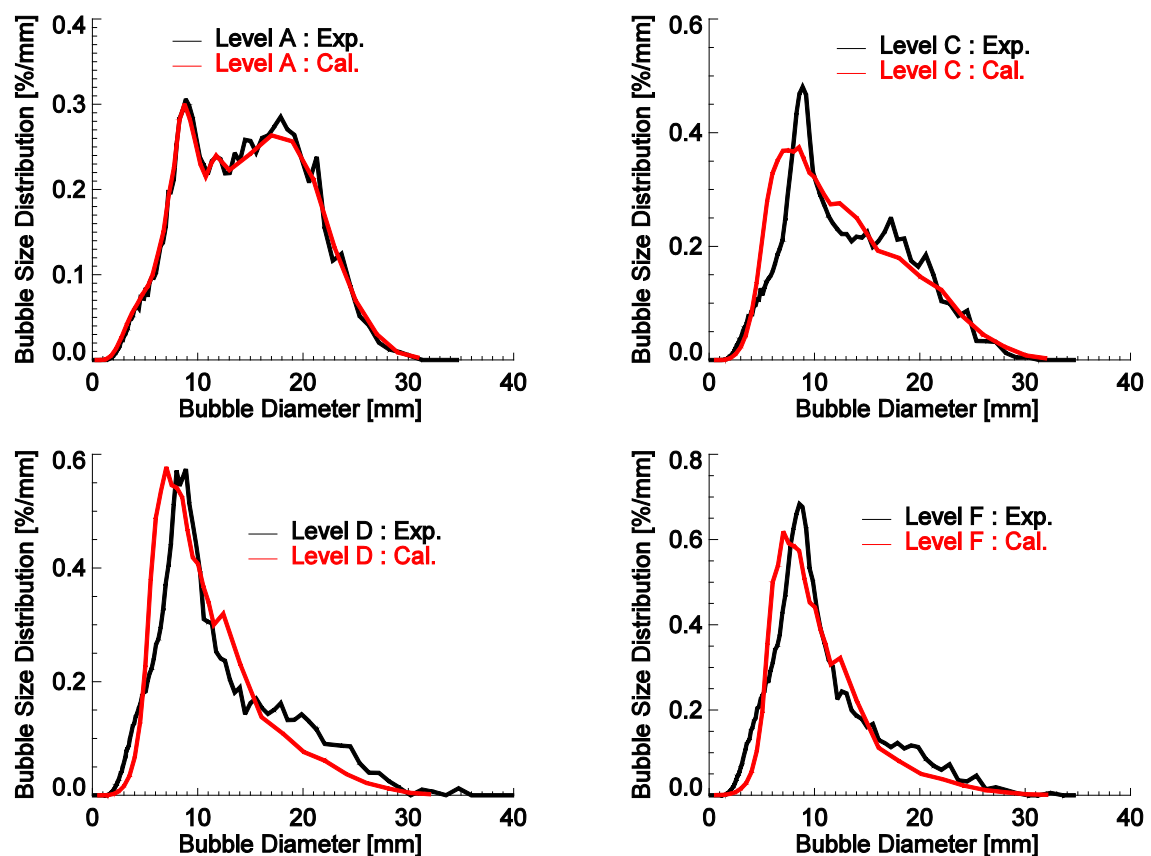


Figure 6.7 Evolution of bubble size distribution along the pipe height (TP072, SST model+Morel [159] BIT model,  $C_k=C_\epsilon=1.0$ , two-phase liquid inlet)

The bidirectional development of the bubble size distribution observed in the test points 085 and 096 becomes more obvious as the superficial liquid velocity decreases, e.g. test points 083 and 094. The evolution of bubble size distribution of the test points 083 and 094 is illustrated in Figure 6.8 and Figure 6.9, respectively. In the case of test point 083, as the mixture flows from Level A to Level F, the peak of small bubbles around  $d=7$  mm increases. Nevertheless, the peak of large bubbles at about  $d=25$  mm decreases and migrates gradually to the  $+x$  direction at the same time. It is usually difficult to trace this tendency due to the complexity of coalescence and breakup mechanisms for large bubbles. From the comparison with the experimental data, one can see that in the predictions the peak of small bubbles increases too fast whereas the evolution of the peak of large bubbles is not well reproduced. Therefore, the breakup rate is too large at the beginning and the simultaneous generation of large bubbles due to coalescence is not reflected, see Figure 6.8.

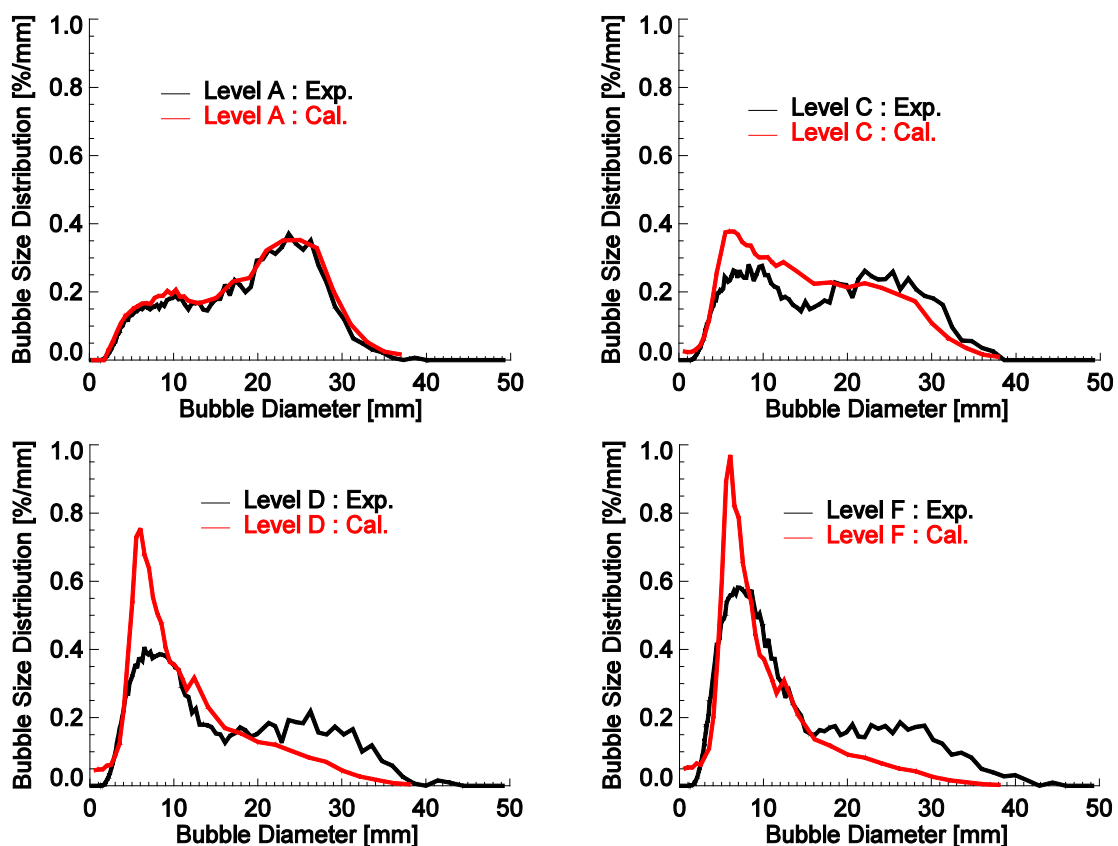


Figure 6.8 Evolution of bubble size distribution along the pipe height (TP083, SST model+Morel [159] BIT model,  $C_k=C_\epsilon=1.0$ , two-phase liquid inlet)

In the case of test point 094, the initial bubble size distribution is again a typical bimodal with two peaks around  $d=5$  mm and 28 mm, respectively. The inlet total gas volume fraction exceeds 8.0% and initial average bubble size is about 24 mm. The breakup rate is obviously larger than other cases discussed above. Similarly, in comparison with the measured bubble size distribution, the new model gives too large a breakup rate at the beginning of the flow. As a result the peak of small bubbles increases too fast, while the predicted volume fraction of large bubbles is lower than the measurement, see Figure 6.9.

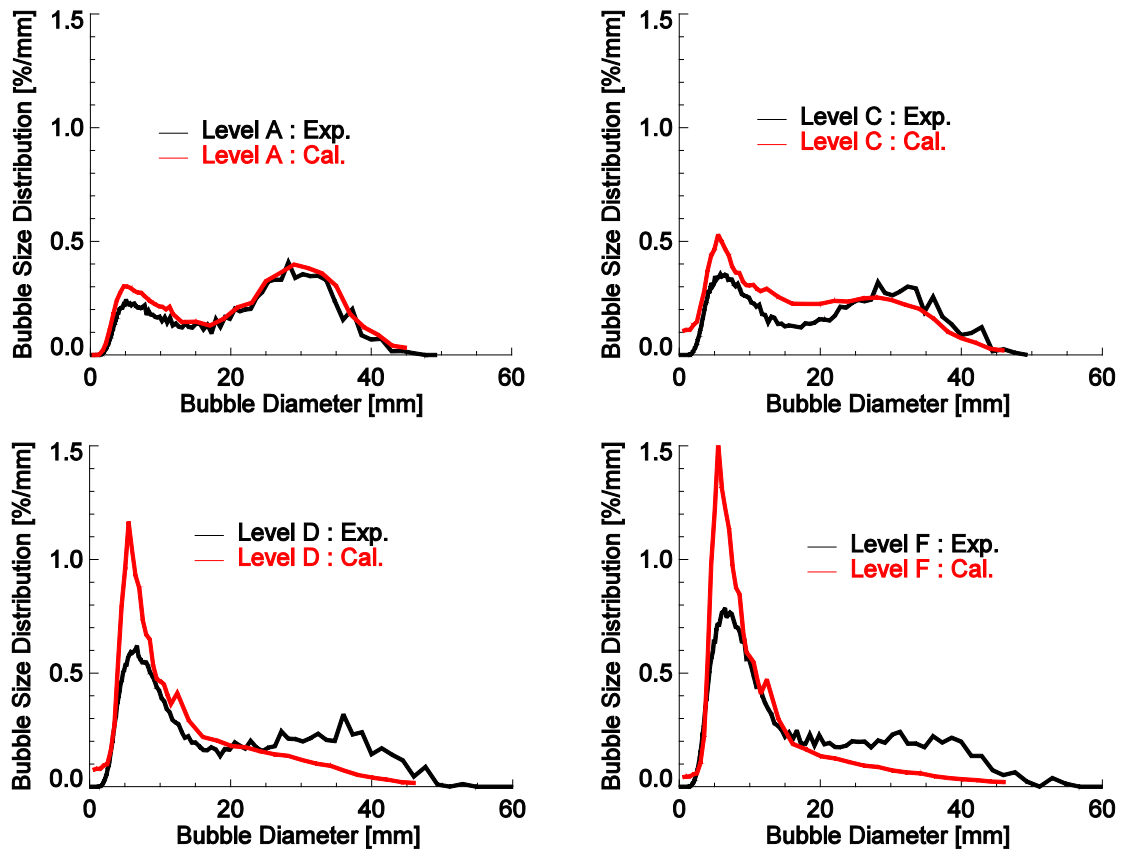


Figure 6.9 Evolution of bubble size distribution along the pipe height (TP094, SST model+Morel [159] BIT model,  $C_k=C_\epsilon=1.0$ , two-phase liquid inlet)

### 8m pipe

In order to obtain more information about the evolution of the air-water mixture inside the pipe, additional simulations for a long pipe with the same height as the test section are performed. In contrast to the case of short pipe, the computation time for the simulation to converge increases dramatically. Therefore, only one example of test point 118 is shown in Figure 6.10 ~ Figure 6.13.

Firstly, Figure 6.10 shows the comparison between the predicted and the measured bubble size distribution for different height levels. It can be seen that the breakup-dominant evolution and the size of daughter bubbles generated during the breakup events can be well reproduced by the new model for bubble coalescence and breakup. However, as discussed before, the predicted breakup rate is too large, especially at the beginning of the flow. That means that the peak of small bubbles increases too fast in comparison to the measurement and the difference gets smaller as the mixture flows along the pipe. On the other hand, the formation of large bubbles is not to be observed in the calculation, which could be caused by too weak a coalescence rate due to wake-entrainment. After Level I a small peak caused by the wake-entrainment appears near the critical bubble size  $d_{crit}$ , which is about 10 mm according to Eq. 3-8.

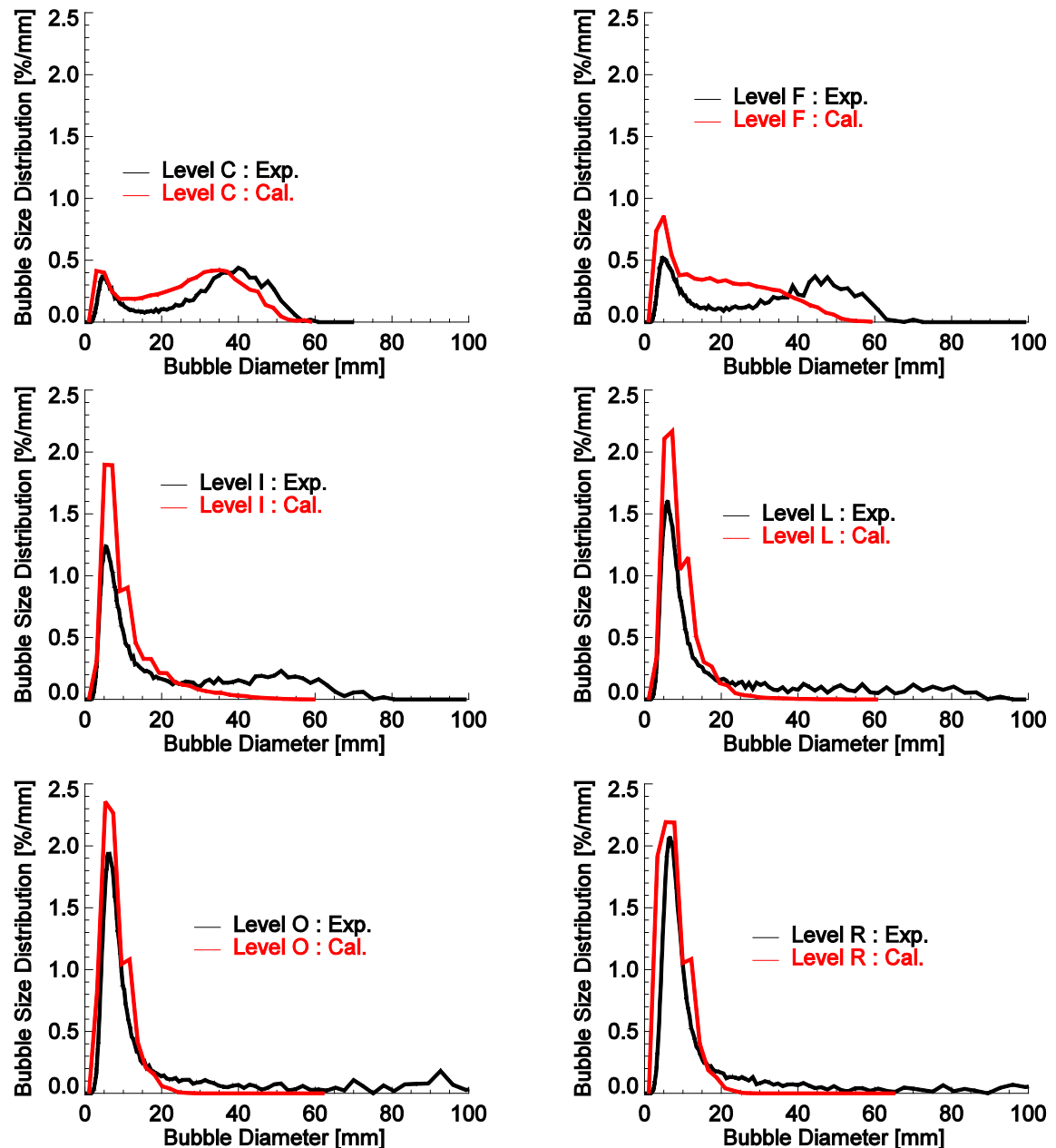


Figure 6.10 Bubble size distribution at different levels (TP118, SST model+Morel [159] BIT model,  $C_k=C_\epsilon=1.0$ , two-phase liquid inlet)

### 6.2.2 Evolution of radial gas volume fraction profile along the pipe

The evolution of gas volume fraction of TP118 along the pipe is shown in Figure 6.11. It can be seen that the predicted velocity of gaseous bubbles migrating from the wall to the center agrees well with the measured results. However, since there are more small bubbles and less large bubbles according to the new model (see Figure 6.10), the predicted radial gas volume fraction profile is more flat than the measured one. This is because small bubbles accumulate at the near wall region while large bubbles preferably at the core. On the other hand, the mean diameter of the large bubbles is also smaller than the measured one so that the lift force is smaller, which also results in a flatter gas volume fraction profile.

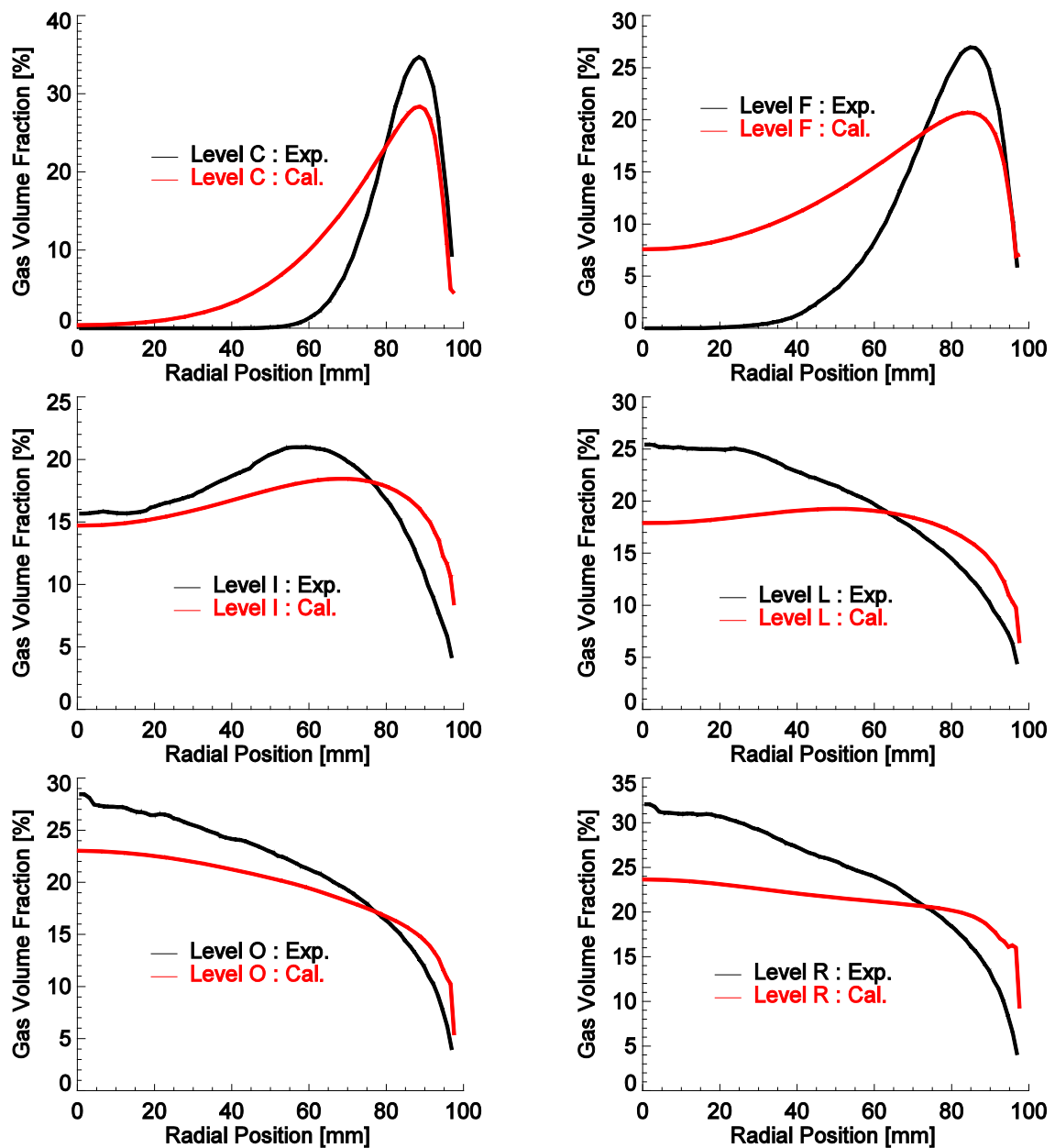


Figure 6.11 Radial total gas volume fraction at different levels (TP118, SST model+Morel [159] BIT model,  $C_k=C_\epsilon=1.0$ , two-phase liquid inlet)

The volume fractions of small and large bubbles from Level C to Level R are shown in Figure 6.12 for the example of test point 118. One can see that in the simulation both small and large bubbles migrate faster than that in the measurement. The volume fraction of small bubbles is higher than the measured one, however, the profile agrees well with the measurement. On the other hand, the fully-developed profile of the volume fraction of large bubbles is flatter than that provided by the experiment, which might be caused by a low percentage of large bubbles and a weak lift force due to the underestimation of the average bubble size.

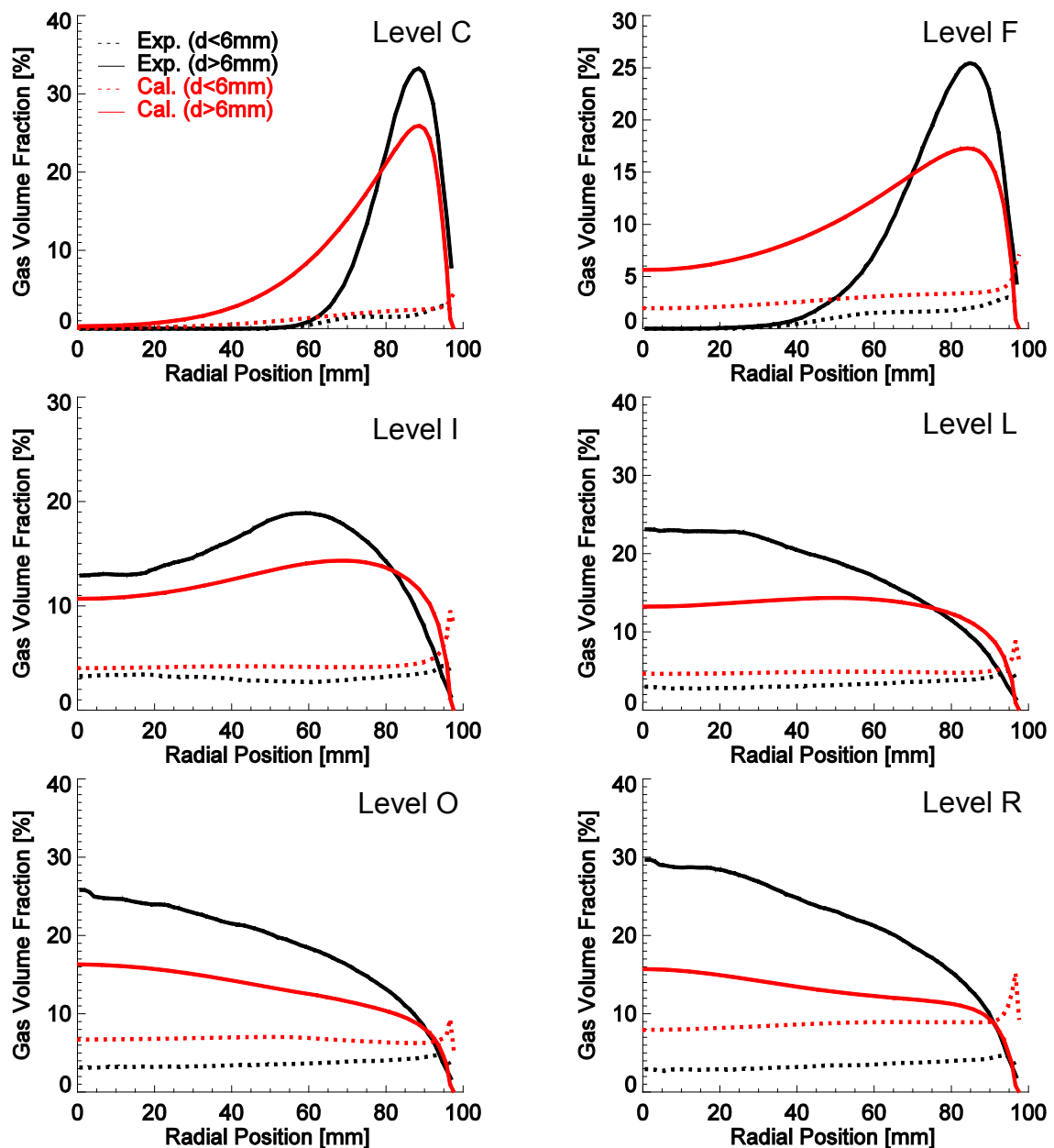


Figure 6.12 Radial gas volume fraction profile for small and large bubbles at different levels (TP118, SST model+Morel [159] BIT model,  $C_k=C_\epsilon=1.0$ , two-phase liquid inlet)

### 6.2.3 Evolution of radial gas velocity profiles along the pipe

The radial gas velocity profile of large bubbles at different height levels is illustrated in Figure 6.13 for the test point 118. It is worth noting that the velocity profiles for small and large bubbles are similar to each other. It can be seen that the velocity profile is in general similar to that of the gas volume fraction. As the peak of gas volume fraction migrates from pipe wall to the centre the velocity profile also changes from a wall-peak to a core-peak. As already mentioned before, the predicted migration or redistribution process is faster than that observed in the measurement and the gas velocity is in general smaller than the measured one. This is again due to the fact that the predicted average bubble size is lower than the measured one caused by an overestimation of breakup rate.



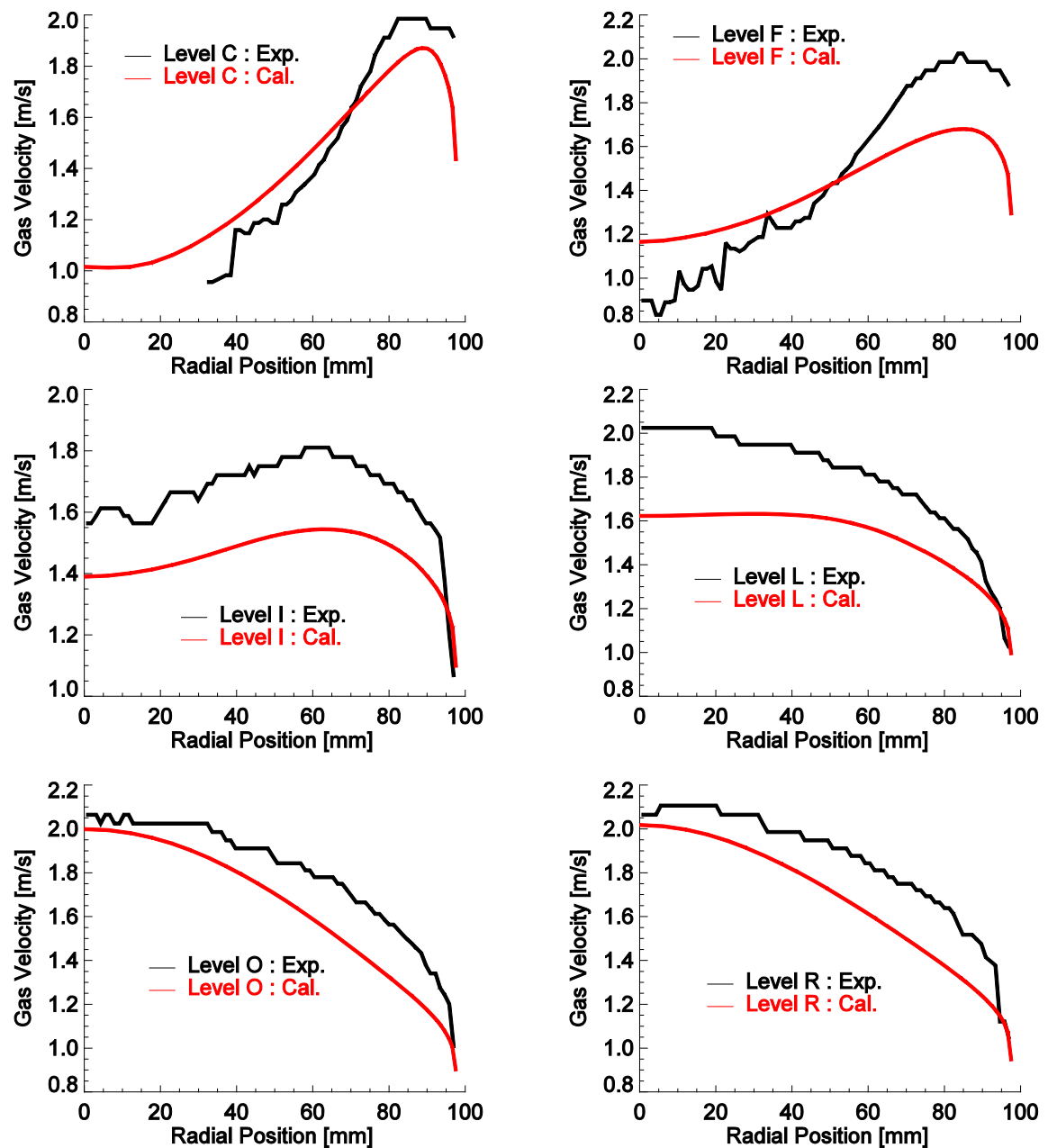


Figure 6.13 Evolution of radial gas velocity profile at different levels (TP118, SST model+Morel BIT model,  $C_k=C_\epsilon=1.0$ , two-phase liquid inlet)

#### 6.2.4 Influence of liquid inlet conditions

As mentioned at the beginning of the chapter, in CFX simulations there are two kinds of inlet conditions assumed for the velocity and turbulence parameters of the liquid phase, which are called two-phase and single-phase respectively in the Figure 6.14 ~ Figure 6.16. The influence of liquid inlet conditions on the evolution of bubble size distribution is depicted in Figure 6.14. It can be seen that the impact is in general trivial and only observed at the beginning of the flow. From Level C to Level F, the breakup rate calculated by using the two-phase inlet condition is a little bit larger than that by the single-phase one but after Level I the difference is imperceptible.

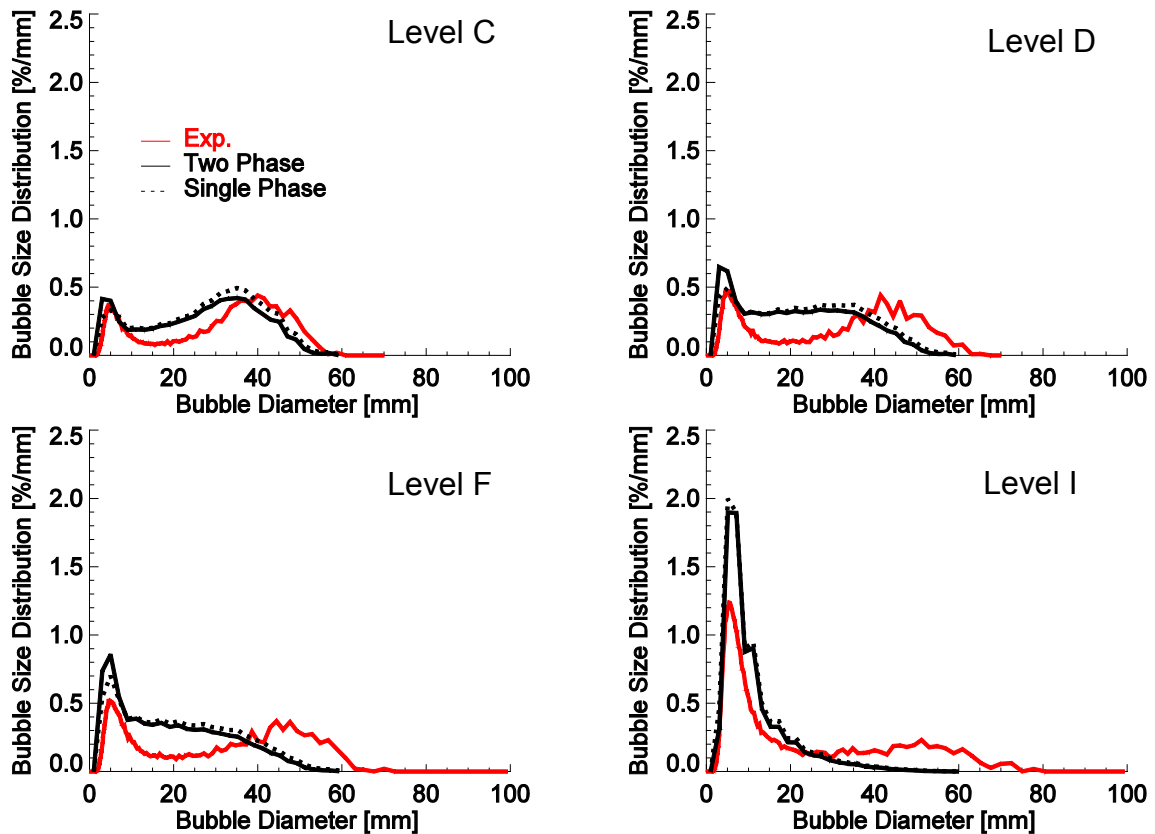


Figure 6.14 Influence of the inlet condition for liquid phase on the bubble size distribution (TP118, SST model+Morel [159] BIT model,  $C_k=C_\epsilon=1.0$ )

As shown in Figure 6.15, the radial gas redistribution velocity from the pipe wall to the centre is much lower in the case of single-phase inlet than that of two-phase one due to a lower liquid eddy viscosity (see Figure 6.16 right side). The agreement with the measured gas volume fraction profiles is improved for Levels C, D, F and I if the single-phase inlet conditions are employed.

The influence of liquid inlet conditions on the evolution of turbulence energy dissipation rate and liquid eddy viscosity is illustrated in Figure 6.16. It can be seen that at the pipe center both turbulence parameters in the case of single-phase condition is much lower than that of two-phase condition at Level F. This deviation can explain the difference in the prediction of bubble size distribution and gas volume fraction shown in Figure 6.14 and Figure 6.15, respectively. In addition, the effect of liquid inlet conditions on the turbulence parameters becomes smaller along the pipe and disappears after Level L.

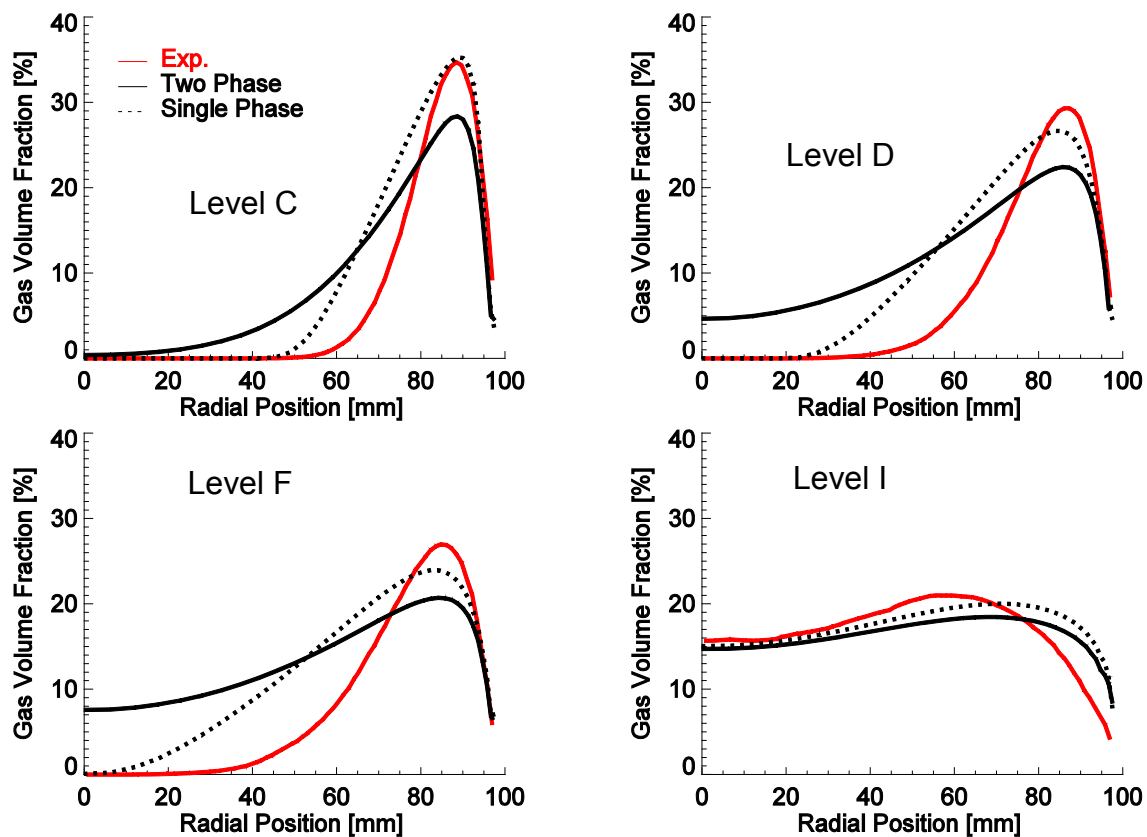


Figure 6.15 Influence of liquid inlet conditions on gas redistribution process (TP118, SST model+Morel [159] BIT model,  $C_k=C_\epsilon=1.0$ )

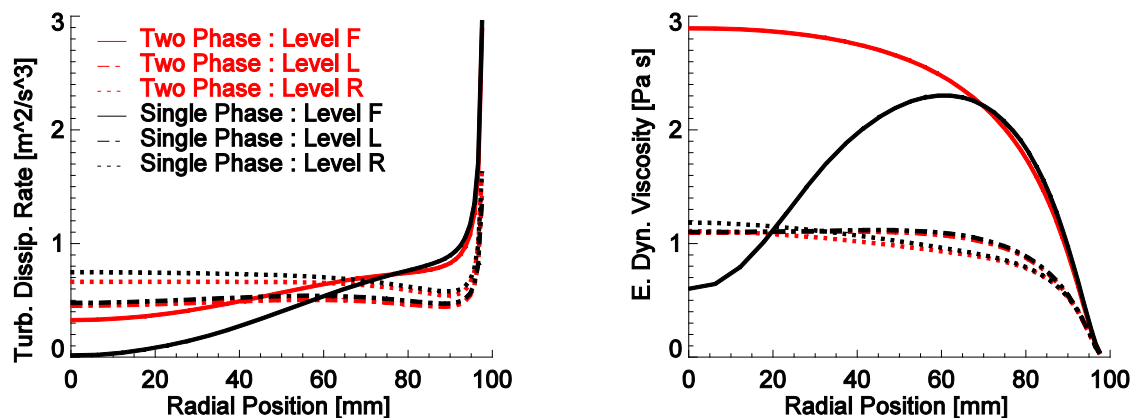


Figure 6.16 Influence of liquid inlet conditions on turbulence parameters (TP118, SST model+Morel [159] BIT model,  $C_k=C_\epsilon=1.0$ )

### 6.2.5 Influence of wall lubrication force

Under single-phase liquid inlet condition, the influence of models for wall lubrication force is analyzed. For the test point 118, predictions delivered by the models proposed by Tomiyama [151] and Antal et al. [153] are compared with each other. The evolution of bubble size distribution shown in Figure 6.17 indicates a negligible influence. The influence of the two wall force models on the evolution of gas volume fraction profiles is illustrated in Figure 6.18. It can be seen that the wall force predicted by the model of Antal et al. [153] is generally smaller than that by

Tomiyaama [151]. As a result, more bubbles accumulate near the pipe wall if the the model of Antal et al. [153] is adopted.

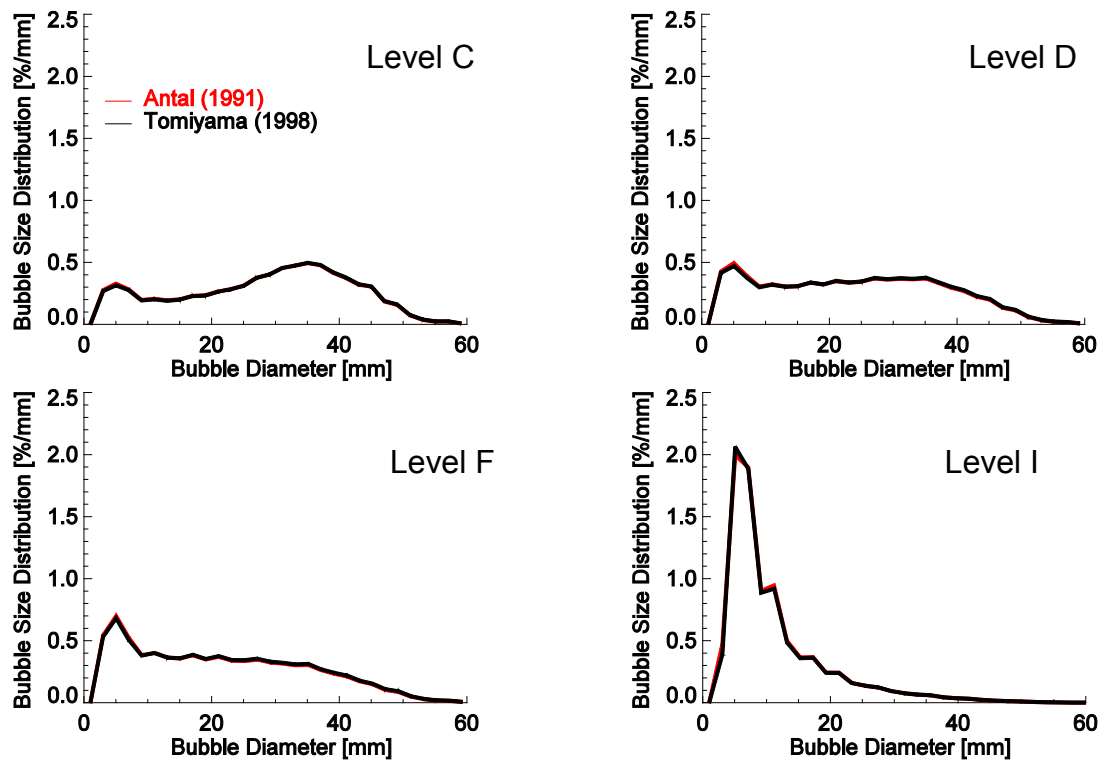


Figure 6.17 Influence of wall lubrication forces on bubble size distribution (TP118, SST model+Morel [159] BIT model,  $C_k=C_\epsilon=1.0$ , single-phase liquid inlet)

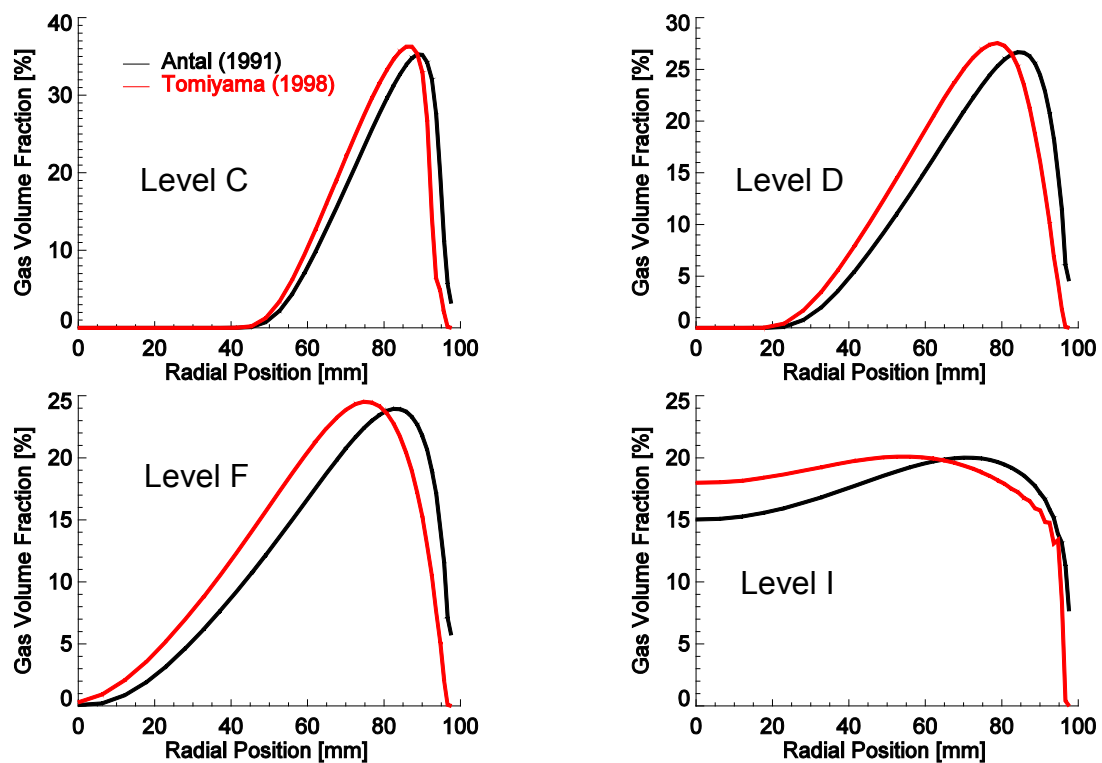


Figure 6.18 Influence of wall lubrication forces on gas volume fraction profile (TP118, SST model+Morel [159] BIT model,  $C_k=C_\epsilon=1.0$ , single-phase liquid inlet)

If the  $k-\epsilon$  turbulence model is adopted instead of the SST model for the liquid phase, the influence of the two wall force models on the radial gas volume fraction becomes much more considerable. As shown in Figure 6.19, a peak appears near the wall region if the model of Antal et al. [153] is used. This is because the viscosity predicted by the  $k-\epsilon$  model is lower than that by the SST model. In other words, the total smoothing effect of turbulent dispersion force and wall lubrication force is insufficient to compensate the accumulation effect of the lift force. As a result, an unreasonable accumulation of small bubbles is observed in the near wall region.

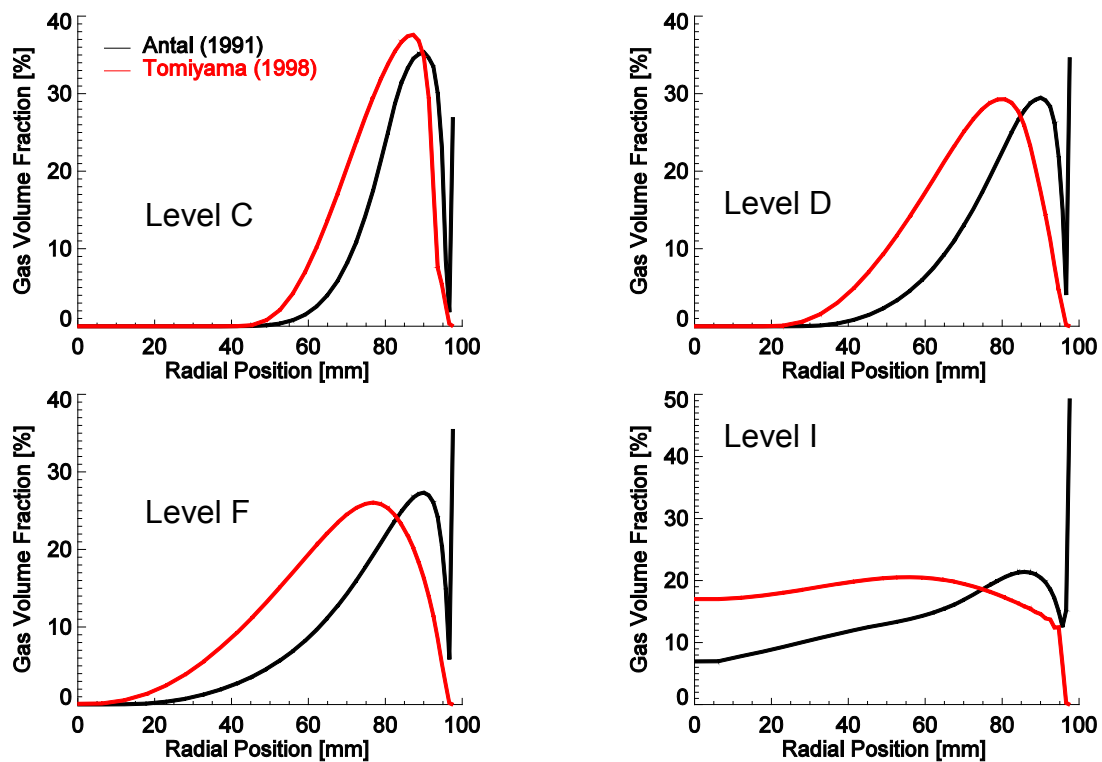


Figure 6.19 Influence of wall lubrication forces on gas volume fraction profile (TP118,  $k-\epsilon$  model+Morel [159] BIT model,  $C_k=C_\epsilon=1.0$ , single-phase liquid inlet)

### 6.3 Influence of two-phase turbulence modeling

#### SST and $k-\epsilon$ model

The influence of turbulence models used for the liquid phase on the predictions of turbulence parameters is shown in Figure 6.20.

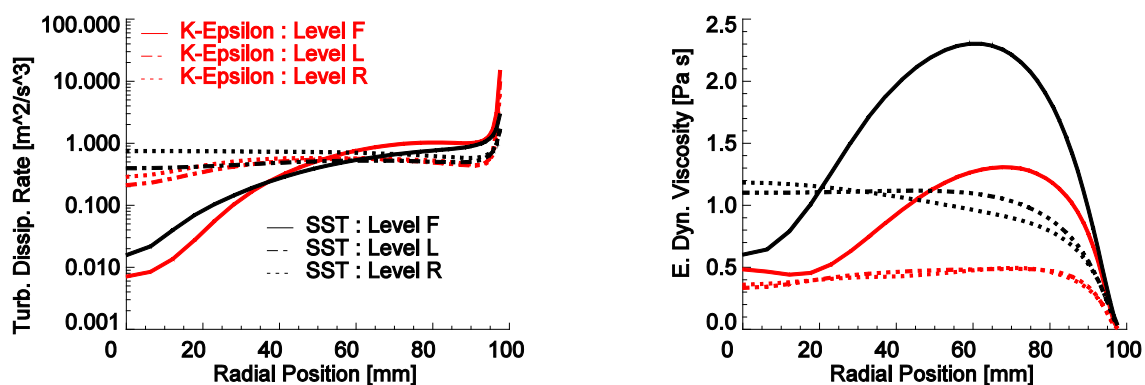


Figure 6.20 Influence of turbulence model on turbulence parameters (TP118, Morel [159] BIT model,  $C_k=C_\epsilon=1.0$ , Antal wall force, single-phase inlet)

In comparison to the  $k-\epsilon$  model, the SST model in general delivers a smaller turbulence dissipation rate in the near-wall region, while a larger eddy viscosity especially at the beginning of the flow. This leads to the difference in the profiles of bubble size distribution and gas volume fraction as shown in Figure 6.21 and Figure 6.22.

From Figure 6.21 one can see that the average bubble size predicted by using the SST model is slightly larger than that by the  $k-\epsilon$  model. As discussed previously, turbulence is one important mechanism leading to bubble coalescence and breakup, and the dissipation rate of energy is one input parameter for the coalescence and breakup models. Furthermore, the influence of dissipation rate on the breakup rate of bubbles is larger than that on the coalescence rate. That means that a large turbulence dissipation rate indicates an increased breakup rate. As a result, the SST model gives a larger average bubble size than the  $k-\epsilon$  model.

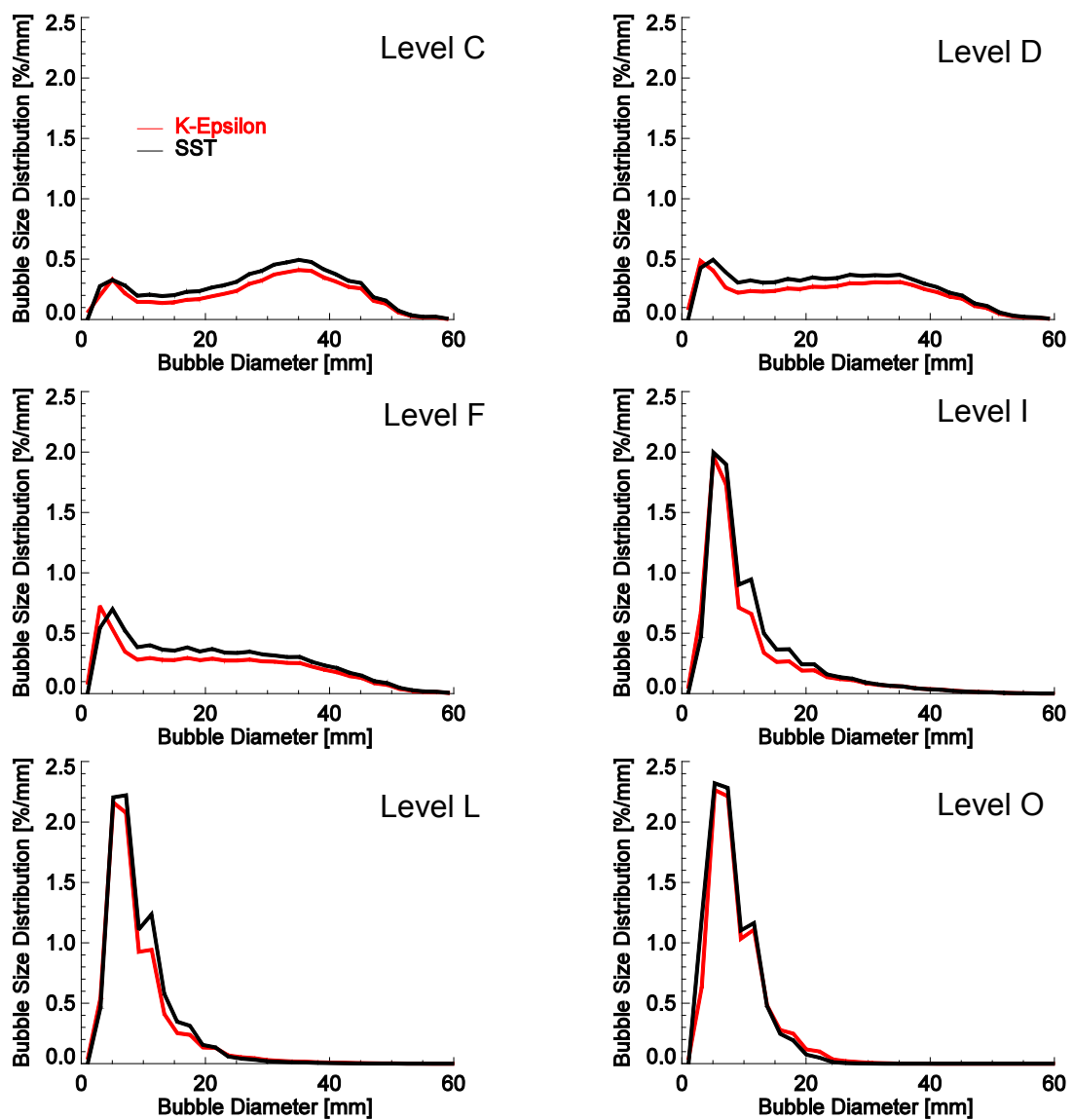


Figure 6.21 Influence of turbulence model on bubble size distribution (TP118, Antal [153] wall force, single-phase inlet, Morel [159] BIT model,  $C_k=C_\epsilon=1.0$ )

The influence of the liquid turbulence model on the radial gas volume fraction profile is depicted in Figure 6.22. As discussed above, a larger liquid eddy viscosity indicates a larger turbulent dispersion force, which tries to smooth the radial profile of gas volume fraction. As shown in Figure 6.20, the SST model delivers a larger eddy viscosity than the  $k-\epsilon$  model. As a result, in the simulation with the  $k-\epsilon$  model an unreasonable accumulation of small bubbles appears near the wall (see Figure 6.22), which is due to too weak a dispersion force and a wall force.

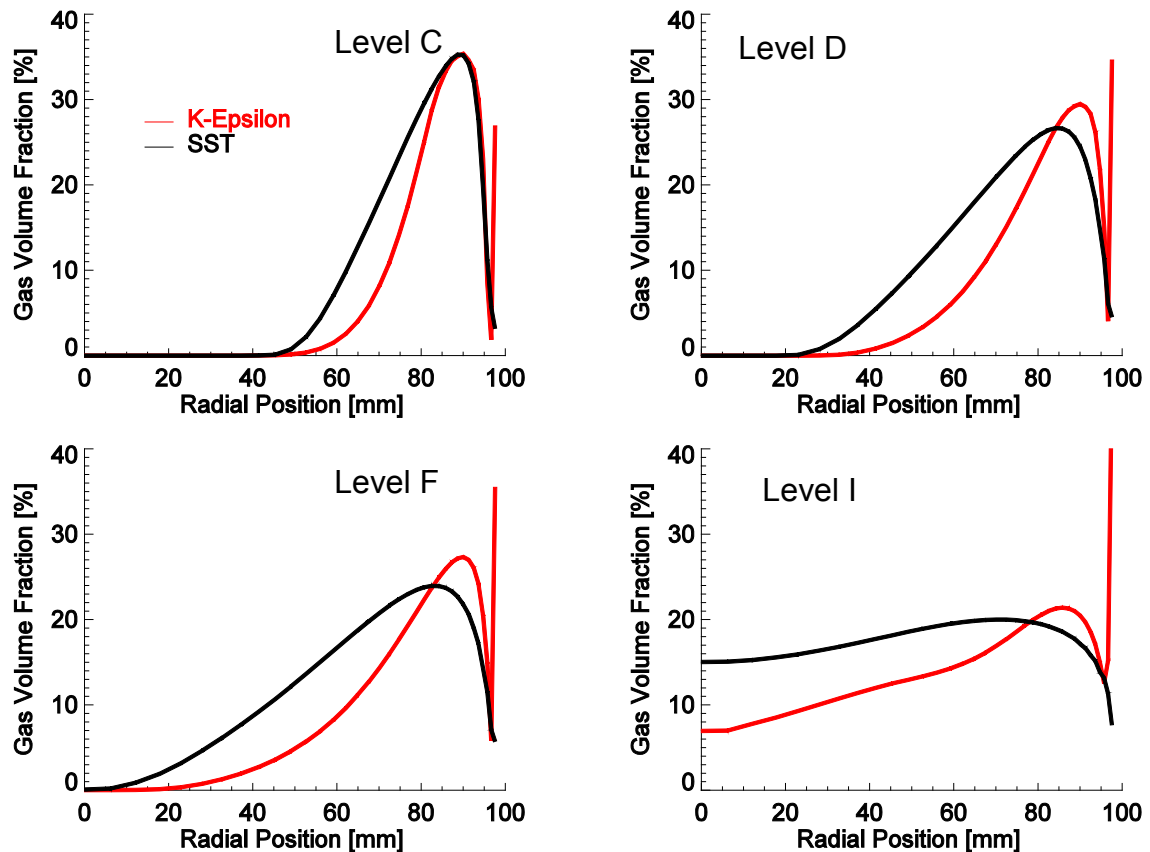


Figure 6.22 Influence of turbulence model on gas volume fraction profile (TP118, Antal [153] wall force, single-phase inlet, Morel [159] BIT model,  $C_k=C_\epsilon=1.0$ )

### **BIT source term models**

Besides the turbulence models self, models for BIT turbulence source and destruction have a remarkable influence on the predictions. Figure 6.23 and Figure 6.24 show the influence of five BIT models on the predicted turbulence energy dissipation rate for two different test points. It can be seen that in two cases the dissipation rate calculated by the Sato [8] model is obviously smaller than that by other models, which might lead to a smaller breakup rate of bubbles.

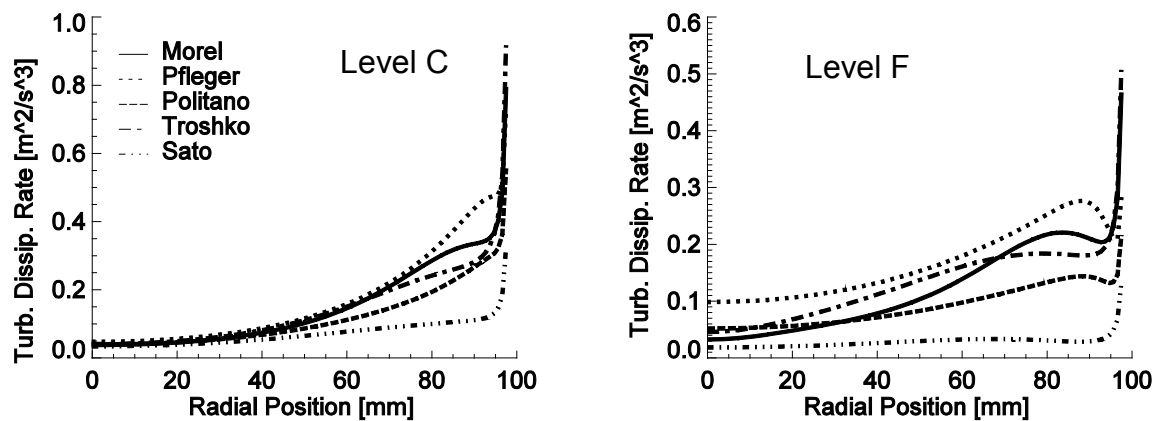


Figure 6.23 Influence of BIT model on turbulence dissipation rate (TP072, Antal [153] wall force, two-phase inlet, SST model)

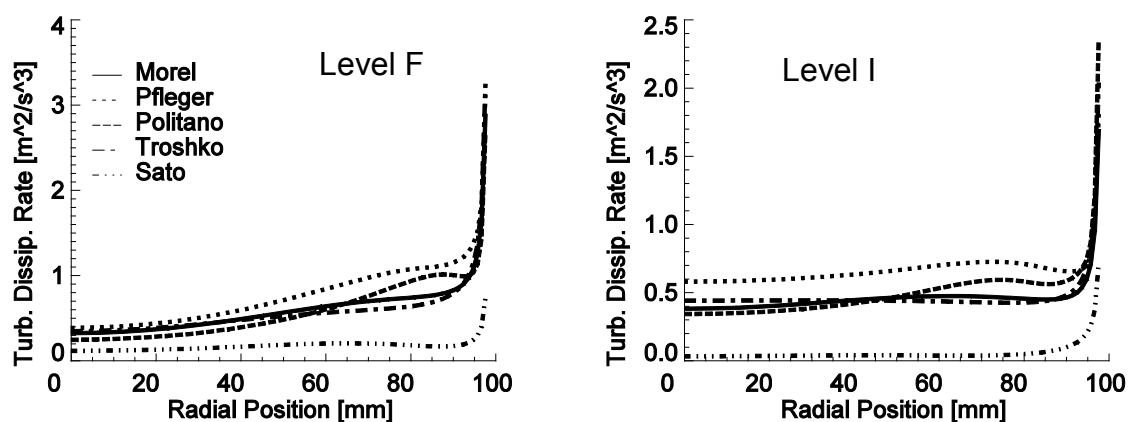


Figure 6.24 Influence of BIT model on turbulence dissipation rate (TP118, Antal [153] wall force, two-phase inlet, SST model)

The liquid eddy viscosity of test points 072 and 118 calculated by different BIT models is shown in Figure 6.25 and Figure 6.26, respectively. It can be seen that the eddy viscosity decreases as the gas-liquid mixture flows along the pipe. In addition, for the case of test point 072 the viscosity predicted by the Morel [159] model and Troshko [163] model is obviously smaller than the other models. At Level F, the viscosity at the pipe center predicted by these two models is even smaller than the maximum which induces a circulation in the flow. This problem caused by the Morel [159] model and the Troshko [163] model is mitigated by an increase in the superficial liquid velocity, e.g. test point 118. However, it is worth noting that for test point 118 with a high superficial gas velocity, the liquid eddy viscosity predicted by the Pflieger [157] model and the Politano [158] model decreases quickly as the two-phase mixture flows from Level F to Level O (see Figure 6.26). The different performance of these models is caused by the time scale they define. The influence of time scale and superficial gas velocity on the eddy viscosity has already been discussed (see the corresponding results for the Test Solver in Figure 5.45 and Figure 5.52).



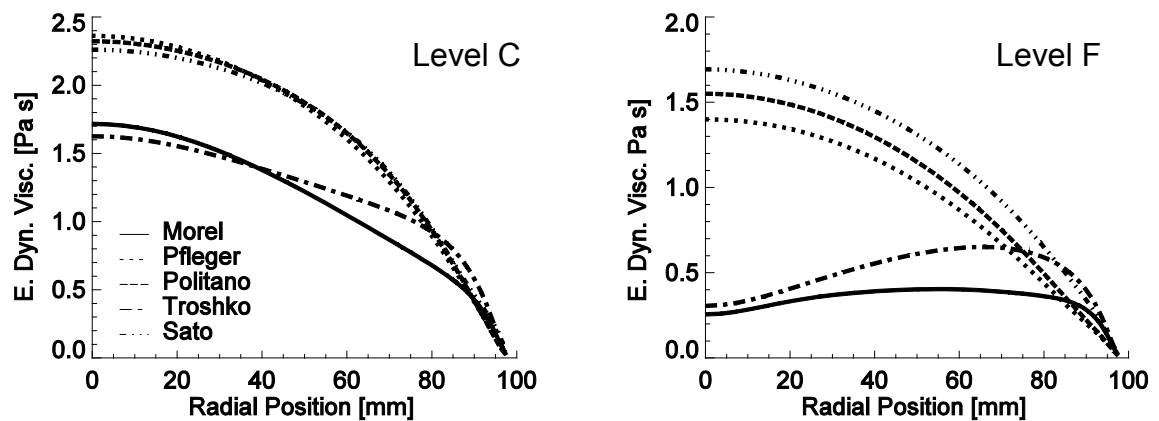


Figure 6.25 Influence of BIT model on eddy dynamic viscosity (TP072, Antal [153] wall force, two-phase inlet, SST model)

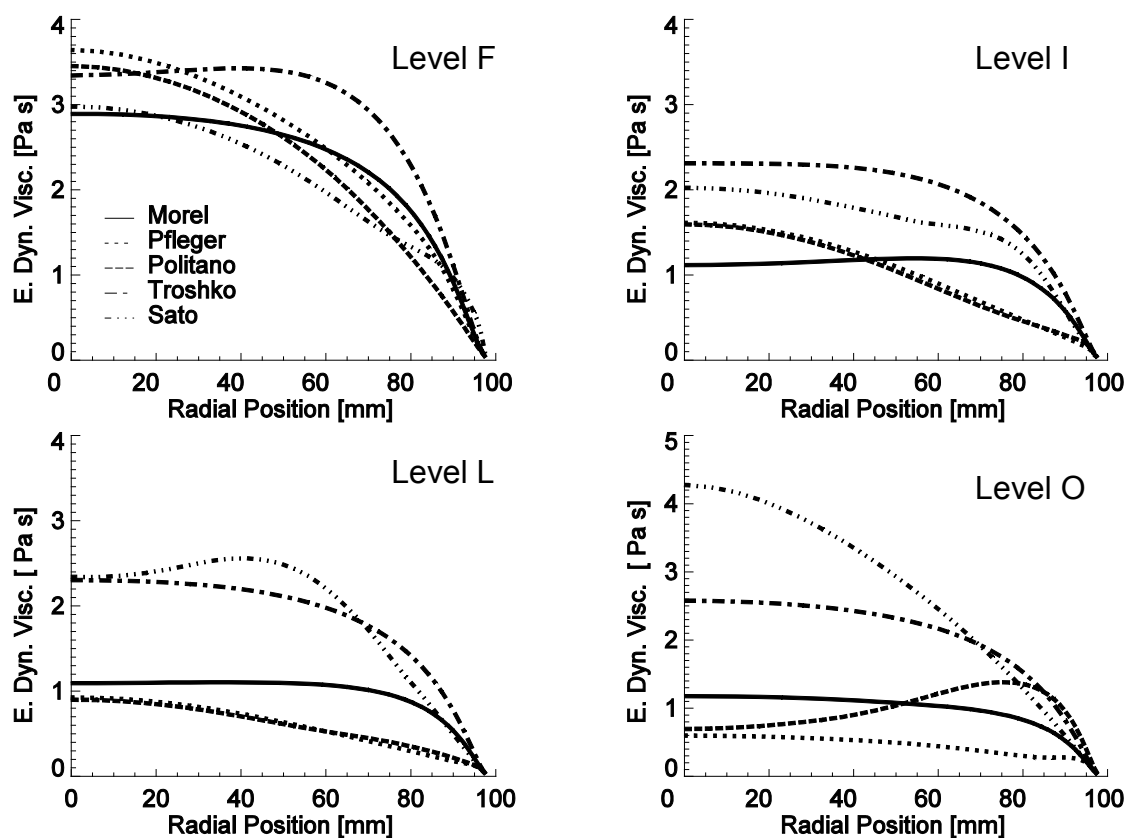


Figure 6.26 Influence of BIT model on eddy dynamic viscosity (TP118, Antal [153] wall force, two-phase inlet, SST model)

The predictions about the evolution of bubble size distribution for test points 072 and 118 are depicted respectively in Figure 6.27 and Figure 6.28. It can be seen that the breakup dominant evolution tendency is underestimated by the Sato [8] model due to low dissipation rate. The results provided by the other four models are similar to each other and the position of small bubbles generated by breakup is well captured by these models in both cases.

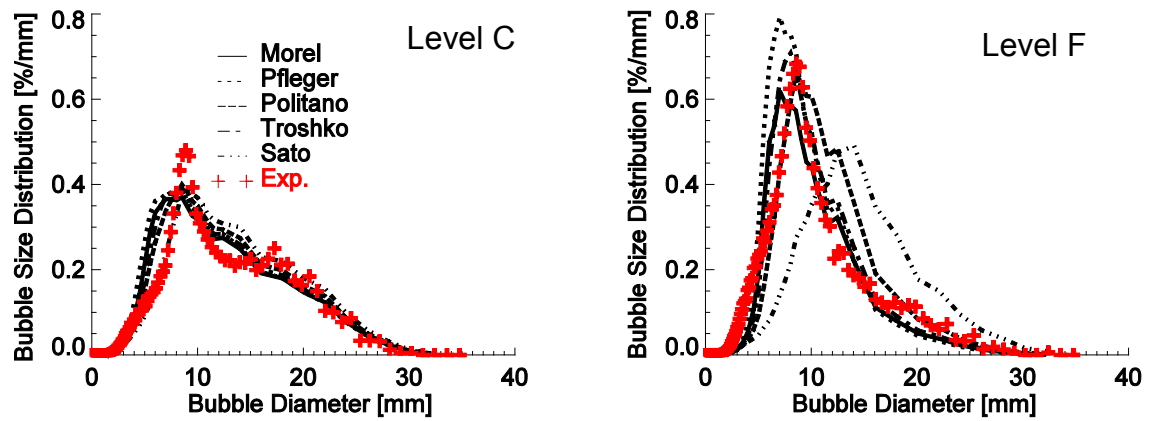


Figure 6.27 Influence of BIT model on the bubble size distribution (TP072, Antal [153] wall force, two-phase inlet, SST model)

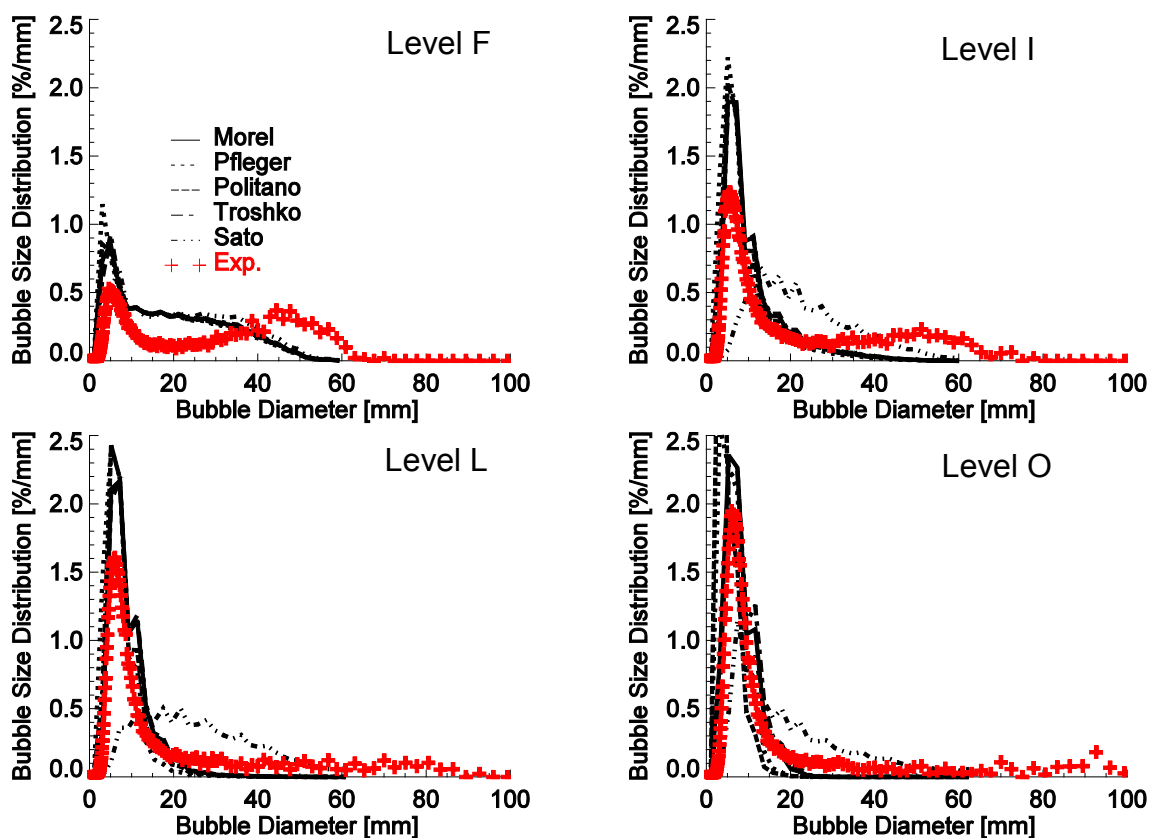


Figure 6.28 Influence of BIT model on bubble size distribution (TP118, Antal [153] wall force, two-phase inlet, SST model)

Figure 6.29 shows the influence of BIT models on the evolution of the gas volume fraction of test point 072. One can see that the radial profiles at Level C are almost the same according to different models. However, the predictions at Level F show that the inconsistency between different models becomes larger. According to the models of Pflieger [157], Politano [158] and Sato [8], the dispersion is faster than that observed in the measurement while the model of Morel [159] achieves the best agreement.

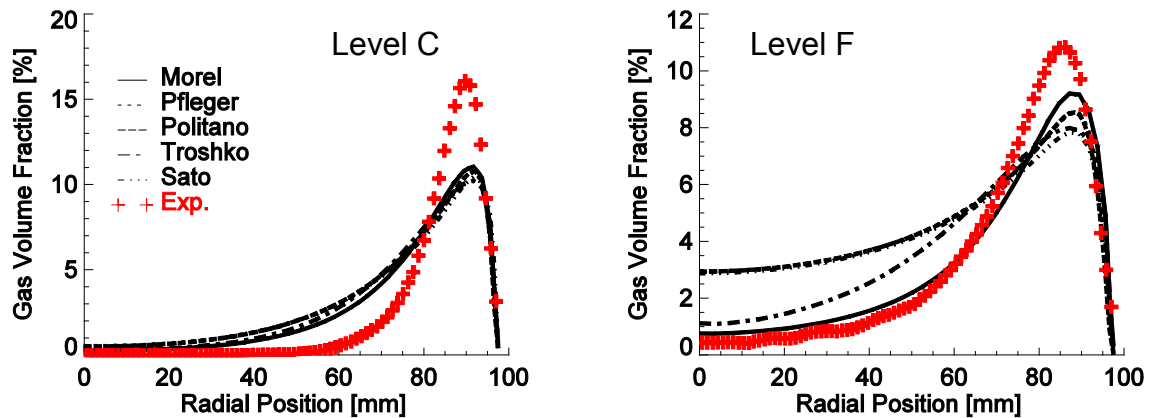


Figure 6.29 Influence of BIT model on gas volume fraction (TP072, Antal [153] wall force, two-phase inlet, SST model)

For test point 118, from Level I to Level O a peak of the gas volume fraction near the pipe wall is observed by using the Pflieger [157] model and the Politano [158] model. As mentioned in the discussion about the influence of the turbulence models, this small peak is caused by too weak a turbulent dispersion due to low eddy viscosity predicted by these two models, see Figure 6.26.

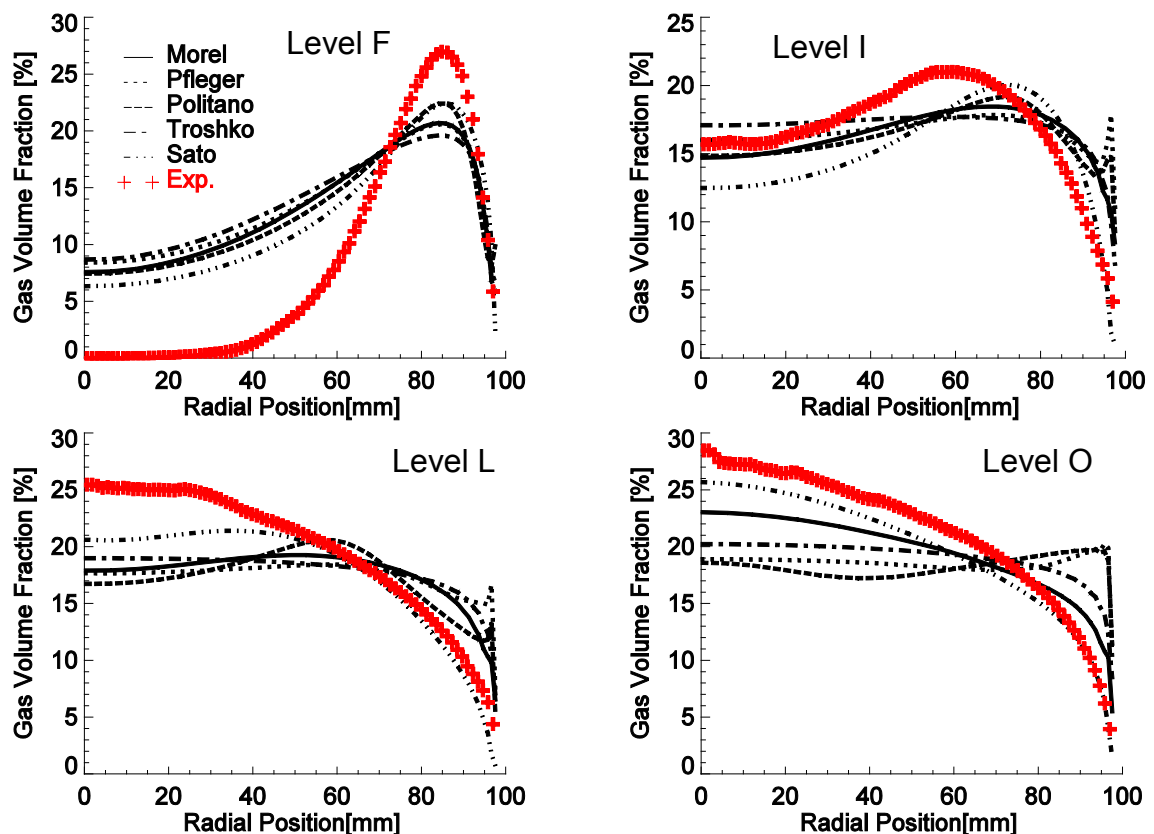


Figure 6.30 Influence of BIT model on gas volume fraction at different levels (TP118, Antal [153] wall force, two-phase inlet, SST model)

#### 6.4 Comparison with the predictions by standard closure models

Figure 6.31 compares the results of the 1 m pipe simulations predicted by the new model with those by the standard ones in ANSYS CFX-12.1, which are the

coalescence model of Prince and Blanch [36] and breakup model of Luo and Svendsen [95]. It shows that for all test cases the new model can deliver acceptable predictions about the bubble size distribution while the standard models provide an unreasonable peak of small bubbles. As a result, if the standard models are used, the predicted breakup rate has to be multiplied by a prefactor much smaller than 1 [7]. Furthermore, neither the new model nor the standard one can trace the extension of bubble size distribution curves towards larger diameter bubbles due to coalescence, although the performance of the new model is much better. This disagreement might be introduced by an underestimation of the wake-entrainment mechanism. However, this is inconsistent with the results obtained in the Test Solver where an overestimation of large bubbles generated by wake-entrainment is observed. This discrepancy could be caused by inherent structural differences between the solvers used.

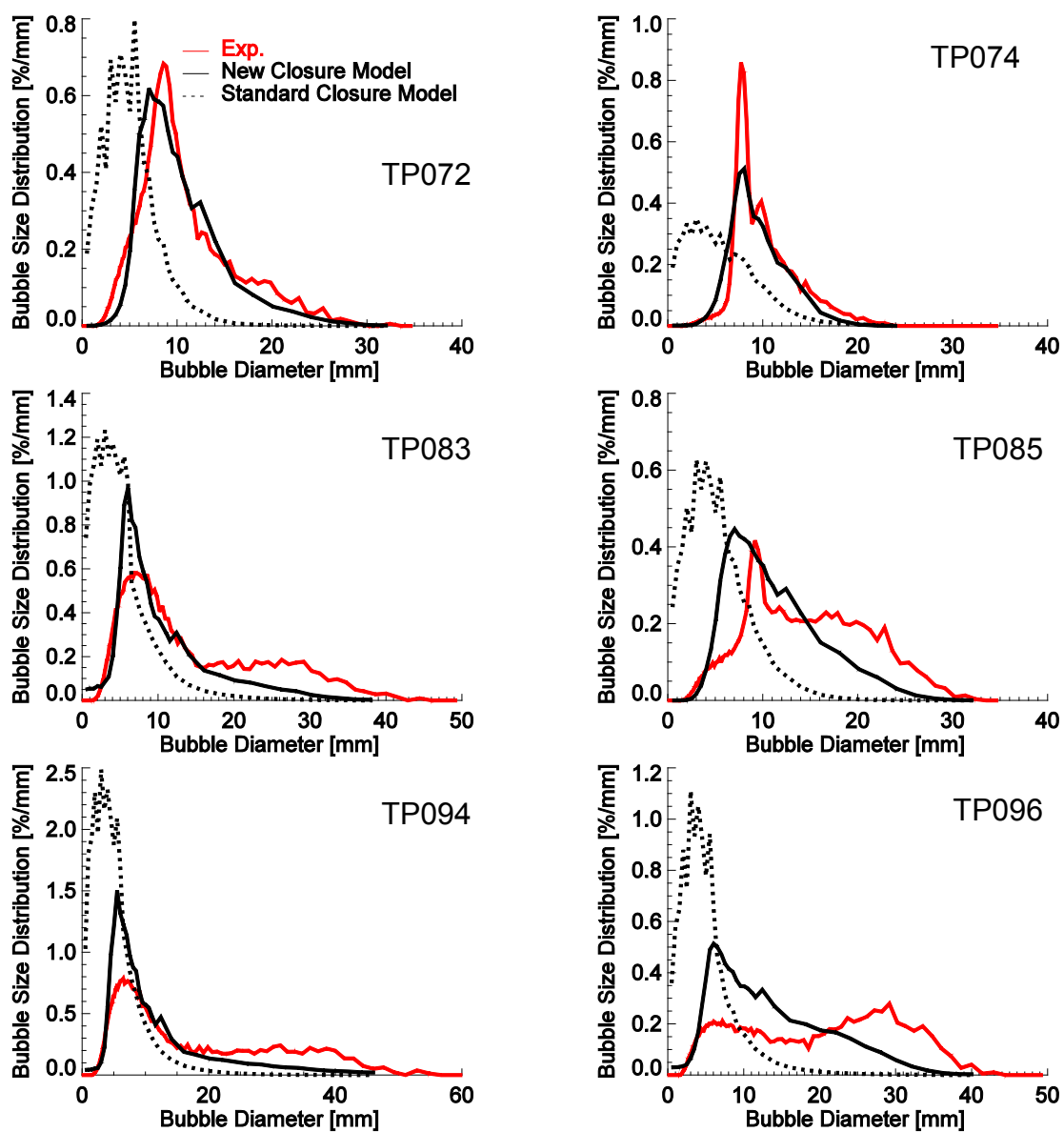


Figure 6.31 Bubble size distribution predicted by the new model and the standard ones (Level F, Antal [153] wall force, two-phase inlet, SST+Morel [159] model,  $C_k=C_\epsilon=1.0$ )

In Figure 6.32 and Figure 6.33, the bubble size distribution and Sauter mean bubble diameter of test point 118 predicted by the new model are compared with those by the standard closure models, respectively. Similarly to the case of the 1 m pipe shown in Figure 6.31, due to an inherent feature of the breakup model of Luo and Svendsen [95], there is almost no limit for the size of the small daughter bubbles generated during the breakup event. As a result, the peak of the small bubbles is determined by the smallest size group in the discretization of bubble size range, which is considered as unrealistic. On the other hand, the new model can capture the evolution of bubble size distribution from Level C to Level R reasonably.

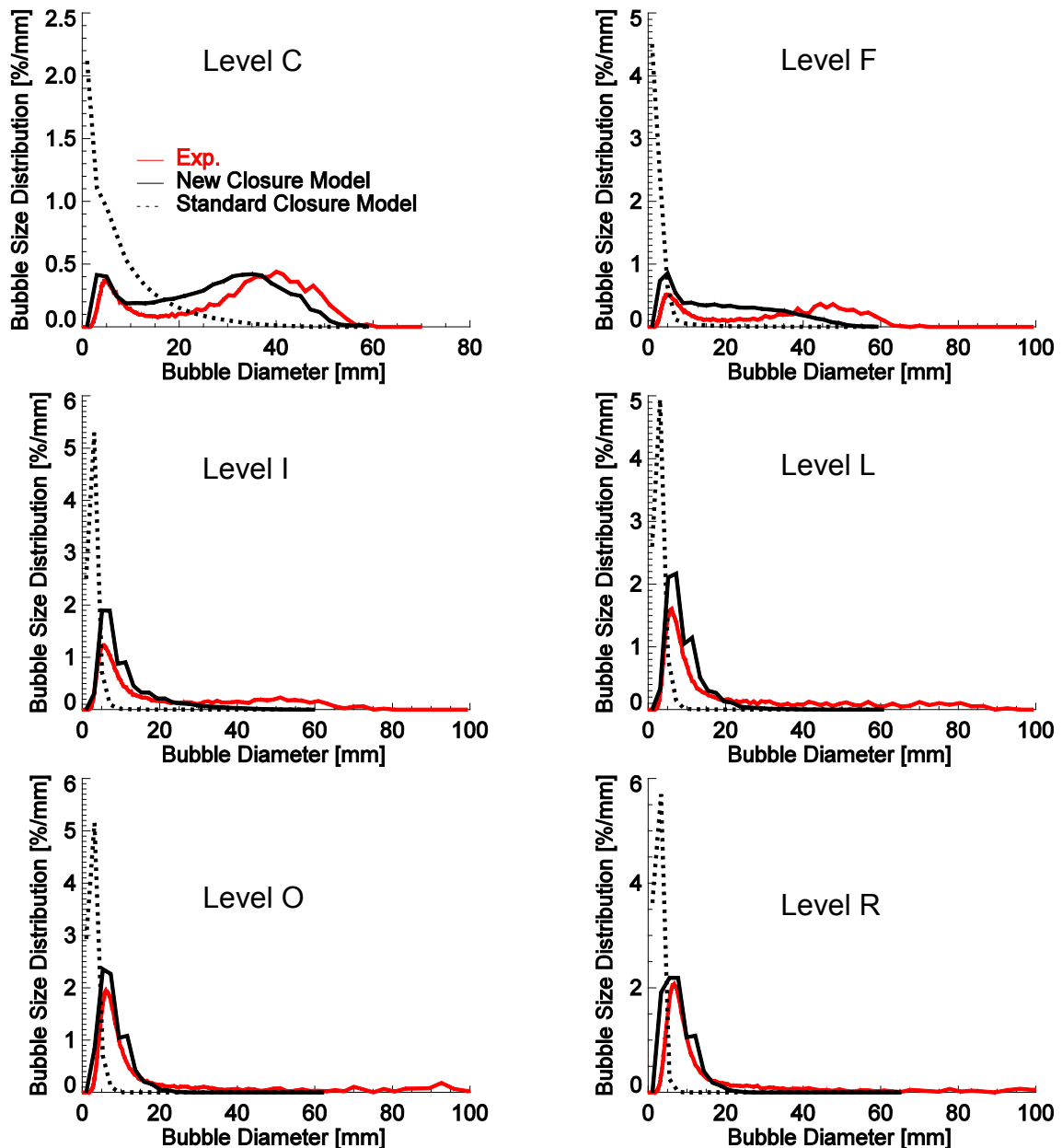


Figure 6.32 Evolution of bubble size distribution predicted by the new model and the standard ones (TP118, Antal wall force, two-phase inlet, SST+Morel [159] model,  $C_k=C_\epsilon=1.0$ )

Figure 6.33 illustrates again the difference in the coalescence and breakup rate predicted by the new model and the standard ones by comparing the Sauter mean

bubble diameter. For the example of test point 118, the mean inlet bubble size is about 18 mm and these large bubbles are extremely unstable against breakup. As a result, in the lower part of the pipe, i.e.  $L < 2\text{m}$ , the mean bubble diameter decreases steeply and later on the breakup rate is slowed down. It is clearly seen from Figure 6.33 that the evolution tendency given by the new model agrees well with the measured data although the predicted value is smaller than the measured one. On the other hand, in the predictions using the standard models, the bubble size decreases much more steeply than the measurements and the bubble size is also greatly underestimated by comparing it to the results of the new model and the measurement. This effect implies a large breakup rate delivered by the standard model.

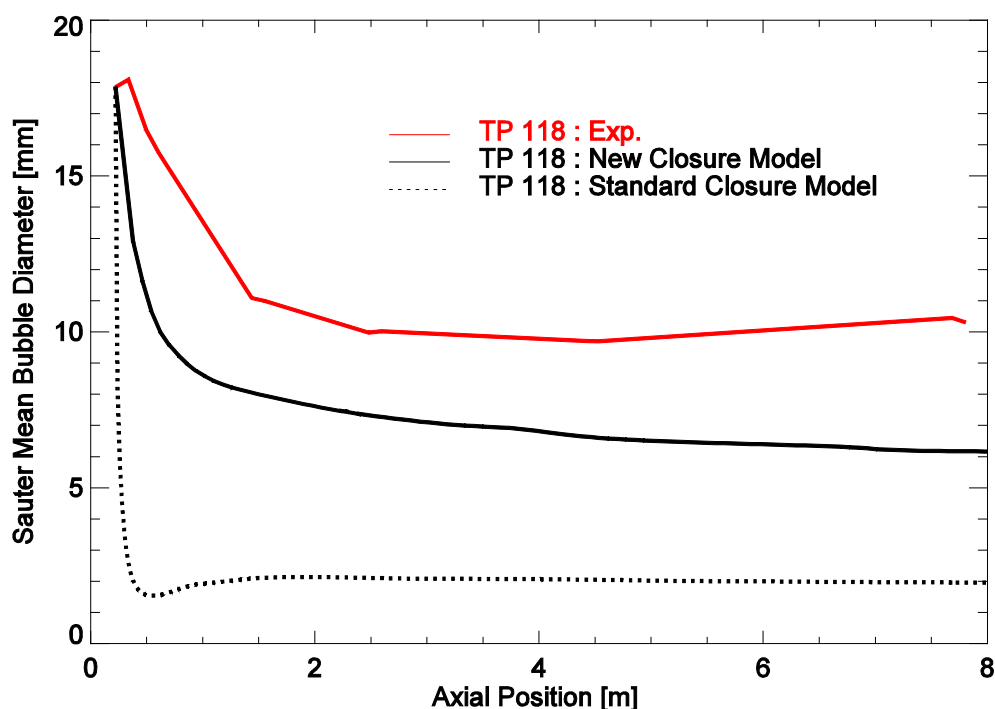


Figure 6.33 Evolution of Sauter mean bubble diameter predicted by the new model and the standard ones (TP118)

## 6.5 Comparison with the results of Test Solver

The comparison between the bubble size distribution predicted by the new model in CFX and Test Solver for four different test points is shown in Figure 6.34. It can be seen that the results provided by the Test Solver and CFX are similar to each other. Both show the breakup dominant tendency of the evolution from Level A to Level F and an overestimation of breakup rate. However, it is clearly noticeable that the breakup rate calculated in CFX is still larger than that in the Test Solver. As a result, the average bubble size predicted by the Test Solver is larger than that by CFX. This discrepancy might be caused by the overprediction of the Test Solver for the migration of bubbles from the wall to the pipe center (see Figure 6.35).

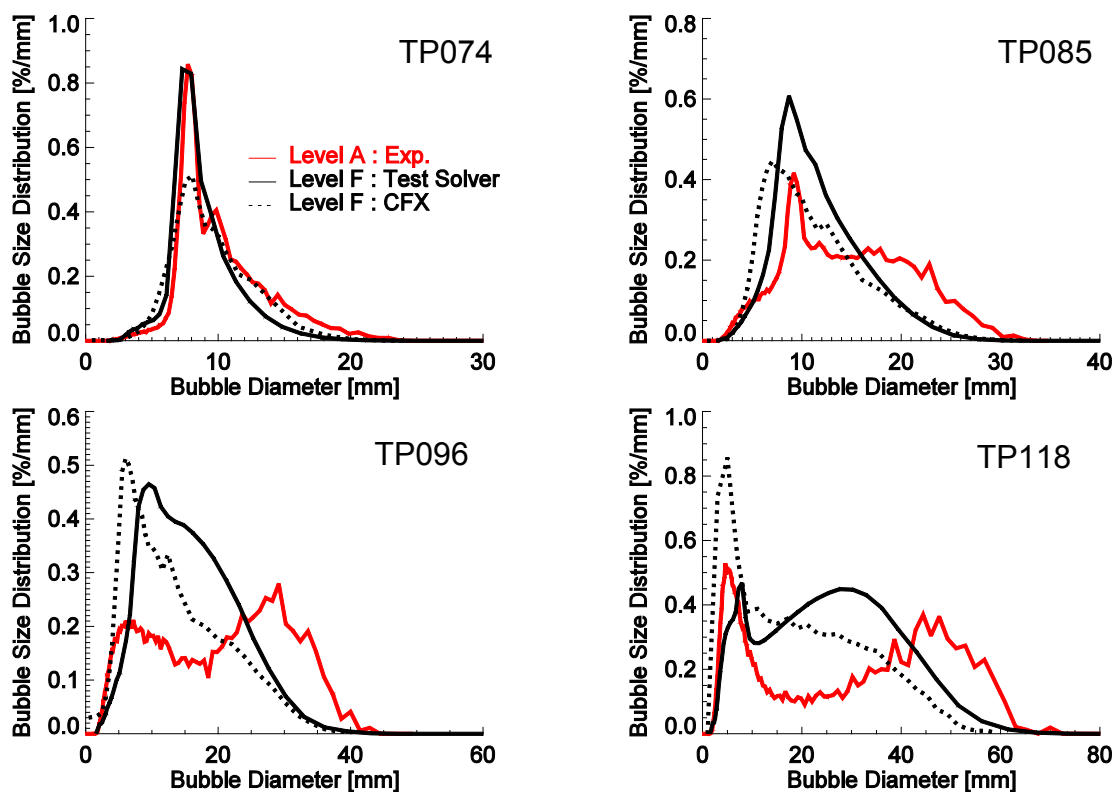


Figure 6.34 Bubble size distribution predicted by the new model implemented in CFX and Test Solver

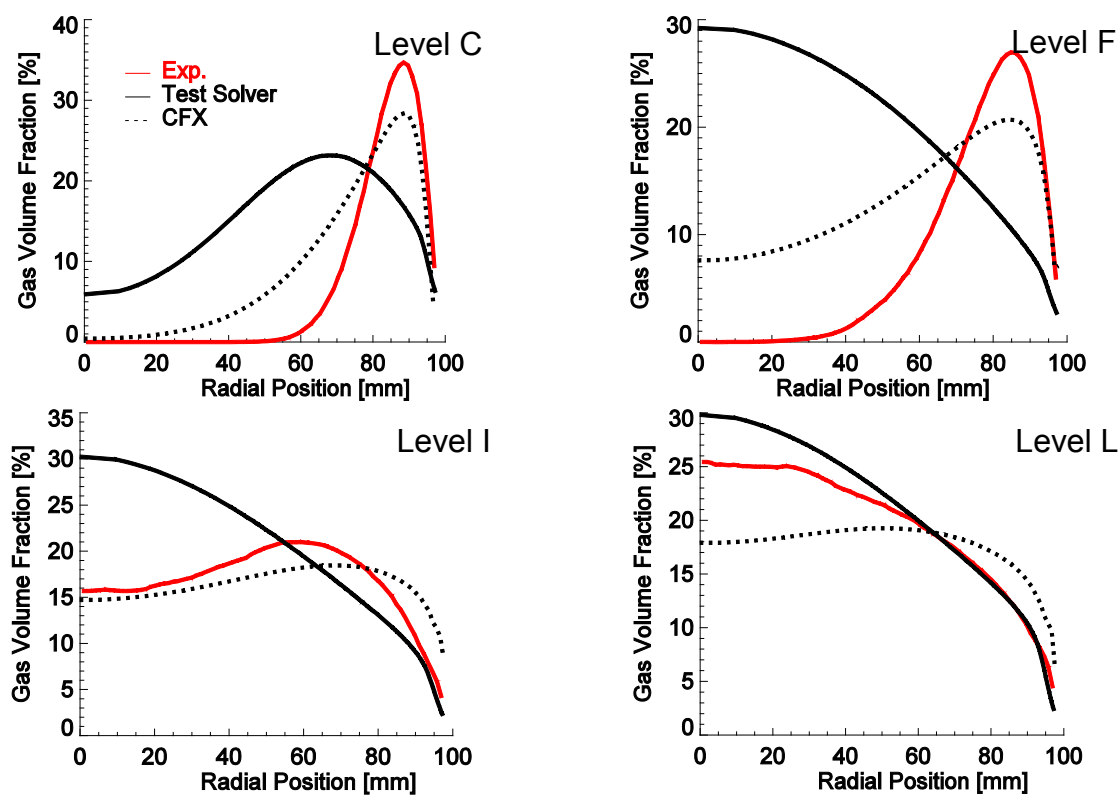


Figure 6.35 Gas volume fraction predicted by the new model implemented in CFX and Test Solver (TP118)

## 6.6 Influence of interphase drag force

Finally, it is worth noting that in all simulations done by the Test Solver the Tomiyama [151] correlation for the interphase drag force is employed while in CFX the drag model of Ishii and Zuber [140], of Grace [98] and of Schiller and Naumann [147] are by default available. The model of Tomiyama [151] is implemented in addition through FORTRAN subroutines. The influence of difference drag models on the predictions about the bubble size distribution, gas volume fraction as well as velocity field is shown in Figure 6.36. It can be seen that the influence of the drag models of Tomiyama [151], Ishii and Zuber [140] and Grace [98] is negligible while the predictions delivered by the model of Schiller and Naumann [147] obviously deviates from those by other three models. The deviation possibly results from the limitation of the model of Schiller and Naumann [147] for solid spherical particles or for fluid particles that are sufficiently small. In addition, according to all drag models, a negative liquid velocity or a circulation region appears at the pipe center, which is caused by the low liquid eddy viscosity delivered by the Morel [159] BIT model (see Figure 6.25).

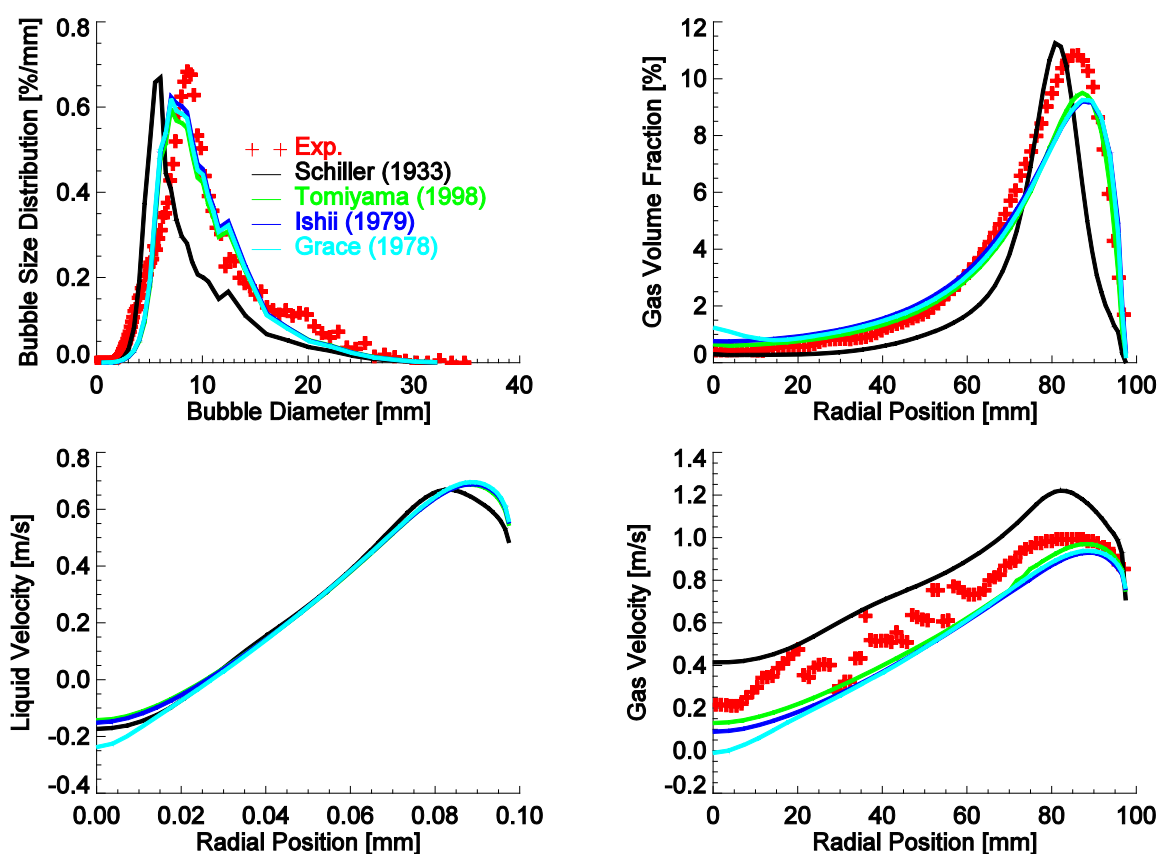


Figure 6.36 Influence of drag model (TP072, Level F, SST model+Morel [159] BIT model,  $C_k=C_\epsilon=1.0$ , two-phase liquid inlet)

## 6.7 Discussion

The new model for bubble coalescence and breakup is implemented in the CFD code ANSYS CFX 12.1 and simulations performed were for air-water mixtures in an upward pipe flow. Several test points with different combinations of gas and liquid superficial velocities are involved. Predictions of the gas volume fraction, gas velocity, bubble size distribution as well as mean bubble size are compared with the



experimental data, the results delivered by the Test Solver and by the standard models, respectively. In addition, the influence of inlet conditions for liquid phase, interfacial forces such as wall lubrication force as well as turbulence models on the evolution of the phase distribution is analyzed.

The results show that the new model can successfully capture the evolution tendency of the gas volume fraction and bubble size distribution. Moreover, considerable improvement is achieved in comparison to the standard models. However, the redistribution process of the gaseous phase near the injection position is too fast in the prediction and the predicted bubble size is generally smaller than the measurement. The redistribution velocity is mainly determined by bubble forces. Besides the lift force and turbulent dispersion force, which are discussed in the results of Test Solver, the influence of wall lubrication force on the radial profile of gas volume fraction is also significant. In comparison to the model of Tomiyama [151], the wall lubrication force calculated by the Antal et al. [153] correlation in Eq. 4-13 and Eq. 4-14 is too small and results in an unrealistic peak of gas volume fraction adjacent to the pipe wall. On the other hand, if instead of the  $k-\epsilon$  model, the SST model is used for the liquid turbulence, this unphysical peak disappears. This is because the liquid eddy viscosity or turbulent dispersion predicted by the SST model is much larger than that by the  $k-\epsilon$  model (Figure 6.22). From influence of the turbulence model on the evolution of bubble size distribution, see Figure 6.21, one can see that dissipation rate predicted by SST model is in general smaller than that by  $k-\epsilon$  model.

The radial profile for gas volume fraction is dependent not only on bubble force models, but also on the inlet conditions for liquid phase, since they determine directly the eddy viscosity near the inlet. If the velocity and turbulence parameters calculated by the Sato [8] model in the Test Solver are used for the inlet conditions of the liquid phase, the predicted migration velocity of gaseous bubbles from the pipe wall to the center is in general overestimated. On the other hand, if the turbulence parameters of a fully-developed single-phase flow with equal liquid volumetric flux are used, the redistribution process of gaseous phase after the injection agrees well with the measurement, but this will bring instability to the radial profile of gas volume fraction due to too low an eddy viscosity.

Finally, the comparison between the predictions provided by the new model and those by the standard models in CFX, see Figure 6.32 and Figure 6.33, shows a considerable improvement. The standard models overestimate the breakup rate and as a result the mean bubble size is much smaller than the measured one. In addition, from the comparison with the results of Test solver, one can see that the breakup rate predicted by CFX is too large or the coalescence rate is under predicted. As a result, the predicted bubble size is generally smaller than the prediction given by the Test Solver. The overestimation of coalescence rate by Test Solver might be caused by an overestimation of gas redistribution velocity.

## 7 Conclusion

Practice has shown that the modeling of bubble coalescence and breakup is one of the bottlenecks in the modern CFD simulation of gas-liquid poly-dispersed flows. An extensive literature research reveals that the performance of existing models is quite inconsistent with each other, since all of them are tested under certain conditions. The purpose of this thesis is to develop a generally-applicable model for bubble coalescence and breakup, which is based on available theories and models. In comparison with other models, the main advantages of the new model can be summarized as follows:

- 1). All important mechanisms leading to bubble coalescence and breakup in a turbulent gas-liquid flow are considered
- 2). Different correlations used for the calculation of collision frequency and coalescence efficiency if different mechanisms are considered
- 3). The breakup model is based on pure kinematic analysis, no information about the size and energy of turbulent eddies is needed.
- 4). Complicated integrals over the size and/or energy of eddies are successfully avoided
- 5). Arbitrary assumptions of daughter bubble size distribution are avoided. The daughter bubble size distribution, which is calculated directly from the partial breakup frequency, obeys the most reasonable 'M-shape'

The new model is tested and validated extensively in the Test Solver and the CFD code ANSYS-12.1 CFX for the case of vertical air-water pipe flow. Two kinds of extensions of the standard multi-fluid model are available in both solvers, i.e. the discrete population model and the inhomogeneous MUSIG model. These extensions with corresponding closure models such as coalescence and breakup are able to predict the evolution of bubble size distribution in poly-dispersed flows and to overcome the mono-dispersed flow limitation of the standard multi-fluid model. In addition, the performance of the Test Solver is first tested by doing parameter studies against corresponding CFX results. The results show that it is difficult for the Test Solver to capture the developing process of the flow near the inlet. In other words, the flow develops immediately into a fully-developed flow and the inlet conditions have almost no influence on the flow structure downstream. This discrepancy is caused by the 1D simplification of the Test Solver and will bring an overestimation of the migration velocity of gaseous bubbles from the pipe wall to the pipe center.

Instead of complicated 3D flow conditions, gas-liquid vertical pipe flow under adiabatic conditions is chosen for the validation of the new model. This is because in such a simple case other complicated phenomena such as liquid circulation can be excluded. In this case, the gaseous phase travels together with the liquid flow stably under well-defined boundary conditions. The evolution of phase distribution is determined mainly by bubble dynamics and bubble forces. In addition, unlike in a bubble column, the change of bubble size distribution can be observed along the pipe over a long vertical distance, which is the most attractive advantage for the test of models for bubble coalescence and breakup.

Experimental data obtained in the L12 test series of air-water vertical pipe flow performed at the TOPFLOW test facility is employed for the validation of the model. This database is chosen according to three key considerations. Firstly, the available information of databases published in the literature for gas-liquid vertical pipe flow is usually incomplete to fulfill the desire of the validation of the new model in the two selected solvers. Especially, measured data of bubble size distributions are rare. Secondly, in the L12 database measurements about the evolution of bubble size distribution and phase distribution along the pipe are comprehensive. For example, data of bubble size distribution, gas velocity, gas volume fraction as well as the decomposition of radial gas volume fractions according to the bubble size classes are available for 12 height positions and 48 test points with different combinations of gas and liquid superficial velocities (see Table 4.1 and Table 4.2). Finally, the quality and plausibility of the measured data was checked extensively. A clear and consistent trend regarding the evolution of the flow with increasing L/D and superficial gas velocity was found. This is a clear advantage compared to previous test series of TOPFLOW facility as well as to databases published in the literature.

Validation simulations are carried out for a wide range of test points from the experiment matrix, which cover the bubbly flow, turbulent-churn flow as well as the transition regime. Predictions about bubble size distribution, gas velocity and volume fraction indicate a generally good agreement with the measurement in the whole selected range. Results provided by the Test Solver can reproduce well the evolution tendency of bubble size distribution along the pipe, which change from coalescence dominant regimes via breakup dominant regimes to wake-entrainment dominant regimes as the superficial gas velocity increases. However, the tendency is almost always overestimated, i.e. too much coalescence in the coalescence-dominant case while too much breakup in breakup-dominant ones.

The analysis of the contribution of each mechanism shows that the overestimation of coalescence rate could be caused by the mechanism of turbulence since it is the most important one in the coalescence-dominant cases. On the other hand, the mechanism of interfacial slip or stresses is responsible for the overprediction of the breakup rate in breakup-dominant cases. Furthermore, according to the new model coalescence caused by wake-entrainment is too large for test points with very high superficial gas velocity.

At the same time, the redistribution of the gaseous phase from the injection position at the pipe wall to the whole cross section can be well traced by the Test Solver with the new closure model. However, in the simulation, the velocity of gas redistribution is too large, which could be caused by the 1D simplification of the Test Solver as discussed above. In addition, the redistribution process is dependent on bubble forces such as turbulent dispersion force and lift force. Reducing the influence of the turbulent dispersion force will lessen the impact of the redistribution process of the gaseous phase after injection. However, too low a dispersion force could bring out an unrealistic peak of gas volume fraction profiles, e.g. small bubbles accumulated at the near-wall region while large bubbles at the pipe center. On the other hand, a smaller lift force will slow down the migration of large bubbles towards pipe center under negative liquid velocity gradient. However, if the sign of velocity gradient changes to positive, e.g. due to the acceleration of gas injection, a small lift force will accelerate the migration of large bubbles to the pipe center. In addition, the wall

lubrication force also has a noticeable influence on the radial gas volume fraction profile. For example, small bubbles will immediately accumulate adjacent to the wall, if the wall force model of Antal et al. [153] together with the  $k$ - $\epsilon$  turbulence model is adopted. This is caused by the fact that the total dispersion effect of the two forces for small bubbles is insufficient to resist the accumulation effect of the lift force.

Simulations performed with ANSYS CFX using the inhomogeneous MUSIG approach with the new closure model can predict the evolution of bubble size distribution and gas volume fraction with acceptable agreement with the measurements. A considerable improvement is observed over the results delivered by the standard closure models available in CFX. Besides that of bubble forces, the influence of inlet conditions for the liquid phase is also analyzed. The results imply that the uncertainty in the liquid inlet conditions has a noticeable influence on the redistribution process of the gaseous phase. This is mainly caused by the difference in the predicted eddy viscosity, which is much smaller in the case of single-phase inlet condition than that of the two-phase inlet condition provided by Test Solver. In addition, the results achieved in CFX are compared with those in the Test Solver, which shows that they are comparable with each other. Nevertheless, the average bubble size predicted by CFX is in general smaller than that by Test Solver. This might be caused by the overestimation of the redistribution process of gaseous bubbles by the Test Solver, which could over predict the coalescence rate while it concurrently underpredicts the breakup rate.

Finally, since the turbulent dispersion force, which has a deciding influence on radial profile of gas volume fraction, is proportional to the eddy viscosity, the influence of the models for liquid turbulence as well as bubble induced turbulence (BIT) generation and destruction is investigated in the Test Solver and CFX, respectively. Predictions show that the influence of turbulence modelling on the bubble size distribution as well as average bubble size is negligible for test points with medium superficial gas velocity such as 085 and 096. This is because for these cases the mechanism of turbulence has a trivial contribution to the total coalescence and breakup rate (see Figure 5.36 and Figure 5.37). Nevertheless, its contribution to the breakup rate increases with the increase in the superficial gas velocity. As a result, for those test points with high superficial gas velocity such as 107 and 118, the predicted average bubble size decreases with the increase of turbulence dissipation rate. On the other hand, the influence of turbulence modeling on the radial gas volume fraction profile is obvious. Furthermore, the results are quite sensitive to the value of the characteristic time scale used by different BIT models. A small time scale will reduce the predicted liquid eddy viscosity, which might bring instability to the radial profile for gas volume fraction. If the turbulent dispersion force, i.e. the eddy viscosity, is too small, there will be an unphysical accumulation of gaseous bubbles at the pipe center due to the effect of the lift force. In addition, the difference in the definitions for the characteristic time scale, the impact of the different BIT models on superficial gas velocity or bubble size is different with each application. For example, for cases with relative small superficial gas velocity but BIT source already plays a role, the model of Morel [159] and of Troshko [163] delivers too small an eddy viscosity while for cases with a very superficial gas velocity, the model of Pfleger [157] and of Politano [158] will bring instability problems. Furthermore, in a case with low superficial liquid velocity, e.g. test point 072, if the predicted viscosity

is too low at the pipe center, there will be a circulation formed and a lot of small bubbles captured there.

Although a general advancement is achieved in comparison with some typical models available in the literature, further investigation and improvement of the new model is indispensable. For example, instead of air-water vertical pipe flow, the model should be validated for other flow situations such as steam-water pipe flow and bubble column. The further validation work is not included here in order to avoid the amount of the current work to be too large. Obviously, it is desirable to validate the model in the cases where only one mechanism is dominant so that more information about the physics of each mechanism can be obtained. In addition, further improvement is indispensable regarding the modeling of two-phase turbulence since the BIT (Bubble-Induce Turbulence) calculated according to different researchers is quite inconsistent.

## 8 Nomenclature

Symbol	Denomination	Unit
$a$	Adjustable parameter in Eq. 2-116	
$\alpha_\alpha$	Volume fraction of phase $\alpha$	
$\alpha_g$	Cross-sectional averaged gas volume fraction	
$\alpha_g(r)$	Radial profile of gas volume fraction	
$\alpha_g(d_i, r)$	Radial profile of gas volume fraction of bubble size group $i$	
$\alpha_g(d_i)$	Cross-sectional averaged gas volume fraction of bubble size group $i$	
$\alpha_j(r)$	Radial profile of gas volume fraction of velocity group $j$	
$\alpha_k(r)$	Radial profile of gas volume fraction of MUSIG sub-size group $k$	
$A$	Frontal area of the leading bubble	$m^2$
$A_e$	Projected area of the bubble onto the hitting eddy	$m^2$
$A_h$	Hamaker constant	J
$\alpha_{max}$	Maximum packing density of gas bubbles	
$b$	Adjustable parameter in Eq. 2-116	
$\beta$	Dimensionless daughter bubble size distribution function	
$B_{bk}, B_{ck}$	Birth term of gas volume fraction of size group $k$ due to coalescence and breakup	$m^{-3}\cdot s^{-1}$
$c$	Tolerance limit for statistic normal distribution function	
$C$	Ratio of the minimum required energy to the parent bubble surface energy	
$C_1 \sim C_{36}$	Adjustable parameters	
$Ca$	Capillary number	
$Ca_{crit}$	Critical capillary number	
$C_D$	Drag coefficient	
$C_e$	Eddy efficiency	
$C_{fbv}$	$f_{bv}^{2/3} + (1 - f_{bv})^{2/3} - 1$	
$C_{fi}$	Interfacial frictional factor	
$C_L$	Lift force coefficient	
$C_0$	Distribution parameter in drift velocity model	
$C_s$	Shape coefficient	
$C_t$	Coefficient considering the difference between the actual velocity of bubbles and that of eddies in turbulent flows	
$C_{\varepsilon 1}, C_{\varepsilon 2}, C_\mu$	Turbulence model constants	
$C_k$	Coefficient in BIT kinetic energy	
$C_\varepsilon$	Coefficient in BIT dissipation rate	
$C_{TD}$	Adjustable constant in turbulence dispersion force	
$C_{VM}$	Virtual mass coefficient	
$C_W$	Wall lubrication force coefficient	
$\xi$	Eddy size divided by the parent bubble size	
$\xi_{min}$	Smallest eddy size divided by the parent bubble size	
$\xi_{ij}$	Size ratio of bubble $i$ to bubble $j$	
$\xi_{so}$	Normalized size of bubbles sheared-off from a large bubble	
$d$	Bubble diameter	m
$D$	Pipe diameter	m
$D_{bk}, D_{ck}$	Death term of gas volume fraction of size group $k$ due to coalescence and breakup	$m^{-3}\cdot s^{-1}$

## Nomenclature

---

$d_{crit}$	Critical bubble size for wake-entrainment to occur	m
$d_e$	Eddy size	m
$d_{eq}$	Equivalent bubble size	m
$d_{e,max}$	Maximum eddy size	m
$d_{e,min}$	Minimum eddy size	m
$\delta_{eff}$	Effective thickness of instable layer at the interface	m
$\Delta t$	Time interval	s
$\Delta d$	Discretization of bubble size	m
$DF(\alpha)$	Damping factor	
$d_i, d_j, d_k, d_l$	Bubble diameter of group i, j, k, l	m
$D_i$	Impeller diameter	m
$d_{max}$	Maximum stable bubble size	m
$\bar{d}$	Average bubble size, $\bar{d} = \int_{d_{min}}^{d_{max}} \alpha_g(d) d \cdot dd_B / \int_{d_{min}}^{d_{max}} \alpha_g(d) \cdot dd_B$	m
$d_{SM}$	Sauter mean diameter, $d_{SM} = \int_{d_{min}}^{d_{max}} \alpha_g(d) \cdot dd_B / \int_{d_{min}}^{d_{max}} \frac{\alpha_g(d)}{d} \cdot dd_B$	m
$d_{so}$	Average size of the sheared-off bubbles	m
$d_{so,max}$	Maximum stable size of the sheared-off bubbles	m
$E_{kin}$	Kinetic energy	kg·m <sup>2</sup> ·s <sup>-2</sup>
$\varepsilon$	Turbulence dissipation rate	m <sup>2</sup> ·s <sup>-3</sup>
$E_{crit}$	critical energy for breakup to occur	kg·m <sup>2</sup> ·s <sup>-2</sup>
$E_e$	Kinetic energy of eddy	kg·m <sup>2</sup> ·s <sup>-2</sup>
$\bar{E}_e$	Average kinetic energy of eddy	kg·m <sup>2</sup> ·s <sup>-2</sup>
$E_{min}$	Energy needed to create the smallest and largest daughter bubbles	kg·m <sup>2</sup> ·s <sup>-2</sup>
$E_{max}$	Energy needed to create two equal-sized daughter bubbles	kg·m <sup>2</sup> ·s <sup>-2</sup>
$E(V_j)$	Energy needed to create two daughters with size $V_j$ and $V_i - V_j$	kg·m <sup>2</sup> ·s <sup>-2</sup>
$E_o$	Eotvos number	
erf	Error function	
erfc	Complementary error function	
$E_\sigma$	Surface energy	kg·m <sup>2</sup> ·s <sup>-2</sup>
$\eta$	Kolmogorov length scale	m
$F$	Interaction force between bubbles	N
$F(\cdot)$	cumulative chi-square distribution	
$F_{\alpha,D}$	Drag force of phase $\alpha$	N
$F_{\alpha,L}$	Lift force of phase $\alpha$	N
$F_{\alpha,TD}$	Turbulent dispersion force of phase $\alpha$	N
$F_{\alpha,W}$	Wall lubrication force of phase $\alpha$	N
$f_{bv}$	Breakage volume fraction, $V_i/V_i$	
$f_{bv,max}$	Possible maximum breakage volume fraction	
$f_{bv,min}$	Possible minimum breakage volume fraction	
$F_D$	Drag force	N
$f_i, f_k, f_l$	Size fraction of the i, k, l group	
$f(p)$	A functional dependency on the viscosity ratio of the dispersed and continuous phase	
$F_\sigma$	Surface tension force	N
$f_{swarm}$	Swarm effect coefficient	

---

## Nomenclature

---

$\varphi_k$	Bubble-induced source term for k-equation	$m^2 \cdot s^{-3}$
$\varphi_\varepsilon$	Bubble-induced source term for $\varepsilon$ -equation	$m^2 \cdot s^{-4}$
$g$	Gravitational acceleration	$m \cdot s^{-2}$
$G$	Gap of the confined flow channel	$m$
$\dot{\gamma}$	Shear rate	$s^{-1}$
$\gamma$	Modification factor for coalescence frequency considering the reduction of free space due to the presence of themselves	
$\Gamma$	Gamma function	
$\Gamma(d_i, d_j)$	Coalescence frequency between bubble i and bubble j	$m^{-3} \cdot s^{-1}$
$h$	Collision frequency between two bubbles	$m^3 \cdot s^{-1}$
$h$	liquid film thickness	$m$
$H$	Height of the batch stirred-tank contactor	$m$
$h_{b,ij}$	Mean distance between bubble i and bubble j	$m$
$h_0$	Initial film thickness	$m$
$h_{crit}$	Critical film thickness	$m$
$h_{t,ij}$	Mean relative turbulent path length scale of bubble i and j	$m$
$h_t$	Average size of eddies that driving bubbles together	$m$
$i, j, k, l$	Subscript representing bubble size groups	
$J_l, J_g, J$	Gas, liquid and total superficial velocity	$m \cdot s^{-1}$
$k$	Wave number of eddies	$m^{-1}$
$k$	Turbulent kinetic energy	$m^2 \cdot s^{-2}$
$L$	Pipe height	$m$
$l_e$	Integral length scale	$m$
$\lambda$	Coalescence efficiency	
$m$	Number of daughter bubbles	
$M$	Surface immobility parameter	
$M$	Morton number	
$m_i, m_k, m_l$	Mass of size group i, k and l	$kg$
$\bar{M}_\alpha$	Interfacial momentum transfer per unit time	$N$
$M_j$	Number of sub-size groups in velocity group j	
$\mu_g$	Dynamic molecular viscosity of gas	$Pa \cdot s$
$\mu_l$	Dynamic molecular viscosity of liquid	
$\mu_b$	Additional BIT viscosity	$Pa \cdot s$
$\mu_t$	Shear-induced viscosity	$Pa \cdot s$
$\mu_t'$	$\mu_b + \mu_t$	$Pa \cdot s$
$n$	Bubble number density	$m^{-3}$
$N$	Agitation speed	$s^{-1}$
$N$	Average number of eddies arriving at the surface in unit time	$s^{-1}$
$n_e$	Number density of eddies	$m^{-4}$
$\nu$	Kinematic viscosity	$m^2 \cdot s^{-1}$
$\Omega(d_i)$	Total breakup frequency of bubble i	$s^{-1}$
$\Omega(d_j, d_i)$	Partial frequency of bubble i breaking into daughter bubble j	$s^{-1}$
$p_\alpha$	Pressure of phase $\alpha$	$Pa$
$\rho$	Viscosity ratio of two phases	
$P_b$	Breakup probability	
$\pi$	Circumference ratio	
$\Pi$	Modification factor for turbulence-induced coalescence frequency considering the limited range of turbulence fluctuation affecting the motion of bubbles	

---



## Nomenclature

---

$P_k$	Shear-induced turbulence production	$m^2 \cdot s^{-3}$
$Pr$	Turbulent Prandtl number	
$r$	Radial position or bubble radius	$m$
$R$	Pipe radius	$m$
$R_a$	Liquid film radius	$m$
$r_{eq}$	Equivalent bubble radius	$m$
$r_i$	Radius of bubble $i$	$m$
$r_j$	Radius of bubble $j$	$m$
$R^+$	Dimensionless pipe radius, $R\sqrt{\tau_w / \rho_l} / \nu$	
$\rho_\alpha$	Density of phase $\alpha$	$kg \cdot m^{-3}$
$\rho_j$	Density of gaseous phase velocity group $j$	$kg \cdot m^{-3}$
$\rho_l$	Density of liquid phase	$kg \cdot m^{-3}$
$\rho_g$	Density of gaseous phase	$kg \cdot m^{-3}$
$\Delta\rho$	$\rho_l - \rho_g$	$kg \cdot m^{-3}$
$S$	Source terms by coalescence and breakup	$m^3 \cdot s^{-1}$
$S_{ij}$	Cross-sectional collision area of bubble $i$ and bubble $j$	$m^2$
$\sigma$	Surface tension	$N \cdot m^{-1}$
$\sigma^2$	Variance of a normal distribution	
$\sigma_\varepsilon, \sigma_k$	Turbulence model constant	
$t$	Time coordinate	$s$
$t_{contact}$	Contact or interaction time of two colliding bubbles	$s$
$t_{drainage}$	Time needed for the liquid film captured between two colliding bubbles to thin down to a critical thickness	$s$
$T$	Vessel diameter	$m$
$\tau$	Stress	$N \cdot m^{-2}$
$\tau$	Characteristic time scale	$s$
$T_i$	Inertial turbulent stress	$N \cdot m^{-2}$
$T_s$	Surface stress	$N \cdot m^{-2}$
$T_t$	turbulent stress	$N \cdot m^{-2}$
$T_v$	Vicious stress	$N \cdot m^{-2}$
$T_w$	Wall shear stress	$N \cdot m^{-2}$
$u$	Velocity	$m \cdot s^{-1}$
$u_{crit}$	Critical approach velocity	$m \cdot s^{-1}$
$u_{D,local}$	Local drift velocity	$m \cdot s^{-1}$
$u_e$	Eddy velocity	$m \cdot s^{-1}$
$\bar{u}_{Gl}$	Void-fraction-weighted mean drift velocity	$m \cdot s^{-1}$
$u_{rel}$	Relative velocity	$m \cdot s^{-1}$
$u_r, u_{ri}, u_{rj}$	Terminal rise velocity of a bubble or bubble of size group $i, j$	$m \cdot s^{-1}$
$u_t, u_{ti}, u_{tj}$	Turbulence velocity fluctuation around a bubble, bubble of size group $i, j$	$m \cdot s^{-1}$
$V, V_i, V_j$	Bubble volume or volume of a bubble of size group $i$ and $j$	$m^3$
$V_i^{BOX}$	Volume influenced by the wake of bubble $i$	$m^3$
$\hat{V}$	Normalized bubble volume	$m^3$
$\bar{V}$	Mean bubble volume	$m^3$
$x, y, z$	Spatial coordinates	$m$
$y^+$	Dimensionless distance from the wall, $y\sqrt{\tau_w / \rho_l} / \nu$	
$w$	Collision frequency between bubbles and eddies	$m^3 \cdot s^{-1}$
$We$	Weber number	
$We_{crit}$	Critical Weber number	

---

## 9 Reference

- [1] Hewitt G. F. Multiphase flow in the energy industries. *Journal of Engineering Thermophysics*, 17, pp.12-23, 2008
- [2] Lucas, D., et al. Prediction of radial gas profiles in vertical pipe flow on the basis of bubble size distribution. *International Journal of Thermal Sciences*, 40, pp.217-225, 2001a
- [3] Sommerfeld, M. Overview and fundamentals, in: V.K.I. for Fluid Mechanics, *Theoretical and Experimental Modelling of ParticulateFlow*, Lecture Series No. 2000-6, pp. 1–62, 2000
- [4] Wieringa, J. A., et al. Droplet breakup mechanisms during emulsification in colloid mills at high dispersed phase volume fraction. *Trans. Inst. Chem. Eng.*, 74, pp.554-562, 1996
- [5] Kawamura, T., Kodama, Y. Numerical simulation method to resolve interactions between bubbles and turbulence. *International Journal of Heat and Fluid Flow*, 23, pp.627-638, 2002
- [6] Lucas, D., Krepper, E. Modeling the evolution of bubbly flow along a large vertical pipe. *Nuclear Technology*, 158, pp.291-303, 2007
- [7] Krepper, E., et al. The inhomogeneous MUSIG model for the simulation of polydispersed flows. *Nuclear Engineering and Design*, 238, pp.1690-1702, 2008
- [8] Sato, Y., et al. Momentum and heat transfer in two-phase bubble flow. *International Journal of Multiphase Flow*, 7, pp.167-177, 1981
- [9] Lucas, D., et al. Benchmark database on the evolution of two-phase flows in a vertical pipe. XCFD4NRS, OECD/NEA & International Atomic Energy Agency (IAEA) Workshop, Grenoble, France, 2008
- [10] ANSYS, Inc. ANSYS CFX, Release 12.1, 2009
- [11] Lahey Jr. R. T., D. A. Drew. The analysis of two-phase low and heat transfer using a multidimensional, four field, two-fluid model. *Nucl. Eng. Des.*, 204, pp.29-44, 2001
- [12] Hulburt, H., Katz, S. Some problems in particle technology. *Chemical Engineering Science*, 19, pp.555-574, 1964
- [13] Ramkrishna, D. The status of population balances. *Reviews in Chemical Engineering*, 3, pp.49-95, 1985
- [14] Randolph, A. D., Larson, M. A. Transient and steady state size distributions in continuous mixed suspension crystallizers. *AIChE Journal*, 8, pp.639-645, 1962
- [15] Ishii, M., Mishima, K. Study of two-fluid model and interfacial area, Argonne National Lab Report ANL-80-111, 1981
- [16] Kocamustafaogullari, G., Ishii, M. Foundation of the interfacial area transport equation and its closure relations. *International Journal of Heat and Mass Transfer*, 38, pp.481-493, 1995
- [17] Ishii, M. et al. Interfacial area transport equation for two-fluid model formulation. *Proceedings of IMuST Meeting, Santa Barbara*, pp.35-42, 1998
- [18] Uhle, J., et al. Dynamic flow regime modeling. *Proceedings of 6th International Conference on Nuclear Engineering, ICONE 6, San Diego, California, May 10-15, 1998*

- [19] Wu, Q., et al. Framework of two-group model for interfacial area transport in vertical two-phase flows. *Transactions of the American Nuclear Society*, 79, pp. 351–352, 1998b
- [20] McGraw, R. Description of aerosol dynamics by the quadrature method of moments. *Aerosol Science and Technology*, 27, pp. 255-265, 1997
- [21] Marchisio, D. L., Fox, R. O. Solution of population balance equations using the direct quadrature method of moments. *Aerosol Science*, 36, pp.43-73, 2005
- [22] Wacker, et al. Parameterization of cloud physics: 3-moment scheme for sedimentation. *Journal of the Atmospheric Sciences*, submitted, 2011
- [23] Lo, S. Application of the MUSIG model to bubbly flows. AEA Technology, AEAT-1096, 1996
- [24] Frank, Th., et al. Validation of CFD models for mono- and polydispersed air-water two-phase flows in pipes. *Nucl. Eng. Des.*, 238, pp.647-659, 2008
- [25] Chesters, A. K. The modeling of coalescence processes in fluid-liquid dispersions: A review of current understanding. *Chemical Engineering Research and Design: Transactions of the Institution of Chemical Engineers: Part A*, 69, pp.259-270, 1991
- [26] Shinnar, R., Church, J. M. Predicting particle size in agitated dispersions. *Industrial and Engineering Chemistry*, 52, pp.253-256, 1960
- [27] Howarth, W. J. Coalescence of drops in a turbulent flow field. *Chemical Engineering Science*, 19, pp.33-38, 1964
- [28] Doublier, L. The drainage and rupture of a non-foaming liquid film formed upon bubble impact with a free surface. *International Journal of Multiphase Flow*, 17, pp.783-803, 1991
- [29] Duineveld, P. C. Bouncing and coalescence of two bubbles in water. PhD Dissertation. University of Twente. The Netherlands, 1994
- [30] Lehr, F., Mewes, D. A transport equation for the interfacial area density applied to bubble columns. *Chemical Engineering Science*, 56, pp.1159-1166, 1999
- [31] Lehr, F., et al. Bubble-size distributions and flow fields in bubble columns. *AIChE Journal*, 48, pp.2426-2443, 2002
- [32] Casamatta, G., Vogelpohl, A. Modeling of fluid dynamics and mass transfer in extraction columns. *German Chemical Engineering*, 8, pp.96-103, 1985
- [33] Kentish, S. E., et al. Estimation of coalescence and breakage rate constants within a Kühni column. *Industrial and Engineering Chemistry Research*, 37, pp.1099-1106, 1998
- [34] Konno, M., et al. Coalescence of dispersed drops in an agitated tank. *Journal of Chemical Engineering of Japan*, 21, pp.335-338, 1988
- [35] Wright, H., Ramkrishna, D. Factors affecting coalescence frequency of droplets in a stirred liquid-liquid dispersion. *AIChE Journal*, 40, pp.767-776, 1994
- [36] Prince, M. J., Blanch, H. W. Bubble coalescence and breakup in air-sparged bubble columns. *AIChE Journal*, 36, pp.1485-1499, 1990
- [37] Wang, T., et al. Theoretical prediction of flow regime transition in bubble columns by the population balance model. *Chemical Engineering Science*, 60, pp.6199-6209, 2005a
- [38] Wang, T., et al. Population balance model for gas-liquid flows: Influence of bubble coalescence and breakup models. *Industrial and Engineering Chemistry Research*, 44, pp.7540-7549, 2005b

- [39] Wu, Q., et al. One-group interfacial area transport in vertical bubbly flow. *International Journal of Heat and Mass Transfer*, 41, pp.1103-1112, 1998a
- [40] Friedlander, S. K. *Smoke, Dust and Haze*. Wiley, New York, 1977
- [41] Howarth, W. J. Measurement of coalescence frequency in an agitated tank. *AIChE Journal*, 13, pp.1007-1013, 1967
- [42] Simon, M. *Koaleszenz von Tropfen und Tropfenschwärmen*. PhD Dissertation, die Teschinschen Universtität Kaiserslautern, 2004
- [43] Sovová, H. Breakage and coalescence of drops in a batch stirred vessel-II Comparison of model and experiments. *Chemical Engineering Science*, 36, pp.1567-1573, 1981
- [44] Davis, R. H., et al. The lubrication force between two viscous drops. *Physics of Fluids A*, 1, pp.77-81, 1989
- [45] Jeffreys, G. V., Davies, G. A. Coalescence of liquid droplets and liquid dispersion: Recent advances in liquid-liquid extraction, in: Pergamon Press, Oxford, UK, 1<sup>st</sup> ed., p. 495, 1971
- [46] Liu, T. J., Bankoff, S. G. Structure of air-water bubbly flow in a vertical pipe —I. Liquid mean velocity and turbulence measurements. *Int. J. Heat Mass Transfer*, 36, pp.1049-1060, 1993a
- [47] Mackay, G. D. M., Mason, S. G. The gravity approach and coalescence of fluid drops at liquid interfaces. *Canadian Journal of Chemical Engineering*, 41, pp. 203-212, 1963
- [48] Vaughn, M. W., Slattery, J. C. Effects of viscous normal stresses in thin draining films. *Ind. Eng. Chem. Res.*, 34, pp.3185-3186, 1995
- [49] Podgorska, W. Drop coalescence in a turbulent flow factors affecting film drainage. *Chem. and Proc. Eng.*, 29, pp.257-269, 2008
- [50] Sagert, N. H., Quinn, M. J. The coalescence of H<sub>2</sub>S and CO<sub>2</sub> bubbles in water. *The Canadian Journal of Chemical Engineering*, 54, pp.392-398, 1976
- [51] Tsouris, C., Tavlarides, L. L. Breakage and coalescence models for drops in turbulent dispersions. *AIChE Journal*, 40, pp.395-406, 1994
- [52] Colella, D., et al. A study on coalescence and breakage mechanisms in three different bubble columns. *Chemical Engineering Science*, 54, pp.4767-4777, 1999
- [53] Hibiki, T., et al. Interfacial area transport of bubbly flow in a small diameter pipe. *Journal of Nuclear Science and Technology*, 38, pp.614-620, 2001a
- [54] Kalkach-Navarro, S., et al. Analysis of the bubbly/slug flow regime transition. *Nuclear Engineering and Design*, 151, 15-39, 1994
- [55] Kennard, E. H. *Kinetic theory of gases*, in: McGraw-Hill, New York, 1938
- [56] Coualoglou, C. A., Tavlarides, L. L. Description of interaction processes in agitated liquid-liquid dispersions. *Chemical Engineering Science*, 32, pp.1289-1297, 1977
- [57] Lee, C. H., et al. Bubble breakup and coalescence in turbulent gas-liquid dispersions. *Chemical Engineering Communications*, 59, pp.65-84, 1987a
- [58] Luo, H. *Coalescence, breakup and liquid circulation in bubble column reactors*. PhD Dissertation, The Norwegian Institute of Technology, Trondheim, 1993
- [59] Martínez-Bazán, C., et al. On the breakup of an air bubble injected into fully developed turbulent flow. Part 1. Breakup frequency. *Journal of Fluid Mechanics*, 401, pp.157-182, 1999a
- [60] Colin, C., et al. Turbulence and shear-induced coalescence in gas-liquid pipe flows. 5<sup>th</sup> International Conference on Multiphase Flow, ICMF'04, Yokohama, Japan, May 30-June 4, 2004

- [61] Hibiki, T., Ishii, M. One-group interfacial area transport of bubbly flows in vertical round tubes. *International Journal of Heat and Mass Transfer*, 43, pp.2711-2726, 2000a
- [62] Hibiki, T., Ishii, M. Two-group interfacial area transport equations at bubbly-to-slug flow transition. *Nuclear Engineering and Design*, 202, pp.39-76, 2000b
- [63] Chesters, A. K., Hofman, G. Bubble coalescence in pure liquids. *Applied Scientific Research*, 38, pp.353-361, 1982
- [64] Clift, R., et al. Bubbles, drops and particles. Academic Press, New York, U.S.A., 1978
- [65] Fan, L. S., Tsuchiya, K. Bubble wake dynamics in liquids and liquid-solid suspensions. MA. Butterworth-Heinemann, Stoneham, 1990
- [66] Komosawa, I., et al. Wake behavior and its effect on interaction between spherical-cap bubbles. *Journal of Chemical Engineering of Japan*, 13, pp.103-109, 1980
- [67] Bilicki, Z., Kestin J. Transition criteria for two-phase flow patterns in vertical upward flow. *International Journal of Multiphase Flow*, 13, pp.283-294, 1987
- [68] Stewart, C. W. Bubble interaction in low-viscosity liquids. *Int. J. Multi. Flow*, 21, pp.1037-1046, 1995
- [69] Schlichting, H. Boundary-layer theory, McGraw-Hill, New York, USA, 1979
- [70] Nevers, N. de, Wu, J. L. Bubble Coalescence in Viscous Fluids. *AIChE Journal*, 17, pp.182-186, 1971
- [71] Richardson, J. F., Zaki, W. M. Sedimentation and fluidization, Part I. *Transactions of the Institution of Chemical Engineers*, 32, pp.35-53, 1954
- [72] Hibiki, T., et al. Interfacial area transport of bubbly flow in a small diameter pipe. *International Conference on Multiphase Flow, ICMF'01*, New Orleans, Louisiana, USA, May 27-June 1, 2001c
- [73] Kuboi, R., et al. Behavior of dispersed particles in turbulent liquid flow. *Journal of Chemical Engineering of Japan*, 5, pp.349-355, 1972a
- [74] Park, J. Y., Blair, L. M.. The effect of coalescence on drop size distribution in an agitated liquid-liquid dispersion. *Chemical Engineering Science*, 30, pp.1057-1064, 1975
- [75] Chatzi, E., Kiparissides, C. Dynamic simulation of bimodal drop size distributions in low-coalescence batch dispersion systems. *Chem. Eng. Sci.*, 47, 445-456, 1992
- [76] Ross, S. L., et al. Droplet breakage and coalescence processes in an agitated dispersion. 2. Measurement and interpretation of mixing experiments. *Industrial and Engineering Chemistry Fundamentals*, 17, pp.101-108, 1978
- [77] Coualoglou, C. A. Dispersed phase interactions in an agitated flow vessel. PhD Dissertation, Illinois Institute of Technology, Chicago, 1975
- [78] Das, P. K., Kumar, R. Coalescence of drops in stirred dispersion. A white noise model for coalescence. *Chemical Engineering Science*, 42, pp.213-220, 1987
- [79] Lee, J. C., Hodgson, T. D. Film flow and coalescence –I Basic relations film shape and criteria for interface mobility. *Chemical Engineering Science*, 23, pp.1375-1397, 1968
- [80] Hagesaether, L. Coalescence and breakup of drops and bubbles. PhD Dissertation. Norwegian University of Science and Technology, Trondheim, Norway, 1999b
- [81] Derjaguin, B. V., Kussakov, M. M. Anomalous properties of thin poly-molecular films. *Acta Physicochim. URSS*, 10, pp.25-30, 1939

- [82] Frankel, S. P., Mysels, K. J. On the dimpling during the approach of two interfaces. *The Journal of Physical Chemistry*, 66, pp.190-191, 1962
- [83] Chappellear, D. C. Models of a liquid drop approaching an interface. *Journal of Colloid Science*, 16, pp.186-190, 1961
- [84] Chesters, A. K. The applicability of dynamic-similarity criteria to isothermal, liquid-gas, two-phase flows without mass transfer. *International Journal of Multiphase Flow*, 2, 191-212, 1975
- [85] Oolman, T. O., Blanch, H. W. Bubble coalescence in stagnant liquids. *Chemical Engineering Communications*, 43, pp.237-261, 1986
- [86] Hasseine, A., et al. Assessment of drop coalescence and breakup for stirred extraction columns. *Chemical Engineering and Technology*, 28, pp.552-560, 2005
- [87] Levich, V. G. *Physicochemical Hydrodynamics*, in: Prentice Hall, Englewood Cliffs, NJ, 1962
- [88] Kamp, A. M., Chesters, A. K. Bubble coalescence in turbulent flows: A mechanistic model for turbulence-induced coalescence applied to microgravity bubbly pipe flow. *International Journal of Multiphase Flow*, 27, pp.1363-1396, 2001
- [89] Jeelani, S. A. K., Hartland, S. Effect of approach velocity on binary and interfacial coalescence. *Chemical Engineering Research and Design: Transactions of the Institution of Chemical Engineers: Part A*, 69, pp.271-281, 1991
- [90] Schwartzberg, H. G., Freybal, R. E. Fluid and particle motion in turbulent stirred tanks. *Industrial Engineering Chemistry Fundamentals*, 7, pp.1-6, 1968
- [91] Carrica, P. M., et al. A polydisperse model for bubbly two-phase flow around a surface shape. *Int. J. Multiphase Flow*, 25, pp.257-305, 1999
- [92] Kolev, N. I. Fragmentation and coalescence dynamics in multiphase flows. *Experimental Thermal and Fluid Science*, 6, pp.211-251, 1993
- [93] Venneker, B. C. H., et al. Population balance modeling of aerated stirred vessels based on CFD. *AIChE Journal*, 48, pp.673-685, 2002
- [94] Müller-Fischer, N., et al. Single bubble deformation and breakup in simple shear flow. *Experiments in Fluids*, 45, pp.917-926, 2008
- [95] Luo, Hean, Svendsen, Hallvard F. Theoretical model for drop and bubble breakup in turbulent dispersions. *AIChE Journal*, 42, pp.1225-1233, 1996a
- [96] Wang, T., et al. A novel theoretical breakup kernel function for bubbles/droplets in a turbulent flow. *Chemical Engineering Science*, 58, pp.4629-4637, 2003
- [97] Zhao, H., Ge, W. A theoretical bubble breakup model for slurry beds or three-phase fluidized beds under high pressure. *Chemical Engineering Science*, 62, pp.109-115, 2007
- [98] Bentley, B. J., Leal, L. G. An experimental investigation of drop deformation and breakup in steady, two-dimensional linear flows. *J. Fluid Mech.*, 167, pp.241-283, 1986
- [99] Grace, H. P. Dispersion phenomena in high viscosity immiscible fluid systems and application of static mixers as dispersion devices in such systems. *Chem. Eng. Commun.*, 14, pp.225-277, 1982
- [100] Pozrikidis, C. Unsteady viscous flow over irregular boundaries. *J. Fluid Mechanics*, 255, pp.11-34, 1993
- [101] Renardy, Y. Direct simulation of drop fragmentation under simple shear. *Interfacial fluid dynamics and transport processes, Lecture Notes in Physics*.

- Springer, Berlin Heidelberg New York, pp.305-325, ISBN 3-540-40583-6, 2003
- [102] Rallison, J. M. A numerical study of the deformation and burst of a viscous drop in general shear flows. *J. Fluid Mech.*, 109, pp.465-482, 1981
- [103] Taylor, G. I. The formation of emulsions in definable fields of flow. *Proc. Roy. Soc.*, 146, pp.501-523, 1934
- [104] Fu, X. Y., et al. Two-group interfacial area transport in vertical air-water flow I. Mechanistic Model. *Nuclear Engineering and Design*, 219, pp.143-168, 2002
- [105] Sun, X., et al. Modeling of bubble coalescence and disintegration in confined upward two-phase flow. *Nucl. Eng. Des.*, 230, pp.3-26, 2004
- [106] Ishii, M., Kojasoy, G. Interfacial area transport equation and preliminary considerations on closure relations, Purdue University Report, PU-NE-93-6, 1993
- [107] Wang, T., et al. A CFD-PBM coupled model for gas-liquid flows. *AIChE Journal*, 52, pp.125-140, 2006
- [108] Elemans, P. H. M., et al. Transient phenomena in dispersive mixing. *Chem. Eng. Sci.*, 48, pp.267-276, 1993
- [109] Chatzi, E. G., et al. Generalized model for prediction of the steady-state drop size distributions in batch stirred vessels. *Industrial and Engineering Chemistry Research*, 28, pp.1704-1711, 1989
- [110] Martínez-Bazón, C., et al. On the breakup of an air bubble injected into fully developed turbulent flow. Part 2. Size PDF of the resulting daughter bubbles. *Journal of Fluid Mechanics*, 401, pp.183-207, 1999b
- [111] Narsimhan, G., Gupta, J. P. A model for transitional breakage probability of droplets in agitated lean liquid-liquid dispersions. *Chemical Engineering Science*, 34, pp.257-265, 1979
- [112] Chatzi, E., et al. Analysis of interactions for liquid-liquid dispersions in Agitated Vessels. *Industrial and Engineering Chemistry Research*, 26, pp.2263-2267, 1987
- [113] Alopaeus, V., et al. Simulation of the population balances for liquid-liquid systems in a nonideal stirred tank. Part 2 Parameter fitting and the use of the multiblock model for dense dispersions. *Chemical Engineering Science*, 57, pp.1815-1825, 2002a
- [114] Alopaeus, V., et al. Gas-liquid stirred tank reactor modeling with CFD and user subroutines. *AIChE Annual Meeting*, Indianapolis, IN, Nov.3-8, 2002b
- [115] Lasheras, J. C., et al. A review of statistical models for the breakup of an immiscible fluid immersed into a fully developed turbulent flow. *Internal Journal of Multiphase Flow*, 28, pp.247-278, 2002
- [116] Lo, S. Application of population balance to CFD modelling of gas-liquid reactors. *Proceedings of Conference on Trends in numerical and physical modelling for industrial multiphase flows*, Corse, September 27-29, 2000
- [117] Lucas, D., et al. Development of bubble size distributions in vertical pipe flow by consideration of radial gas fraction profiles. 4<sup>th</sup> International Conference on Multiphase Flow, ICMF'01, New Orleans, LA, U.S.A., May 27-June 1, 2001b
- [118] Krepper, E., et al. Application of a population balance approach for polydispersed bubbly flows. 6<sup>th</sup> International Conference on Multiphase Flow, ICMF'07, Leipzig, Germany, July 9-13, 2007
- [119] Hagesaether, L., et al. Theoretical analysis of fluid particle collisions in turbulent flow. *Chemical Engineering Science*, 54, pp.4749-4755, 1999a

- [120] Hagesaether, L., et al. A model for turbulent binary breakup of dispersed fluid particles. *Chemical Engineering Science*, 57, pp.3251-3267, 2002
- [121] Wang, T., et al. An efficient numerical algorithm for "A novel theoretical breakup kernel function of bubble/droplet in a turbulent flow". *Chemical Engineering Science*, 59, pp.2593-2595, 2004
- [122] de Bruijn, R.A. Deformation and breakup of drops in simple shear flows. PhD thesis. Tech. Univ. Eindhoven. 1989
- [123] Lo, S., Zhang, D. Modelling of breakup and coalescence in vertical bubbly two-phase flows. 6<sup>th</sup> International Conference on CFD in Oil and Gas, Metallurgical and Process Industries SINTEF/NTNU, Trondheim Norway, 10-12 June, 2008
- [124] Bin, A. Gas entrainment by plunging liquid jets. *Chem. Eng. Sci.*, 48, pp.3585-3630, 1993
- [125] Evans, G. M., et al. Prediction of the bubble size generated by a plunging liquid jet bubble column, *Chem. Eng. Sci.*, 47, pp.3265-3272
- [126] Carrica, P. M., Clausse, A. A. Mathematical description of the critical heat flux as nonlinear dynamic instability. *Instabilities in Multiphase Flow*, Plenum Press, New York, 1993
- [127] Hesketh, R. P., et al. Bubble size in horizontal pipelines. *AIChE Journal*, 33, pp.663-667, 1987
- [128] Hesketh, R. P., et al. Experimental observations of bubble breakage in turbulent flow. *Industrial and Engineering Chemistry Research*, 30, pp.835-841, 1991
- [129] Valentas, K. J., et al. Analysis of breakage in dispersed phase systems. I and *EC Fundamentals*, 5, pp.271-279, 1966
- [130] Hsia, A. M., Tavlarides, L. L. Simulation analysis of drop breakage, coalescence, and micromixing in liquid-liquid stirred tanks. *Chemical Engineering Science*, 26, pp.89-199, 1983
- [131] Konno, M., et al. Scale effect on breakup process in liquid-liquid agitated tanks. *Journal of Chemical Engineering of Japan*, 16, pp.312-319, 1983
- [132] Lee, C.H., et al. Dynamics of bubble size distribution in turbulent gas-liquid dispersions. *Chemical Engineering Communications*, 61, pp.181-195, 1987b
- [133] Randolph, A. D. Effect of crystal breakage on crystal size distribution in a mixed suspension crystallizer. *Industrial and Engineering Chemistry Fundamentals*, 8, pp. 58-63, 1969
- [134] Ross, S. L. Measurements and models of the dispersed phase mixing process. PhD Dissertation, The University of Michigan, Ann Arbor, 1971
- [135] Verhoff, F.H., et al. Breakage and Coalescence Processes in an agitated dispersion. *Experimental System and Data Reduction. Industrial and Engineering Chemistry Fundamentals*, 16, pp.371-377, 1977
- [136] Konno, M., et al. Simulation model for breakup process in an agitated tank. *Journal of Chemical Engineering of Japan*, 13, pp.67-73, 1980
- [137] Collins, S.B., Knudsen, J. G. Drop-size distributions produced by turbulent pipe flow of immiscible liquids, *AIChE Journal*, 16, pp.1072-1080, 1970
- [138] Nambiar, D. K. R., et al. A new model for the breakage frequency of drops in turbulent stirred dispersions. *Chemical Engineering Science*, 47, pp.2989-3002, 1992
- [139] Kuboi, R., et al. Collision and coalescence of dispersed drops in turbulent liquid flow. *Journal of Chemical Engineering of Japan*, 5, pp.423-424, 1972b



- [140] Ishii, M., Zuber, N. Drag coefficient and relative velocity in bubbly, droplet or particulate flows. *AIChE J.*, 25, pp.843-855, 1979
- [141] Kirkpatrick, R. D., Lockett, M. J. The influence of approach velocity on bubble coalescence. *Chem. Eng. Sci.*, 29, pp.2363-2372, 1974
- [142] Kim, W. K., Lee, K. L. Coalescence behavior of two bubbles in stagnant liquids. *J. Chem. Eng. Jap.*, 20, pp. 448-453. 1987
- [143] Ervin, E.A., Tryggvason, G. The rise of bubbles in a vertical shear flow. *J. of Fluids Engineering*, 119, pp.443-449, 1977
- [144] Tomiyama, A., et al. Effects of Eotvos number and dimensionless liquid volumetric flux on lateral motion of a bubble in a laminar duct flow. In : Serizawa, A., Fukano, T., Bataille, J., Editors, *Advances in Multiphase Flow*, Elsevier, Amsterdam, pp.3-15, 1995
- [145] Tomiyama, A., et al. Drag coefficients of single bubbles under normal and micro gravity conditions. *JSME International Journal, Series B*, 41, pp.472-479, 1998a
- [146] Lucas, D., et al. Experimental investigations and modeling on the transition from bubble to slug flow in vertical pipes. *German-Japanese Workshop on Multiphase Flow, Karlsruhe, August 25-27, 2000*
- [147] Schiller, L., Naumann, A. Über die grundlegenden Berechnungen beider Schwer kraftaufbereitung. *Duetscher Ingenieure*, 77, pp.318, 1933
- [148] Burns, A.D., et al. The favre averaged drag model for turbulence dispersion in Eulerian multi-phase flows. 5<sup>th</sup> Int. Conf. on Multiphase Flow, ICMF'2004, Yokohama, Japan, 2004
- [149] Drew, D. A. A turbulent dispersion model for particles or bubbles. *J. of Engineering Mathematics*, 41, pp.259-274, 2001
- [150] Gosman, A.D., et al. Multidimensional modeling of turbulent two-phase flows in stirred vessels. *AIChE Journal*, 38, pp. 1946-1956, 1992
- [151] Tomiyama, A. Struggle with computational bubble dynamics. *Proceedings of the 3rd International Conference Multiphase Flow, ICMF'98, Lyon, France, June 8–12, 1998b*
- [152] Wellek, L.Y. et al. Shape of liquid drops moving in liquid media. *AICHE J.*, 12, pp.854-862, 1966
- [153] Antal, S. P., et al. Analysis of phase distribution in fully developed laminar bubbly two-phase flow. *Int. J. Multiphase Flow*, 17, pp.635-652, 1991
- [154] Hill, D. P., et al. Numerical predictions of two-phase bubbly flow in a pipe. *Proc. 2nd Int. Conf. on Multiphase Flow, Kyoto, Japan, 1995*
- [155] Kataoka, I., Serizawa, A. Turbulence characteristics and their application to multi-dimensional analysis of two-phase flow. *Proc. 8th Int. Topical Meeting on Nuclear Reactor Thermal-Hydraulics, Kyoto, Japan, 1997*
- [156] Morel, C. Turbulence modeling and first numerical simulations in turbulent two-phase flows. *Proc. 11th Symp. on Turbulent Shear Flows, Grenoble, France, pp. P3-10, 1997*
- [157] Pflieger, D., Becker, S. Modelling and simulation of the dynamic flow behaviour in a bubble column. *Chem. Eng. Sci.*, 56, pp.1737-1747, 2001
- [158] Politano, M. S., et al. A model for turbulent polydisperse two-phase flow in vertical channels. *Int. J. Multiphase Flow*, 29, pp.1153-1182, 2003
- [159] Yao, W., Morel, C. Volumetric interfacial area prediction in upward bubbly Two-Phase Flow. *International Journal of Heat and Mass Transfer*, 47, pp.307–328, 2004

- [160] Lee et al. The prediction of two-phase turbulence and phase distribution phenomena using a k- $\epsilon$  model. *Japanese Journal of Multiphase Flow*, 3, pp.335-368, 1989
- [161] Lopez de Bertodano, M. Two-fluid model for two-phase turbulent jets. *Engineering and Design*, 179, pp.65-74, 1998
- [162] Lopez de Bertodano, M. A. Turbulent bubbly two-phase flow in a triangular duct, Ph. D. dissertation, Rensselaer Polytechnic Institute, 2003
- [163] Troshko, A. A., Hassan, Y. A. A two-equation model of turbulent bubbly flows. *Int. J. Multiphase Flow*, 27, pp.1965-2000, 2001
- [164] Lucas, D., Krepper, E., Prasser, H.-M. Modeling of the evolution of bubbly flow along a large vertical pipe. The 11<sup>th</sup> International Topical Meeting on Nuclear Reactor Thermal-Hydraulics (NURETH-11), Popes' Palace Conference Center, Avignon, France, October 2-6, 2005
- [165] Hibiki, T., et al. Local measurement of interfacial area, interfacial velocity and liquid turbulence in two-phase flow. *Nucl. Eng. Des.*, 184, pp.287-304, 1998
- [166] Hibiki, T., et al. Local flow measurements of vertical upward air-water flow in a round tube. *Int. J. Heat Mass Transfer*, 44, pp.1869-1888, 2001b
- [167] Liu, T.J., Bankoff, S. G. Structure of air-water bubbly flow in a vertical pipe —II. Void fraction, bubble velocity and bubble size distribution. *Int. J. Heat Mass Transfer*, 36, pp.1061-1072, 1993b
- [168] Liu, T. J. Investigation of the wall shear stress in vertical bubbly flow under different bubble size distribution. *Int. J. Multiphase Flow*, 23, pp.1085-1109, 1997
- [169] Ohnuki, A., Akimoto, H. Experimental study on transition of flow pattern and phase distribution in upward air-water two-phase flow along a large vertical pipe. *Int. J. Multi. Flow*, 26, pp.367-386, 2000
- [170] Shen, X., et al. Two-phase distribution in a vertical large diameter pipe. *Int. J. Heat and Mass Transfer*, 48, pp.211-225, 2005
- [171] Schaffrath, A., et al. TOPFLOW-a new multipurpose thermalhydraulic test facility for the investigation of steady state and transient two-phase flow phenomena. *Kerntechnik*, 66, 2001
- [172] Beyer, M., et al. *Betriebshandbuch für die Mehrzweck-Thermohydraulikversuchsanlage TOPFLOW. FZR-405, Juli 2004*
- [173] Chen, P., et al. Three-dimensional simulation of bubble column flows with bubble coalescence and breakup. *AIChE J.*, 51, pp.696-712, 2005
- [174] Martín-Valdepeñas, J. M., et al. A CFD comparative study of bubble breakup models in a turbulent multiphase jet. *Heat Mass Transfer*, 43, pp.787-799. 2007
- [175] Luo, H., Svendsen, H. F. Modeling and simulation of binary approach by energy conservation analysis. *Chem. Eng. Comm.*, 145, pp.145-153, 1996b
- [176] Celata, G.P., et al. Measurements of rising velocity of a small bubble in a stagnant fluid in one- and two-component systems. *Experimental Thermal and Fluid Science*, 31, pp.609-623, 2007
- [177] Shawakt, M. E., et al. Bubble and liquid turbulence characteristics of bubbly flow in a large diameter vertical pipe, *International Journal of Multiphase Flow*, 34, pp.767-785, 2008
- [178] Tomiyama, A., et al. Transverse migration of single bubbles in simple shear flows. *Chem. Eng. Sci.*, 57, pp.1849-1858, 2002

## 10 List of Publications

- [1] Liao, Y., et al. Development of a generalized coalescence and breakup closure for the inhomogeneous MUSIG model. Nucl. Eng. Des., 241, pp.1024-1033, 2011
- [2] Liao, Y., Lucas, D. Modeling of the evolution of bubble size distribution of gas-liquid flow inside a large vertical pipe: influence of bubble coalescence and breakup models. Proceedings of Annual Meeting on Nuclear Technology, Berlin Congress Center, May 17 – 19, 2011
- [3] Liao, Y., Lucas, D. A literature review on mechanisms and models for the coalescence process of fluid particles. Chemical Engineering Science, 65, pp-2851-2864, 2010a
- [4] Liao, Y., et al. Validation of a generalized model for bubble coalescence and breakup in MUSIG approach. Proceedings of Annual Meeting on Nuclear Technology, Berlin Congress Center, May 4 – 6, paper 204, 2010b
- [5] Liao, Y., et al. Influence of two-phase turbulence models on the bubble coalescence and breakup behavior in bubbly pipe flow. Proceedings of the 8th International Topical Meeting on Nuclear Thermal-Hydraulics, Operation and Safety (NUTHOS-8), Shanghai, China, October 10-14, 2010c
- [6] Liao, Y., Lucas, D. A literature review of theoretical models for drop and bubble breakup in turbulent dispersions. Chemical Engineering Science, 64, pp.3389-3406, 2009a
- [7] Liao, Y., Lucas, D. Breakup and coalescence models for turbulent air-water mixtures in a vertical pipe. Proceedings of Annual Meeting on Nuclear Technology, Congress centre Dresden, May 12 – 14, paper 219, 2009b
- [8] Liao, Y., Lucas, D. A new model for bubble coalescence and breakup in poly-disperse bubbly flows. Proceedings of the 13th International Topical Meeting on Nuclear Reactor Thermal Hydraulics (NURETH - 13), Kanazawa City, Ishikawa Prefecture, Japan, September 27 – October 2, Paper N13P1124, 2009c
- [9] Liao, Y., et al. Development of new coalescence and breakup closures for the Inhomogeneous MUSIG model. Proceedings of Nuclear Energy for New Europe, Bled, Slovenia, September 14-17, 2009d